

DOCTORAL THESIS

Multiscale microstructural modeling in cement and concrete: from hydration to poroelasticity, creep, and strength

submitted in satisfaction of the requirements for the degree
Doctor of Science in Civil Engineering
of the Vienna University of Technology, Department of Civil Engineering

DISSERTATION

Mehrskalenmodellierung der Mikrostruktur in Zement und Beton: von der Hydratation zu Poroelastizität, Kriechen und Festigkeit

ausgeführt zum Zwecke der Erlangung des akademischen Grades eines
Doktors der technischen Wissenschaften
eingereicht an der Technischen Universität Wien, Fakultät für Bauingenieurwesen

von

Dipl.-Ing. **Markus Königsberger**
Matrikelnr.: 0728166

Gutachter:

Univ. Prof. Dipl.-Ing. Dr. techn. **Christian Hellmich**
Institut für Mechanik der Werkstoffe und Strukturen
Technische Universität Wien

Assoc. Prof. Dipl.-Ing. Dr. techn. **Bernhard Pichler**
Institut für Mechanik der Werkstoffe und Strukturen
Technische Universität Wien

Univ. Prof. Dipl.-Ing. Dr. mont. **Paul Mayrhofer**
Institut für Werkstoffwissenschaft und Werkstofftechnologie
Technische Universität Wien

Univ. Prof. **Karen Scrivener** PhD
Construction Materials Laboratory
École Polytechnique Fédérale de Lausanne

Wien, im Oktober 2016

.....

Danksagung

Zuallererst möchte ich meinen beiden Betreuern Christian Hellmich und Bernhard Pichler des Instituts für Mechanik der Werkstoffe und Strukturen danken, die mir während meiner Arbeit stets mit Rat und Tat zur Seite gestanden sind. Ich danke ihnen für die vielen inspirierenden Diskussionen zu den einzelnen Themenbereichen der Arbeit, für die zahlreichen neuen Ideen und für die wertvollen steuernden Eingriffe bezüglich des Inhalts der Arbeit. Sie haben mir eine Modellierungsphilosophie nähergebracht, die stets auf die physikalischen Mechanismen hinter den beobachteten Phänomenen abzielt und nicht auf phänomenologische Beschreibungen mit unzähligen Parametern setzt. Dies wird meine weitere Ingenieurlaufbahn stark prägen – herzlichen Dank dafür. Bernhard Pichler danke ich im Besonderen für die Einführung in das spannende Gebiet der Mikromechanik, für sein unermüdliches Engagement und die intensive Unterstützung bei den Berechnungen, sowie für seine zahlreichen Korrekturen und Anmerkungen in der Ausarbeitungsphase. Bei Christian Hellmich bedanke ich mich einerseits für die Chance, mich im Rahmen meiner Dissertation mit einem solch komplexen Thema, das am vordersten Rand der Forschung angesiedelt ist, auseinandersetzen zu dürfen. Andererseits hat er durch sein umfangreiches Verständnis für physikalische Zusammenhänge und seine große Weitsicht diese Arbeit stark positiv beeinflusst.

Ebenfalls herzlich bedanken möchte ich mich bei meinen Kollegen des Instituts. Sie sind verantwortlich für das stets positive Arbeitsklima, das am Institut vorherrscht und das nicht unwesentlich dazu beitrug, die fordernden Forschungsaufgaben voller Motivation und Zuversicht zu lösen. Namentlich erwähnen möchte ich meinen langjährigen Bürokollegen Stefan Scheiner. Ihm danke ich einerseits besonders für die anregenden Diskussionen und guten Ratschläge in wissenschaftlichen Bereichen, andererseits auch für die vielen humorvollen Gespräche über gemeinsame Interessen abseits der Arbeit. Nicht zuletzt möchte ich mich auch für die ausgezeichnete Zusammenarbeit beim Festigkeitslehre-Team bedanken, als dessen Teil ich bei Lehraufgaben viel Erfahrung sammeln konnte. Außerdem danke ich Muhammad Irfan-ul-Hassan und Michal Hlobil für die fruchtbare wissenschaftliche Zusammenarbeit in den letzten Abschnitten meiner Dissertation.

Großer Dank gebührt meinem Lebensmenschen, meiner Partnerin Stefanie. Nur dank ihrer Unterstützung konnte ich privat den nötigen Ausgleich finden, und mich mit viel Leidenschaft und Forscherdrang in das Studium der Betonmikrostruktur stürzen. Besonders in Zeiten von Rückschlägen hat sie mich durch Verständnis und Zuspruch stets davor bewahrt, die Motivation zu verlieren. Abschließend danke ich meinen Eltern für den nötigen Rückhalt und die stetige Unterstützung während meiner gesamten Schul- und Studienzeite.

Abstract

Concrete is a microheterogeneous material. Therefore, mechanical properties of concrete are related to the hierarchically organized microstructure of the material. At an observation scale of millimeters to centimeters, one can visually distinguish sand grains, gravel aggregates, and the surrounding cement paste matrix. Resolving the cement paste matrix at smaller scales of observation reveals a surprisingly complex material microstructure. It consists of cement grains, pores, and hydrates; whereby the latter represent products of the chemical reaction between cement and water. Material modeling is particularly challenging at early material ages, because the microstructure of cement paste undergoes a continuous transformation due to the progressive consumption of cement and water, and the corresponding precipitation of hydrates.

Describing the evolving microstructures within a mathematical framework is the first objective of this work. We aim at quantifying the volumes occupied by the material constituents, as functions of the initial volumetric composition and of the maturity of the material. Thereby, we account for recently quantified phenomena like the progressive densification of calcium-silicate-hydrates (C-S-H) and the “internal curing” capacity provided by water residing in the open surface porosity of aggregates. Additional important challenges tackled in this thesis are: identification of the morphology of the individual material constituents and of their arrangement within the hierarchically organized microstructure, quantification of their mechanical properties, and modeling their interactions. Corresponding multiscale models are fed with measured or modeled input data, taken from several fields of cement science reported in the open literature. The mass density and the elastic stiffness of solid C-S-H nanoparticles are taken from small angle scattering experiments and from atomistic modeling, respectively. Strength properties and the densification behavior of C-S-H gel are taken from limit state analysis of nanoindentation tests and from nuclear magnetic resonance relaxometry tests, respectively. This way, the number of model parameters is kept at an absolute minimum and all involved quantities are physically meaningful.

Methods of continuum micromechanics are used as vehicles for scale transitions, i.e. for establishing links between microstructure and microstructural properties, on the one hand, and macroscopic mechanical properties of cementitious materials, on the other hand. Bottom-up homogenization is used to upscale physical laws introduced at material microscales and top-down identification is used to quantify constants of material constituents, which are nowadays not accessible by direct material testing. Thereby, the present thesis addresses all three major *mechanical* properties of cementitious materials: their elastic stiffness, their creep properties, and their uniaxial compressive strength. As for poroelasticity, it is shown that stiffness homogenization starting at nanoscopic solid C-S-H particles all the way up to the macroscopic elastic behavior of cement paste is possible, if one considers that space confinements in the water-filled pore spaces govern (i) the shape of precipitating solid C-S-H particles and (ii) the overall density of the evolving C-S-H gel. As for creep, it is shown that the maturity- and composition-dependent creep properties of cement pastes, mortars, and concretes – as quantified in several *thousands* of macroscopic creep experiments – can be traced back to *one* universal creep function of microscopic hydrates. As for strength, it is shown that hydrates of environmentally friendly “green” cement pastes and mortars, produced with slag or fly ash as cement replacement materials, are considerably stronger than the hydrates in ordinary Portland cement pastes.

Kurzfassung

Die makroskopischen mechanischen Materialeigenschaften von Beton werden durch seine hierarchisch organisierte, heterogene Mikrostruktur bestimmt. Auf einem Beobachtungsmaßstab von einigen Milli- bis Zentimetern kann man visuell zwischen Sand- und Gesteinszuschlagskörnern und der sie umgebenden Zementsteinmatrix unterscheiden. Betrachtet man die Matrix auf einem kleineren Beobachtungsmaßstab, offenbart sich ein überraschend komplexes Materialsystem, bestehend aus unhydrierten Zementpartikeln, Poren, Hohlräumen und Hydraten, die aus der chemischen Reaktion von Zement mit Wasser entstehen. Besonders die Modellierung des jungen Betons ist herausfordernd, da, aufgrund des ständigen Ausfallens weiterer Hydrate, die Mikrostruktur einer kontinuierlichen Transformation unterzogen ist.

Das Erfassen dieser komplexen, sich entwickelnden Mikrostruktur mithilfe eines mathematischen Modellierungskonzepts stellt das erste Ziel dieser Arbeit dar. Die Volumina der Materialbestandteile sollen als Funktion der volumetrischen Zusammensetzung und des Aushärtgrades ermittelt werden, wobei auf erst kürzlich entdeckte Phänomene, wie die zunehmende Verdichtung der Calciumsilicathydrate (C-S-H) oder die durch Wasser in der zugänglichen Oberflächenporosität der Zuschlagskörner ermöglichte "innere Nachbehandlung", eingegangen werden soll. Die Bestimmung der Hierarchie der Materialbestandteile, deren Morphologie, deren mechanischer Eigenschaften und deren Interaktion sind weitere Themen, die in dieser Arbeit behandelt werden. Die Mehrskalen-Mikrostrukturmodelle werden mit publizierten Mess- oder Modellergebnissen aus unterschiedlichen Disziplinen der Betonwissenschaften gespeist. Die Festigkeitskennwerte und das Verdichtungsverhalten von C-S-H, beispielsweise, stammen von Nanoindentationstests bzw. von Messungen der Kernspinresonanzrelaxation. Dadurch verbleibt die Anzahl der Modellparameter auf einem absoluten Minimum und alle eingeführten Materialkonstanten sind direkt physikalisch interpretierbar.

Methoden der Kontinuumsmechanik ermöglichen den Skalenübergang zwischen Mikrostruktur und makroskopischen mechanischen Materialverhalten. Durch einen Bottom-up Ansatz werden die homogenisierten mechanischen Eigenschaften auf der Makroskala basierend auf physikalischen Gesetzen auf der Mikrostruktur bestimmt; ein Top-down Ansatz quantifiziert Materialkonstanten auf der Mikrostruktur, die bis heute experimentell nicht zugänglich sind. Dabei wird auf die drei zentralen *mechanischen* Eigenschaften der zementgebundenen Materialien eingegangen: poroelastisches Verhalten und Kriechverhalten sowie auf die einaxiale Druckfestigkeit. Es wird gezeigt, dass die Steifigkeitshomogenisierung ausgehend von den Nanometer großen C-S-H Festkörpern bis hinauf zum makroskopischen elastischen Materialverhalten möglich ist, wenn man berücksichtigt, dass die beengten Platzverhältnisse in den wassergefüllten Porenräumen die Dichte und die Morphologie des C-S-H steuert. Die alters- und zusammensetzungsabhängige Kriechaktivität von Zementstein, Mörtel und Beton – die aus mehreren *tausenden* von Kriechtests bestimmt wurde – kann auf *eine einzige* universelle Kriechfunktion in den Hydraten zurückgeführt werden. Außerdem wird gezeigt, dass Hydrate in umweltfreundlichen "grünen" Zementsteinen und Mörteln, hergestellt mit Hochofenschlacke oder Flugasche als Zementersatz, wesentlich fester sind als in gewöhnlichen Portlandzementsteinen.

Contents

1	Introduction	1
1.1	Motivation	1
1.2	Main objectives of the research	5
1.3	Mathematical modeling philosophy	6
1.4	Outline of the thesis	8
2	Fundamentals of continuum micromechanics in the framework of the eigen-stress influence tensor concept	10
2.1	Representative volume element	10
2.2	Field equations	11
2.3	Homogeneous boundary condition and average rules	11
2.4	Concentration-influence relations and stiffness homogenization	12
2.5	Consideration of phase averages	13
2.6	Homogenization schemes based on matrix-inclusion problems	14
2.7	Links between the matrix-inclusion problem and the RVE	15
2.8	Conditions for phase strain concentration tensors and for eigenstress influence tensors	18
3	Hydration-driven evolution of compressive strength of OPC and blended cementitious materials: microstructural characterization, strength testing, and multiscale modeling	20
3.1	Introduction	21
3.2	Elasto-brittle multiscale strength modeling of ordinary Portland cement pastes and mortars	24
3.2.1	Micromechanical representation	24
3.2.2	Volume fractions and mechanical constants of material phases	24
3.2.3	Concentration of loading imposed on RVEs of mortar into cement paste: quantification of stress peaks	26
3.2.4	Concentration of loading imposed on RVEs of cement paste into hydrates	27
3.2.5	Identification of location and of orientation of most heavily loaded hydrate needles	30
3.2.6	Model validation on OPC pastes	32
3.2.7	Model validation on OPC mortars	34
3.2.8	Location and orientation of most heavily loaded hydrate needles	35
3.3	Strength evolution of blended cement mortars: microstructural characterization, strength testing, and multiscale modeling	36
3.3.1	Microstructural characterization: phase volume evolutions	36

3.3.2	Uniaxial compressive strength testing of blended mortars	40
3.3.3	Revisiting strength homogenization of OPC mortar based on microstructural characterization results	40
3.3.4	Strength homogenization of inert filler-blended mortars: consideration of quartz and limestone as reinforcements of the hydrate foam	42
3.3.5	Strength homogenization of SCM-blended mortars: the strength-increasing effects of slag and fly ash hydration	43
3.4	Discussion	46
3.5	Conclusions	47
	Acknowledgments	48
	Appendix A: Scale transitions, stiffness upscaling and stress concentrations	49
	Appendix B: Numerical realization of the strength criterion	50
	Appendix C: Nomenclature	51
4	Downscaling-based identification of non-aging power-law creep of cement hydrates	54
4.1	Introduction	55
4.2	Micromechanics of creeping cement pastes	56
4.2.1	Micromechanical representation of cement pastes	56
4.2.2	Homogenization of hydrate foam properties	57
4.2.3	Homogenization of cement paste properties	60
4.3	Identification of power-law creep properties of well-saturated cement hydrates	61
4.3.1	Downscaling minute-long creep test data from cement paste to hydrate level	61
4.3.2	Confirmation of hydrate creep properties by data from weeks-long creep test on 30-year-old cement paste	63
4.4	General characteristics of the creep of well-saturated hydrates	65
4.5	Discussion and conclusion	65
	Appendix A: Analytical expressions facilitating upscaling in LC space	69
	Appendix B: Notation	71
5	How water-aggregate interactions affect concrete creep: a multiscale analysis	74
5.1	Introduction	75
5.2	Modeling hydration-dependent water migration to and from the aggregates	76
5.3	Creep homogenization of mortars and concretes	79
5.4	Comparison of ultrashort creep experiments and corresponding micromechanics predictions – identification of water absorption capacities of quartz aggregates and of paste void filling extent	82
5.4.1	Experimental campaign on the mortar/concrete level	82
5.4.2	Micromechanical predictions of experimental data	85
5.4.3	Identification of water uptake capacity of “Normensand” quartz aggregates and of the paste void filling extent, from experimental data concerning Mortar #1	85

5.4.4	Confirmation of the water uptake capacity of "Normensand" quartz aggregates and of the paste void filling extent, through experimental data concerning Mortar #2	86
5.4.5	Identification of water uptake capacity of "Pannonia Kies" aggregates and of entrapped air content, from experimental data concerning Concrete #1	88
5.4.6	Confirmation of water uptake capacity of "Pannonia Kies" aggregates, through experimental data concerning Concrete #2	90
5.5	Conclusions	92
	Appendix A: Analytical expressions facilitating upscaling in LC space	94
	Appendix B: Nomenclature	95
6	Densification of C-S-H is mainly driven by available precipitation space, as quantified through an analytical cement hydration model based on NMR data	99
6.1	Introduction	100
6.2	C-S-H gel densification quantified from NMR water mass fractions	101
6.2.1	NMR quantification of water mass fractions in hydrating Portland cement pastes	101
6.2.2	Evolution of C-S-H gel density with time	102
6.2.3	Specific precipitation space controls C-S-H gel density	103
6.2.4	Interpretation of gel densification: introduction of two C-S-H classes and three hydration regimes	105
6.2.5	Nonlinear gel density evolution in hydration regime II results from linear densification of class B C-S-H gel	106
6.3	Development of a mathematical hydration model for C-S-H gel densification	108
6.3.1	Hydration chemistry of typical Portland cement pastes	109
6.3.2	Phase volumes as functions of hydration degree	110
6.3.3	Relation between hydration degree and specific precipitation space	111
6.3.4	Partition of total water volume into gel and capillary pore volumes	111
6.3.5	Identification of fitting parameters	112
6.3.6	Model consistency: quantification of C-S-H gel densification	113
6.3.7	Phase volume fraction evolutions derived from new C-S-H densification model	115
6.4	Discussion	117
6.4.1	Assessment of uncertainty regarding NMR signal fractions	118
6.4.2	Relation between existing C-S-H classifications and the new categories "class A/class B C-S-H"	118
6.4.3	Is the density of solid C-S-H indeed constant?	119
6.4.4	Sensitivity of the presented models, with respect to the density of solid C-S-H	120
6.4.5	Sensitivity of model-predicted phase volume evolutions with respect to reaction rates of tricalcium silicate and dicalcium silicate	121
6.4.6	Theoretically reachable ultimate hydration degrees	122
6.5	Conclusion	122
	Appendix A: Nomenclature	124

7	Molecular-to-continuum poroelasticity upscaling of hydrating cement pastes, considering progressive C-S-H gel densification	125
7.1	Introduction	126
7.2	Homogenization of poromechanical properties and micromechanical representation of hydrating cement paste	127
7.3	Phase volume evolutions considering progressive C-S-H gel densification . . .	128
7.4	Microporoelasticity of cement paste	130
7.5	Microporoelasticity of C-S-H foam	132
7.6	Microporoelasticity of C-S-H gel	134
7.7	Pore pressure determination for drained and undrained conditions	137
7.8	Macroscopic poromechanics state equations and undrained stiffness of cement paste	138
7.9	Model validation	140
7.9.1	Fully hydrated cement paste	140
7.9.2	Early age cement paste	141
7.10	Discussion and conclusion	142
	Appendix A: Base frames and numerical integration over the surface of a unit sphere	147
	Appendix B: Discretized aspect ratio distribution	149
	Appendix C: Computational implementation based on 15 element orientations and 20 aspect ratio families	150
	Appendix D: Accounting for phase shapes: Eshelby and Hill tensors	158
	Appendix E: Notation	160
8	Conclusions and outlook	164
8.1	Summary of the developed models	164
8.2	Research contribution and main findings	165
8.3	Perspectives	166
	Bibliography	168
	Personal information	184
	Curriculum Vitae	184
	Scientific Dissemination	185

Chapter 1

Introduction

1.1 Motivation

With an annual global production of 25 billion tons – or 3.4 tons per person each year – concrete is, after water, the most consumed substance on the planet (Klee, 2009). Given these numbers and the 250-year-long research history which goes back to French engineers trying to decipher the secret for the remarkable hardness of mortars in brick walls built in the Roman age, see Blezard (1998) for a comprehensive historical review, one might think that the material is sufficiently studied. However, the material is still far from being fully understood, mainly due to the tremendously complex microstructure of concrete which reveals itself on very small scales of observations.

Concrete consists of sand and gravel aggregates (occupying typically 60-70% of the volume), cement clinker, and water. After mixing, the clinker continuously dissolves in the water and hydration products (called “hydrates”) precipitate from the supersaturated solution. The hydrates form a binding agent that glues the aggregates together and provides the material with its strength. At the observation scale of some centimeters, concrete may look like a simple composite material where aggregates are embedded in a matrix of cement paste, which continuously hardens as the material matures, but the complexity of cement paste at observation scales of micrometers or even nanometers renders cementitious materials a challenging field of research. Understanding the macroscopic material behavior and quantitative modeling require careful consideration of these small scales of observation, where physical phenomena and processes prevail, which govern the macroscopic mechanical properties of concrete. Two well known illustrative examples underlining this statement are discussed next:

- The elastic limit of concrete, i.e. the end of the linear elastic regime of the material is triggered by microcracks occurring around the aggregates (Hsu et al., 1963; Shah and Sankar, 1987), see Fig. 1.1. In order to model the macroscopic elastic limit, one has to study the microstructure at micrometer-large observation scales. In narrow zones around the aggregates, referred to as interfacial transition zones (ITZs), the porosity is significantly larger than in the bulk of the cement paste (Ollivier et al., 1995; Diamond and Huang, 2001; Scrivener et al., 2004), in particular in young concrete. They are typically considered to be the weakest link within the microstructure of concrete (Hsu et al., 1963; Shah and Chandra, 1968; Zimbelmann, 1985). Only if microscopic failure mechanisms at the micrometer large scale of the ITZ (either ITZ-aggregate separation or ITZ cracking) are taken into account, the macroscopic elastic limits can be accurately

predicted, as it was shown by a multiscale approach (Königsberger et al., 2014a,b).

- Another example where macroscopic phenomena can be traced back to micromechanical processes is the complex creep behavior of concrete, i.e. the material feature that time-invariant stresses applied on a piece of concrete result not only in instantaneous elastic deformation, but also in progressive delayed deformation. Even several years after loading these creep strains still increase (Bažant et al., 2011) causing severe problems with concrete bridges, because traditional design codes envisioned creep to be asymptotically vanishing process. It is likely that the macroscopic creep results from microstructural sliding processes along viscous interfaces in the layered calcium-silicate-hydrates (C-S-H), see Fig. 1.2 and (Manzano et al., 2012; Shahidi et al., 2014). Therefore, studying concrete creep from a purely macroscopic viewpoint can never explain the whole complexity of the creep phenomenon simple because the physical origin is only “visible” at smaller observation scales.

Both examples show that promising and physically sound models for the complex behavior of cementitious materials require the consideration of the physical mechanism at small scales of observation. Such type of modeling is typically referred to as *micromechanical modeling* (Li and Gao, 2013) or *multiscale modeling*, respectively.

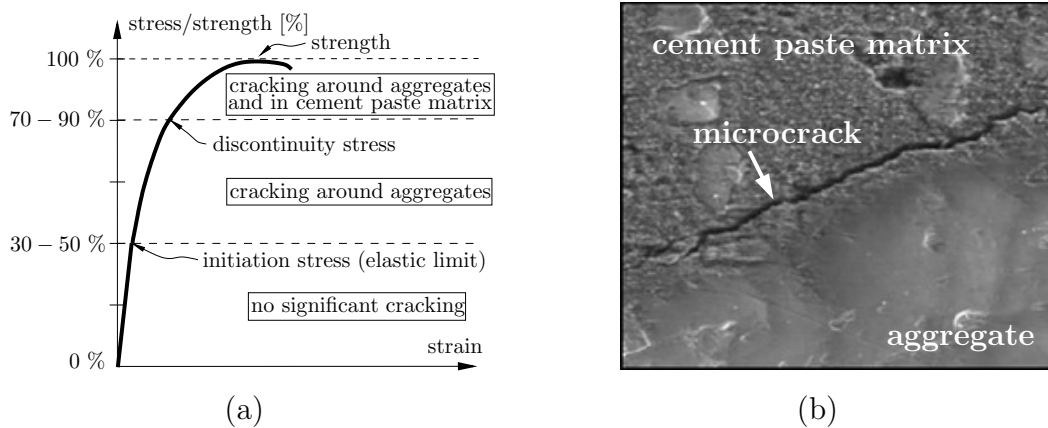


Figure 1.1: (a) Typical stress-strain diagram of concrete subjected to uniaxial compression: the elastic limit occurs at stress magnitudes of 30-50 % with respect to the uniaxial compressive strength; (b) microcrack in the interfacial transition zone (ITZ) around the aggregates which is responsible for prepeak nonlinearities in the stress-strain diagram and thus governs the elastic limit

Experimental investigations of the microstructure of cement paste provide a valuable basis for multiscale modeling. Catalyzed by the possibilities which are provided by state-of-the-art experimental techniques, concrete researchers have gained comprehensive insight into the material characteristics at micro- and nanoscales, see e.g. Fig. 1.3. The most relevant findings are very briefly summarized next. The first optical insight into cementitious microstructures was presented by Chatterji and Jeffery (1966) who showed, by using electron microscopy techniques with resolution of several micrometers, that the cement paste consists of unhydrated clinker grains, of hydration products, and of capillary pores (either filled by water or air). Calcium-Silicate-Hydrates (C-S-H) form dense areas of inner product around the unhydrated clinker grains (Diamond, 2004), see the grey shells around the white particles in Fig. 1.3(a) and the dense area of hydration products in the top left corner of Fig. 1.3(c). Further away

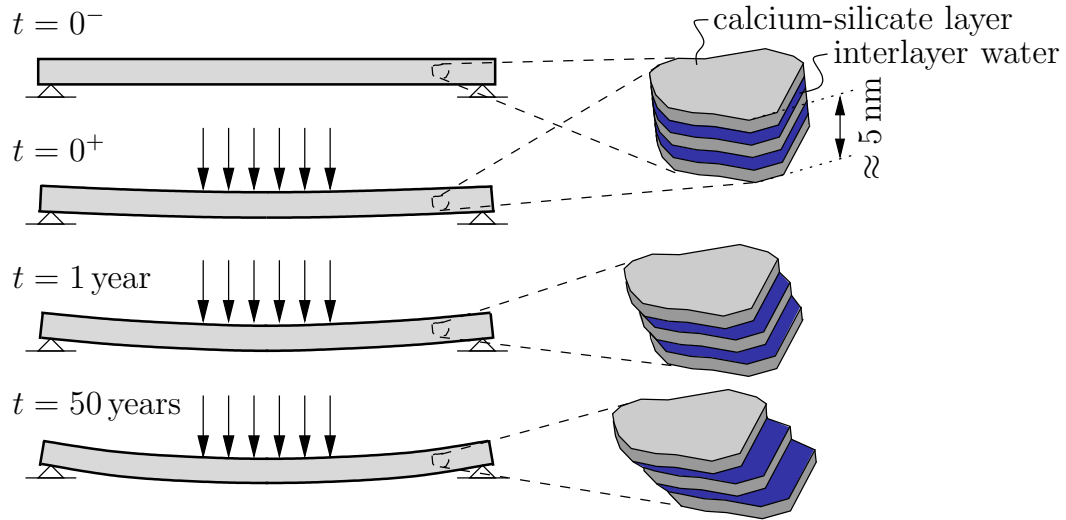


Figure 1.2: Creep deformation of concrete structures at the macroscopic scale are likely to result from microstructural sliding processes at viscous interfaces within the solid C-S-H nanoparticles

from the clinker grains, the microstructure is less dense and very heterogeneous. Pores, different crystalline hydrates (plate-like portlandite, rod-like ettringite, and monosulfate) and amorphous C-S-H are intermixed, see Fig. 1.3(b). Given that the C-S-H phase exhibits the largest sub-volume, it plays a major role in mechanics of cementitious materials. Although visual insight for this nanomaterial is challenging, significant steps towards understanding its microstructure have been accomplished during the last two decades. C-S-H is considered to be a “gel”-type material which consists of so called *solid* C-S-H nanoparticles and of water-filled gel pores with characteristic sizes of only a few nanometers (Jennings, 2000; Allen et al., 2007; Jennings, 2008). The approximately 5 nm thick solid C-S-H particles exhibit a layered structure. Calcium-silicate layers alternate with “glassy” interlayer water (Pellenq et al., 2009), whereby typically 2-3 water layers are found in one nanoparticle (Allen et al., 2007; Chiang et al., 2012; Muller et al., 2013), see the schematic representation of solid C-S-H nanoparticles in Fig. 1.2.

The microstructure of cement paste is far from being constant. First and foremost, the hydration reaction i.e. the continuous dissolution of clinker and precipitation of hydration products results in an evolving microstructure and adds another level of complexity to the material. Moreover, the choice of raw materials and their initial dosages considerably influence the microstructural properties and their evolutions. For instance, it is quite obvious from a – micromechanical point of view – that the cement paste microstructure is denser in a paste with a high cement content, i.e. with a low water-to-cement mass ratio. Given the fact the cement production alone is responsible for 5–7 % of global anthropogenic CO₂ emissions (Worrell et al., 2001; Gao et al., 2015), attempts to reduce the cement content have gained a lot of popularity in recent years. Therefore, cement clinker is blended by hydraulic waste materials (so-called supplementary cementitious materials – SCM) or by inert filler materials. Typically, this SCMs result in a delayed hydration reaction, in particular in cement pastes blended with fly ash or granulated blast furnace slag (Pane and Hansen, 2005). Because the calcium content in most of the replacement materials is smaller than in ordinary Portland cement clinker, hydration products itself are different as well, both from a chemical and a mechanical

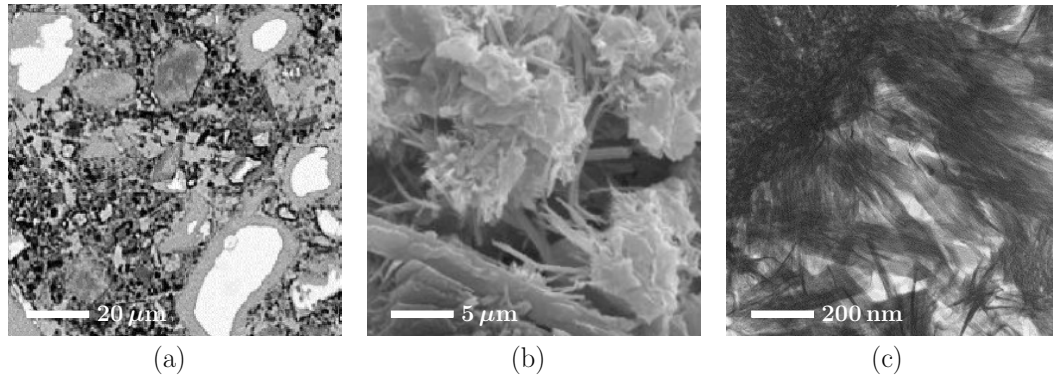


Figure 1.3: Microstructure of cement paste at various scales of observation as observed by electron microscopy imaging techniques: (a) cement paste at a scale of several tens of microns observed by backscatter-mode electron microscopy after Diamond (2004), unhydrated clinker grains in white, surrounded by dense inner product C-S-H, and embedded in a “foam” consisting of different hydrates and capillary pores; (b) hydrates at a scale of several microns observed by secondary electron microscopy after Stutzman (2001), portlandite (plate-like) and ettringite crystals (rod-like) are intermixed with amorphous C-S-H and pores; (c) inner product and outer product C-S-H at the scale of several hundreds of nanometers as observed by transmission electron microscopy after Richardson (2004)

perspective (Lothenbach et al., 2011; Zadeh and Bobko, 2013). In summary, cement and concrete researchers have to deal with a great variety of materials and microstructures.

Given the aforescribed microstructural complexity and variety, multiscale micromechanics modeling of cementitious materials is a challenging field of research. Several modeling approaches qualify for such aspects. Discrete numerical approaches such as Finite Element modeling (FEM), Discrete Element modeling (DEM), or Lattice Discrete Particle models (LDPM) have shown to be very useful to model several aspects of the mechanical behavior of cementitious materials, see e.g. (Hentz et al., 2004; Haecker et al., 2005; Wriggers and Moftah, 2006; Cusatis et al., 2011; Hlobil et al., 2016). In general, such approaches face difficulties, since they require the generation of detailed microstructures and they are computationally expensive. Within this thesis, a *continuum* micromechanics approach is applied. Thereby, the material’s microstructure is not resolved in every single detail. Instead, subdomains (called material phases) with constant micromechanical and micromorphological properties and their interaction are identified. This allows for very elegant modeling of the material in an analytical fashion. Indeed, continuum micromechanics approaches, see e.g. (Bernard et al., 2003b; Sanahuja et al., 2007; Scheiner and Hellmich, 2009; Pichler et al., 2009; Pichler and Hellmich, 2011; Stefan et al., 2010; Bary, 2011; Venkovic et al., 2013), have turned out to be efficient and successful for predicting the macroscopic properties of cementitious materials, and this provides the motivation to continue this line of research.

The most fundamental challenge in developing micromechanical models is to accurately predict the phase volumes fractions. Customarily, they are estimated from the Powers model (Powers and Brownyard, 1947; Powers, 1958), relying on experimentally determined water vapor isotherms. The model provides analytical expressions for the phase volume evolutions of clinker, hydrates, water-filled capillary pores, and air-filled voids as functions of the pastes’ composition in terms of the initial water-to-cement mass ratio and of the pastes’ maturity in terms of the hydration degree. Notably, the Powers model implies a proportionality between

the hydrate volume and the hydration degree. Given its predictive character, the model has survived for almost 60 years, although it has some shortcomings and limitations. In the context of the C-S-H hydrates, the Powers-predicted linearity is nowadays questioned from nuclear magnetic resonance frequency experiments (Muller et al., 2012, 2013). The C-S-H hydrates are found to progressively densify during ongoing hydration. Still, the governing mechanism for the experimentally observed composition-dependent densification behavior is under debate and there is dire need for a mathematical description of the process. Moreover, the Powers model considers cement paste as a thermodynamically closed system, and as such it is not able to model water migration processes between cement paste and aggregates. Depending on the type of aggregates and on their initial water content, however, such migration processes are of significant importance for mortars or concretes. Part of the mixing water might initially be absorbed from by the aggregates, but later on, it might be soaked back to the water-consuming cement paste. Such a water supply of aggregates is referred to as internal curing (Bentz et al., 2005; Jensen and Lura, 2006). Building up a mathematical framework which still keeps the predictive capabilities of Powers' approach but incorporates the aforementioned phenomena is another motivation of the research.

1.2 Main objectives of the research

The main objective of the present thesis is to predict a variety of mechanical properties of cementitious materials by means of continuum micromechanics approaches. In the context of macroscopic mechanical properties, the focus is on strength, creep, and poroelastic properties, as described next.

- **Strength:**

The uniaxial compressive strength, which is the first focus of the thesis, is the central material property for structural applications. During the last years, continuum micromechanics-based modeling was successfully applied to predict the strength evolution of ordinary Portland cement paste (Pichler et al., 2009; Pichler and Hellmich, 2011; Pichler et al., 2013a). Based on these achievements, the model should be extended in two directions,

- to the mortar scale by explicitly considering the stress concentrations around the sand aggregates which are driven by the stiffness contrast between cement paste matrix and sand aggregates; and
- to different types of blended cement pastes and mortars by incorporating replacement type-specific microstructural peculiarities and measured microstructural phase evolutions

- **Creep:**

Quantifying creep mechanisms at the microscale is a major challenge in concrete research. Relying on a recently launched experimental creep campaign (Irfan-ul-Hassan et al., 2016) and again on the existing continuum micromechanics representation of cement paste developed from (Pichler and Hellmich, 2011), we aim for downscaling-based identification of the creep behavior of the hydrates. In particular, we aim at clarifying, whether or not, the creep behavior of hydrates in Portland cement pastes is universal, although the cement paste creep potential reduces significantly during the maturation of the paste. Moreover, we aim at upscaling the creep behavior of cement pastes to the scale of mortars and concretes.

- **Poroelastic behavior:**

The strength and creep predictions will be based on the microstructural representation developed by Pichler and Hellmich (2011), which starts at the micrometer-large scale of the hydrates. In the context of elasticity upscaling, we seek for going even further down to the nanometer-large scale of solid C-S-H nanoparticles. This way, we might be able to transfer the stiffness, obtained from solid C-S-H simulations at the atomic level (Pellenq et al., 2009; Manzano et al., 2012) all the way up to the macroscopic stiffness of cement paste. Hence, our micromechanics model is required to bridge several magnitudes of length scales. Moreover, we aim at understanding the role of water in gel and capillary pores on the elastic behavior of the paste and for quantifying the stiffening effect resulting from pore water pressures.

The sought models should be valid for all maturity states of cementitious materials, i.e. hydration-induced hardening should be captured by our approach. This requires access to the phase volume evolutions accompanying to the hydration process. Overcoming the aforementioned limitations of the customarily used Powers model (Powers and Brownyard, 1947; Powers, 1958) is an important secondary objective of the thesis. Aiming at accurate micromechanics predictions for mortar and concrete, water migration processes from the paste to the aggregates and then back from the aggregates to the paste have to be considered. Consequently, we seek for an engineering approach to model this water migration processes. In a similar fashion, we also aim at taking into account the experimentally observed C-S-H densification. In the spirit of the ready-to-use mathematical expressions provided by the Powers model, a mathematical model for the phase volume evolutions should be developed.

1.3 Mathematical modeling philosophy

A model is typically understood as (Dym, 2004)

a miniature representation of something; a pattern of something to be made; an example for imitation or emulation; a description or analogy used to help visualize something (e.g., an atom) that cannot be directly observed; a system of postulates, data and inferences presented as a mathematical description of an entity or state of affairs.

Using the precise and concise “language” of mathematics has considerably improved modeling activities and has led to several *mathematical models* which can be defined as (Meyer, 2012)

a model whose parts are mathematical concepts, such as constants, variables, functions, equations, inequalities, etc.

In the context of material modeling, new modeling concepts together with the progressively increasing computational power have led to a whole new generation of models, potentially of multiscale and interdisciplinary character. Typical objectives are:

- increasing the scientific understanding of material phenomena through their quantification, e.g. through identification of the central physical mechanisms which govern the phenomena
- predicting scenarios which are difficult to be accessed experimentally insight is limited, e.g. because respective test campaigns would span over very large time intervals

- study the sensitivity of changes regarding the material composition or the environmental conditions on the physical phenomena
- provide a scientifically sound foundation for decision makers

Achieving the aforementioned objectives requires careful model development. The following steps are essential and have to be sequentially tackled (Dym, 2004; Scheiner, 2009):

1. Identification of the underlying physical mechanisms:

First and foremost, the physical mechanisms which govern the phenomenon to be studied have to be identified. In this context, micromechanical multiscale models have gained a lot of popularity during the recent years, since they are able to capture the physical mechanisms at the scale where they occur. By means of upscaling or homogenization techniques, the macroscopic material behavior is obtained. Rather than trying to incorporate all physical processes potentially occurring in the material, it is of central importance to consider especially those mechanisms which do have a significant effect on the phenomenon, according to the principle “*as simple as possible, as complex as necessary*”. Such models typically require only a very limited amount of material parameters which is beneficial for the robustness and the reliability of modeling results.

2. Mathematization of the mechanisms:

The underlying physical mechanisms have to be put into a mathematical framework, which typically yields a set of governing equations. Again, simple mathematical forms are preferred, e.g. a non-linear function for quantifying a physical relation is only preferable if it significantly increases the reliability in comparison to a linear function.

3. Choice of solution method:

The priority is to solve as much of the problem in an analytical or semi-analytical fashion. Thanks to the continuum micromechanics approach used in this thesis, numerical methods are required only very rarely. Consequently, inevitable problems which come along with numerical methods such as the Finite Element Method, e.g. mesh size dependence, are avoided.

4. Code verification:

If the mathematical model is implemented into a computer program, code verification attempts such as debugging and plausibility checks are of utmost importance for obtaining proper model results. Therefore, we strive, at every possible position, to check the obtained results based on independent, mostly simpler models. For instance, the homogenized stiffness tensor of a material, which is estimated based on the Mori-Tanaka or the self-consistent scheme can be verified by checking whether or not, the estimate falls in between the Voigt and Reuss bounds, or the much stricter Hashin-Shtrikman bounds (Hashin and Shtrikman, 1962), respectively.

5. Parameter identification:

Preferably, the developed model is based on readily measurable and physically interpretable universal material constants only. Any other parameter should be avoided. Clearly, this guideline cannot be obeyed in a strict sense in some application, as e.g. neither the elastic stiffness nor the strength of the nanometer-sized solid C-S-H particle can be determined experimentally. As a remedy, parameters might be identified by means of a top-down approach based on macroscopic experimental data, a process which is typically referred to as model calibration.

6. Model validation based on experimental data:

In the sense of Popper (1959), model validation by means of comparing model predictions to experimental results has to be performed based on falsification attempts. The more experimental campaigns the model withstands unfalsified, the more relevant it is. Notably, the experimental data used for model validation has to be *independent*. Hence, if experimental results are used for top-down identification of material parameters of a model, the very same data disqualify per se for model validation purposes. In other words, only “blind” predictions allow for falsification attempts.

7. Improvement of the model:

Within an iterative loop, unsuccessful validation attempts should lead to an improvement of the model. In this context, one should start at the very beginning, check whether or not an important physical process might have been overlooked and question the underlying mathematical assumptions, etc.

A model which is successfully developed according to the described model philosophy, can be evaluated in order to *predict* the material behavior for situations of interest. Thus, it might be able to replace expensive experimental campaigns, as targeted in Chapters 6 where a model is sought which provides access to the density of the C-S-H gel for arbitrary maturity states and arbitrary compositions (in terms of the water-to-cement mass ratio) of the cement paste or as targeted in Chapter 5 where the creep behavior of different mortars or concretes should be predicted based on the measured creep behavior of the cement paste used to produce the mortar/concrete. Mathematical modeling might be also useful to identify the physical behavior at very small scales, where trustworthy experimental data is still not available. In Chapter 4, we aim for such an identification, in more detail we downscale the experimentally determined creep behavior at the scale of cement paste in order to identify the universal creep constants of the hydrates. Moreover, the mathematical models which are developed herein aim at providing valuable insight into microstructural features and physical mechanism at the level of the cement hydrates. For instance, it we aim at studying whether or not, the cohesion of the C-S-H in blended cements is significantly larger than the cohesion of C-S-H in ordinary Portland cement paste (see Chapter 3 for more details). We also strive for a knowledge gain from the microporomechanical modeling campaign for hydrating cement paste, see Chapter 7, where the potential stiffening effect of the water entrapped in the nanometer-sized porosity should be deciphered.

1.4 Outline of the thesis

In accordance with the objectives of the research, the thesis is structured as follows. The fundamentals of continuum micromechanics, including the eigenstress influence tensor concept, are revisited in Chapter 2. The following five chapters contain either already accepted or published papers, or quite mature paper drafts which are planned to be submitted for publication– potentially in further improved form. Chapter 3 deals with modeling the uniaxial compressive strength of cement pastes and mortars made from pure Portland cement clinker or from blended clinker. This is followed by a two chapters for creep modeling. Firstly, the hydrate creep behavior is identified by means of downscaling macroscopic material tests performed on cement pastes (see Chapter 4). Secondly, the measured creep behavior of cement paste is upscaled to the level of mortar and concrete, taking into account that water migrates from the paste to aggregates directly after mixing and vice versa during the hydration. In Chapter 6 we use experimental results from nuclear magnetic resonance relaxometry,

available in the open literature, to study the evolution of the C-S-H gel density based on space confinement considerations. This further allows for obtaining quantitative expressions for phase volume evolutions accompanying the hydration reaction. Next, we develop a three-scale representation of cement paste incorporating gel pores and capillary pores (see Chapter 7). Based on the mathematical expression for the phase volume evolutions and on this new micromechanical representation, the pore pressures and the phase stiffnesses are upscaled to poroelastic properties at the macroscopic scale of cement paste. Finally, the thesis is concluded and completed with a future outlook (see Chapter 8).

Fundamentals of continuum micromechanics in the framework of the eigenstress influence tensor concept

2.1 Representative volume element

Continuum micromechanics approaches for material modeling rely on the concept of representative volume elements (RVE). The studied volume is representative for the actual microstructure of the material if it fulfills the principle of scale separation. This principle requires, on the one hand, that the structural dimensions and the characteristic dimensions of external loading, \mathcal{L} , are considerably larger than the characteristic size of the RVE, ℓ , and, on the other hand, that the characteristic size of the RVE is significantly larger than the characteristic length of the inhomogeneities within the RVE, d . In mathematical terms, this reads as

$$\mathcal{L} \gg \ell \gg d. \quad (2.1)$$

As for the first inequality condition in (2.1), factors of 5 to 10 between the size of the structure and the RVE size are typically considered in order to enable differential calculus. Notably, a factor of 7 is found to be sufficient in order to deal with RVEs subjected to uniform stress and strain boundary conditions for ultrasonic wave experiments where the wavelength λ takes the role of the characteristic size \mathcal{L} , see Kohlhauser and Hellmich (2013) for details. The second inequality condition in (2.1) allows for assigning homogenized properties of the RVE (such as a homogenized stiffness). Drugan and Willis (1996) studied two-phase RVEs with randomly distributed non-overlapping identical spheres embedded in a matrix phase. By using a variational nonlocal formulation they compared the strain variations under consideration of a homogenized modulus based on the RVE to the strain variations by applying the load on the actual microstructure. Surprisingly, an error of 5 % is already achieved if the RVE size is only by a factor of two larger than the inclusion size, and a factor 4.5 leads to errors of 1 % or smaller. Notably, these factors refer to inclusion volume fractions of 25% and to a stiffness contrast between matrix and inclusion which goes to infinity (inclusions are pores). For all other scenarios, the maximum RVE size would be even smaller if similar errors were tolerated.

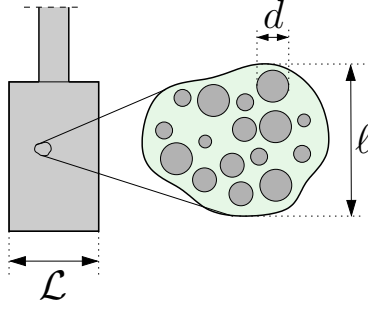


Figure 2.1: Illustration of the principle of scale separation: a representative volume element (RVE) with characteristic size ℓ contains inhomogeneities with characteristic size d and is embedded in a structure with characteristic size \mathcal{L}

2.2 Field equations

Within the RVE, Ω , we formulate the field equations of linear elasticity. The stress-strain relation reads as

$$\boldsymbol{\sigma}(\underline{x}) = \mathbb{C}(\underline{x}) : [\boldsymbol{\varepsilon}(\underline{x}) - \boldsymbol{\eta}(\underline{x})] , \quad (2.2)$$

where $\boldsymbol{\sigma}$ and $\boldsymbol{\varepsilon}$ are the (second-order) stress and strain tensors, \mathbb{C} is the (fourth-order) elastic stiffness tensor, \underline{x} is for the location vector, labeling positions within and on the boundary of the RVE, and $\boldsymbol{\eta}(\underline{x})$ denotes the second-order eigenstrain tensor which considers potential thermal strains, plastic strains, or pore pressures. The static equilibrium conditions disregarding volume forces and read as

$$\text{div } \boldsymbol{\sigma}(\underline{x}) = 0 . \quad (2.3)$$

Finally we consider linear strain-displacement relations, reading as

$$\boldsymbol{\varepsilon}(\underline{x}) = \frac{1}{2} \left[\nabla \underline{\xi} + (\nabla \underline{\xi})^T \right] , \quad (2.4)$$

where $\underline{\xi}$ stands for the displacement vector and $\nabla \underline{\xi}$ for the gradient of this field.

2.3 Homogeneous boundary condition and average rules

Homogeneous (macroscopic) strains \boldsymbol{E} , are prescribed at the boundary of the RVE, $\partial\Omega$. They are applied in terms of microscopic displacements $\underline{\xi}$ of the form

$$\underline{\xi}(\underline{x}) = \boldsymbol{E} \cdot \underline{x} \quad \forall \underline{x} \in \partial\Omega . \quad (2.5)$$

For a field of compatible (kinematically admissible) microstrains $\boldsymbol{\varepsilon}(\underline{x})$, the strain boundary condition (2.5) implies that the (spatial) average of the microstrain field is equal to the macrostrain (Hill, 1963; Hashin, 1983; Zaoui, 2002), i.e.

$$\boldsymbol{E} = \frac{1}{\Omega} \int_{\Omega} \boldsymbol{\varepsilon}(\underline{x}) dV . \quad (2.6)$$

The microscopic deformations (2.5) provoke microstresses inside the RVE and tractions \underline{T} at the boundary of the RVE, reading as

$$\underline{T} = \boldsymbol{\sigma}(\underline{x}) \cdot \underline{n}(\underline{x}) , \quad (2.7)$$

with \underline{n} denoting the unit (outward) normal vector to the boundary $\partial\Omega$. The external work done by these tractions reads as

$$W^{ext} = \frac{1}{\Omega} \int_{\partial\Omega} \underline{T}(\underline{x}) \cdot \underline{\xi}(\underline{x}) dS. \quad (2.8)$$

Inserting Eqs. (2.5) and (2.7) into (2.8) and making use of the divergence theorem yields

$$W^{ext} = \underline{E} : \frac{1}{\Omega} \int_{\Omega} \underline{\sigma}(\underline{x}) dV = \underline{E} : \underline{\Sigma} \quad (2.9)$$

The force quantity in (2.9), which is doing work on the macrostrains is the spatial average of the microstresses, and is therefore denoted as macrostress $\underline{\Sigma}$, reading as

$$\underline{\Sigma} = \frac{1}{\Omega} \int_{\Omega} \underline{\sigma}(\underline{x}) dV. \quad (2.10)$$

This also implies that the (spatial) average of the local work done from equilibrated microstresses and compatible microstrains is equal to the work done from macrostresses and macrostrains, typically referred to as Hill's lemma (Hill, 1963; Zaoui, 2002):

$$\underline{\Sigma} : \underline{E} = \frac{1}{\Omega} \int_{\Omega} \underline{\sigma}(\underline{x}) : \underline{\varepsilon}(\underline{x}) dV. \quad (2.11)$$

A similar average rule for the local power $\underline{\sigma}(\underline{x}) : \dot{\underline{\varepsilon}}(\underline{x})$ (with $\dot{\underline{\varepsilon}}$ denoting the time derivative of the strains) applies.

2.4 Concentration-influence relations and stiffness homogenization

Next we aim at deriving relations between macroscopic and microscopic quantities. The relationship between local microscopic strains $\underline{\varepsilon}(\underline{x})$, and the applied macrostrain \underline{E} as well as the eigenstrains $\underline{\eta}(\underline{x})$ has to be linear due to the linearity of the field equations (2.2) to (2.4) and the boundary condition (2.5). It might be written as (Pichler and Hellmich, 2010)

$$\underline{\varepsilon}(\underline{x}) = \underline{\mathbb{A}}(\underline{x}) : \underline{E} + \int_{\Omega} \underline{\mathbb{D}}(\underline{x}, \underline{y}) : \underline{\eta}(\underline{y}) d\Omega(\underline{y}), \quad (2.12)$$

where $\underline{\mathbb{A}}(\underline{x})$ denotes the fourth-order strain concentration tensor quantifying the concentration of macrostrains into microstrains, $\underline{\mathbb{D}}(\underline{x}, \underline{y})$ denotes the eigenstrain influence tensors, quantifying the effect of eigenstrains at location \underline{y} on microstrains at position \underline{x} . Eq. (2.12) depicts that strain concentration tensors and eigenstrain influence tensors are essential for the strain concentrations from the macroscale to the microscale. Since the eigenstrains $\underline{\eta}(\underline{x})$ can be given in terms of eigenstresses $\underline{\pi}(\underline{x})$ as

$$\underline{\eta}(\underline{y}) = -\underline{\mathbb{C}}(\underline{y})^{-1} : \underline{\pi}(\underline{y}), \quad (2.13)$$

Eq. (2.12) can be reformulated as

$$\underline{\varepsilon}(\underline{x}) = \underline{\mathbb{A}}(\underline{x}) : \underline{E} - \int_{\Omega} \underline{\mathbb{Q}}(\underline{x}, \underline{y}) : \underline{\pi}(\underline{y}) d\Omega(\underline{y}), \quad (2.14)$$

where $\mathbb{Q}(\underline{x}, \underline{y})$ denotes, the eigenstress influence tensor, quantifying the effect of eigenstresses at location \underline{y} on microstrains at position \underline{x} . Combination of (2.12) to (2.14) allows for obtaining eigenstress influence tensors from eigenstrain influence tensor as

$$\mathbb{Q}(\underline{x}, \underline{y}) = \mathbb{D}(\underline{x}, \underline{y}) : \mathbb{C}(\underline{y})^{-1}. \quad (2.15)$$

Based on the strain concentration relations (2.12) and (2.14), we aim at stiffness homogenization next, i.e. we aim at upscaling the local stiffness $\mathbb{C}(\underline{x})$ to the homogenized (macroscopic) stiffness of the RVE \mathbb{C}_{hom} . In order to derive the homogenized stiffness, we focus on an eigenstrain/eigenstress-free case, $\boldsymbol{\eta}(\underline{y}) = \boldsymbol{\pi}(\underline{y}) = 0$. Specification of Eq. (2.14) for $\boldsymbol{\pi}(\underline{y}) = 0$, insertion of the resulting expression into the elastic constitutive law (2.2), and further inserting the resulting expression into the stress average rule (2.10) yields

$$\boldsymbol{\Sigma} = \frac{1}{\Omega} \int_{\Omega} \mathbb{C}(\underline{x}) : \mathbb{A}(\underline{x}) dV : \boldsymbol{E}. \quad (2.16)$$

Comparison of (2.16) with the macroscopic elastic law reading as

$$\boldsymbol{\Sigma} = \mathbb{C}_{hom} : \boldsymbol{E}, \quad (2.17)$$

allows for the identification of the homogenized stiffness tensor, \mathbb{C}_{hom} , as (Zaoui, 2002)

$$\mathbb{C}_{hom} = \frac{1}{\Omega} \int_{\Omega} \mathbb{C}(\underline{x}) : \mathbb{A}(\underline{x}) dV. \quad (2.18)$$

Eq. (2.18) implies that the strain concentration tensor is also a prerequisite for stiffness upscaling.

2.5 Consideration of phase averages

An macrohomogeneous but microheterogeneous material is typically too complex as to resolve its microstructure in full detail. As a remedy, n_p quasi-homogeneous subdomains (called material phases) are considered to represent the microstructure, whereby the phases exhibit a specific shape, a specific elastic stiffness \mathbb{C}_j , a specific eigenstress $\boldsymbol{\pi}_j$, and specific volume fractions f_j . The latter is defined as

$$f_j = \frac{\Omega_j}{\Omega}, \quad \text{with} \quad \Omega = \Omega_1 \cup \Omega_2 \cup \dots \cup \Omega_{n_p}, \quad (2.19)$$

where Ω denotes the total RVE volume and Ω_j denoted the subvolume of phase j .

Next, we define volume averages of microstrains and microstresses in phase j , $\boldsymbol{\varepsilon}_j$ and $\boldsymbol{\sigma}_j$, respectively, reading as

$$\boldsymbol{\varepsilon}_j = \frac{1}{\Omega_j} \int_{\Omega_j} \boldsymbol{\varepsilon}(\underline{x}) dV \quad \text{and} \quad \boldsymbol{\sigma}_j = \frac{1}{\Omega_j} \int_{\Omega_j} \boldsymbol{\sigma}(\underline{x}) dV. \quad (2.20)$$

Consideration of (2.19) in (2.20) and insertion into the average rules (2.10) and (2.6), respectively, yields strain and stress average rules in terms of average phase strains and average phases stresses, respectively, reading as

$$\boldsymbol{E} = \sum_{i=1}^{n_p} f_i \boldsymbol{\varepsilon}_i \quad \text{and} \quad \boldsymbol{\Sigma} = \sum_{i=1}^{n_p} f_i \boldsymbol{\sigma}_i \quad (2.21)$$

The strain concentration relation (2.14) can be also specified for phase averages, resulting in

$$\varepsilon_j = \mathbb{A}_j : \mathbf{E} - \sum_{i=1}^{n_p} \mathbb{Q}_{ji} : \boldsymbol{\pi}_i, \quad (2.22)$$

where \mathbb{A}_j stands for the fourth-order *phase* strain concentration tensor of phase j and \mathbb{Q}_{ji} stands for the eigenstress influence tensors quantifying the influence of eigenstresses in phase i , $\boldsymbol{\pi}_i$, on the average microstrains of phase j . Combining the elastic law of the j -th phase, $\boldsymbol{\sigma}(\underline{x}) = \mathbb{C}_j : \boldsymbol{\varepsilon}(\underline{x})$, with Eqs. (2.6), yields

$$\boldsymbol{\sigma}_j = \mathbb{C}_j : \boldsymbol{\varepsilon}_j. \quad (2.23)$$

By analogy to Section 2.3, the homogenized stiffness is derived by considering $\boldsymbol{\pi}_j = 0$ in (2.22), by inserting the obtained expression into Eq. (2.23), and by inserting of the established expression for $\boldsymbol{\sigma}_j$ into (2.21)₂ and by comparing the result with (2.17), providing access to Hill's expression for the macroscopic stiffness (Hill, 1963):

$$\mathbb{C}_{hom} = \sum_{j=1}^{n_p} f_j \mathbb{C}_j : \mathbb{A}_j \quad (2.24)$$

It turns out that the concentration and influence tensors are the key to both macro-to-micro concentration and to micro-to-macro homogenization. Throughout this thesis, the aforementioned tensors are *estimated* based on matrix-inclusion problems as described next.

2.6 Homogenization schemes based on matrix-inclusion problems

In general, phase strain concentration tensors and eigenstress influence tensors are not known up to analytical precision. However, micromechanical *estimates* for these tensors can be derived from so-called matrix-inclusion problems.

We consider a single ellipsoidal inclusion (with uniform stiffness \mathbb{C}_i and uniform eigenstress $\boldsymbol{\pi}_i$) to be embedded in an infinite matrix (with uniform stiffness \mathbb{C}_0 and uniform eigenstress $\boldsymbol{\Pi}_0$), see Fig. 2.2. The infinite boundary of the matrix is subjected to homogeneous strains,

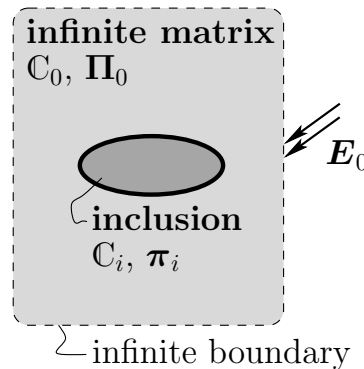


Figure 2.2: Eshelby problem: ellipsoidal inclusion embedded in an infinite matrix

\mathbf{E}_0 . Remarkably, the stress state in the inclusion is homogeneous and can be written as (Eshelby, 1957; Laws, 1977; Pichler and Hellmich, 2010):

$$\bar{\boldsymbol{\varepsilon}}_i = \mathbb{A}_{\infty,i} : \left[\mathbf{E}_0 - \mathbb{P}_i^0 : (\boldsymbol{\pi}_i - \boldsymbol{\Pi}_0) \right], \quad \text{with} \quad \mathbb{A}_{\infty,i} = \left[\mathbb{I} + \mathbb{P}_i^0 : (\mathbb{C}_i - \mathbb{C}_0) \right]^{-1}. \quad (2.25)$$

In Eq. (2.25), \mathbb{I} stands for the fourth-order unity tensor with components $I_{ijkl} = \frac{1}{2} \delta_{ik} \delta_{jl} + \delta_{il} \delta_{kj}$, where Kronecker delta δ_{ij} being 1 for $i = j$ and 0 otherwise. Moreover, \mathbb{P}_i^0 denotes the fourth-order Hill tensor which depends on the shape of the inclusion, as well as on the elastic properties of the infinite matrix, and $\mathbb{A}_{\infty,i}$ denotes the Eshelby problem-related strain concentration tensor. The latter tensor provides, in the eigenstress-free situation, the link between boundary strains \mathbf{E}_0 and inclusion strains $\boldsymbol{\varepsilon}_i$.

In continuum micromechanics, the strain state $(2.25)_1$ is used as an estimate for the average strain within one phase $\boldsymbol{\varepsilon}_j$, Zaoui (2002)

$$\bar{\boldsymbol{\varepsilon}}_i = \boldsymbol{\varepsilon}_j = \mathbb{A}_{\infty,i} : \left[\mathbf{E}_0 - \mathbb{P}_i^0 : (\boldsymbol{\pi}_i - \boldsymbol{\Pi}_0) \right]. \quad (2.26)$$

To this end, the link between the actual RVE on the one hand and the matrix inclusion problem on the other hand has to be established, as discussed in the following section.

2.7 Links between the matrix-inclusion problem and the RVE

First and foremost, the properties of the inclusion (shape, eigenstress and stiffness) are set equal to the corresponding properties of the material phase in the RVE. Accordingly an n_p -phase RVE relates to n_p matrix-inclusion problems.

In the context of linking the Eshelby problem-related boundary strains \mathbf{E}_0 to the RVE-related macrostrains \mathbf{E} , we specify the phase strain average rule $(2.21)_1$ for (2.26) and solve the resulting expression for \mathbf{E}_0 , resulting in

$$\mathbf{E}_0 = \left(\sum_{i=1}^{n_p} f_i \mathbb{A}_{\infty,i} \right)^{-1} : \left[\mathbf{E} + \sum_{i=1}^{n_p} f_i \mathbb{A}_{\infty,i} : \mathbb{P}_i^0 : (\boldsymbol{\pi}_i - \boldsymbol{\Pi}_0) \right]. \quad (2.27)$$

Insertion of Eq. (2.27) into the expression for the estimated phase strains (2.26) yields

$$\boldsymbol{\varepsilon}_j = \bar{\mathbb{A}}_j : \left[\mathbf{E} + \sum_{i=1}^{n_p} f_i \mathbb{A}_{\infty,i} : \mathbb{P}_i^0 : (\boldsymbol{\pi}_i - \boldsymbol{\Pi}_0) \right] - \mathbb{A}_{\infty,j} : \mathbb{P}_j^0 : (\boldsymbol{\pi}_j - \boldsymbol{\Pi}_0), \quad (2.28)$$

with the abbreviation $\bar{\mathbb{A}}_j$ standing for

$$\bar{\mathbb{A}}_j = \mathbb{A}_{\infty,j} : \left(\sum_{i=1}^{n_p} f_i \mathbb{A}_{\infty,i} \right)^{-1}. \quad (2.29)$$

Comparison of the coefficients of \mathbf{E} in (2.28) and in (2.22) allows for the identification of the auxiliary tensor $\bar{\mathbb{A}}_j$ as the phase strain concentration tensor \mathbb{A}_j . The estimated phase strain concentration tensor is independent of the eigenstresses, see Eq. (2.29). Consequently, the homogenized stiffness is not influenced by eigenstresses as well [see Eq. (2.24)]. A closed-form expression for the homogenized stiffness is obtained by inserting Eq. (2.29) into Hill's relation of the homogenized stiffness (2.24) and considering the expression for the infinite strain concentration tensor $(2.25)_2$:

$$\begin{aligned} \mathbb{C}_{hom} = & \left\{ \sum_i f_i \mathbb{C}_i : \left[\mathbb{I} + \mathbb{P}_i^0 : (\mathbb{C}_i - \mathbb{C}_0) \right]^{-1} \right\} : \\ & \left\{ \sum_j f_j \left[\mathbb{I} + \mathbb{P}_j^0 : (\mathbb{C}_j - \mathbb{C}_0) \right]^{-1} \right\}^{-1}. \end{aligned} \quad (2.30)$$

Concerning the link between the auxiliary stiffness of the infinite matrix, \mathbb{C}_0 , and a corresponding quantity of the RVE, two different approaches are discussed. As long as the RVE exhibits a matrix-inclusion-type morphology, i.e. if the RVE is a composite material [e.g. concrete at a scale of several centimeters, see Fig. 2.3(a)], \mathbb{C}^0 is chosen to be equal to the stiffness of RVE-related matrix phase (Zaoui, 2002). This concept is referred to as the Mori-Tanaka scheme (Mori and Tanaka, 1973; Benveniste, 1987). In case of a polycrystalline

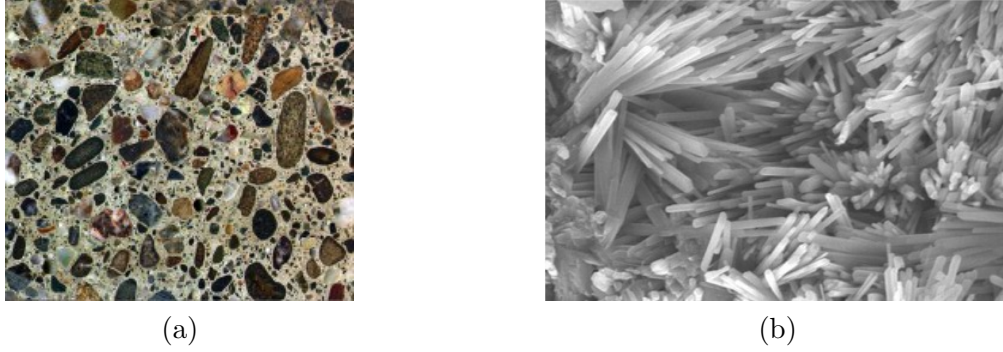


Figure 2.3: Microstructures of two materials: (a) concrete at the scale of several centimeters exhibits a matrix-inclusion-type morphology with aggregates embedded in a cement paste matrix, from <http://monteiro.ce.berkeley.edu/lectures.html>; (b) gypsum at the scale of several micrometers exhibits a polycrystalline morphology with needle-shaped crystals orientated in all space directions, from (Carvalho et al., 2008)

RVE, constituted by a disordered arrangement of phases which are in direct mutual interaction [e.g. gypsum at a scale of several microns, see Fig. 2.3(b)], \mathbb{C}_0 is set to be equal to the homogenized RVE stiffness \mathbb{C}_{hom} (Zaoui, 2002). This concept, in turn, is referred to as self-consistent scheme (Hershey, 1954; Kröner, 1958), and it results in an implicit definition of \mathbb{C}_{hom} , rendering an iterative computation of the expression for the homogenized stiffness necessary.

We are left with linking the auxiliary matrix eigenstress with a corresponding quality of the RVE. There are two independent ways to calculate the macroscopic stresses, Σ , Levin's theorem (Levin, 1967) on the one hand and the stress average rule (2.21)₂ on the other hand (Pichler and Hellmich, 2010). Levin's theorem-predicted macrostresses, specified for phase-wise constant eigenstresses read as,

$$\Sigma = \mathbb{C}_{hom} : \mathbf{E} + \mathbf{\Pi}_{hom} = \mathbb{C}_{hom} : \mathbf{E} + \sum_{i=1}^{n_p} f_i \pi_i : \mathbb{A}_i, \quad (2.31)$$

where $\mathbf{\Pi}_{hom}$ denotes the homogenized eigenstress. Specification of stress average rule (2.20)₂ under consideration of the expression for the volume fraction (2.19) for the average phase strains (2.22) and considering Hill's expression of the homogenized stiffness (2.24) yields

$$\begin{aligned} \Sigma = \mathbb{C}_{hom} : & \left[\mathbf{E} + \sum_{i=1}^{n_p} f_i \mathbb{A}_{\infty,i} : \mathbb{P}_i^0 : (\pi_i - \mathbf{\Pi}_0) \right] \\ & - \sum_{i=1}^{n_p} f_i \mathbb{C}_i : \mathbb{A}_{\infty,i} : \mathbb{P}_i : (\pi_i - \mathbf{\Pi}_0) + \sum_{i=1}^{n_p} f_i \pi_i. \end{aligned} \quad (2.32)$$

Setting Eqs. (2.31) and (2.32) equal, i.e. satisfying the stress admissibility condition, delivers an expression for the auxiliary eigenstress of the infinite matrix, $\mathbf{\Pi}_0$ (Pichler and Hellmich,

2010):

$$\begin{aligned} \mathbf{\Pi}_0 = & \left[\sum_{i=1}^{n_p} f_i (\mathbf{C}_{hom} - \mathbf{C}_i) : \mathbf{A}_{\infty,i} : \mathbf{P}_i \right]^{-1} : \\ & \left\{ \sum_{i=1}^{n_p} f_i [\boldsymbol{\pi}_i : (\mathbb{I} - \mathbf{A}_i) + (\mathbf{C}_{hom} - \mathbf{C}_i) : \mathbf{A}_{\infty,i} : \mathbf{P}_i : \boldsymbol{\pi}_i] \right\}. \end{aligned} \quad (2.33)$$

This allows for identifying the introduced eigenstress influence tensors, \mathbf{Q}_{ji} , by inserting (2.33) into (2.28), considering $\bar{\mathbf{A}}_i = \mathbf{A}_i$, and comparing the result with the formulation of the average phase strains (2.22), reading as

$$\begin{aligned} \mathbf{Q}_{ij} = & [\delta_{ij}\mathbb{I} - f_i \mathbf{A}_i] : \mathbf{A}_{\infty,i} : \mathbf{P}_i + \left[\mathbf{A}_i : \sum_{k=1}^{n_p} f_k \mathbf{A}_{\infty,k} : \mathbf{P}_k - \mathbf{A}_{\infty,i} : \mathbf{P}_i \right] \\ & : \left[\sum_{k=1}^{n_p} f_k (\mathbf{C}_{hom} - \mathbf{C}_k) : \mathbf{A}_{\infty,k} : \mathbf{P}_k \right]^{-1} \\ & : f_i \left[(\mathbb{I} - \mathbf{A}_i)^T + (\mathbf{C}_{hom} - \mathbf{C}_i) : \mathbf{A}_{\infty,i} : \mathbf{P}_i \right]. \end{aligned} \quad (2.34)$$

Analogous expressions for eigenstrain influence tensors \mathbf{D}_{ji} are given by Pichler and Hellmich (2010), which only differ in the concluding tensor-multiplication of the whole expression with the stiffness tensor (2.15). They showed, that the eigenstrain influence tensors, specified for Mori-Tanaka estimates and multiphase composites, where all phases are of identical shape, are equal to the corresponding result of transformation field analysis, according to Dvorak and Benveniste (1992).

In case of a polycrystal, the homogenized stiffness is equal to the stiffness of the infinite matrix. By analogy, it can be expected, that the homogenized eigenstress, is equal to the eigenstress of the infinite matrix. Although there is no mathematical evidence, numerical computations confirm this expectation (Pichler and Hellmich, 2010). Considering Eq. (2.31), this leads to

$$\mathbf{\Pi}_0 = \mathbf{\Pi}_{hom} = \sum_{i=1}^{n_p} f_i \boldsymbol{\pi}_i : \mathbf{A}_i, \quad (2.35)$$

which is again inserted into the estimated phase strains (2.26), yielding, by comparing the result with (2.22), eigenstress influence tensors for self consistent estimates \mathbf{Q}_{ji}^{sc} as

$$\mathbf{Q}_{ij}^{sc} = [\delta_{ij}\mathbb{I} - f_i \mathbf{A}_i] : \mathbf{A}_{\infty,i} : \mathbf{P}_i + \left[\mathbf{A}_i : \sum_{k=1}^{n_p} f_k \mathbf{A}_{\infty,k} : \mathbf{P}_k - \mathbf{A}_{\infty,i} : \mathbf{P}_i \right] : f_i \mathbf{A}_i^T. \quad (2.36)$$

If the RVE contains only phases with similar shapes, all Hill Tensors are equal

$$\mathbf{P}_i = \mathbf{P}, \forall i = 1, 2, \dots, n_p, \quad (2.37)$$

and hence, \mathbf{P} can be put out of the sum $\sum_{k=1}^{n_p} f_k \mathbf{A}_{\infty,k} : \mathbf{P}_k$. Having in mind the definition of the strain concentration tensor according to Eq. (2.29), the identity

$$\mathbf{A}_i : \sum_{k=1}^{n_p} f_k \mathbf{A}_{\infty,k} : \mathbf{P}_k = \mathbf{A}_{\infty,i} : \mathbf{P} \quad (2.38)$$

is found. The expressions for the influence tensors (2.34) therefore degenerate to:

$$\mathbf{Q}_{ij} = [\delta_{ij}\mathbb{I} - f_i \mathbf{A}_i] : \mathbf{A}_{\infty,i} : \mathbf{P} \quad (2.39)$$

2.8 Conditions for phase strain concentration tensors and for eigenstress influence tensors

Herein, mathematical conditions for strain concentration tensors and eigenstress influence tensors are derived, which turn out to be useful for code verification purposes. A condition for the phase strain concentration tensor is obtained, by specification of the phase strains (2.22) for a RVE with vanishing eigenstresses $\boldsymbol{\pi}_i = 0$ for all n_p phases, yielding

$$\boldsymbol{\varepsilon}_i = \mathbb{A}_j : \boldsymbol{E}. \quad (2.40)$$

Insertion of this expression into the strain average rule (2.21)₁ readily shows that the average of the phase concentration tensors is equal to the symmetric fourth order identity tensor, \mathbb{I} ,

$$\sum_i^{n_p} f_i \mathbb{A}_i = \mathbb{I}. \quad (2.41)$$

According to Dvorak and Benveniste (1992) three independent conditions for the eigenstress influence tensors can be obtained based on three physical prerequisites: (i) strain compatibility, (ii) stress admissibility, and (iii) the reciprocal theorem.

1. Consider an RVE, where only one phase, namely phase k , is exposed to an eigenstrain, $\boldsymbol{\eta}_k = -\mathbb{C}_k^{-1} : \boldsymbol{\pi}_k$. Specification of the strain average rule (2.21)₁ (which is valid as long as the microstrains are kinematically compatible) for the phase strains (2.22) induced by arbitrary macrostrains \boldsymbol{E} and by the nonzero eigenstress $\boldsymbol{\pi}_k = -\mathbb{C}_k : \boldsymbol{\eta}_k$ yields:

$$\sum_j^{n_p} f_j (\mathbb{A}_j : \boldsymbol{E} + \mathbb{Q}_{jk} : \boldsymbol{\pi}_k) = \boldsymbol{E} \quad (2.42)$$

Considering the previously established condition for the average of the phase strain concentration tensors (2.41), the strain compatibility implies that

$$\sum_j^{n_p} f_j \mathbb{Q}_{jk} = 0. \quad (2.43)$$

2. Consider a multiphase composite, where only one phase, namely phase k , is exposed to a nonzero eigenstress $\boldsymbol{\pi}_k$. As long as the microstrains are statically admissible, the stress average rule (2.21)₂ is valid, and allows for calculation of the macroscopic stresses $\boldsymbol{\Sigma}$. Expressing the statically admissibly microstresses through microstrains and eigenstresses, in terms of $\boldsymbol{\sigma}_j = \mathbb{C}_j : \boldsymbol{\varepsilon}_j + \boldsymbol{\pi}_j$ and the microstrains in terms of Eq. (2.22), yields

$$\begin{aligned} \boldsymbol{\Sigma} &= \sum_j^{n_p} f_j \boldsymbol{\sigma}_j = f_k \boldsymbol{\pi}_k + \sum_j^{n_p} f_j \mathbb{C}_j : \boldsymbol{\varepsilon}_j = \\ &= f_k \boldsymbol{\pi}_k + \sum_j^{n_p} f_j \mathbb{C}_j : \mathbb{A}_j : \boldsymbol{E} - \sum_j^{n_p} f_j \mathbb{C}_j : \mathbb{Q}_{jk} : \boldsymbol{\pi}_k \end{aligned} \quad (2.44)$$

Also Levin's theorem (2.31), specified for the vanishing eigenstress expect for that of phase k , allows for calculation of the macrostresses:

$$\boldsymbol{\Sigma} = \sum_j^{n_p} f_j \mathbb{C}_j : \mathbb{A}_j : \boldsymbol{E} + f_k \boldsymbol{\pi}_k : \mathbb{A}_k \quad (2.45)$$

Setting this two expressions equal yields the identity

$$f_k \left(\mathbb{I} - \mathbb{A}_k^T \right) = \sum_j^{n_p} f_j \mathbb{C}_j : \mathbb{Q}_{jk}, \quad (2.46)$$

where the transpose of a fourth-order tensor \mathbb{T} is given in terms of $T_{ijkl}^T = T_{klij}$.

3. Finally, consider a macrostrain-free multiphase RVE, where two independent loading cases are applied: In loading case one, an eigenstress $\boldsymbol{\pi}_r$ only occurs in the r -th phase, in loading case two, an eigenstress $\boldsymbol{\pi}_s$ only occurs in the s -th phase. Calculation of the corresponding strain fields $\boldsymbol{\varepsilon}(x, \boldsymbol{\pi}_r)$ for loading case one, and $\boldsymbol{\varepsilon}(x, \boldsymbol{\pi}_s)$ for loading case two, allows for computation of the work done by the eigenstresses $\boldsymbol{\pi}_s$ along the strains $\boldsymbol{\varepsilon}(x, \boldsymbol{\pi}_r)$ and, vice versa, the work done by $\boldsymbol{\pi}_r$ along $\boldsymbol{\varepsilon}(x, \boldsymbol{\pi}_s)$. The reciprocal theorem implies the equality of these two work expressions, resulting in a condition for the eigenstress influence tensor (Dvorak and Benveniste, 1992):

$$f_s \mathbb{Q}_{sr} = f_r \mathbb{C}_s^{-1} : \mathbb{C}_s^T : \mathbb{Q}_{rs}^T \quad (2.47)$$

If the phases exhibit linear elastic behavior, $\mathbb{C}^T = \mathbb{C}$, Eq. (2.47) simplifies to

$$f_s \mathbb{Q}_{sr} = f_r \mathbb{Q}_{rs}^T \quad (2.48)$$

Since we used both, that the average of the microstrains is equal to the macrostrain and that the average of the microstress is equal to the Levin's theorem-predicted macrostress during the derivation of the eigenstress influence tensors, the strain compatibility and the stress admissibility conditions are satisfied *by construction* (Pichler and Hellmich, 2010). Therefore, apart from the code verification, only the reciprocal theorem constitutes a condition for the eigenstress influence tensors.

Hydration-driven evolution of compressive strength of OPC and blended cementitious materials: microstructural characterization, strength testing, and multiscale modeling

Authored by: Michal Hlobil, Markus Königsberger, Pipat Termkhajornkit, Rémi Barbarulo, Christian Hellmich, and Bernhard Pichler

Publication outlook: At the time of finalizing this thesis, it is planned to submit this quite mature paper draft – after incorporation of further improvements – for publication to *Cement and Concrete Research*.

Abstract: This contribution refers to early-age strength of pastes and mortars produced either with ordinary Portland cement (OPC) or with blended OPC where part of cement clinker is replaced either by quartz, limestone, slag, or fly ash. The study combines multiscale elasto-brittle modeling with microstructural characterization and early-age macroscopic testing of blended mortars. In the context of modeling, the elasto-brittle strength model for cement pastes presented in [CCR 41:467-476, 2011] is extended towards mortars. Loading imposed on mortar samples is first concentrated down to stress peaks in cement paste volumes which are directly bonded to stiff sand grains. Further stress concentration down to micron-sized needle-shaped hydrates is quantified based on *strain energy*-related stress averages. This is motivated by the envisioned failure mode of hydrates, which is *energy*-driven shear cracking at the nanometric scale, with a shear strength that increases with increasing pressure acting on the crack plane. The friction angle and the cohesion intervening in the newly adopted Mohr-Coulomb failure criterion are taken from limit state analysis of grid indentation testing on low-density calcium-silicate-hydrates. Therefore, the model is free of fitting parameters. Blind predictions of the macroscopic compressive strength of OPC pastes and mortars agree very well with experimental results from three different laboratories. This is the motivation to continue with mortars produced with binders representing blends of OPC and limestone,

quartz, slag, and fly ash, respectively. Early-age phase evolutions are quantified based on state-of-the-art microstructural characterization, including thermogravimetric analysis and X-ray diffraction with Rietveld refinement, and scanning electron microscopy. As for modeling, very finely ground quartz and limestone are introduced as reinforcements of the hydrate foam, i.e. they directly interact with needle-shaped hydrates and capillary porosity. The coarser hydraulic supplementary cementitious materials (SCM) slag and fly ash, in turn, are introduced at the same scale as unhydrated clinker grains. Comparison of model-predicted strength evolutions agree well with test results, as long as the blending materials do not hydrate. Hydration of slag and fly ash is shown to increase the hydrate cohesion significantly, and this is consistent with recent nanoindentation studies on mature OPC and blended pastes.

Contribution: Bernhard Pichler and Christian Hellmich set up the overall research strategy, supervised the research progress, checked key results, and supported the documentation process. Michal Hlobil implemented a software script for compressive strength predictions, produced mortar specimens, tested them, documented research results, and produced diagrams for the paper. Markus Königsberger provided support for Michal Hlobil during model implementation and code verification, produced figures and wrote the first draft of the paper. Pipat Termkhajornkit and Rémi Barbarulo coordinated, supervised and carried out microstructural characterization.

Keywords: supplementary cementitious materials, compressive strength, micromechanics, cement paste, mortar

3.1 Introduction

The hydration-induced development of strength of cementitious materials is of highest practical relevance, because the uniaxial compressive strength of concrete is the central material property for classification and design used by codes and regulations (European Committee for Standardization, 2004; American Concrete Institute (ACI) Committee 318, 2014; Japan Society of Civil Engineers (JSCE), 2010). In the second half of the 20th century, concrete technology was challenged to satisfy high – and to a certain extent contradicting – demands from construction industry. This includes the following requirements.

- As for flexible construction, fresh concrete shall remain workable for hours, i.e. significant hydration of cement shall not start prior to placement of concrete.
- As for efficient construction, hydration shall be a speedy process after placement, i.e. early-age strength shall develop so fast that formworks can be stripped 24 hours after production.
- The final product shall be durable, in order to guarantee serviceability of structures over their entire designed lifetime.

Available concrete mixes based on ordinary Portland cement (OPC) satisfy the described demands. At the end of the 20th century, in turn, reduction of CO₂ emissions became an additional challenging requirement. The favorite solution was to replace part of OPC clinker either by hydraulic waste materials from other industries, such as the supplementary cementitious materials (SCMs) blast furnace slag or fly ash from combustion power plants, or by inert fillers, such as quartz or limestone. The resulting blended binders make the sought

reduction of CO₂ emissions possible, they comply with the requirements regarding fresh concrete properties and the long-term performance, but the early-age strength development is slower compared to traditional OPC. This has initiated intensive research on early-age properties of cementitious materials produced with blended binders, see e.g. (Feldman et al., 1990; Lam et al., 2000; Pane and Hansen, 2005; Lothenbach et al., 2011; Zadeh and Bobko, 2013; Hlobil et al., 2016).

Use of blended binders adds, on the one hand, a lot of flexibility for the development of innovative mix designs, given that different clinker replacement ratios can be used and that several clinker replacement materials are available, see above. On the other hand, the early-age evolutions of mechanical properties such as stiffness and strength are significantly different as compared to pure OPC materials. First and foremost, this is a consequence of modified hydration kinetics (Pane and Hansen, 2005). Finely ground non-reactive fillers made of limestone or quartz are known to speed up reaction kinetics, since the small particles represent preferred precipitation sites for hydrates (Lothenbach et al., 2011), although the fillers themselves do not dissolve considerably (Ye et al., 2007; Wang et al., 2013). While SCM particles exhibit (to a certain extent) a similar filler effect, they start to hydrate typically much later than OPC, because the pH value of the pore solution must exceed a certain threshold to initiate SCM hydration (Lothenbach et al., 2011). Delayed hydration results in the delayed development of early-age stiffness and strength. In addition to the influence on reaction kinetics, interaction between SCM hydration and clinker hydration may lead to chemical hydrate compositions which are significantly different from those precipitating in pure OPC pastes (Bonavetti et al., 2001; Chindaprasirt et al., 2007). The fibrillar morphology of hydrates, known from OPC, may gradually change into a more foil-like morphology under the influence of blast furnace slag (Richardson, 2000). Fly ash, in turn, may result in a more uniform microstructure and a decreased average pore size relative to the OPC reference (Chindaprasirt et al., 2007). Other sources report on an influence of grinding fineness on the resulting pore size distribution (Chindaprasirt et al., 2007) and, consequently, also on the macroscopic compressive strength (Chindaprasirt et al., 2005). Finally, nanoindentation tests imply that hydrates in SCM-blended pastes are considerably stronger than in OPC paste (Zadeh and Bobko, 2013), while inert calcareous fillers do not alter the hydrates' strength (Vandamme, 2008).

The present contribution further extends this line of research by studying the strength evolution of (cement pastes and) mortars produced with pure OPC or blended binders, in the framework of a combined experimental-computational approach. Given that predictive modeling of the phase evolution of blended pastes is out of reach, state-of-the-art microstructural characterization techniques are combined in order to quantify the phase volume evolutions of one pure OPC paste and of four blended pastes, where 45 % of the clinker volume are replaced either by quartz, limestone, slag, or fly ash. In addition, blended mortar cylinders are crushed under uniaxial compression at material ages amounting to 3 days and to 28 days. This experimental database serves as the motivation for related modeling activities, which are based on methods of continuum micromechanics (Zaoui, 2002). As for OPC materials, these methods have shown to be valuable for homogenization of elastic stiffness (Bernard et al., 2003a; Sanahuja et al., 2007; Pichler et al., 2009; Stefan et al., 2010; Bary, 2011; Venkovic et al., 2013), creep (Scheiner and Hellmich, 2009; Königsberger et al., 2016b), and strength (Pichler et al., 2009; Pichler and Hellmich, 2011; Pichler et al., 2013a). Notably, the elasto-brittle strength models consider that the macroscopic strength of OPC cement pastes is reached, once stresses in microscopic hydration products reach the corresponding hydrate strength. In the context of the present paper, aspects of the strength model (Pichler and Hellmich, 2011;

Pichler et al., 2013a) are further elaborated:

1. The range of applicability of the strength models (Pichler and Hellmich, 2011; Pichler et al., 2013a) is first extended from cement pastes to mortars. The latter are considered as matrix-inclusion composites, with rather stiff sand grains embedded in a less stiff cement paste matrix. Because of the stiffness contrast, we consider that stress peaks of the cement paste matrix occur in representative volumes that are directly attached to the surface of sand grains. Such stress peaks are evidenced by the formation of cracks in this region (Shah and Winter, 1966; Shah and Sankar, 1987). We here quantify these stress peaks by means of the stress concentration concept developed in (Königsberger et al., 2014a,b).
2. Envisioning that hydrate failure is related to shear cracking at the nanoscopic scale, and that the corresponding shear strength increases with increasing pressure acting on the crack plane, the *von Mises*-type elastic limit criterion used in (Pichler and Hellmich, 2011; Pichler et al., 2013a) is replaced by a *Mohr-Coulomb* criterion. Related strength constants are taken from limit state analysis of nanoindentation studies on low-density calcium-silicate-hydrates (Sarris and Constantinides, 2013).
3. When it comes to the scale transition from cement paste down to micron-sized needle-shaped hydrates, we consider that cracking of hydrates is an *energy*-driven phenomenon. Therefore, we quantify principal hydrate stresses intervening in the Mohr-Coulomb criterion based on *energy density*-related stress averages, i.e. we provide a mechanical explanation why so-called “higher-order” or “second-order” stress averages intervene in the strength models (Pichler and Hellmich, 2011; Pichler et al., 2013a), rather than simple volume averages which are also referred to as “first-order” averages.
4. While the models (Pichler and Hellmich, 2011; Pichler et al., 2013a) are based on only one *average* hydrate type, we here extend the microstructural representation towards all types of hydrates that are identified by means of microstructural characterization, and they include C-S-H, portlandite, ettringite, monosulfate, etc.
5. Finally, consideration of blended binders (rather than pure OPC cements) requires an extension of the microstructural representation towards consideration of the cement replacement materials quartz, limestone, slag, and fly ash.

The paper is structured as follows. Section 3.2 refers to strength of OPC pastes and mortars. We extend the multiscale strength homogenization model of (Pichler and Hellmich, 2011; Pichler et al., 2013a) by newly adding the scale of mortar and by implementing the Mohr-Coulomb criterion for hydrate failure. The extended model is validated for OPC cement pastes and mortars, by comparing blind predictions of early-age strength evolutions with experimental data from three different laboratories. Section 3.3 refers to strength of pastes and mortars produced with blended binders. Phase volume evolutions of four blended binders and of the underlying OPC are quantified based on state-of-the-art methods for microstructural characterization. Compressive strength values are determined on mortar samples at ages of 3 days and 28 days. The strength model of Section 3.2 is further extended towards consideration of the replacement materials and of all hydrate types that were identified by means of microstructural characterization. Model predicted strength values are compared with their experimental counterparts. Finally, the paper is closed with a discussion (Section 3.4) and conclusions (Section 3.5).

3.2 Elasto-brittle multiscale strength modeling of ordinary Portland cement pastes and mortars

Following the concept of quasi-brittle strength upscaling developed by Pichler et al. (2008, 2009) and Pichler and Hellmich (2011), it is considered that the macroscopic strength of cement paste or mortar is reached once microstresses in hydration products reach the hydrate strength. Therefore, a multiscale representation of cementitious materials is required, which accounts for key features of their microstructure.

3.2.1 Micromechanical representation

In continuum micromechanics a material is understood as a micro-heterogeneous representative volume element (RVE) with characteristic size ℓ fulfilling the separation of scales requirement (Zaoui, 2002):

$$d \ll \ell \ll D, \quad (3.1)$$

where d and D , respectively, stand for the characteristic sizes of inhomogeneities and of the structure containing the RVE (such as structural dimensions or the wavelength of loading). RVEs of cementitious materials are too complex to be resolved in full detail. As a remedy, quasi-homogeneous material subdomains (referred to as material phases), are identified as microstructural key features. The overall (“homogenized”) mechanical properties of cementitious materials are governed by the mechanical properties of the material phases, their shapes, volume dosages, and mutual interaction.

Following Pichler and Hellmich (2011) as well as Pichler et al. (2013a), we resolve the microstructure of mortar across three separated scales of observation, see Fig. 3.1. At the

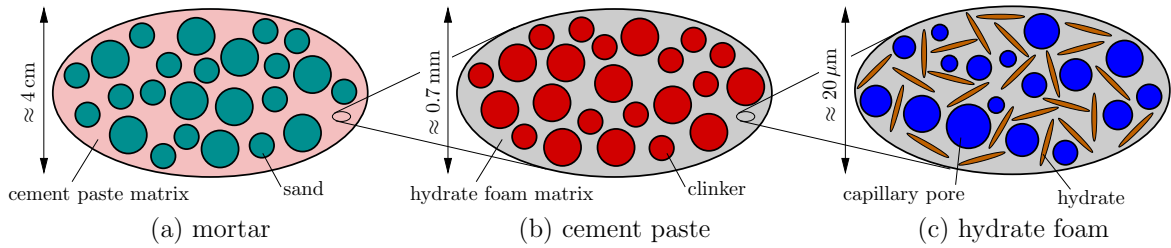


Figure 3.1: Multiscale micromechanics representation of mortar (“material organogram”) after (Pichler and Hellmich, 2011; Pichler et al., 2013a); two-dimensional sketches of three-dimensional representative volume elements

largest scale of observation, we envision a centimeter-sized RVE of mortar, which consists of spherical sand grains that are embedded in a cement paste matrix, see Fig. 3.1(a). At the intermediate scale of observation, we envision a (sub-)millimeter-sized RVE of cement paste, which consists of spherical unhydrated clinker grains that are embedded in a hydrate foam matrix, see Fig. 3.1(b). At the smallest scale of observation, we envision a micrometer-sized RVE of hydrate foam, which consists of spherical capillary pores and needle-shaped hydrates that are uniformly orientated in all space directions, see Fig. 3.1(c).

3.2.2 Volume fractions and mechanical constants of material phases

The Powers-Acker model Acker (2001); Powers and Brownyard (1947) provides analytical expressions for phase volume fractions as functions of the initial water-to-cement mass ratio

w/c , the initial sand-to-cement mass ratio s/c , and the degree of clinker hydration ξ_{clin} , defined as the volume of already hydrated clinker divided by its initial volume. At the scale of mortar, the volume fractions of sand f_{sand}^{mor} and of the cement paste matrix f_{cp}^{mor} read as (Bernard et al., 2003a)

$$f_{sand}^{mor} = \frac{\frac{s/c}{\rho_{sand}}}{\frac{1}{\rho_{clin}} + \frac{w/c}{\rho_{H_2O}} + \frac{s/c}{\rho_{sand}}}, \quad f_{cp}^{mor} = 1 - f_{sand}^{mor}. \quad (3.2)$$

At the scale of cement paste, the volume fractions of clinker f_{clin}^{cp} and of the hydrate foam matrix f_{hf}^{cp} read as (Acker, 2001; Powers and Brownyard, 1947; Pichler and Hellmich, 2011)

$$f_{clin}^{cp} = \frac{20(1 - \xi_{clin})}{20 + 63w/c} \geq 0, \quad f_{hf}^{cp} = 1 - f_{clin}^{cp}. \quad (3.3)$$

At the scale of the hydrate foam, the volume fractions of capillary pores f_{pore}^{hf} and of hydrates f_{hyd}^{hf} read as (Pichler and Hellmich, 2011)

$$f_{pore}^{hf} = \frac{63(w/c - 0.367\xi_{clin})}{20\xi + 63w/c} \geq 0, \quad f_{hyd}^{hf} = 1 - f_{pore}^{hf}. \quad (3.4)$$

All material phases are considered to exhibit isotropic elastic properties, which allows for expressing the phase stiffness tensor \mathbb{C}_i in terms of bulk moduli k_i and shear moduli μ_i

$$\mathbb{C}_i = 3k_i \mathbb{I}^{vol} + 2\mu_i \mathbb{I}^{dev}, \quad (3.5)$$

where index i refers to the material phase i , see Table 3.1 for phase-specific constants. In Eq. (3.5), \mathbb{I}^{vol} and \mathbb{I}^{dev} denote the volumetric and deviatoric parts of the symmetric fourth-order identity tensor \mathbb{I} , defined as $I_{ijkl} = 1/2(\delta_{ik}\delta_{jl} + \delta_{il}\delta_{jk})$, $\mathbb{I}^{vol} = 1/3(\mathbf{1} \otimes \mathbf{1})$, and $\mathbb{I}^{dev} = \mathbb{I} - \mathbb{I}^{vol}$, respectively, whereby $\mathbf{1}$ denotes the second-order identity tensor with components equal to the Kronecker delta δ_{ij} , namely $\delta_{ij} = 1$ for $i=j$, and 0 otherwise.

Table 3.1: Isotropic elasticity constants of material phases

	Bulk modulus		Shear modulus		Source
		k [GPa]		μ [GPa]	
clinker	k_{clin}	116.58	μ_{clin}	53.81	(Velez et al., 2001)
hydrates	k_{hyd}	18.69	μ_{hyd}	11.76	(Pichler and Hellmich, 2011)
quartz	k_{quartz}	36.44	μ_{quartz}	31.20	(Ahrens, 1995)
limestone	$k_{limestone}$	67.19	$\mu_{limestone}$	29.24	(Presser et al., 2010)
slag	k_{slag}	36.44	μ_{slag}	31.19	(Němeček et al., 2011)
fly ash	k_{FA}	58.33	μ_{FA}	43.75	(Šmilauer et al., 2011)
sand	k_{sand}	35.35	μ_{sand}	29.91	(Vorel et al., 2012)
pores	k_{pore}	0.00	μ_{pore}	0.00	

As for strength properties, we consider that hydrates are the weakest links in cementitious microstructures. In (Pichler and Hellmich, 2011; Pichler et al., 2013a), it was considered that

hydrate failure follows a (von Mises-type) elastic limit criterion and the corresponding (shear failure-related) deviatoric hydrate strength was identified by top-down analysis, i.e. from macroscopic strength measurements on young cement pastes. Considering the nanogranular nature of C-S-H Constantinides and Ulm (2007), we now consider a Mohr-Coulomb-type elastic limit criterion (Coulomb, 1776; Mohr, 1900), expressing that the shear strength of gliding planes increases with increasing normal pressure acting on the gliding planes:

$$f(\boldsymbol{\sigma}_{hyd}) = \sigma_{hyd,I} \frac{1 + \sin \varphi_{hyd}}{2 c_{hyd} \cos \varphi_{hyd}} - \sigma_{hyd,III} \frac{1 - \sin \varphi_{hyd}}{2 c_{hyd} \cos \varphi_{hyd}} - 1 \leq 0, \quad (3.6)$$

where $\boldsymbol{\sigma}_{hyd}$ denotes the hydrate stress tensor (with $\sigma_{hyd,I}$ and $\sigma_{hyd,III}$ as largest and smallest principal stress component), φ_{hyd} the angle of internal friction, and c_{hyd} the cohesion. Notably, $f < 0$ refers to elastic hydrate behavior and $f = 0$ corresponds to hydrate failure. The material constants of low density calcium-silicate-hydrates are considered to be representative for all the hydrates Pichler et al. (2013b), and they were quantified using limit state analysis of nanoindentation test data Constantinides and Ulm (2004); Sarris and Constantinides (2013) as

$$\varphi_{hyd} = 12^\circ, \quad c_{hyd} = 50 \text{ MPa}. \quad (3.7)$$

Evaluation of the the Mohr-Coulomb criterion (3.6) requires quantification of hydrate stress states $\boldsymbol{\sigma}_{hyd}$. They follow from concentration of macrostress states imposed on RVEs of cement paste or mortar down to the level of needle-shaped hydrates, discussed next.

3.2.3 Concentration of loading imposed on RVEs of mortar into cement paste: quantification of stress peaks

Because sand grains are stiffer than the cement paste matrix (particularly so at early ages), sand grains exhibit – on average – larger stresses than the cement paste matrix. Therefore stress peaks of cement paste occur in the immediate vicinity of the sand grains. In order to quantify these stress peaks, we follow the two-step procedure developed by Königsberger et al. (2014a), i.e. we concentrate first the loading imposed on RVEs of mortar down to average stresses and strains of sand grains. Subsequently, we apply firm bond-related stress and strain compatibility conditions at the sand-to-cement paste interface \mathcal{I}_{sand}^{cp} , in order to obtain the sought cement paste stress states representing stress peaks in the immediate vicinity of sand grains, as detailed next.

Concentration from homogeneous macrostresses imposed on an RVE of mortar, $\boldsymbol{\Sigma}_{mor}$, down to average stresses of sand grains, $\boldsymbol{\sigma}_{sand}$, reads as

$$\boldsymbol{\sigma}_{sand} = \mathbb{B}_{sand}^{mor} : \boldsymbol{\Sigma}_{mor}, \quad (3.8)$$

with \mathbb{B}_{sand}^{mor} as the stress concentration tensor which is a function of the volume fractions and of the elastic properties of sand grains and cement paste. Based on the micromechanical representation of mortar as a matrix-inclusion composite, see Fig. 3.1, a Mori-Tanaka-scheme (Mori and Tanaka, 1973; Benveniste, 1987) is appropriate for homogenization (Zaoui, 2002). The scheme provides analytical access to the concentration tensor \mathbb{B}_{sand}^{mor} , see Appendix A for details. Averages strains of sand grains, $\boldsymbol{\varepsilon}_{sand}$, are obtained from the elasticity law

$$\boldsymbol{\varepsilon}_{sand} = (\mathbb{C}_{sand})^{-1} : \boldsymbol{\sigma}_{sand}, \quad (3.9)$$

where \mathbb{C}_{sand} stands for the isotropic stiffness tensor of sand, see Eq. (3.5) and Table 3.1.

Consideration of firm bond between sand grains and the surrounding cement paste matrix, implies interfacial continuity conditions of tractions and displacements. Displacement continuity can be expressed as the following relation (Salençon, 2001; Königsberger et al., 2014a) between sand strains $\boldsymbol{\varepsilon}_{sand}$ and cement paste strains $\boldsymbol{\varepsilon}_{cp}(\underline{x})$

$$\underline{t}_1(\underline{x}) \cdot [\boldsymbol{\varepsilon}_{sand} - \boldsymbol{\varepsilon}_{cp}(\underline{x})] \cdot \underline{t}_2(\underline{x}) = 0 \quad \forall \underline{x} \in \mathcal{I}_{sand}^{cp}, \quad (3.10)$$

where $\underline{t}_1(\underline{x})$ and $\underline{t}_2(\underline{x})$ denote all possible pairs of tangent vectors in the tangential plane to the interface \mathcal{I}_{sand}^{cp} at position \underline{x} . Traction continuity, in turn, can be expressed as the following relation (Salençon, 2001; Königsberger et al., 2014a) between sand stresses $\boldsymbol{\sigma}_{sand}$ and cement paste stresses $\boldsymbol{\sigma}_{cp}(\underline{x})$

$$[\boldsymbol{\sigma}_{sand} - \boldsymbol{\sigma}_{cp}(\underline{x})] \cdot \underline{n}(\underline{x}) = 0 \quad \forall \underline{x} \in \mathcal{I}_{sand}^{cp}, \quad (3.11)$$

where $\underline{n}(\underline{x})$ denotes a unit vector orientated perpendicular to the interface \mathcal{I}_{sand}^{cp} at position \underline{x} . Stresses and strains of cement paste are related to each other by isotropic elasticity law

$$\boldsymbol{\sigma}_{cp}(\underline{x}) = \mathbb{C}_{cp} : \boldsymbol{\varepsilon}_{cp}(\underline{x}), \quad (3.12)$$

where \mathbb{C}_{cp} denotes the homogenized stiffness of cement paste, which is obtained by two-step upscaling starting at needle-shaped hydrates and capillary pores. Their polycrystalline arrangement (direct mutual interaction) renders the self-consistent scheme (Hershey, 1954; Kröner, 1958; Hill, 1965) appropriate for homogenization of the hydrate foam. Subsequent homogenization of the matrix-inclusion composite cement paste is carried out based on the abovementioned Mori-Tanaka scheme, see Appendix A for details.

The sought cement paste stress states prevailing in the immediate vicinity of the sand-to-cement paste interface \mathcal{I}_{sand}^{cp} follow from combination of relations (3.8)-(3.12) as (Königsberger et al., 2014a)

$$\boldsymbol{\sigma}_{cp}(\underline{x}) = \mathbb{B}_{cp}^{sand}(\underline{x}) : \boldsymbol{\sigma}_{sand} = \mathbb{B}_{cp}^{sand}(\underline{x}) : \mathbb{B}_{sand}^{mor} : \boldsymbol{\Sigma}_{mor} \quad \forall \underline{x} \in \mathcal{I}_{sand}^{cp}, \quad (3.13)$$

with \mathbb{B}_{cp}^{sand} denoting the sand-to-cement paste stress concentration tensor, see Appendix A for details. Notably, the stress states $\boldsymbol{\sigma}_{cp}$ depend on the location vector \underline{x} , e.g. stress concentrations around the equator of the sand grains are quite different from the ones at the poles (Königsberger et al., 2014a), see Fig. 3.2.

3.2.4 Concentration of loading imposed on RVEs of cement paste into hydrates

As for quantification of hydrates stresses $\boldsymbol{\sigma}_{hyd}$ intervening in the Mohr-Coulomb criterion (3.6), we now consider, at any point \underline{x} of the interface \mathcal{I}_{sand}^{cp} , the microstructure of cement paste in terms of a three-dimensional RVE, such as illustrated in Fig. 3.1(b). In agreement with that, we consider specific stress states $\boldsymbol{\sigma}_{cp}(\underline{x})$ from Eq. (3.13) as “macroscopic” loading imposed on RVEs of cement paste, $\boldsymbol{\Sigma}_{cp}$, representing the starting point for further multiscale stress concentration, i.e. $\boldsymbol{\sigma}_{cp}(\underline{x}) \rightarrow \boldsymbol{\Sigma}_{cp}$.

The Mohr-Coulomb criterion (3.6) implies that failure of hydrates is governed by cracking processes at the nanometric scale *inside* hydrate needles which is not explicitly resolved herein. Given that cracking is a dissipative phenomenon, failure of hydrates is a strain energy-dependent process, and this provides the motivation to perform strain energy-related stress concentration into hydrate needles (Dormieux et al., 2002; Pichler et al., 2008, 2009),

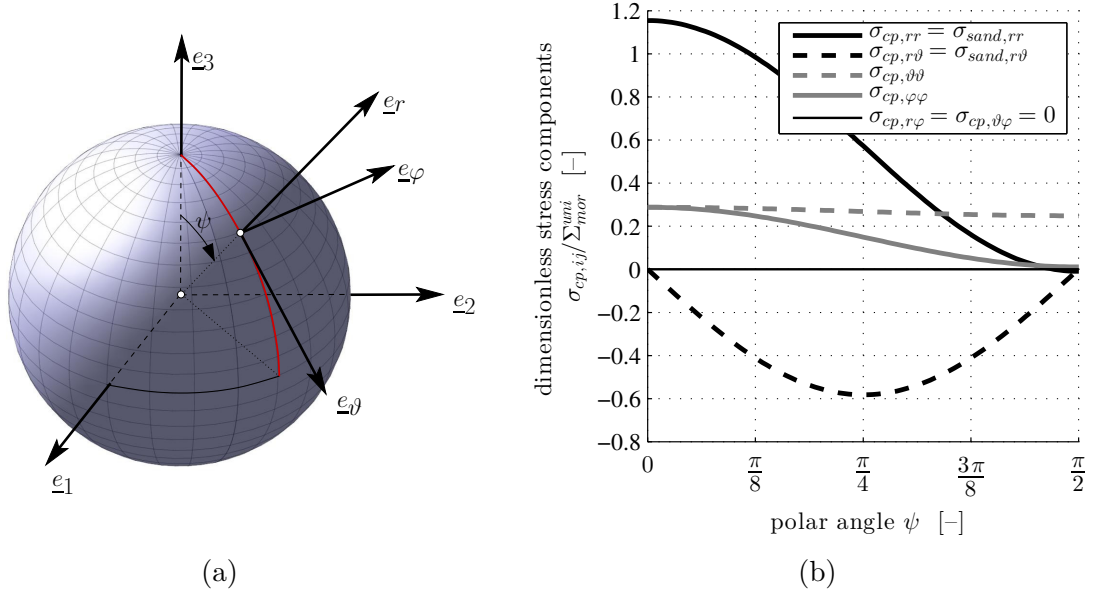


Figure 3.2: Concentration of uniaxial loading imposed on an RVE of mortar, see (3.28), to stress states of cement paste in the immediate vicinity of sand grains: (a) sand grain with global Cartesian base frame $\underline{e}_1, \underline{e}_2, \underline{e}_3$ and local spherical base frame $\underline{e}_r, \underline{e}_\theta, \underline{e}_\phi$; (b) cement paste stress components in the immediate vicinity of the sand-to-cement paste interface \mathcal{I}_{sand}^{cp} as a function of polar angle ψ ; evaluation of (3.13) for $w/c = 0.50$, $s/c = 3.0$, and $\xi_{clin} = 0.50$

rather than quantifying spatial averages of stresses. To this end, the elastic energy W stored in the RVE of cement paste is expressed both macroscopically (W^{macro}) and microscopically (W^{micro}). In the latter case, it is considered that cement paste is made up of three constituents: isotropically orientated hydrate needles, capillary pores, and clinker grains:

$$W = W^{macro} = \frac{V_{cp}}{2} \mathbf{E}_{cp} : \mathbb{C}_{cp} : \mathbf{E}_{cp}, \quad (3.14)$$

$$W = W^{micro} = \int_0^{2\pi} \int_0^\pi \int_{V_{hyd;\varphi,\vartheta}} \frac{1}{2} \boldsymbol{\varepsilon}(\underline{x}) : \mathbb{C}_{hyd} : \boldsymbol{\varepsilon}(\underline{x}) dV \frac{\sin \vartheta}{4\pi} d\vartheta d\varphi \\ + \int_{V_{pore}} \frac{1}{2} \boldsymbol{\varepsilon}(\underline{x}) : \mathbb{C}_{pore} : \boldsymbol{\varepsilon}(\underline{x}) dV + \int_{V_{clin}} \frac{1}{2} \boldsymbol{\varepsilon}(\underline{x}) : \mathbb{C}_{clin} : \boldsymbol{\varepsilon}(\underline{x}) dV \quad (3.15)$$

whereby φ and ϑ define the orientation of the hydrate needles by azimuth and zenith angle (see Fig. 3.3), $\boldsymbol{\varepsilon}(\underline{x})$ denotes the microscopic strain field, and V_i and \mathbb{C}_i denote the volume and the elastic stiffness tensor of material phase i ; whereby i refers to hydrates, to capillary pores, to clinker grains, or to cement paste, $i \in \{hyd, cpor, clin, cp\}$. Again, \mathbb{C}_{cp} is the homogenized stiffness of cement paste, see Appendix A for details. In Eq. (3.14), \mathbf{E}_{cp} refers to the macro-homogeneous strain state at the considered RVE of cement paste. The strains \mathbf{E}_{cp} are related to the stresses $\boldsymbol{\Sigma}_{cp}$ by the isotropic elasticity law

$$\mathbf{E}_{cp} = (\mathbb{C}_{cp})^{-1} : \boldsymbol{\Sigma}_{cp}. \quad (3.16)$$

Setting equal the microscopic and the macroscopic expressions of the elastic energy, see Eqs. (3.14) and (3.15), and deriving them either with respect to bulk modulus or to shear

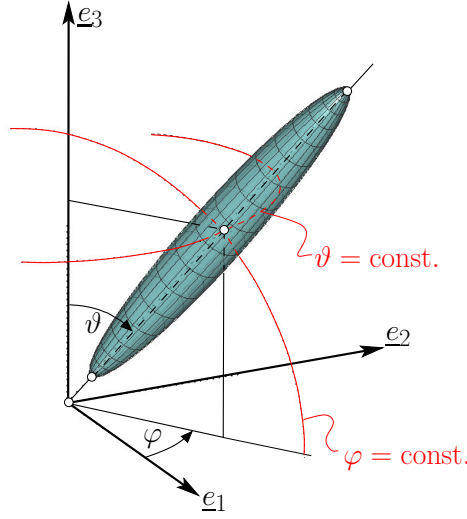


Figure 3.3: Definition of azimuth and zenith angle for identification of the orientation of the needle-shaped hydrates

modulus of φ, ϑ -orientated hydrate needles (Fig. 3.3), yields under consideration of isotropic phases (3.5) and kinematically admissible displacement fields Dormieux et al. (2002)

$$\frac{\partial W}{\partial k_{hyd;\varphi,\vartheta}} = \frac{V_{cp}}{2} \mathbf{E}_{cp} : \frac{\partial \mathbf{C}_{cp}}{\partial k_{hyd;\varphi,\vartheta}} : \mathbf{E}_{cp} = \frac{3}{2} \int_{V_{hyd;\varphi,\vartheta}} \boldsymbol{\varepsilon}(\underline{x}) : \mathbb{I}^{vol} : \boldsymbol{\varepsilon}(\underline{x}) dV, \quad (3.17)$$

$$\frac{\partial W}{\partial \mu_{hyd;\varphi,\vartheta}} = \frac{V_{cp}}{2} \mathbf{E}_{cp} : \frac{\partial \mathbf{C}_{cp}}{\partial \mu_{hyd;\varphi,\vartheta}} : \mathbf{E}_{cp} = \int_{V_{hyd;\varphi,\vartheta}} \boldsymbol{\varepsilon}(\underline{x}) : \mathbb{I}^{dev} : \boldsymbol{\varepsilon}(\underline{x}) dV, \quad (3.18)$$

where $V_{hyd;\varphi,\vartheta}$, $k_{hyd;\varphi,\vartheta}$, and $\mu_{hyd;\varphi,\vartheta}$ denote the volume, the bulk modulus, and the shear modulus of the hydrate needles orientated in φ, ϑ -direction. Under consideration of the definition of volumetric/deviatoric strain decomposition $\boldsymbol{\varepsilon} = \boldsymbol{\varepsilon}^{vol} + \boldsymbol{\varepsilon}^{dev}$, with $\boldsymbol{\varepsilon}^{vol} = \mathbb{I}^{vol} : \boldsymbol{\varepsilon}$ and $\boldsymbol{\varepsilon}^{dev} = \mathbb{I}^{dev} : \boldsymbol{\varepsilon}$, Eqs. (3.17) and (3.18) are divided by $V_{hyd;\varphi,\vartheta}$ and rearranged as

$$\frac{1}{3 f_{hyd;\varphi,\vartheta}^{cp}} \mathbf{E}_{cp} : \frac{\partial \mathbf{C}_{cp}}{\partial k_{hyd;\varphi,\vartheta}} : \mathbf{E}_{cp} = \frac{1}{V_{hyd;\varphi,\vartheta}} \int_{V_{hyd;\varphi,\vartheta}} \boldsymbol{\varepsilon}^{vol}(\underline{x}) : \boldsymbol{\varepsilon}^{vol}(\underline{x}) dV = \left(\bar{\bar{\varepsilon}}_{hyd;\varphi,\vartheta}^{vol} \right)^2 \quad (3.19)$$

$$\frac{1}{2 f_{hyd;\varphi,\vartheta}^{cp}} \mathbf{E}_{cp} : \frac{\partial \mathbf{C}_{cp}}{\partial \mu_{hyd;\varphi,\vartheta}} : \mathbf{E}_{cp} = \frac{1}{V_{hyd;\varphi,\vartheta}} \int_{V_{hyd;\varphi,\vartheta}} \boldsymbol{\varepsilon}^{dev}(\underline{x}) : \boldsymbol{\varepsilon}^{dev}(\underline{x}) dV = \left(\bar{\bar{\varepsilon}}_{hyd;\varphi,\vartheta}^{dev} \right)^2 \quad (3.20)$$

where $f_{hyd;\varphi,\vartheta}^{cp} = V_{hyd;\varphi,\vartheta}/V_{cp}$ stands for the cement paste-related volume fraction of φ, ϑ -orientated hydrate needles, and $\bar{\bar{\varepsilon}}_{hyd;\varphi,\vartheta}^{vol}$ and $\bar{\bar{\varepsilon}}_{hyd;\varphi,\vartheta}^{dev}$ are scalars representing strain energy-related averages of volumetric and deviatoric strains in hydrate needles orientated in φ, ϑ -

direction. Corresponding scalar stress averages can be quantified as (Dormieux et al., 2006)

$$\bar{\bar{\sigma}}_{hyd;\varphi,\vartheta}^{vol} = 3 k_{hyd} \bar{\bar{\varepsilon}}_{hyd;\varphi,\vartheta}^{vol} = \sqrt{\frac{3 k_{hyd}^2}{f_{hyd;\varphi,\vartheta}^{cp}} \mathbf{E}_{cp} : \frac{\partial \mathbb{C}_{cp}}{\partial k_{hyd;\varphi,\vartheta}} : \mathbf{E}_{cp}}, \quad (3.21)$$

$$\bar{\bar{\sigma}}_{hyd;\varphi,\vartheta}^{dev} = 2 \mu_{hyd} \bar{\bar{\varepsilon}}_{hyd;\varphi,\vartheta}^{dev} = \sqrt{\frac{2 \mu_{hyd}^2}{f_{hyd;\varphi,\vartheta}^{cp}} \mathbf{E}_{cp} : \frac{\partial \mathbb{C}_{cp}}{\partial \mu_{hyd;\varphi,\vartheta}} : \mathbf{E}_{cp}}. \quad (3.22)$$

While details about the numerical computation of the partial derivatives in (3.21) and (3.22) are given in (Pichler et al., 2008, 2009), Eqs. (3.19)-(3.22) allow for expressing the volume average of elastic strain energy stored in hydrate needles orientated in φ, ϑ -direction as

$$\frac{1}{V_{hyd;\varphi,\vartheta}} \int \frac{1}{2} \boldsymbol{\varepsilon}(\underline{x}) : \mathbb{C}_{hyd} : \boldsymbol{\varepsilon}(\underline{x}) dV = \frac{1}{2} \left(\bar{\bar{\sigma}}_{hyd;\varphi,\vartheta}^{vol} \bar{\bar{\varepsilon}}_{hyd;\varphi,\vartheta}^{vol} + \bar{\bar{\sigma}}_{hyd;\varphi,\vartheta}^{dev} \bar{\bar{\varepsilon}}_{hyd;\varphi,\vartheta}^{dev} \right) \quad (3.23)$$

We are left with calculating the largest and the smallest principal stress intervening in the Mohr-Coulomb criterion (3.6) based on the scalar stress measures $\bar{\bar{\sigma}}_{hyd;\varphi,\vartheta}^{vol}$ and $\bar{\bar{\sigma}}_{hyd;\varphi,\vartheta}^{dev}$. This requires access to the full tensorial expression of the strain energy-related stress tensor $\bar{\bar{\sigma}}_{hyd;\varphi,\vartheta}$. The latter is estimated by scaling the volume-averaged stress tensor $\bar{\sigma}_{hyd;\varphi,\vartheta}$ such that it is related to the same strain energy as $\bar{\bar{\sigma}}_{hyd;\varphi,\vartheta}$, see (3.23). To this end, we decompose the sought stress tensor $\bar{\bar{\sigma}}_{hyd}$ into its volumetric and deviatoric part as

$$\bar{\bar{\sigma}}_{hyd;\varphi,\vartheta} = \bar{\bar{\sigma}}_{hyd;\varphi,\vartheta}^{vol} + \bar{\bar{\sigma}}_{hyd;\varphi,\vartheta}^{dev}. \quad (3.24)$$

and we express these parts as being equal to their volume-averaged counterparts $\bar{\sigma}_{hyd;\varphi,\vartheta}^{vol}$ and $\bar{\sigma}_{hyd;\varphi,\vartheta}^{dev}$, multiplied with scalar scaling factors

$$\bar{\bar{\sigma}}_{hyd;\varphi,\vartheta}^{vol} = \bar{\sigma}_{hyd;\varphi,\vartheta}^{vol} \frac{\bar{\bar{\sigma}}_{hyd;\varphi,\vartheta}^{vol}}{\bar{\sigma}_{hyd;\varphi,\vartheta}^{vol}}, \quad \bar{\bar{\sigma}}_{hyd;\varphi,\vartheta}^{dev} = \bar{\sigma}_{hyd;\varphi,\vartheta}^{dev} \frac{\bar{\bar{\sigma}}_{hyd;\varphi,\vartheta}^{dev}}{\bar{\sigma}_{hyd;\varphi,\vartheta}^{dev}}. \quad (3.25)$$

The volume-averaged stress tensor $\bar{\sigma}_{hyd;\varphi,\vartheta}$ follows from the stress concentration rule which involves stress concentration tensor $\mathbb{B}_{hyd;\varphi,\vartheta}^{cp}$ as

$$\bar{\sigma}_{hyd;\varphi,\vartheta} = \mathbb{B}_{hyd;\varphi,\vartheta}^{cp} : \boldsymbol{\Sigma}_{cp}, \quad (3.26)$$

for details see Appendix A, and the scalar stress quantities $\bar{\sigma}_{hyd;\varphi,\vartheta}^{vol}$ and $\bar{\sigma}_{hyd;\varphi,\vartheta}^{dev}$ follow by analogy to Eqs. (3.19)-(3.22) as

$$\bar{\sigma}_{hyd;\varphi,\vartheta}^{vol} = \sqrt{\bar{\sigma}_{hyd;\varphi,\vartheta} : \mathbb{I}^{vol} : \bar{\sigma}_{hyd;\varphi,\vartheta}}, \quad \bar{\sigma}_{hyd;\varphi,\vartheta}^{dev} = \sqrt{\bar{\sigma}_{hyd;\varphi,\vartheta} : \mathbb{I}^{dev} : \bar{\sigma}_{hyd;\varphi,\vartheta}}. \quad (3.27)$$

3.2.5 Identification of location and of orientation of most heavily loaded hydrate needles

Herein, we consider that uniaxial compressive loading in \underline{e}_3 -direction is either imposed on an RVE of mortar or of cement paste

$$\boldsymbol{\Sigma}_i = -\Sigma_i^{uni} \underline{e}_3 \otimes \underline{e}_3, \quad i \in \{mor, cp\} \quad (3.28)$$

where Σ_i^{uni} denotes the absolute value of the imposed uniaxial traction. The *location* in the immediate vicinity of sand grains and the *orientation* of most heavily loaded hydrate needles inside RVEs of cement paste are identified as follows.

As for strength predictions for cement paste, macroloading Σ_{cp} is first concentrated into strain energy-related stress averages of hydrate needles, using Eqs. (3.16), (3.21) and (3.22), (3.26)-(3.27), and (3.25) and (3.24). The obtained hydrate stress tensors are functions of the macroloading and of the orientation angles φ and ϑ of the hydrate needles

$$\bar{\bar{\sigma}}_{hyd} = \bar{\sigma}_{hyd}(\Sigma_{cp}^{uni}; \varphi, \vartheta) . \quad (3.29)$$

The largest and smallest eigenvalues of $\bar{\bar{\sigma}}_{hyd}$, i.e. $\bar{\bar{\sigma}}_{hyd,I}(\Sigma_{cp}^{uni}; \varphi, \vartheta)$ and $\bar{\bar{\sigma}}_{hyd,III}(\Sigma_{cp}^{uni}; \varphi, \vartheta)$, are inserted into the Mohr-Coulomb failure criterion, see (3.6) and (3.7). Next, the intensity of macroscopic loading Σ_{cp}^{uni} is conceptually increased (starting from zero) and the failure criteria are checked in all hydrate orientations, i.e. for all φ, ϑ -directions (see Fig. 3.3). The specific orientation angles φ_{fail} and ϑ_{fail} , for which the corresponding failure criterion is satisfied first, refer to the most heavily loaded hydrate orientation, and the corresponding load intensity represents the uniaxial compressive strength of cement paste, $\Sigma_{cp}^{uni,ult}$.

As for strength predictions for mortar, macroloading Σ_{mor} according to (3.28) is first concentrated into cement paste stress states around sand grains, see Eq. (3.13). This problem exhibits axial symmetry with respect to the macroscopic loading direction, i.e. cement paste stress states are a function of the polar angle ψ (see Fig. 3.2):

$$\sigma_{cp} = \sigma_{cp}(\Sigma_{mor}^{uni}; \psi) . \quad (3.30)$$

The calculated stress states represent macroscopic loading of cement paste RVEs, i.e. $\sigma_{cp} \rightarrow \Sigma_{cp}$, and further stress concentration down to hydrate needles is performed as described in the preceding paragraph, such that hydrate stress tensors are also functions of the orientation angles φ and ϑ of hydrate needles

$$\bar{\bar{\sigma}}_{hyd} = \bar{\sigma}_{hyd}(\Sigma_{mor}^{uni}; \psi; \varphi, \vartheta) . \quad (3.31)$$

The largest and smallest eigenvalues of $\bar{\bar{\sigma}}_{hyd}$, i.e. $\bar{\bar{\sigma}}_{hyd,I}(\Sigma_{mor}^{uni}; \psi; \varphi, \vartheta)$ and $\bar{\bar{\sigma}}_{hyd,III}(\Sigma_{mor}^{uni}; \psi; \varphi, \vartheta)$ are inserted into the Mohr-Coulomb failure criterion, see (3.6) and (3.7), and the intensity of macroscopic loading, Σ_{mor}^{uni} is conceptually increased (starting from zero). The Mohr-Coulomb failure criteria are checked for all polar angles ψ marking positions of cement paste RVEs around sand grains [see Fig. 3.2(a)] as well as for all angles φ and ϑ defining the orientation of hydrate needles within RVEs of cement paste (see Fig. 3.3). The specific position and orientation angles ψ_{fail} , φ_{fail} , and ϑ_{fail} , for which the corresponding failure criterion is satisfied first, refer to the most heavily loaded hydrate location and orientation, and the corresponding load intensity represents the uniaxial compressive strength of mortar, $\Sigma_{mor}^{uni,ult}$. Appendix B contains details about the numerical realization.

Notably, the described multiscale model for strength of OPC-based cementitious materials does not contain any fitting parameters. The only input parameters are the initial water-to-cement mass ratio w/c , the initial sand-to-cement mass ratio s/c , and the degree of hydration ξ_{clin} , intervening in the expressions of phase volume fractions, see Eqs. (3.2)-(3.4). All other inputs, i.e. the elastic properties of all involved material phases as well as the strength properties of hydrates, are material *constants*, see Table 3.1 and Eq. (3.7).

3.2.6 Model validation on OPC pastes

Herein, the presented micromechanical model is used to predict strength tests on cement pastes performed at Lafarge Centre de Recherche (LCR), TU Wien – Vienna University of Technology (TUW), and Swiss Federal Laboratories for Materials Science and Technology (EMPA), respectively. All considered strength tests were performed on elongated samples (either cylinders or prisms), such that determined strength values can be interpreted as genuine (“material”) uniaxial compressive strength values and *not* as shear-enhanced (“structural”) cube compressive strength values.

Four sets of tests were carried out at LCR on cement paste cylinders (with a diameter of 7 mm and a height of 22 mm) exhibiting w/c ratios ranging from 0.33 up to 0.508 produced from three distinct OPC cements (referred to as LCR I, LCR II, and LCR III), see Pichler et al. (2013a) for more details. Specimens were cured at 20 °C, tested 1, 3, 7, and 28 days after production, and their hydration degree was determined by XRD/Rietveld coupled with thermogravimetric analysis, as specified in Termkhajornkit and Barbarulo (2012). Blind model predictions agree well with experimental results, see Fig. 3.4, as quantified through the quadratic correlation coefficient $R^2 = 0.897$ for samples with $w/c = 0.33$, and $R^2 = 0.867$ for samples with $w/c \approx 0.50$.

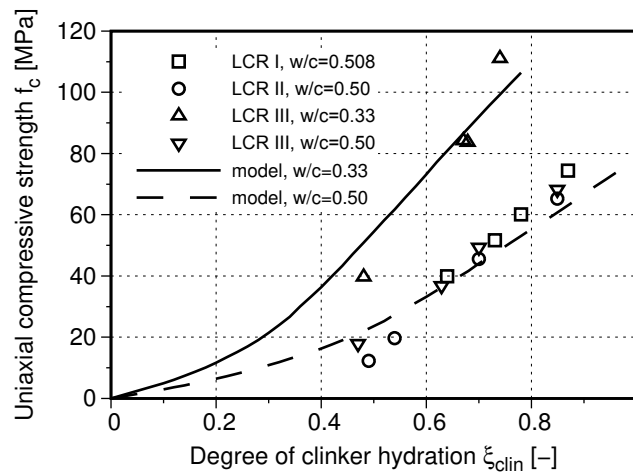


Figure 3.4: Model validation on OPC pastes tested at LCR, as for strength data see (Pichler et al., 2013a)

Two sets of independent strength tests were performed at TUW, referred to as TUV I and TUV II. The testing campaign TUV I was carried out on cylindrical cement paste specimens (with diameter of 29.0 ± 0.3 mm and a height of 58.0 ± 1.3 mm) exhibiting $w/c = 0.42$ from commercial CEM I 42.5 N cement and distilled water, see Pichler et al. (2013a) for details. After demoulding, the specimens were cured in lime-saturated water at 25 °C until testing. The clinker hydration degree was identified from isothermal calorimetry carried out at 25 °C. In the testing campaign TUV II, cement paste prisms (with dimensions of $40 \times 40 \times 80$ mm³) were tested 24 h after production, immediately after demoulding Kosse (2015). Clinker type (CEM I) and mix design ($w/c = 0.42$) were the same as in test campaign TUV I. Molded specimens were continuously stored in a climate chamber at 20 °C, and isothermal calorimetry tests were carried out at the same temperature to get access to the hydration degree. Model predicted strength evolutions for $w/c = 0.42$ agree very well with both experimental campaigns;

the corresponding quadratic correlations coefficient amounts to $R^2 = 0.977$.

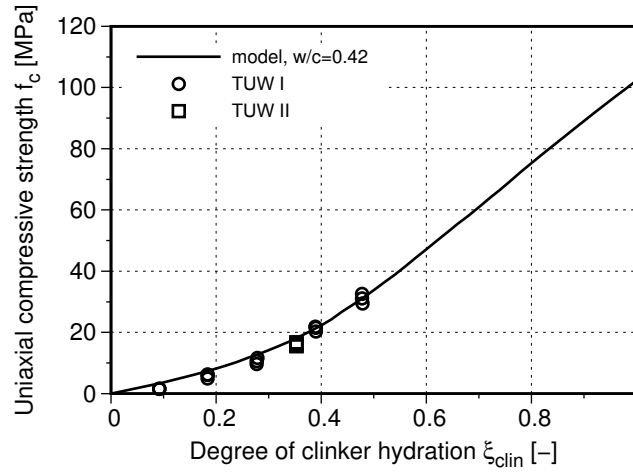


Figure 3.5: Model validation on OPC pastes tested at TUW, as for strength data see (Pichler and Hellmich, 2011; Kosse, 2015)

Strength values of another test campaign performed at EMPA were provided in the framework of the COST action TU1404 (TU1404, 2016), see also Wyrzykowski and Lura (2013). Prismatic cement paste samples ($25 \times 25 \times 100 \text{ mm}^3$) were produced in vacuum from CEM I 42.5 N with two different water-to-cement mass ratios $w/c = \{0.25, 0.30\}$, cured under sealed conditions at 20°C , and tested 1, 3, and 7 days after production. The hydration degree was measured by isothermal calorimetry, see (Wyrzykowski and Lura, 2013). Model predictions agree very well with experimental results, see Fig. 3.6, as quantified by quadratic correlation coefficients amounting to $R^2 = 0.994$ for $w/c = 0.25$ and to $R^2 = 0.993$ for $w/c = 0.30$.

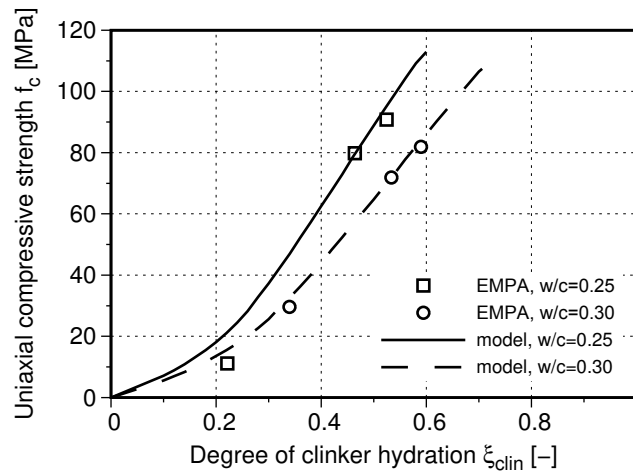


Figure 3.6: Model validation on OPC pastes tested at EMPA, as for strength data see (TU1404, 2016; Wyrzykowski and Lura, 2013)

3.2.7 Model validation on OPC mortars

After the successful model validation at the level of cement paste, we now proceed at the mortar scale, where we consider two sets of experimental data: tests performed at TUW and a test campaign carried out at LCR within the framework of NANOCEM's Core Project 10 (CP 10), see the acknowledgment.

Mortar tests at TUW were carried out on prisms with volume $4 \times 4 \times 8 \text{ cm}^3$, produced with $w/c = 0.50$ (CEM I 42.5 N and distilled water) and sand-to-cement ratio of $s/c = 3.0$, using oven-dried standard quartz sand from the company "Normensand", with diameters smaller than 2 mm. The same material was also characterized by means of hourly repeated three-minute-long creep tests Irfan-ul Hassan et al. (2014), which allowed for quantification of internal curing processes, i.e. water is partly uptaken – upon mixing of raw materials – by the open porosity of the quartz grains, and – during hydration – this water is progressively soaked back into the cement paste matrix, such that the effective water-to-cement mass ratio w_{cp}/c increases linearly with increasing hydration degree

$$w_{cp}/c = 0.47 + 0.0317 \xi_{clin} \leq 0.50. \quad (3.32)$$

Given that strength tests were carried out one day after production, and that calorimetry implies that the degree of clinker hydration reached $\xi_{clin} = 0.353$ at that time, Eq. (3.32) allows for quantifying the effective water-to-cement mass ratio of the tested specimens as $w_{cp}/c = 0.481$. Evaluation of the described strength model for these inputs delivers predictions which agree very well with the measured strength values, see Fig. 3.7.

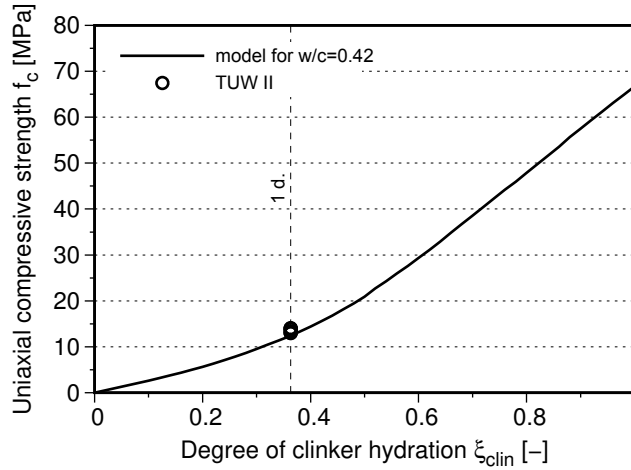


Figure 3.7: Model validation on OPC mortar tested at TUW, as for strength data see (Kosse, 2015)

Experiments from CP 10 were carried out on cylindrical mortar specimens (with a diameter of 70 mm and a height of 150 mm) produced using sand-to-cement mass ratio $s/c = 3.0$ and initial water-to-cement mass ratio $w/c = 0.51$ from CEM I 52.5 N. Moulds were removed 24 hours after production and the specimens were subsequently exposed to air conditioned to 20°C and 99% relative humidity until testing. Tests were carried out 3 and 28 days after production. The clinker hydration degree was identified from XRD/Rietveld and thermogravimetric analysis, amounting to $\xi_{clin} = 0.69$ and $\xi_{clin} = 0.84$ at material ages of 3 days and 28 days, respectively, see also Section 3.3.1 for more details. Evaluating the model

for the tested composition and comparing the results with the experimentally determined strength values, see the thick solid line in Fig. 3.8, shows that the model predicts the strength evolution in OPC mortars quite reliably, as quantified by $R^2 = 0.809$.

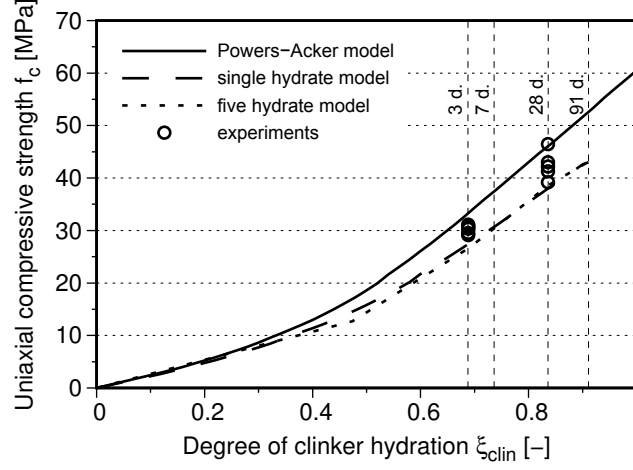


Figure 3.8: Model validation on OPC mortar tested at LCR in the framework of NANOCEM's Core Project 10

3.2.8 Location and orientation of most heavily loaded hydrate needles

For all analyzed OPC mortars, the model-predicted location and orientation of the most heavily loaded hydrate needle is the same, i.e. location angle $\psi_{fail} \approx \pi/6$, and orientation angles $\vartheta_{fail} = 0$, $\varphi_{fail} \in [0; 2\pi]$. Polar angle $\psi_{fail} \approx \pi/6$ indicates that strength-relevant stress peaks in cement paste occur at the shoulder of sand grains, approximately one third of the distance between the poles and the equator, see Fig. 3.9(b). At the microscale of cement paste, the most heavily loaded hydrate needle is virtually aligned with the direction of macroscopic loading ($\vartheta \approx 0$), see Fig. 3.9(c), and the normal of the nanoscopic plane of shear failure is inclined by an angle of $\approx \pi/4$ with respect to the loading direction, see Fig. 3.9(d).

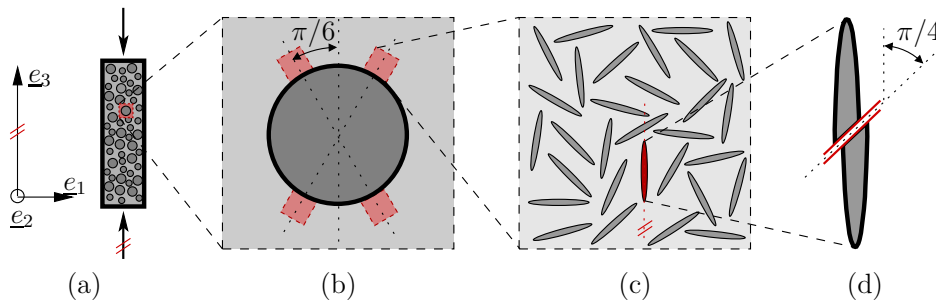


Figure 3.9: Multiscale failure mechanism in mortar: (a) uniaxially compressed mortar sample, (b) location of failure-inducing stress peaks of cement paste attached to a sand grain, (c) most heavily loaded hydrate needle which is part of the microstructure of cement paste (see also Fig. 3.1), (d) orientation of nanoscopic failure plane inside the most heavily loaded hydrate needle

3.3 Strength evolution of blended cement mortars: microstructural characterization, strength testing, and multiscale modeling

The satisfactory model performance regarding OPC pastes and mortars is the motivation to extend our study to blended cement materials. Four blended cement binders were obtained by replacing 45 % of cement volume either by finely ground fillers (quartz or limestone, respectively) or by supplementary cementitious materials (ground granulated blast furnace slag or fly ash, respectively), for mass densities and Blaine fineness values see Table 3.2. The fifth binder, i.e. pure ordinary Portland cement, served as a reference. Replacing cement clinker

Table 3.2: Physical properties of used raw materials

Material	Density [kg/m ³]	Blaine [cm ² /g]	Granulometry			
			d90 [μ m]	d50 [μ m]	d10 [μ m]	d4.3 [μ m]
OPC	3 170	3 630	41.78	15.44	2.45	19.21
Quartz	2 650	6 172	—	—	—	—
Limestone	2 715	4 015	—	—	—	—
Slag	2 930	3 400	—	—	—	—
Fly ash	2 090	3 686	—	—	—	—

by volume (rather than by mass) ensures that the composition of the different materials is identical in terms of initial volume fractions. Also to this end, the initial water-to-solid volume ratio amounting to 1.6 is the same for all pastes. Consequently, pure OPC paste exhibited a water-to-cement mass ratio amounting to $w/c = 0.53$ while this mass ratio was equal to 0.93 for all blended mixes. Notably, water-to-solid *mass* ratios differed from mix to mix, because of the differences in specific mass densities of blending materials, see Table 3.3. All materials were demoulded 1 day after production and subsequently exposed to air conditioned to 20 °C and 99 % relative humidity.

Table 3.3: Investigated paste compositions

Paste type	Initial water/solid volume ratio [-]	Cement replacement volume [%]	Initial water/cement mass ratio [-]	Initial water/solid mass ratio [-]
OPC	1.60	0	0.51	0.51
Quartz blend	1.60	45	0.93	0.55
Limestone blend	1.60	45	0.93	0.54
Slag blend	1.60	45	0.93	0.53
Fly ash blend	1.60	45	0.93	0.60

3.3.1 Microstructural characterization: phase volume evolutions

Microstructural characterization was performed on the dry binders as well as on pastes 1, 3, 7, 28, and 91 days after their production, in order to quantify the evolution of paste volume fractions, see Figs. 3.10(a)-3.14(a). To this end, several methods were combined as follows.

Thermogravimetric analysis and X-ray diffraction including Rietveld refinement allowed for determination of the crystalline phases clinker, portlandite (CH), and ettringite (AFt) as well as the amount of total amorphous matter together with the hydration degree of clinker. The amounts of the poorly crystalline amorphous phases calcium silicate hydrates C-S-H, monosulfoaluminate (AFm), and monosulfocarboaluminates (AFmC) are obtained as follows. Volume and mass balance equations allowed for relating C-S-H and portlandite to hydration of C_3S and C_2S under the assumption that both clinker phases lead to the same type of C-S-H, as suggested also by TEM analysis Richardson (2000). The amount of AFm hydrates was determined based on the amount of dissolved C_3A which was not transformed into ettringite. Finally, the capillary pore volume was calculated as the total paste volume minus the solid volume. As for the supplementary cementitious materials, the degree of reaction of slag and fly ash was determined based on SEM/BSE image analysis. A pozzolanic reaction is assumed for both slag and fly ash materials leading to the formation of additional C-S-H (with a lower calcium-to-silica ratio) and consumption of portlandite in such pastes.

Results from microstructural characterization underline that C-S-H is by far the most frequently produced hydration product, followed by portlandite and by aluminate hydrates, see Figs. 3.10-3.14. As for OPC, the limestone blend, and the quartz blend, the overall hydrate volume increases in very good approximation *linearly* with increasing degree of cement clinker reaction. Although quartz and limestone volumes remain virtually constant throughout the hydration process, they increase the speed of the hydration, compare hydration degrees reached 3, 7, 28, and 91 days after production in Figs. 3.10-3.12. This is typically referred to as a “microfiller effect” (Lothenbach et al., 2011). In addition, the presence of limestone seems to have an influence on the composition of the produced aluminate hydrates, which is in agreement with previous experimental observations (Taylor, 1997).

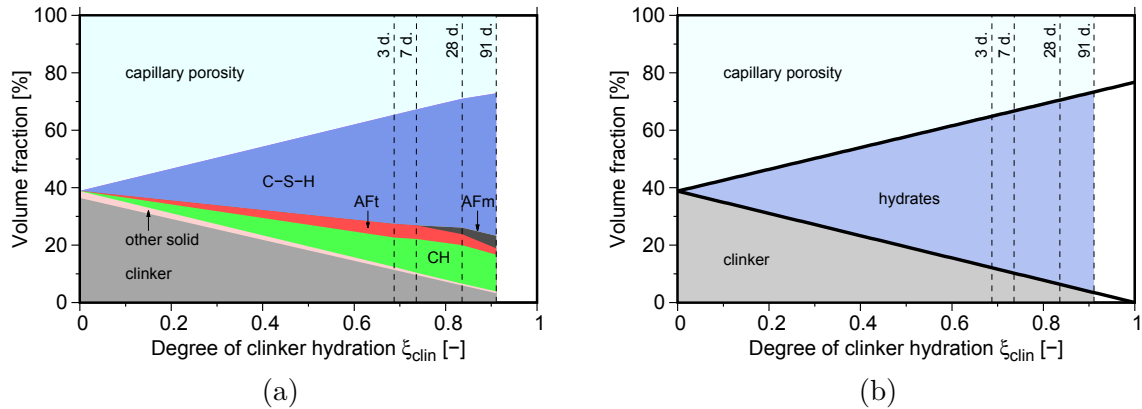


Figure 3.10: Phase assemblage of OPC paste: (a) results from microstructural characterization; and (b) subdivision into clinker, hydrates, and capillary pores according to Eq. (3.33)

As for slag- and fly ash-blended pastes, the overall hydrate volume increases *linearly* with increasing degree of cement clinker hydration, as long as the supplementary cementitious materials remain inert. Slag hydration appears to start around 3 days after production, and the subsequent increase of the degree of slag reaction is virtually a linear function of the degree of clinker hydration. Fly ash hydration, in turn, appears to start around 7 days after production, and the subsequent increase of the degree of fly ash hydration appears to be an overlinear function of the degree of cement clinker hydration. Notably, the unexpected kink in the C-S-H volume fraction developing between the 3rd and the 7th day after production

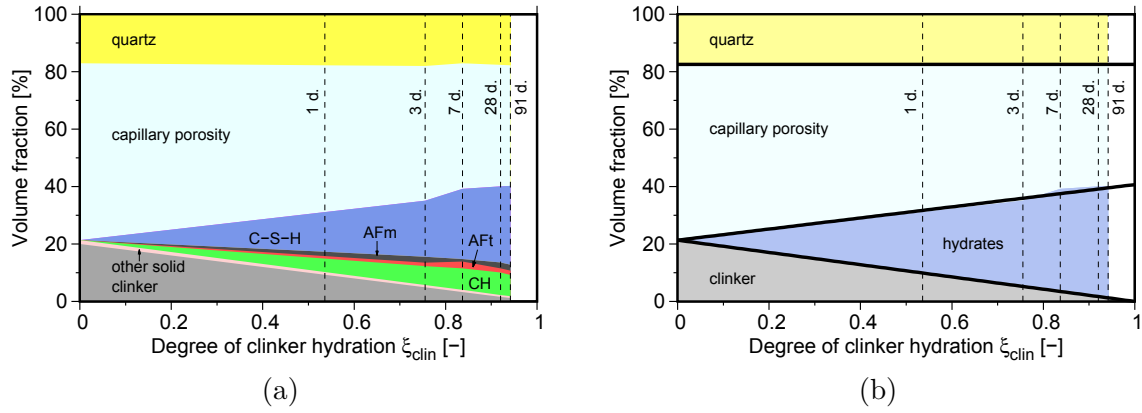


Figure 3.11: Phase assemblage of quartz-blended paste: (a) results from microstructural characterization; and (b) subdivision into clinker, hydrates, capillary pores, and quartz according to Eq. (3.34)

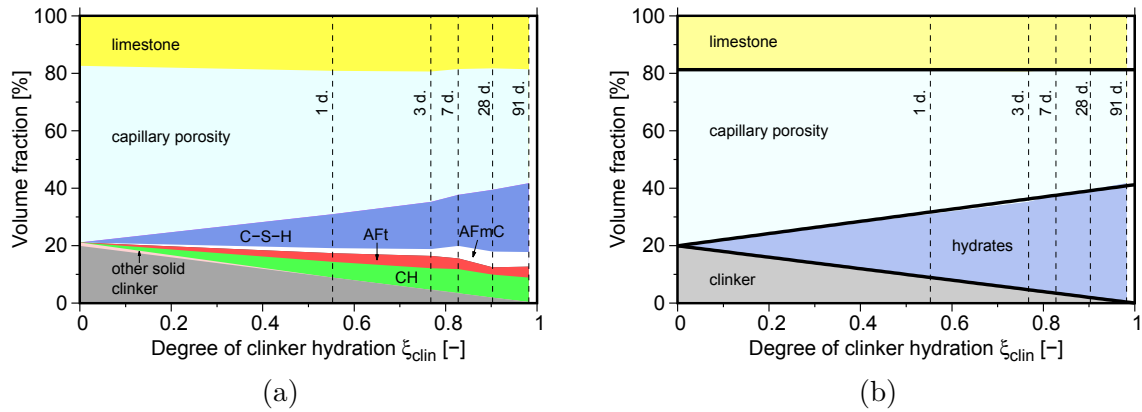


Figure 3.12: Phase assemblage of limestone-blended paste: (a) results from microstructural characterization; and (b) subdivision into clinker, hydrates, capillary pores, and limestone according to Eq. (3.35)

[Fig. 3.14(a)] indicates that microstructural characterization was particularly challenging for the fly ash-blended material. The microfiller effects of the used SCMs was less effective than the one observed with the inert fillers, compare hydration degrees reached 3, 7, 28, and 91 days after production in Figs. 3.10-3.14.

In order to obtain simple closed-form expressions describing monotonous evolutions of phase volumes of clinker, hydrates, capillary porosity, and blending solids, the point-wisely measured phase volume evolutions are approximated by linear, piecewise linear, and piecewise cubic fitting functions. The latter are computed based on a least square approach, which is constrained by the requirement that the volume fractions must sum up to one. The obtained volume fraction evolutions are depicted in Figs. 3.10(b)-3.14(b), and the corresponding functions are given next. For the OPC paste, they read as

$$f_{clin}^{cp} = 0.388 (1 - \xi_{clin}) , \quad f_{hyd}^{cp} = 0.767 \xi_{clin} , \quad f_{pore}^{cp} = 1 - f_{clin}^{cp} - f_{hyd}^{cp} , \quad (3.33)$$

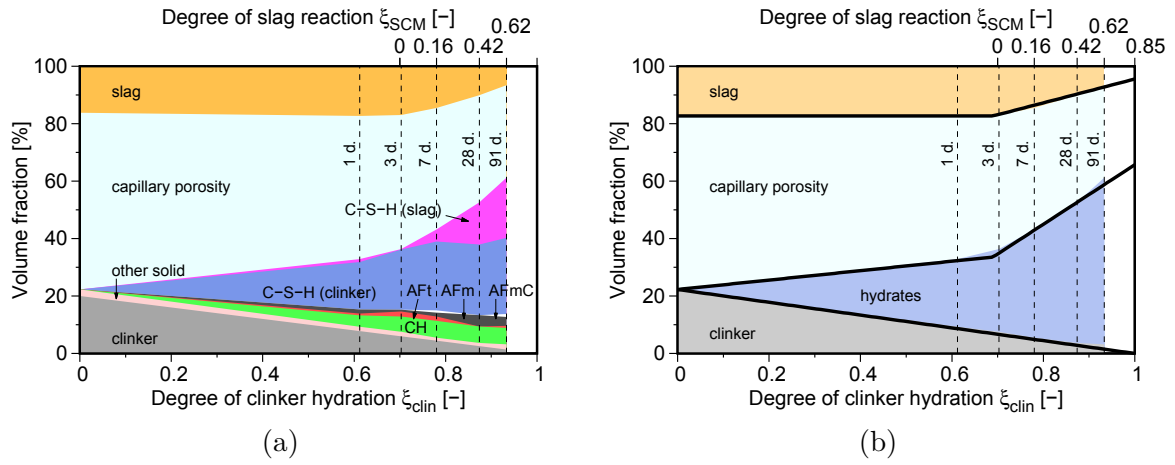


Figure 3.13: Phase assemblage of slag-blended paste: (a) results from microstructural characterization; and (b) subdivision into clinker, hydrates, capillary pores, and slag according to Eq. (3.36)

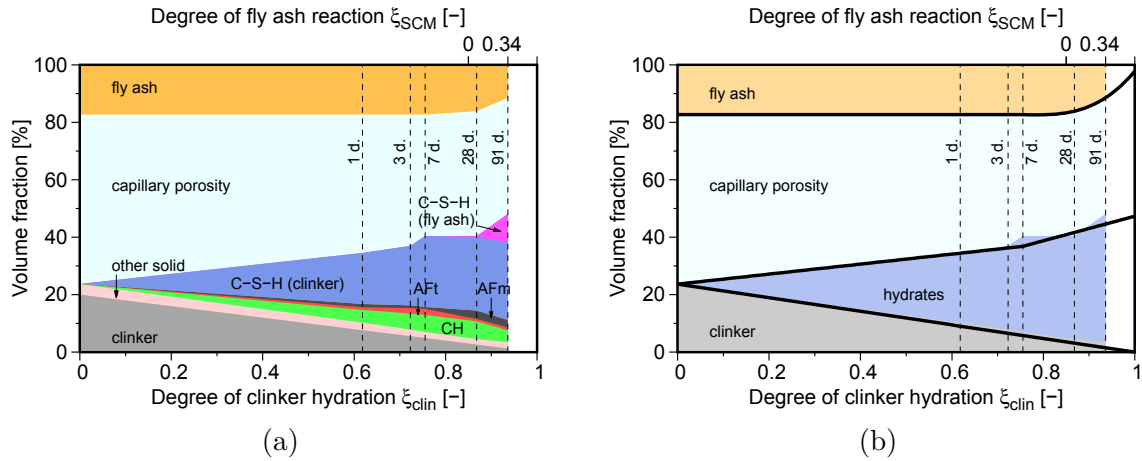


Figure 3.14: Phase assemblage of fly ash-blended paste: (a) results from microstructural characterization; and (b) subdivision into clinker, hydrates, capillary pores, and fly ash according to Eq. (3.37)

for the quartz-blended paste, they read as

$$\begin{aligned} f_{clin}^{cp} &= 0.213 (1 - \xi_{clin}) , & f_{quartz}^{cp} &= 0.174 , \\ f_{hyd}^{cp} &= 0.407 \xi_{clin} , & f_{pore}^{cp} &= 1 - f_{clin}^{cp} - f_{quartz}^{cp} - f_{hyd}^{cp} , \end{aligned} \quad (3.34)$$

for limestone-blended paste, they read as

$$\begin{aligned} f_{clin}^{cp} &= 0.200 (1 - \xi_{clin}) , & f_{limestone}^{cp} &= 0.188 , \\ f_{hyd}^{cp} &= 0.412 \xi_{clin} , & f_{pore}^{cp} &= 1 - f_{clin}^{cp} - f_{limestone}^{cp} - f_{hyd}^{cp} , \end{aligned} \quad (3.35)$$

for the slag-blended paste, they reads as

$$\begin{aligned}
 f_{clin}^{cp} &= 0.223 (1 - \xi_{clin}) \\
 f_{slag}^{cp} &= \begin{cases} 0.173 & \text{if } \xi_{clin} < 0.69 \\ 0.173 - 0.415 (\xi_{clin} - 0.69) & \text{if } \xi_{clin} \geq 0.69 \end{cases} \\
 f_{hyd}^{cp} &= \begin{cases} 0.387 \xi_{clin} & \text{if } \xi_{clin} < 0.69 \\ 0.387 \xi_{clin} + 0.872 (\xi_{clin} - 0.69) & \text{if } \xi_{clin} \geq 0.69 \end{cases} \\
 f_{pore}^{cp} &= 1 - f_{clin}^{cp} - f_{slag}^{cp} - f_{hyd}^{cp},
 \end{aligned} \tag{3.36}$$

and for fly ash-blended paste, they read as

$$\begin{aligned}
 f_{clin}^{cp} &= 0.237 (1 - \xi_{clin}) \\
 f_{FA}^{cp} &= \begin{cases} 0.173 & \text{if } \xi_{clin} < 0.755 \\ 0.173 - 1.081 (\xi_{clin} - 0.755)^3 + 0.031 (\xi_{clin} - 0.755) & \text{if } \xi_{clin} \geq 0.755 \end{cases} \\
 f_{hyd}^{cp} &= \begin{cases} 0.411 \xi_{clin} & \text{if } \xi_{clin} < 0.755 \\ 0.411 \xi_{clin} + 0.254 (\xi_{clin} - 0.755) & \text{if } \xi_{clin} \geq 0.755 \end{cases} \\
 f_{pore}^{cp} &= 1 - f_{clin}^{cp} - f_{FA}^{cp} - f_{hyd}^{cp}
 \end{aligned} \tag{3.37}$$

3.3.2 Uniaxial compressive strength testing of blended mortars

Blended mortars were produced with paste compositions according to Table 3.3 as well as standard sand with mass ratio of sand-to-“sum of cement clinker and of replacement materials” amounting to 3.0. Fresh mortar was cast into cylindrical steel moulds with diameters amounting to 70 mm and heights amounting to 150 mm. Specimens were demoulded after 24 hours and subsequently exposed to air conditioned to 20 °C and 99% relative humidity until testing. Top and bottom surfaces of the mortar cylinders were ground prior to testing in order to ensure close-to-perfect coplanarity required for a central load application. Five to six specimens of each given composition were tested 3 and 28 days after production.

3.3.3 Revisiting strength homogenization of OPC mortar based on microstructural characterization results

Herein, we perform two sensitivity analyses complementing the OPC mortar predictions of Subsections 3.2.7: At first, we stay with representing all hydrates as isotropically orientated needles [see Fig. 3.1(c)], with elastic constants according to Table 3.1 and strength properties according to Eqs. (3.7), but rather than using the Powers-Acker phase evolution model (3.2)-(3.4), we now use the *measured* phase volume evolutions as illustrated in Fig. 3.10(b), see also Eqs. (3.33). Obtained model predictions, referred to as “single hydrate” model (see the dashed line in Fig. 3.8), explain the available strength data similarly well as the Powers-Acker model-related predictions (see the thick solid line in Fig. 3.8), but the former are by some 15 % smaller than the latter. This is because the microstructural characterization results suggest that hydration products are denser than foreseen by the Powers-Acker model, and denser hydrates result in an increased capillary porosity which effectively reduces the strength of the material.

As for the second sensitivity analysis, we consider five types of hydrates within the RVE of hydrate foam (rather than only one type), see Fig. 3.15 for a conceptual illustration and Table 3.4 for elastic properties and characteristic phase shapes. The Mohr-Coulomb strength properties of Eqs. (3.7) are now assigned to C-S-H only. Corresponding strength homogenization results, referred to as “five hydrates” model (see the thin dashdotted line in Fig. 3.8), are very similar to the ones obtained using the “single hydrate” approach. The sensitivity analyses suggest that investments into a reliable quantification of the overall phase volume fraction of *all hydrates* is more important than investments into a very detailed representation of *different hydration products*; at least for OPC mortars.

Table 3.4: Elastic and micromorphological hydrate properties

	Bulk modulus		S hear modulus		Source	Shape
	k [GPa]		μ [GPa]			
C-S-H gel	k_{CSH}	18.7	μ_{CSH}	11.8	[1]	needle [1,2]
portlandite	k_{CH}	40.00	μ_{CH}	16.00	[3,4]	sphere
ettringite	k_{AFt}	27.20	μ_{AFt}	9.45	[5]	needle [1,6]
monosulfate	k_{AFm}	40.00	μ_{AFm}	16.00	*	sphere
monocarbonate	k_{AFmC}	40.00	μ_{AFmC}	16.00	*	sphere

* chosen to be equal to portlandite, see also (Termkhajornkit et al., 2014)

[1] from (Pichler and Hellmich, 2011)

[2] from (Richardson, 2004)

[3] from (Holuj et al., 1985a)

[4] from (Monteiro and Chang, 1995)

[5] from (Speziale et al., 2008)

[6] from (Scrivener, 2004)

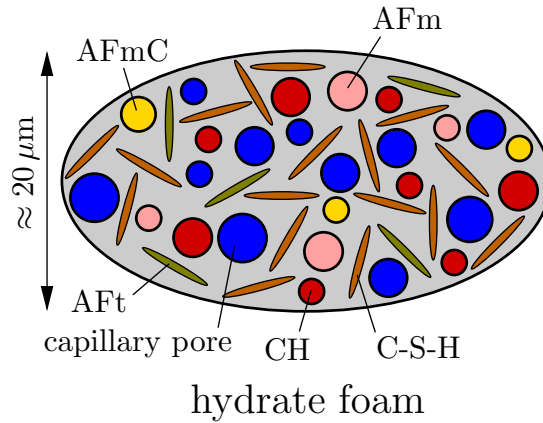


Figure 3.15: RVE of hydrate foam with five types of hydrates (“material organogram”); two-dimensional sketches of three-dimensional representative volume elements

3.3.4 Strength homogenization of inert filler-blended mortars: consideration of quartz and limestone as reinforcements of the hydrate foam

When it comes to include quartz or limestone fillers into the micromechanical representation of mortar (Fig. 3.1), it is noteworthy that the Blaine fineness of the used fillers is considerably higher than the one of the cement clinker, see Table 3.2. Higher Blaine values imply smaller particle sizes, and this motivates us to introduce the fillers as spherical inclusions at the scale of the hydrates, i.e. one scale below the cement clinker, see Fig. 3.16. In addition, the finely

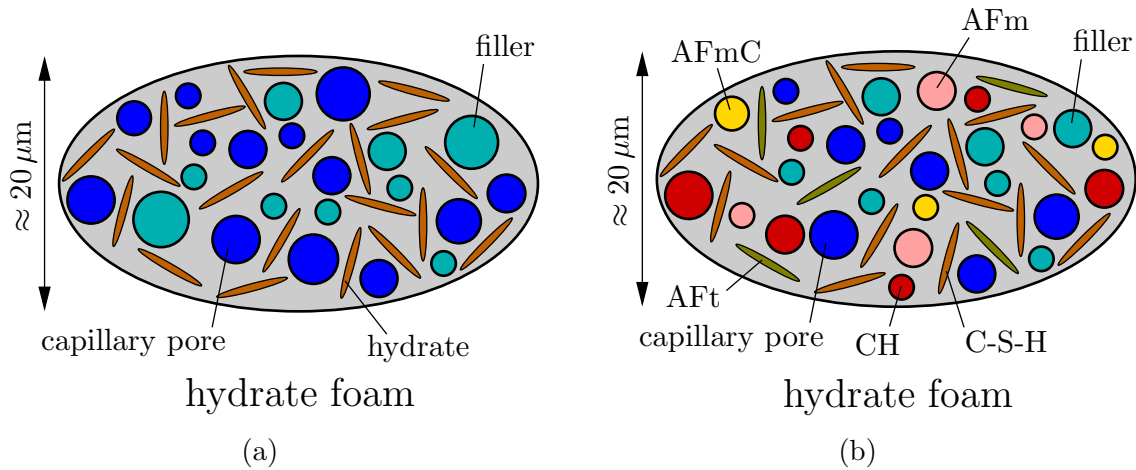


Figure 3.16: RVEs of hydrate foam including the finely ground fillers quartz or limestone (“material organograms”): (a) one hydrate type, (b) five types of hydrates; two-dimensional sketches of three-dimensional representative volume elements

ground filler grains act as preferred precipitation sites for hydrates, as underlined by the observed microfiller effect, and this is a further argument to consider filler particles as part of the hydrate foam matrix. By analogy to the sensitivity analysis described in the previous subsection, we compare two modeling options: (i) consideration of one hydrate type [see Fig. 3.16(a)] with elastic constants, strength properties and phase volume evolutions according to Table 3.1, Eq. (3.7), and Figs. 3.11(b) and 3.12(b), respectively; and (ii) five hydrate types [see Fig. 3.16(b)] with elastic properties and shapes according to Table 3.4 as well as phase volume evolutions according to Fig. 3.11(a) and 3.12(a). Strength values predicted by the “single hydrate” model overestimate strength values measured 3 days after production and underestimate 28 day strength values, see the dashed lines and the circles in Figs. 3.17(a) and (b). The multiscale model with the more detailed representation of hydrates (“five hydrates” model), in turn, explains the strength values measured after 3 days very reliably, but also underestimates the 28 day strength values, see the solid lines and circles in Figs. 3.17(a) and (b).

Model-predicted strength evolutions as function of hydration degree of cement clinker exhibit the following remarkable features. While compressive strength is well known to increase initially overlinearly and later virtually linearly (Taplin, 1959; Pichler and Hellmich, 2011; Pichler et al., 2013a), the obtained strength evolution of both filler-blended mortars show a surprising *underliner* increase of strength as function of hydration degree during the age period from 3 to 28 days, see the solid lines in Figs. 3.17. This phenomenon particularly concerns the quartz-blended mortar. It is a consequence of the microstructural characterization results

which have served as input for strength homogenization, see particularly Fig. 3.11, where the difference quotient $\Delta f_{CSH}^{cp}/\Delta \xi_{clin}$ (i.e. the increase of the C-S-H volume fraction over the increase of the hydration degree of cement clinker) in the age interval from 3 to 7 days is *larger* than in the age interval from 7 to 28 days. This suggests that microstructural characterization is particularly challenging 28 and 91 days after production, because extrapolating, in Fig. 3.17(a), the model-predicted strength evolution from 7 to 28 days, based on the obtained trend from 0 to 7 days, would explain the strength data measured 28 days after production. While this suggests a considerable uncertainty regarding the microstructural characterization results at mature stages, model-predicted strength evolutions also suggest that consideration of only one hydrate type or several hydrate types renders a considerable difference for strength homogenization of inert filler-blended mortars, see Figs. 3.17.

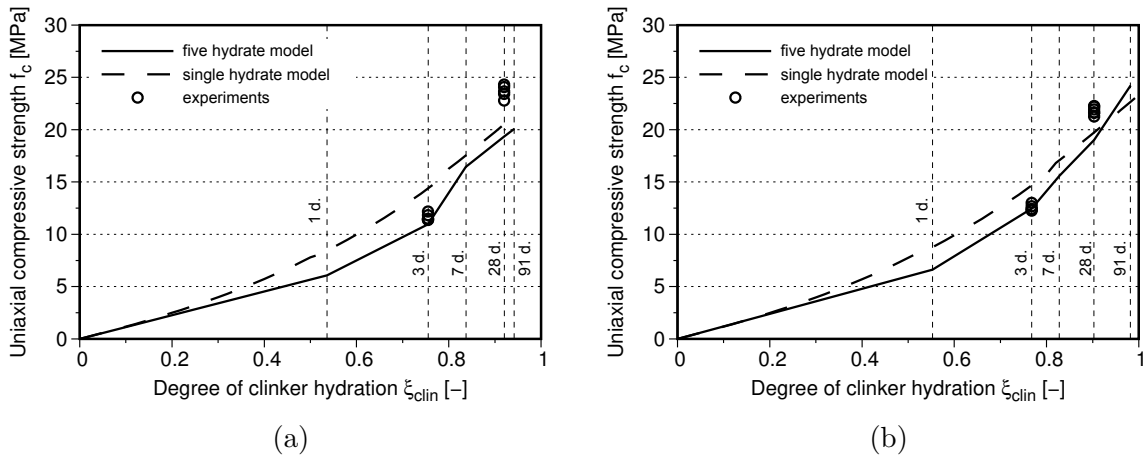


Figure 3.17: Comparison of model-predicted strength evolutions with experimental data from Core Project 10 for (a) quartz-blended mortar, and (b) limestone-blended mortar

3.3.5 Strength homogenization of SCM-blended mortars: the strength-increasing effects of slag and fly ash hydration

As for including slag or fly ash into the microstructural representation of mortar (Fig. 3.1), it is noteworthy that the Blaine fineness of the used SCMs is comparable or smaller than to the one of the OPC clinker, see Table 3.2. Similar Blaine values imply similar particle sizes, and this motivates us to introduce SCMs as spherical inclusions at the same scale as the clinker grains, see Fig. 3.18. In addition, the microfiller effect of the SCMs was significantly less effective compared to the one of the inert fillers, and this is a further argument to consider SCM particles at the *same* scale as clinker grains.

Slag and fly ash are inert during the first few days after production, such that the OPC-related hydrate strength values (3.7) are expected to apply for macroscopic strength predictions. However, as soon as the SCMs start to react, the characteristic hydrate strength increases, as described next. Nanoindentation experiments of Zadeh and Bobko (2013) showed that the strength-related indentation hardness of low density C-S-H in mature slag- and fly ash-blended pastes is by almost 50 % larger than the one in conventional OPC. This SCM hydration-related strength increase is even more pronounced for high density C-S-H (Zadeh and Bobko, 2013). Stiffness-related indentation moduli, however, are virtually unaffected by SCM hydration (Zadeh and Bobko, 2013). The increased strength might originate from the fact that slag and fly ash contain significantly more silicon oxide than clinker, yielding a smaller

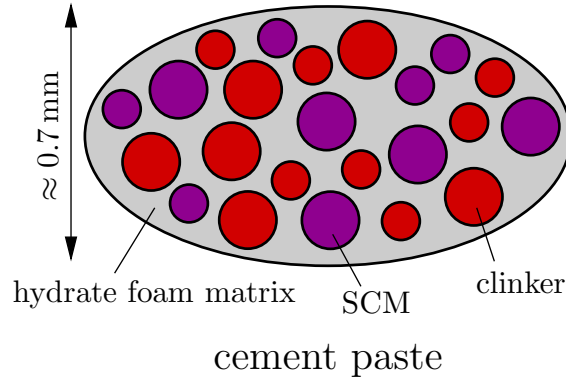


Figure 3.18: RVE of cement paste including SCMs slag or fly ash (“material organogram”); two-dimensional sketches of three-dimensional representative volume elements

calcium-to-silica ratio of C-S-H (Feldman et al., 1990; Lam et al., 2000). Using rigidity theory of glass science, Bauchy et al. (2014) showed that decreasing calcium-to-silica ratio increases the hydrates’ strength, because more bonds between the atoms develop. In order to capture this effect in the model, the hydrates’ cohesion is considered to increase as soon as slag or fly ash start to react. In the sense of a first approach, the increase of the cohesion is considered to be proportional to the volume of already consumed SCM, ΔV_{SCM} , divided by the volume of already consumed clinker, ΔV_{clin} :

$$c_{hyd} = \left(1 + \alpha_{SCM} \frac{\Delta V_{SCM}}{\Delta V_{clin}}\right) 50 \text{ MPa} \quad \forall SCM \in \{slag, FA\} \quad (3.38)$$

with α_{SCM} denoting a dimensionless proportionality constant. The hydrates’ friction angle, in contrast, is considered to remain constant, motivated by the fact that low and high density C-S-H exhibit markedly different cohesion values but the *same* friction angle Sarris and Constantinides (2013). As for the unknown quantities α_{slag} and α_{FA} , we perform sensitivity analyses, as discussed next. Motivated by the aforementioned nanoindentation results (Zadeh and Bobko, 2013), we consider that slag-blended hydrates are, 28 days after production, by 50 % stronger than OPC hydrates, implying that $\alpha_{slag} = 1.812$, see Eq. (3.38). This serves as a starting point for the sensitivity analyses for slag- and fly ash blended pastes, i.e.

$$\alpha_{SCM} \in \{0.000, 0.906, 1.812, 3.624\} \quad (3.39)$$

is considered for the study. In addition, we compare the modeling approach with one type of hydrate [Fig. 3.1(c)] with the alternative approach based on five hydrates (Fig. 3.15). Both modeling approaches slightly underestimate measured strength values 3 days after production, see Figs. 3.19 and 3.20. As for slag-blended mortars, the measured strength evolution from 3 to 28 days after production is nicely reproduced based on $\alpha_{slag} = 1.812$ of the studied interval (3.39), see Fig. 3.19. As for fly ash-blended mortars, the volume ratio $\Delta V_{SCM}/\Delta V_{clin}$ is quite small at 28 days after production. Consequently, also the strengthening effect is rather small, see Figs. 3.20. Reminiscent of the situation encountered with the quartz-blended mortar, the underestimated strength values 28 days after production might well be a consequence of the microstructural characterization results, see the kinky evolution of the point-wisely resolved phase volume evolutions from 3 days to 91 days after production (Fig. 3.14). The corresponding uncertainties render a detailed assessment of the used multiscale strength model in the context of the fly ash-blended mortar impossible.

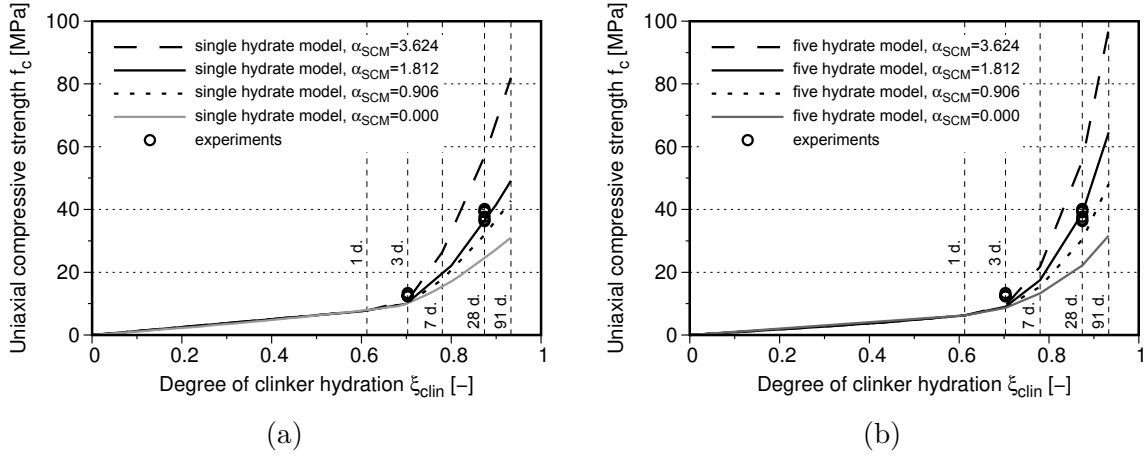


Figure 3.19: Comparison of model-predicted strength evolutions with experimental data from NANOCEM's Core Project 10 for slag-blended mortar: (a) single hydrate model, and (b) five hydrate model; SCM hydration related strengthening of C-S-H is modeled according to Eq. (3.38) and (3.39).

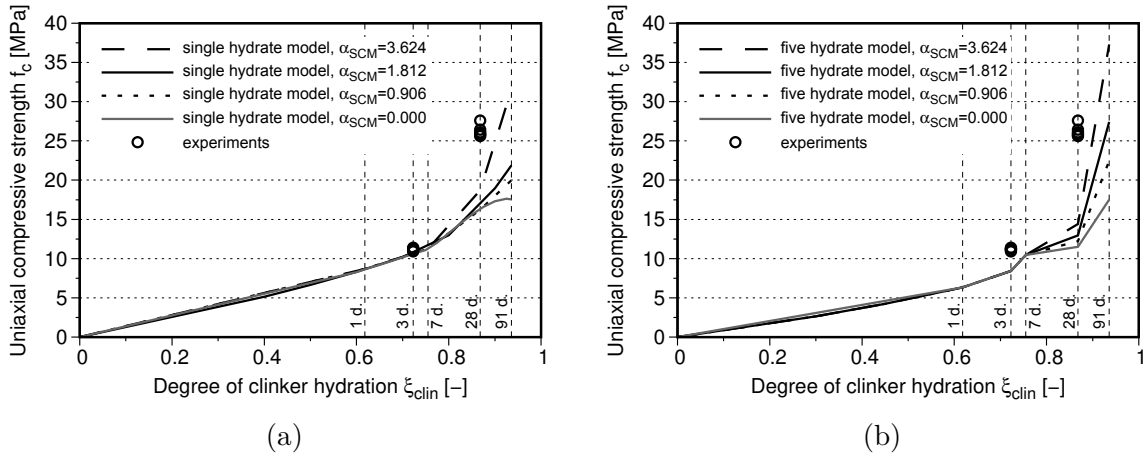


Figure 3.20: Comparison of model-predicted strength evolutions with experimental data from NANOCEM's Core Project 10 for fly ash-blended mortar: (a) single hydrate model, and (b) five hydrate model; SCM hydration related strengthening of C-S-H is modeled according to Eq. (3.38) and (3.39).

3.4 Discussion

Two aspects related to multiscale stress concentration deserve discussion: (i) stress redistributions resulting from potential partial debonding of sand grains from the surrounding cement paste matrix, prior to reaching the uniaxial compressive strength of mortar, and (ii) stress peaks in the hydrate foam occurring in the immediate vicinity of unhydrated clinker grains.

As regards uniaxial compressive strength tests on *concretes*, it is well known that partial debonding of aggregates from the surrounding cement paste matrix typically starts once the macroscopic loading exceeds one third of the compressive strength (Mang and Hofstetter, 2000). Debonding is driven by tensile stresses, and it may either develop in form of cracking *inside* the 15 to 30 microns thin interfacial transition zone (ITZ) which is located between the aggregates and the cement paste matrix, or in form of separation of the ITZ from the aggregate (Königsberger et al., 2014a,b). In addition, debonding is spatially limited to regions where significant tensile stresses occur, and – under macroscopic uniaxial compression – this is observed only in lateral parts of aggregates (Königsberger et al., 2014a,b). Therefore, debonding results in rather localized stress re-distributions, and the latter are on the order of magnitude of the debonding strength. Because the latter is by one order of magnitude smaller than the compressive strength, debonding-induced stress redistributions are of secondary importance for compression-dominated stress states in the shoulder region of aggregates, where cement paste fails once the compressive strength of concrete is reached. Therefore, consideration of firm bonding between sand grains and the surrounding cement paste matrix is a reasonable assumption when it comes to quantifying compression-dominated stress states of cement paste in the immediate vicinity of sand grains.

Unhydrated clinker grains are significantly stiffer than the average stiffness of the surrounding hydrate foam matrix. This raises the question whether failure of the hydrate foam starts in the immediate vicinity of clinker grains, by analogy to the situation encountered with sand grains and the cement paste matrix, see above. In this context, it is noteworthy that the hydrate foam exhibits density gradients. Close to unhydrated clinker grains, namely, so called “inner products” form, and they are denser than the “outer products” forming in the interstitial space between unhydrated clinker grains (Taplin, 1959; Richardson, 2000). Considering that mass density, stiffness, and strength are typically well-correlated properties, also stiffness and strength of the hydrate foam decrease with increasing distance from unhydrated clinker grains. The stiffer a microstructural region, in turn, the larger is the stress concentration, and vice versa (Salençon, 2001). Therefore, also hydrate foam stresses decrease with increasing distance from the unhydrated clinker grains (Hlobil et al., 2016), such that failure of the hydrate foam will start in characteristic distance from unhydrated clinker grains, where the stress-to-strength ratio reaches a maximum. This is likely to happen in the domain of outer products, i.e. in the region of low-density C-S-H, rather than in the immediate vicinity of the unhydrated clinker grains. This explains why we have used different modes of stress concentration around sand grains and around unhydrated clinker grains, respectively. In addition, it is noteworthy that the hydrate foam densifies progressively during hydration, i.e. *quantitatively* the density increases, while the density *distribution* can be expected to stay *qualitatively* the same, as suggested recently by Finite Element-based homogenization of cement pastes (Hlobil et al., 2016). This renders simple consideration of hydration-dependent *average* hydrate foam properties (density and stiffness) reasonable for quantification of stress concentration.

3.5 Conclusions

In order to study the early-age strength evolution of OPC and blended mortars, we have carried out several extensions of the multiscale elasto-brittle strength model of Pichler and Hellmich (2011):

- As for the extension towards mortars, the presented model accounts for stress peaks in representative volumes of cement paste, which are directly attached to the surface of sand grains.
- The elasto-brittle failure criterion of micron-sized hydrate needles was extended from a *von Mises* approach to a *Mohr-Coulomb* approach.
- The microstructural representation of “hydrates” was extended from on one *average* hydrate type towards several types of hydrates, including C-S-H, portlandite, ettringite, monosulfate, etc.
- The microstructural representation of the “binder” phase was extended from consideration of cement clinker towards additional consideration of the cement replacement materials quartz, limestone, slag, and fly ash.

From the satisfactory model performance regarding blind predictions of strength of OPC pastes and mortars, tested in three different laboratories, we draw the following conclusions:

- When subjecting mortars to uniaxial compression, the most heavily loaded representative volume of cement paste is directly attached to sand grains. Related stress peaks of cement paste can be quantified by calculation of spatial averages of stresses and strains in sand grains, and by “translating” them to adjacent cement paste volumes which are directly attached to the sand grains. As for this sand-to-cement paste transition, it is adequate to consider firm bond-related continuity conditions for displacements and tractions in the interfaces between sand grains and cement paste.
- As for the stress concentration from (stress peaks of) cement paste down to micron-sized needle-shaped hydrates, strain energy-related stress averages, i.e. so called “higher-order” or “second-order” stress averages, are relevant, because hydrate failure is very likely related to *energy-driven* shear cracking at nanometric scales *inside* hydrate needles, whereby the shear strength increases with increasing pressure acting on the crack plane.
- The described failure mode of hydrate needles is accounted for by the newly adopted Mohr-Coulomb criterion. As for OPC materials, the two involved strength constants of hydrates, i.e. the cohesion and the angle of internal friction, may be set equal to the corresponding quantities of low-density C-S-H, which are known from limit state analysis of grid nanoindentation studies (Sarris and Constantinides, 2013).
- Virtually the same model-predicted strength evolutions of OPC mortars are obtained, no matter whether just one *average* hydrate type was considered or several types of hydrates.
- Microstructural characterization has delivered phase volume evolutions that are related to denser hydrates, compared to the Powers-Acker phase volume evolution model. Denser hydrates, in turn, result in larger amounts of capillary pores, and this results in smaller model-predicted strength values.

As for cementitious materials produced with blended binders, phase evolution models are, unfortunately, still out of reach. Therefore, microstructural characterization data are required prerequisites for multiscale strength predictions. In this context, the following conclusions are drawn

- Microstructural characterization based on thermogravimetric analysis, X-ray diffraction with Rietveld refinement, and scanning electron microscopy remains to be a challenging task. The nowadays achievable accuracy is, unfortunately, not high enough as to allow for a *detailed* assessment of the predictive capabilities of multiscale strength models which use the microstructural characterization results as input. Still, the following additional conclusions appear to be justified.
- Compared to OPC mortars, strength predictions for blended mortars appear to be significantly more sensitive to the microstructural representation of hydrates either in form of just one *average* hydrate type or in form of several different types of hydrates. The latter more detailed representation appears to deliver better strength predictions.
- Finely ground inert fillers (quartz and limestone) exhibit a significant filler effect. It is well-known that they are accelerating hydration kinetics, because small filler particles represent preferred precipitation sites for hydrates. In addition to this “filler effect on reaction kinetics”, the present study suggests that finely ground fillers also exhibit a “mechanical filler effect”, because they appear to act as strength-increasing reinforcements of the hydrate foam, i.e. at the fine scale of observation of individual hydration products and of capillary porosity.
- Supplementary cementitious materials (slag and fly ash) are hydraulic materials which are well known to react – during the first few days after production – significantly slower than ordinary Portland cement. Notably, the present study suggests that SCM hydration *significantly* increases the strength of cementitious materials already during the second, third, and fourth week after production, and – very remarkably – this strengthening effect appears to be not only related to an increase of hydrate volume and to a corresponding decrease of capillary porosity, but also to an increase of the strength of those hydrates which represent the weakest links of the microstructure. While this hydrate strengthening effect of SCMs is consistent with results from nanoindentation testing of pure OPC and blended pastes, see Zadeh and Bobko (2013), and with theoretical considerations inspired by glass physics (Bauchy et al., 2014), a more detailed analysis is required to identify the evolution of the increase of the hydrate strength, driven by the hydration of SCMs.

Acknowledgments

Funding of the first author provided by the industrial academic nanoscience research network for sustainable cement and concrete “NANOCEM” (<http://www.nanocem.org>) within the framework of Core Project 10 entitled “Micromechanical Analysis of Blended Cement-Based Composites” is gratefully acknowledged. In addition, we appreciate stimulating discussions at NANOCEM events, particularly with Dr. Gilles Chanvillard (Lafarge) and Dr. Klaus-Alexander Rieder (GCPAT).

Appendix A: Scale transitions, stiffness upscaling and stress concentrations

Stiffness homogenization starts with the hydrate foam (Fig. 3.1). Given the polycrystalline arrangement of hydrate needles and capillary pores, the self consistent scheme (Hershey, 1954; Kröner, 1958; Hill, 1965) is appropriate for homogenization, yielding the following implicit expression for the homogenized stiffness of the hydrate foam (Pichler et al., 2009)

$$\begin{aligned} \mathbb{C}_{hf} = & \left(f_{pore}^{hf} \mathbb{C}_{pore} : \left\{ \mathbb{I} + \mathbb{P}_{sph}^{hf} : [\mathbb{C}_{pore} - \mathbb{C}_{hf}] \right\}^{-1} \right. \\ & \left. + f_{hyd}^{hf} \mathbb{C}_{hyd} : \int_0^{2\pi} \int_0^\pi \left\{ \mathbb{I} + \mathbb{P}_{cyl}^{hf}(\varphi, \vartheta) : [\mathbb{C}_{hyd} - \mathbb{C}_{hf}] \right\}^{-1} \frac{\sin \vartheta}{4\pi} d\vartheta d\varphi \right) : \\ & \left(f_{pore}^{hf} \left\{ \mathbb{I} + \mathbb{P}_{sph}^{hf} : [\mathbb{C}_{pore} - \mathbb{C}_{hf}] \right\}^{-1} \right. \\ & \left. + f_{hyd}^{hf} \int_0^{2\pi} \int_0^\pi \left\{ \mathbb{I} + \mathbb{P}_{cyl}^{hf}(\varphi, \vartheta) : [\mathbb{C}_{hyd} - \mathbb{C}_{hf}] \right\}^{-1} \frac{\sin \vartheta}{4\pi} d\vartheta d\varphi \right)^{-1}. \end{aligned} \quad (3.40)$$

whereby f_j^{hf} denote the hydrate foam-related phase volume fractions and \mathbb{C}_j denote the elastic phase stiffness for hydrates and capillary pores $j \in \{hyd, cpor\}$. The spherical and cylindrical phase shape, respectively, is taken into account by using the corresponding Hill tensors \mathbb{P}_{sph}^{hf} and \mathbb{P}_{cyl}^{hf} , see (Pichler et al., 2009) for details. Notably, orientation angles φ and ϑ refer to the azimuth and zenith angles of the hydrate needle. As for the homogenization of the matrix-inclusion composites cement paste and mortar, the Mori-Tanaka scheme (Mori and Tanaka, 1973; Benveniste, 1987) is appropriate, resulting in homogenized stiffness tensors of cement paste reading as (Pichler et al., 2009)

$$\begin{aligned} \mathbb{C}_{cp} = & \left(\{1 - f_{clin}^{cp}\} \mathbb{C}_{hf} + f_{clin}^{cp} \mathbb{C}_{clin} : \left\{ \mathbb{I} + \mathbb{P}_{sph}^{hf} : [\mathbb{C}_{clin} - \mathbb{C}_{hf}] \right\}^{-1} \right) : \\ & \left(\{1 - f_{clin}^{cp}\} \mathbb{I} + f_{clin}^{cp} \left\{ \mathbb{I} + \mathbb{P}_{sph}^{hf} : [\mathbb{C}_{clin} - \mathbb{C}_{hf}] \right\}^{-1} \right)^{-1}, \end{aligned} \quad (3.41)$$

with cement paste-related clinker volume fraction f_{clin}^{cp} , and in the homogenized stiffness tensor of mortar as (Pichler et al., 2013a)

$$\begin{aligned} \mathbb{C}_{mor} = & \left(\{1 - f_{sand}^{mor}\} \mathbb{C}_{cp} + f_{sand}^{mor} \mathbb{C}_{sand} : \left\{ \mathbb{I} + \mathbb{P}_{sph}^{cp} : [\mathbb{C}_{sand} - \mathbb{C}_{cp}] \right\}^{-1} \right) : \\ & \left(\{1 - f_{sand}^{mor}\} \mathbb{I} + f_{sand}^{mor} \left\{ \mathbb{I} + \mathbb{P}_{sph}^{cp} : [\mathbb{C}_{sand} - \mathbb{C}_{cp}] \right\}^{-1} \right)^{-1}, \end{aligned} \quad (3.42)$$

with mortar-related sand volume fraction f_{sand}^{mor} and cement paste-related Hill tensor \mathbb{P}_{sph}^{cp} .

As for downscaling of macrostresses to the spatial average of hydrate stresses (first-order concentration) the following stress concentration tensors are used: \mathbb{B}_{sand}^{mor} , \mathbb{B}_{cp}^{sand} , and $\mathbb{B}_{hyd;\varphi,\vartheta}^{cp}$,

see Eqs. (3.8) and (3.26). The mortar-to-sand stress concentration tensor \mathbb{B}_{sand}^{mor} is isotropic and reads as (Königsberger et al., 2014a) reads as

$$\begin{aligned} \mathbb{B}_{sand}^{mor} = \mathbb{C}_{sand} : \left\{ \mathbb{I} + \mathbb{P}_{sph}^{cp} : [\mathbb{C}_{sand} - \mathbb{C}_{cp}] \right\}^{-1} : \\ \left(\{1 - f_{sand}^{mor}\} \mathbb{I} + f_{sand}^{mor} \left\{ \mathbb{I} + \mathbb{P}_{sph}^{cp} : [\mathbb{C}_{sand} - \mathbb{C}_{cp}] \right\}^{-1} \right)^{-1} : (\mathbb{C}_{mor})^{-1} \end{aligned} \quad (3.43)$$

The aggregate-to-cement paste stress concentration tensor B_{cp}^{sand} can be given in a compact form in a local spherical base frame with base vectors $\underline{e}_r, \underline{e}_\theta, \underline{e}_\phi$ moving along the sand grain surface. The non-zero components read as (Königsberger et al., 2014a)

$$\begin{aligned} B_{cp,rrrr}^{sand} &= 1 \\ B_{cp,\theta\theta\theta\theta}^{sand} &= B_{cp,\phi\phi\phi\phi}^{sand} = \mu_{cp} (3 k_{sand} k_{cp} + 2 k_{sand} \mu_{cp} + 2 k_{cp} \mu_{sand}) / \Delta \\ B_{cp,\theta\theta\phi\phi}^{sand} &= B_{cp,\phi\phi\theta\theta}^{sand} = 2 \mu_{cp} (k_{cp} \mu_{sand} - k_{sand} \mu_{cp}) / \Delta \\ B_{cp,\theta\theta rr}^{sand} &= B_{cp,\phi\phi rr}^{sand} = [3 k_{sand} k_{cp} (\mu_{sand} - \mu_{cp}) - 2 \mu_{sand} \mu_{cp} (k_{sand} - k_{cp})] / \Delta \\ B_{cp,r\theta r\theta}^{sand} &= B_{cp,r\phi r\phi}^{sand} = \frac{1}{2} \quad B_{cp,\theta\phi\theta\phi}^{sand} = \frac{\mu_{cp}}{2 \mu_{sand}} \end{aligned} \quad (3.44)$$

with $\Delta = k_{sand} \mu_{sand} (3 k_{cp} + 4 \mu_{cp})$ and symmetries $B_{cp,ijkl}^{sand} = B_{cp,jikl}^{sand} = B_{cp,ijlk}^{sand} = B_{cp,jilk}^{sand}$. Finally, the stress concentration from the cement paste scale to φ, ϑ -orientated hydrates, quantified by the stress concentration tensor $\mathbb{B}_{hyd;\varphi,\vartheta}^{cp}$ is discussed. It is readily obtained by combining the two stress concentrations, first the one from the cement paste to the hydrate foam scale, with the one from the hydrate foam to the hydrate, reading as

$$\begin{aligned} \mathbb{B}_{hyd;\varphi,\vartheta}^{cp} = \mathbb{C}_{hyd} : \left(\{1 - f_{clin}^{cp}\} \mathbb{C}_{hf} + f_{clin}^{cp} \mathbb{C}_{clin} : \left\{ \mathbb{I} + \mathbb{P}_{sph}^{hf} : [\mathbb{C}_{clin} - \mathbb{C}_{hf}] \right\}^{-1} \right) : \\ \left\{ \mathbb{I} + \mathbb{P}_{cyl}^{hf}(\varphi, \vartheta) : [\mathbb{C}_{hyd} - \mathbb{C}_{hf}] \right\}^{-1} : \left(f_{pore}^{hf} \left\{ \mathbb{I} + \mathbb{P}_{sph}^{hf} : [\mathbb{C}_{pore} - \mathbb{C}_{hf}] \right\}^{-1} \right. \\ \left. + f_{hyd}^{hf} \int_0^{2\pi} \int_0^\pi \left\{ \mathbb{I} + \mathbb{P}_{cyl}^{hf}(\varphi, \vartheta) : [\mathbb{C}_{hyd} - \mathbb{C}_{hf}] \right\}^{-1} \frac{\sin \vartheta}{4\pi} d\vartheta d\varphi \right) \end{aligned} \quad (3.45)$$

Appendix B: Numerical realization of the strength criterion

Herein, we describe the strategy to find the critical position along the sand grain surface, the critical hydrate orientation, and correspondingly, the critical macroscopic stress magnitude (macroscopic material strength) which governs the material failure according to the microscopic Mohr-Coloumb strength criterion (3.6). In order to minimize the amount of the time consuming derivatives related to the critical hydrate orientation, the macroscopic loading is rotated while only the \underline{e}_3 -orientated hydrate is considered, see also (Pichler et al., 2008). Provided the symmetry of the problem, the azimuth and zenith angle related to the loading rotation are resolved for 31 homogeneously distributed points within the interval $[0, \pi/2]$, respectively.

The zenith angle ψ , which marks the position of the critical cement paste RVE at the sand grain surface, in turn, is resolved for 91 points within the interval $[0, \pi/2]$. In summary, we are checking $31 \times 31 \times 91 = 87,451$ combinations for position with (respect to the aggregate surface) and orientation of the critical hydrate.

Appendix C: Nomenclature

Abbreviations

AFt	ettringite hydrates
AFm	monosulfoaluminate hydrates
$AFmC$	monocarbosulfoaluminate hydrates
$clin$	cement clinker
CH	portlandite hydrates
cp	cement paste
cyl	cylindrical (needle-shaped)
$C-S-H, CSH$	calcium-silicate-hydrates
hf	hydrate foam
H_2O	water
hyd	hydrates
mor	mortar
$pore$	pores
RVE	representative volume element
sph	spherical
SCM	supplementary cementitious materials

Mathematical operators

\cdot	inner product
$:$	second-order tensor contraction
\otimes	dyadic product
∂	partial derivative
d	derivative

Mathematical symbols

$\mathbf{1}$	second-order identity tensor
\mathbb{B}_{cp}^{sand}	stress concentration tensor relating sand stresses down to stresses in the cement paste
\mathbb{B}_{sand}^{mor}	stress concentration tensor relating mortar stresses down to stresses in the sand grains
$\mathbb{B}_{hyd;\varphi,\vartheta}^{cp}$	stress concentration tensor relating cement paste stresses down to stresses in the φ, ϑ -orientated hydrate needles
\mathbb{C}_j	elastic stiffness tensor of phase j with $j \in \{clin, cp, hf, hyd, mor, pore\}$
c_{hyd}	cohesion of hydrates
d	characteristic size of the inclusion in an RVE
D	characteristic size of the structure containing an RVE

$\underline{e}_1, \underline{e}_2, \underline{e}_3$	unit base vectors of the global Cartesian base frame
$\underline{e}_r, \underline{e}_\theta, \underline{e}_\phi$	unit base vectors of the local spherical base frame
\underline{E}_{cp}	macroscopic strain tensor at the cement paste scale
f_j^{cp}	cement paste-related volume fraction of phase j
	with $j \in \{clin, hf, hyd, pore; quartz, limestone, slag, FA\}$
$f_{hyd;\varphi,\vartheta}^{cp}$	cement paste-related volume fraction of φ, ϑ -orientated hydrate needles
f_j^{hf}	hydrate foam-related volume fraction of phase j with $j \in \{hyd, pore\}$
f_j^{mor}	mortar-related volume fraction of phase j with $j \in \{cp, sand\}$
\mathbb{I}	fourth-order identity tensor
$\mathbb{I}^{vol}, \mathbb{I}^{dev}$	volumetric and deviatoric parts of fourth-order identity tensor
\mathcal{I}_{sand}^{cp}	sand-to-cement paste interface
k_j	bulk modulus of phase j with $j \in \{clin, cp, hf, hyd, pore, sand; quartz, limestone, slag, FA; CSH, CH, AFt, AFm, AFmC\}$
$k_{hyd;\varphi,\vartheta}$	bulk modulus of φ, ϑ -orientated hydrates
ℓ	characteristic size of an RVE
\underline{n}	unit (outward) normal vector acting perpendicular to the interface \mathcal{I}_{sand}^{cp}
\mathbb{P}_j^{hf}	Hill tensor of an inclusion with shape j , embedded in an infinite hydrate foam matrix, $j \in \{sph, cyl\}$
\mathbb{P}_{sph}^{cp}	Hill tensor of a spherical inclusion embedded in an infinite cement paste matrix
R^2	quadratic correlation coefficient
s/c	initial sand-to-cement mass ratio
$\underline{t}_1, \underline{t}_2$	pairs of tangent vectors in the tangential plane to the interface \mathcal{I}_{sand}^{cp}
V_j	volume of phase j with $j = \{hyd; \varphi, \vartheta\}$ or $j = \{pore\}$
w/c	initial water-to-cement mass ratio
w_{cp}/c	effective water-to-cement mass ratio
W	elastic energy stored in an RVE, expressed macroscopically W^{macro} and microscopically W^{micro}
\underline{x}	position vector
α_{SCM}	dimensionless proportionality constant for slag ($SCM = slag$) or fly ash ($SCM = FA$)
δ_{ij}	Kronecker delta
Δ	Auxiliary variable
$\Delta V_{SCM}, \Delta V_{clin}$	volume of already consumed SCM or clinker
$\underline{\epsilon}_j$	strain tensor of phase j with $j \in \{cp, sand\}$
$\underline{\epsilon}^{vol}, \underline{\epsilon}^{dev}$	volumetric and deviatoric part of the strain tensor
$\overline{\epsilon}_{hyd;\varphi,\vartheta}^{vol}, \overline{\epsilon}_{hyd;\varphi,\vartheta}^{dev}$	volumetric and deviatoric strain scalars of the strain energy-related strain tensor of φ, ϑ -orientated hydrate needles
ϑ	zenith angle marking the orientation of hydrate needles
ϑ_{fail}	azimuth angle ϑ of failing hydrate needles
μ_j	shear modulus of phase j with $j \in \{clin, cp, hf, hyd, pore, sand; quartz, limestone, slag, FA; CSH, CH, AFt, AFm, AFmC\}$
ξ_{clin}	hydration degree of cement clinker
ξ_{SCM}	hydration degree of SCM
ρ_j	mass density of phase j with $j \in \{sand, H_2O, clin\}$
$\underline{\sigma}_j$	stress tensor of phase j with $j \in \{cp, hyd, sand\}$
$\overline{\overline{\sigma}}_{hyd}$	strain energy-related stress tensor of hydrates

$\bar{\sigma}_{hyd;\varphi,\vartheta}$	volume average-related stress tensor of φ, ϑ -orientated hydrates
$\bar{\sigma}_{hyd;\varphi,\vartheta}^{vol}, \bar{\sigma}_{hyd;\varphi,\vartheta}^{dev}$	volumetric and deviatoric part of $\bar{\sigma}_{hyd;\varphi,\vartheta}$
$\bar{\bar{\sigma}}_{hyd;\varphi,\vartheta}$	strain energy-related stress tensor of φ, ϑ -orientated hydrates
$\bar{\bar{\sigma}}_{hyd;\varphi,\vartheta}^{vol}, \bar{\bar{\sigma}}_{hyd;\varphi,\vartheta}^{dev}$	volumetric and deviatoric part of $\bar{\bar{\sigma}}_{hyd;\varphi,\vartheta}$
$\bar{\sigma}_{hyd;\varphi,\vartheta}^{vol}, \bar{\sigma}_{hyd;\varphi,\vartheta}^{dev}$	volumetric and deviatoric stress scalars of $\bar{\sigma}_{hyd;\varphi,\vartheta}$
$\bar{\bar{\sigma}}_{hyd;\varphi,\vartheta}^{vol}, \bar{\bar{\sigma}}_{hyd;\varphi,\vartheta}^{dev}$	volumetric and deviatoric stress scalars of $\bar{\bar{\sigma}}_{hyd;\varphi,\vartheta}$
$\sigma_{hyd,I}, \sigma_{hyd,III}$	largest and smallest principal stress component of σ_{hyd}
$\bar{\sigma}_{hyd,I}, \bar{\sigma}_{hyd,III}$	largest and smallest principal stress component of $\bar{\sigma}_{hyd}$
Σ_j	macroscopic stress tensor at scale j with $j \in \{cp, mor\}$
Σ_j^{uni}	absolute value of imposed uniaxial loading at scale j with $j \in \{cp, mor\}$
$\Sigma_j^{uni,ult}$	magnitude of Σ_j^{uni} corresponding to the macroscopic material strength at scale j with $j \in \{cp, mor\}$
φ	azimuth angle marking the orientation of hydrate needles
φ_{fail}	azimuth angle φ of failing hydrate needles
φ_{hyd}	angle of internal friction of hydrates
ψ	polar angle marking locations at the sand grain surface
ψ_{fail}	polar angle ψ of most heavily loaded RVE of cement paste

Chapter 4

Downscaling-based identification of non-aging power-law creep of cement hydrates

Authored by: Markus Königsberger, Muhammad Irfan-ul-Hassan, Bernhard Pichler, and Christian Hellmich

Published in: *Journal of Engineering Mechanics*, DOI: 10.1061/(ASCE)EM.1943-7889.0001169, 2016

The final publication is available at:

<http://ascelibrary.org/doi/abs/10.1061/%28ASCE%29EM.1943-7889.0001169>

Abstract: Creep of cementitious materials results from the viscoelastic behavior of the reaction products of cement and water, called hydrates. In the present paper, a single isochoric creep function characterizing well-saturated Portland cement hydrates is identified through downscaling of 500 different non-aging creep functions derived from three minute-long tests on differently old cement pastes with three different initial water-to-cement mass ratios. A two-scale micromechanics representation of cement paste is used for downscaling. At a scale of 700 microns, spherical clinker inclusions are embedded in a continuous hydrate foam matrix. The latter is resolved, at the smaller scale of 20 microns, as a highly disordered arrangement of isotropically oriented hydrate needles, which are interacting with spherical water and air pores. Homogenization of viscoelastic properties is based on the correspondence principle, involving transformation of the time-dependent multiscale problem to Laplace-Carson space, followed by quasi-elastic upscaling and numerical back-transformation. With water, air, and clinker behaving elastically according to well-accepted published data, the hydrates indeed show one single power law-type creep behavior with a creep exponent being surprisingly close to those found for the different cement pastes tested. The general validity of the identified hydrate creep properties is further corroborated by using them for predicting the creep performance of a 30 years old cement paste in a 30 day-lasting creep test: the respective model predictions agree very well with results from creep experiments published in the open literature.

Contribution: Christian Hellmich and Bernhard Pichler set up the overall strategy for top-down identification of hydrate creep properties by means of three-scale creep homogenization of cement pastes. They supervised the research progress, checked key results, and supported

the documentation process. Markus Königsberger developed a Maple code for three-scale creep homogenization of cement pastes, identified universal creep properties of (sub)micron-sized needle-shaped cement hydrates, carried out model validation based on data he found in the open literature, and documented the research results. Muhammad Irfan-ul-Hassan provided his experimental data in suitable numerical formats, contributed to the discussion processes, and helped proof reading the paper.

Keywords: micromechanics, viscoelasticity, cement paste, creep

4.1 Introduction

It is well accepted in the cement and concrete research community that the creep properties of cementitious materials stem from the viscoelastic nature of the reaction products between cement and water, called hydrates; while the remaining solid material constituents, namely unhydrated clinker grains and aggregates, do not exhibit delayed deformations under time-invariant stresses (Neville, 1964; Bažant and Prasannan, 1989a,b; Acker, 2001). It is also a widely acknowledged idea that the aging, i.e. time variant, creep properties of concrete are due to the hydration process, i.e. the subsequent formation of increasingly many hydrates, while the hydrates themselves may actually exhibit non-aging, i.e. time-invariant, creep properties (Bažant and Prasannan, 1989a,b; Scheiner and Hellmich, 2009). However, quantification of such non-aging hydrate creep properties, both short and long term, remains an unsettled challenge – and this challenge is tackled in the present contribution. In this context, ultra-short term creep tests are of interest (Boulay et al., 2012; Delsaute and Staquet, 2014; Delsaute et al., 2016), and we here build upon a very recent experimental campaign consisting of three-minute-long creep tests on ordinary Portland cement pastes with different water-to-cement ratios and different maturity degrees (Irfan-ul-Hassan et al., 2016). Over this short creep measuring time, the pastes virtually do not age at all, and their creep behavior is almost perfectly represented (see Fig. 4.1) by a uniaxial power-law creep function of the form

$$J_{cp}^{exp}(t - \tau) = J_{e,cp}^{exp} + J_{v,cp}^{exp}(t - \tau) = \frac{1}{E_{cp}^{exp}} + \frac{1}{E_{c,cp}^{exp}} \left(\frac{t - \tau}{t_{ref}} \right)^{\beta_{cp}^{exp}}, \quad (4.1)$$

with t as chronological time, τ as time instant of loading, and $t_{ref} = 1 \text{ d} = 86\,400 \text{ s}$ as a fixed reference time (Irfan-ul-Hassan et al., 2016); with E_{cp}^{exp} denoting the Young's elastic modulus, $E_{c,cp}^{exp}$ denoting the Young's creep modulus, and β_{cp}^{exp} representing a dimensionless power-law exponent. Notably, the latter three quantities depend on the microstructural composition of the cement paste encountered at the time instant of loading, τ .

In the remainder of the present paper, we will test whether the maturity- and composition-dependent parameters $E_{c,cp}^{exp}$ and β_{cp}^{exp} reported by Irfan-ul-Hassan et al. (2016) may actually be traced back to only one “universal” Portland cement-related, isochoric hydrate creep tensor function

$$\mathbb{J}_{hyd}(t - \tau) = \frac{1}{3k_{hyd}} \mathbb{I}^{vol} + \frac{1}{2} \left[\frac{1}{\mu_{hyd}} + \frac{1}{\mu_{c,hyd}} \left(\frac{t - \tau}{t_{ref}} \right)^{\beta_{hyd}} \right] \mathbb{I}^{dev}, \quad (4.2)$$

with the (elastic) bulk and shear modulus of the hydrates denoted as k_{hyd} and μ_{hyd} , and with the shear creep modulus and the power-law creep exponent of hydrates denoted as $\mu_{c,hyd}$ and β_{hyd} . \mathbb{I}^{vol} and \mathbb{I}^{dev} are the volumetric and deviatoric parts of the fourth-order identity tensor \mathbb{I} , defined as $I_{ijkl} = 1/2(\delta_{ik}\delta_{jl} + \delta_{il}\delta_{jk})$, $\mathbb{I}^{vol} = 1/3(\mathbf{1} \otimes \mathbf{1})$, and $\mathbb{I}^{dev} = \mathbb{I} - \mathbb{I}^{vol}$, respectively,

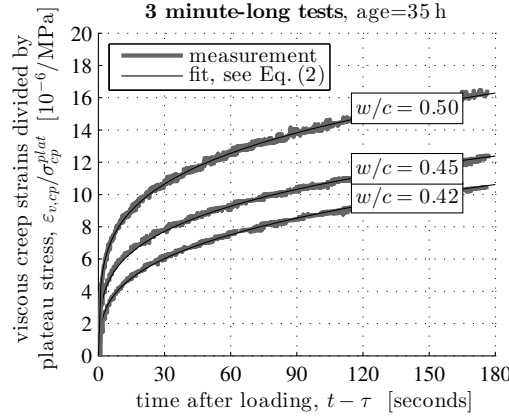


Figure 4.1: Experimentally measured temporal evolutions of viscous creep strains (divided by the applied stress at the loading plateau) and corresponding power-law fits according to Eq. (4.1) for 35-hours-old cement paste with $w/c \in \{0.42, 0.45, 0.50\}$; quadratic correlation coefficients amount to $R^2 = \{99.7\%, 99.6\%, 99.5\%\}$; see (Irfan-ul-Hassan et al., 2016) for details

whereby $\mathbf{1}$ denotes the second-order identity tensor with components equal to the Kronecker delta δ_{ij} , namely $\delta_{ij} = 1$ for $i = j$, and 0 otherwise. For “downscaling” from the cement paste to the hydrate level, we use the micromechanical representation of cement paste as developed by Pichler and Hellmich (2011), in combination with the theory of viscoelastic homogenization (Laws and McLaughlin, 1978; Scheiner and Hellmich, 2009; Sanahuja and Dormieux, 2010).

The present paper is organized as follows: after a review of micromechanics and viscoelastic scale transitions, mixture-independent hydrate creep is back-analyzed from the aforementioned three-minute test campaign over various mixtures. The resulting hydrate creep function is then further validated through Tamtsia and Beaudoin’s classical test on very old cement paste (Tamtsia and Beaudoin, 2000). Corresponding results are carefully discussed thereafter, followed by concluding remarks.

4.2 Micromechanics of creeping cement pastes

4.2.1 Micromechanical representation of cement pastes

Cement pastes are microheterogeneous materials exhibiting a scale-separated hierarchical organization. In agreement with our focus on creep of cement paste, we here account for four quasi-homogeneous constituents (or material phases), namely for cement clinker, water, hydration products, and air. Their characteristic sizes, their characteristic phase shapes, and their specific modes of mutual interaction motivate the two-scale representation of cement pastes according to Pichler and Hellmich (2011), sketched in Fig. 4.2.

- At the scale of a few tens of microns, we envision a representative volume element (RVE) of *hydrate foam*, consisting of single micron-sized or even smaller spherical water and air phases, as well as of similarly thick hydrate needles oriented uniformly in all space directions. All three material phases are in direct mutual interaction, i.e. they are arranged in a polycrystalline fashion.

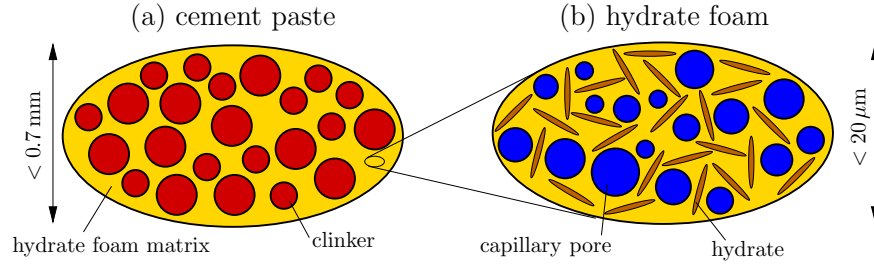


Figure 4.2: Micromechanical representation of cement paste by means of the two-step homogenization scheme of Pichler and Hellmich (2011): (a) RVE of matrix-inclusion composite “cement paste” where a spherical clinker phase is embedded in a hydrate foam matrix [modeled by means of a Mori-Tanaka scheme (Mori and Tanaka, 1973; Benveniste, 1987; Bernard et al., 2003b)]; (b) polycrystalline RVE of “hydrate foam” built up of spherical capillary porosity (water and air phases), as well as of needle-shaped hydrate phases oriented uniformly in all space directions [modeled by means of a self-consistent scheme (Hershey, 1954; Hill, 1965; Fritsch et al., 2006)]; all schematic 2D sketches refer to 3D volume elements

- At the significantly larger scale of several hundreds of microns, we envision a representative volume element of *cement paste*, consisting of a quasi-homogeneous hydrate foam matrix and a spherical cement clinker phase. Their interaction is the one typically encountered in matrix-inclusion composites.

4.2.2 Homogenization of hydrate foam properties

The RVE of Fig. 4.2 (b) is subjected to homogeneous (“macroscopic”) strains $\boldsymbol{\varepsilon}_{hf}$, in terms of “microscopic” displacements $\underline{\xi}(\underline{x}, t)$ fulfilling

$$\underline{\xi}(\underline{x}, t) = \boldsymbol{\varepsilon}_{hf}(t) \cdot \underline{x}, \quad (4.3)$$

with \underline{x} labeling positions inside as well as at the boundary of the RVE. Boundary condition (4.3) and compatibility of the microstrains inside the RVE, reading as

$$\boldsymbol{\varepsilon}(\underline{x}, t) = \frac{1}{2} \left[\nabla \underline{\xi}(\underline{x}, t) + \nabla^T \underline{\xi}(\underline{x}, t) \right], \quad (4.4)$$

imply the so-called strain average rule (Hashin, 1983; Zaoui, 2002)

$$\boldsymbol{\varepsilon}_{hf}(t) = \frac{1}{V_{hf}} \int_{V_{hf}} \boldsymbol{\varepsilon}(\underline{x}, t) dV, \quad (4.5)$$

with V_{hf} as the volume of the RVE. Moreover, these deformations provoke traction forces \underline{T} at the boundary ∂V_{hf} of the RVE, and equilibrated microstresses $\boldsymbol{\sigma}$ throughout the RVE. They fulfill

$$\underline{T}(\underline{x}, t) = \boldsymbol{\sigma}(\underline{x}, t) \cdot \underline{n}(\underline{x}) \quad \text{and} \quad \text{div} \boldsymbol{\sigma}(\underline{x}, t) = 0, \quad (4.6)$$

with \underline{n} as the normal to the surface ∂V_{hf} of the RVE. The (external) work density done by these traction forces reads as

$$\begin{aligned} W_{hf}^{ext}(t) &= \frac{1}{V_{hf}} \int_{\partial V_{hf}} \underline{T}(\underline{x}, t) \cdot \underline{\xi}(\underline{x}, t) dS \\ &= \frac{1}{V_{hf}} \int_{\partial V_{hf}} [\boldsymbol{\varepsilon}_{hf}(t) \cdot \underline{x}] \cdot [\boldsymbol{\sigma}(\underline{x}, t) \cdot \underline{n}(\underline{x})] dS = \boldsymbol{\varepsilon}_{hf}(t) : \frac{1}{V_{hf}} \int_{V_{hf}} \boldsymbol{\sigma}(\underline{x}, t) dV. \end{aligned} \quad (4.7)$$

Hence, the force quantity doing work on the macroscopic strains $\boldsymbol{\varepsilon}_{hf}$ is the spatial average over the microscopic stresses. Thus, this average qualifies as the macroscopic stress, i.e. here as the stress tensor $\boldsymbol{\sigma}_{hf}$ related to the hydrate foam,

$$\boldsymbol{\sigma}_{hf}(t) = \frac{1}{V_{hf}} \int_{V_{hf}} \boldsymbol{\sigma}(\underline{x}, t) dV. \quad (4.8)$$

Given the morphological representation of the hydrate foam RVE [see Fig. 4.2 (b)], the strain average rule (4.5) takes the particular form

$$\boldsymbol{\varepsilon}_{hf}(t) = f_{por}^{hf} \boldsymbol{\varepsilon}_{por}(t) + f_{hyd}^{hf} \int_0^{2\pi} \int_0^\pi \boldsymbol{\varepsilon}_{hyd}(\varphi, \vartheta, t) \frac{\sin \vartheta}{4\pi} d\vartheta d\varphi. \quad (4.9)$$

In Eq. (4.9), f_{por}^{hf} , and f_{hyd}^{hf} denote the volume fractions of capillary pores and of the hydrates, within the RVE of hydrate foam. $\boldsymbol{\varepsilon}_{por}$ is the microstrain averaged over the RVE-subvolume $V_{por} = V_{air} + V_{H_2O}$, occupied by the capillary pores, namely

$$\boldsymbol{\varepsilon}_{por}(t) = \frac{1}{V_{por}} \int_{V_{por}} \boldsymbol{\varepsilon}(\underline{x}, t) dV, \quad (4.10)$$

and $\boldsymbol{\varepsilon}_{hyd}(\varphi, \vartheta)$ relates to the average strains in the needle-shaped hydrate phase oriented in φ, ϑ -direction,

$$\boldsymbol{\varepsilon}_{hyd}(\varphi, \vartheta, t) = \frac{1}{\ell(\varphi, \vartheta)} \int_{\ell(\varphi, \vartheta)} \boldsymbol{\varepsilon}(\underline{x}, t) ds, \quad (4.11)$$

with $\ell(\varphi, \vartheta)$ as the length of all needle-shaped hydrates oriented in φ, ϑ -direction. Analogously, the stress average rule (4.8) specifies to

$$\boldsymbol{\sigma}_{hf}(t) = f_{por}^{hf} \boldsymbol{\sigma}_{por}(t) + f_{hyd}^{hf} \int_0^{2\pi} \int_0^\pi \boldsymbol{\sigma}_{hyd}(\varphi, \vartheta, t) \frac{\sin \vartheta}{4\pi} d\vartheta d\varphi. \quad (4.12)$$

The hydrates exhibit viscoelastic behavior (Acker, 2001),

$$\boldsymbol{\sigma}_{hyd}(t) = \int_{-\infty}^t \mathbb{R}_{hyd}(t - \tau) : \frac{\partial \boldsymbol{\varepsilon}_{hyd}(\tau)}{\partial \tau} d\tau, \quad \boldsymbol{\varepsilon}_{hyd}(t) = \int_{-\infty}^t \mathbb{J}_{hyd}(t - \tau) : \frac{\partial \boldsymbol{\sigma}_{hyd}(\tau)}{\partial \tau} d\tau, \quad (4.13)$$

where the creep and relaxation tensor functions, \mathbb{J}_{hyd} and \mathbb{R}_{hyd} , fulfill the convolution condition (Schwarzl and Struik, 1968)

$$\int_{-\infty}^t \mathbb{J}_{hyd}(t - \tau) : \mathbb{R}_{hyd}(\tau) d\tau = \int_{-\infty}^t \mathbb{R}_{hyd}(t - \tau) : \mathbb{J}_{hyd}(\tau) d\tau = t \mathbb{I}, \quad (4.14)$$

and where the hydrate creep function has the format of Eq. (4.2). On the other hand, the capillary pore phase behaves elastically,

$$\boldsymbol{\sigma}_{por}(t) = \mathbb{C}_{por} : \boldsymbol{\varepsilon}_{por}(t), \quad (4.15)$$

with the stiffness tensors \mathbb{C}_{por} playing the role of time-invariant (constant) relaxation “functions”,

$$\mathbb{C}_{por} = \mathbb{R}_{por}(t - \tau) = 3 k_{por} \mathbb{I}^{vol} + 2 \mu_{por} \mathbb{I}^{dev} \quad (4.16)$$

whereby $k_{por}=0$ and $\mu_{por}=0$ denote the vanishing (elastic) bulk and shear modulus of the pores, i.e. we consider, from a poromechanical viewpoint, drained pores.

Upscaling of this material behavior, up to the level of the hydrate foam, is particularly easily done in the Laplace-Carson (rather than the time) domain. The Laplace-Carson (LC) transform $f^*(p)$ of any time-dependent function $f(t)$ is defined as

$$f^*(p) = p\hat{f}(p) = p \int_0^\infty f(t)e^{-pt} dt, \quad (4.17)$$

where p is the complex variable in the Laplace-Carson domain, and $\hat{f}(p)$ is the Laplace transform of $f(t)$. Applying the transformation rule (4.17) to the viscoelastic behavior of the hydrates (4.13) as well as to the elastic behavior of air and water (4.16) yields algebraic constitutive equations in the LC space, reading as (Gurtin and Sternberg, 1962)

$$\boldsymbol{\varepsilon}_j^*(p) = \mathbb{J}_j^*(p) : \boldsymbol{\sigma}_j^*(p), \quad \boldsymbol{\sigma}_j^*(p) = \mathbb{R}_j^*(p) : \boldsymbol{\varepsilon}_j^*(p) \quad \forall j \in \{por, hyd\}, \quad (4.18)$$

whereby, interestingly, the convolution condition (4.14) is transformed into a simple inversion rule,

$$\mathbb{R}_j^*(p) = [\mathbb{J}_j^*(p)]^{-1}. \quad (4.19)$$

Hence, LC transformation (4.17) of the creep function (4.2), followed by insertion of the respective result for $\mathbb{J}_{hyd}^*(p)$ into (4.19), yields the LC-transformed relaxation function of the hydrates as

$$\begin{aligned} \mathbb{R}_{hyd}^*(p) &= 3k_{hyd}\mathbb{I}^{vol} + 2\mu_{hyd}^*(p)\mathbb{I}^{vol} \\ &= 3k_{hyd}\mathbb{I}^{vol} + 2 \left[\frac{1}{\mu_{hyd}} + \frac{1}{\mu_{c,hyd}} \left(\frac{1}{t_{ref}} \right)^{\beta_{hyd}} \Gamma(\beta_{hyd} + 1) p^{-\beta_{hyd}} \right]^{-1} \mathbb{I}^{dev}, \end{aligned} \quad (4.20)$$

with Γ denoting the gamma function. Note that Eqs. (4.18) are formally identical to the relations encountered with linear elasticity homogenization. Thus, upscaling of viscoelastic properties to the hydrate foam can be done as quasi-elastic homogenization in the LC space [this is referred to as the correspondence principle (Read Jr, 1950; Sips, 1951; Laws and McLaughlin, 1978; Beurthey and Zaoui, 2000)]. This process is based on the LC-transformed average rules (4.9) and (4.12) reading as

$$\boldsymbol{\varepsilon}_{hf}^*(p) = f_{por}^{hf} \boldsymbol{\varepsilon}_{por}^*(p) + f_{hyd}^{hf} \int_0^{2\pi} \int_0^\pi \boldsymbol{\varepsilon}_{hyd}^*(\varphi, \vartheta, p) \frac{\sin \vartheta}{4\pi} d\vartheta d\varphi, \quad (4.21)$$

$$\boldsymbol{\sigma}_{hf}^*(p) = f_{por}^{hf} \boldsymbol{\sigma}_{por}^*(p) + f_{hyd}^{hf} \int_0^{2\pi} \int_0^\pi \boldsymbol{\sigma}_{hyd}^*(\varphi, \vartheta, p) \frac{\sin \vartheta}{4\pi} d\vartheta d\varphi. \quad (4.22)$$

Linearity of the problem defined by (4.4), (4.6), and (4.18) implies a *linear* strain concentration rule from the LC-transformed macrostrains to the LC-transformed microstrains in phase j , reading as

$$\boldsymbol{\varepsilon}_j^*(p) = \mathbb{A}_j^*(p) : \boldsymbol{\varepsilon}_{hf}^*(p) \quad \forall j \in \{por, hyd\}, \quad (4.23)$$

where \mathbb{A}_j^* denotes the LC-transformed phase strain concentration tensor, which can be accessed from classical Eshelby-type matrix inclusion problems (Eshelby, 1957; Laws, 1977; Benveniste,

1987; Zaoui, 2002), while considering the polycrystalline morphology of the hydrate foam by means of the self-consistent scheme (Hershey, 1954; Kröner, 1958). This results in

$$\begin{aligned} \mathbb{A}_j^*(p) &= \left\{ \mathbb{I} + \mathbb{P}_j^{hf,*}(p) : \left[\mathbb{R}_j^*(p) - \mathbb{R}_{hf}^*(p) \right] \right\}^{-1} : \\ &\left(f_{por}^{hf} \left\{ \mathbb{I} + \mathbb{P}_{sph}^{hf,*}(p) : \left[\mathbb{R}_{por}^*(p) - \mathbb{R}_{hf}^*(p) \right] \right\}^{-1} \right. \\ &\quad \left. + f_{hyd}^{hf} \int_0^{2\pi} \int_0^\pi \left\{ \mathbb{I} + \mathbb{P}_{cyl}^{hf,*}(p, \varphi, \vartheta) : \left[\mathbb{R}_{hyd}^*(p) - \mathbb{R}_{hf}^*(p) \right] \right\}^{-1} \frac{\sin \vartheta}{4\pi} d\vartheta d\varphi \right)^{-1} \\ &\quad \forall j \in \{por, hyd\}. \end{aligned} \quad (4.24)$$

In Eq. (4.24), $\mathbb{P}_j^{hf,*}$ denotes the LC transform of the fourth-order Hill tensor, which accounts for the shape of phase j embedded in a fictitious matrix with “stiffness” \mathbb{R}_{hf}^* . Pores are considered to be spherical inclusions, hydrates are cylindrical (needle-shaped), see Fig. 4.2, and the corresponding LC-transformed Hill tensors read as $\mathbb{P}_{sph}^{hf,*}$, and $\mathbb{P}_{cyl}^{hf,*}$, see the Appendix A for corresponding mathematical details. Insertion of the macro-to-micro strain concentration relation (4.23) and of the constitutive behavior (4.18)₂, into the LC-transformed stress average rule (4.22) leads, after comparison to the LC-transformed constitutive law at hydrate foam level, $\boldsymbol{\sigma}_{hf}^*(p) = \mathbb{R}_{hf}^*(p) : \boldsymbol{\varepsilon}_{hf}^*(p)$, to an implicit expression for the LC-transformed homogenized relaxation tensor of the hydrate foam, \mathbb{R}_{hf}^* , reading as

$$\begin{aligned} \mathbb{R}_{hf}^*(p) &= \sum_j f_j \mathbb{R}_j^*(p) : \mathbb{A}_j^*(p) \\ &= \left(f_{por}^{hf} \mathbb{R}_{por}^*(p) : \left\{ \mathbb{I} + \mathbb{P}_{sph}^{hf,*}(p) : \left[\mathbb{R}_{por}^*(p) - \mathbb{R}_{hf}^*(p) \right] \right\}^{-1} \right. \\ &\quad \left. + f_{hyd}^{hf} \mathbb{R}_{hyd}^*(p) : \int_0^{2\pi} \int_0^\pi \left\{ \mathbb{I} + \mathbb{P}_{cyl}^{hf,*}(p, \varphi, \vartheta) : \left[\mathbb{R}_{hyd}^*(p) - \mathbb{R}_{hf}^*(p) \right] \right\}^{-1} \frac{\sin \vartheta}{4\pi} d\vartheta d\varphi \right) \\ &\quad : \left(f_{por}^{hf} \left\{ \mathbb{I} + \mathbb{P}_{sph}^{hf,*}(p) : \left[\mathbb{R}_{por}^*(p) - \mathbb{R}_{hf}^*(p) \right] \right\}^{-1} \right. \\ &\quad \left. + f_{hyd}^{hf} \int_0^{2\pi} \int_0^\pi \left\{ \mathbb{I} + \mathbb{P}_{cyl}^{hf,*}(p, \varphi, \vartheta) : \left[\mathbb{R}_{hyd}^*(p) - \mathbb{R}_{hf}^*(p) \right] \right\}^{-1} \frac{\sin \vartheta}{4\pi} d\vartheta d\varphi \right)^{-1}. \end{aligned} \quad (4.25)$$

4.2.3 Homogenization of cement paste properties

We are left with homogenization of the RVE of cement paste. Given the matrix-inclusion type morphology of the RVE, the Mori-Tanaka scheme (Mori and Tanaka, 1973; Benveniste, 1987) is appropriate to account for phase interactions. Accordingly, the LC-transformed relaxation function of the infinite matrix in the corresponding matrix-inclusion problems is set equal to

the LC-transformed homogenized relaxation function of the hydrate foam. This results in an explicit expression for the LC-transformed relaxation function of cement paste, \mathbf{R}_{cp}^* , reading, by analogy to (4.25), as

$$\begin{aligned} \mathbf{R}_{cp}^*(p) = & \left(\{1 - f_{clin}^{cp}\} \mathbf{R}_{hf}^*(p) + f_{clin}^{cp} \mathbf{R}_{clin}^*(p) : \left\{ \mathbb{I} + \mathbb{P}_{sph}^{hf,*}(p) : [\mathbf{R}_{clin}^*(p) - \mathbf{R}_{hf}^*(p)] \right\}^{-1} \right) \\ & : \left(\{1 - f_{clin}^{cp}\} \mathbb{I} + f_{clin}^{cp} \left\{ \mathbb{I} + \mathbb{P}_{sph}^{hf,*}(p) : [\mathbf{R}_{clin}^*(p) - \mathbf{R}_{hf}^*(p)] \right\}^{-1} \right)^{-1}. \end{aligned} \quad (4.26)$$

This relaxation function, as well as its creep analogue, $\mathbf{J}_{cp}^*(p) = [\mathbf{R}_{cp}^*(p)]^{-1}$, is then back-transformed from the LC domain, back to the time domain. This is done by means of the Gaver-Wynn-Rho algorithm (Abate and Valkó, 2004; Valkó and Abate, 2004), which allows for reliable numerical back-transformation, provided that the quantities in the LC space are available in a multiprecision number format. In more detail, the approximation accuracy of the back-transformation increases with the “order of approximation” quantified by the even integer M , see (Scheiner and Hellmich, 2009) for details. Herein, $M = 10$ is chosen, which requires all computations in the LC space to be done with a precision higher than 21 digits (Abate and Valkó, 2004; Valkó and Abate, 2004). In this way, the implicit equation (4.25) is solved iteratively, and the calculation is stopped once subsequent homogenized relaxation functions differ by a value smaller than 10^{-25} GPa.

4.3 Identification of power-law creep properties of well-saturated cement hydrates

4.3.1 Downscaling minute-long creep test data from cement paste to hydrate level

We here identify the viscous behavior of the only creeping phase, the hydrate phase, by minimizing the error between the experimental creep functions (4.1) resulting from three-minute-long creep tests, and corresponding model predictions according to Eq. (4.26). The aforementioned creep tests were conducted in parallel to the hydration process of ordinary Portland cement pastes exhibiting compositions of $w/c \in \{0.42, 0.45, 0.50\}$ and material ages ranging from approximately 1 to 8 days, see (Irfan-ul-Hassan et al., 2016) for details on the test protocol. As the experiments also allowed for determination of the (elastic) Young’s moduli (which was confirmed by ultrasonic tests, see (Irfan-ul-Hassan et al., 2016) for details), we isolate the elastic strains from the overall creep strains and restrict the minimization process to the viscous part of the creep function, which can be almost exactly fitted with a power-law function $J_{v,cp}^{exp}$ reading as (Irfan-ul-Hassan et al., 2016)

$$J_{v,cp}^{exp}(t - \tau) = \frac{1}{E_{c,cp}^{exp}} \left(\frac{t - \tau}{t_{ref}} \right)^{\beta_{cp}^{exp}}, \quad (4.27)$$

with $E_{c,cp}^{exp}$ denoting the creep modulus and β_{cp}^{exp} representing a dimensionless power-law exponent. Both parameters are functions of the initial water-to-cement mass ratio w/c and of the (calorimetry-based) hydration degree ξ , the latter being defined as the hydrated clinker volume divided by the initial clinker volume (Irfan-ul-Hassan et al., 2016).

As concerns the aforementioned model predictions, the elastic phase properties are given in Table 4.1, and the volume fractions occurring in (4.25) and (4.26) are determined from the

famous Powers' model (Powers and Brownyard, 1947; Powers, 1958). Accordingly, the cement

Table 4.1: Isotropic elastic phase properties from Pichler and Hellmich (2011); corresponding phase stiffness tensors read as $\mathbb{C}_j = 3 k_j \mathbb{I}^{vol} + 2 \mu_j \mathbb{I}^{dev}$

Phase j	Bulk modulus k_j [GPa]	Shear modulus μ_j [GPa]
Air	$k_{air} = 0$	$\mu_{air} = 0$
Water	$k_{H_2O} = 0$	$\mu_{H_2O} = 0$
Hydrates	$k_{hyd} = 18.69$	$\mu_{hyd} = 11.76$
Clinker	$k_{cem} = 116.7$	$\mu_{cem} = 53.80$

paste-related phase volume fractions of clinker f_{clin}^{cp} , of capillary pores f_{por}^{cp} , and of hydrates f_{hyd}^{cp} , and read as (Pichler and Hellmich, 2011):

$$\begin{aligned}
 f_{clin}^{cp} &= \frac{20(1-\xi)}{20+63w/c} \geq 0, \\
 f_{por}^{cp} &= \frac{63(w/c - 0.367\xi)}{20+63w/c} \geq 0, \\
 f_{hyd}^{cp} &= \frac{43.15\xi}{20+63w/c}.
 \end{aligned} \tag{4.28}$$

Given the two-scale representation of cement paste (see Fig. 4.2), we also need access to hydrate foam-related volume fractions of capillary pores and hydrates (f_{por}^{hf} and f_{hyd}^{hf}). They follow from dividing the cement paste-related volume fractions by the total hydrate foam volume, $(1 - f_{clin}^{cp})$, according to

$$f_j^{hf} = \frac{f_j^{cp}}{1 - f_{clin}^{cp}} \quad \forall j \in \{por, hyd\}. \tag{4.29}$$

Given the substantial computational effort associated with the inversion of the LC transformation, it is more efficient to compare the model-predicted and experimentally measured creep function in the LC space. This requires the LC transformation (4.17) of $J_{v,cp}^{exp}$, in order to obtain an experimentally determined LC-transformed viscous creep function $J_{v,cp}^{exp,*}$ in the form

$$J_{v,cp}^{exp,*}(p) = \frac{1}{E_{c,cp}^{exp}} \left(\frac{1}{t_{ref}} \right)^{\beta_{cp}^{exp}} \Gamma(\beta_{cp}^{exp} + 1) p^{-\beta_{cp}^{exp}}. \tag{4.30}$$

The model-predicted (homogenized) counterpart $J_{v,cp}^{mod,*}$ is the 1111-component of the fourth-order tensor $\mathbb{J}_{v,cp}^{mod,*}(p) = [\mathbb{R}_{cp}^*(p)]^{-1} - [\mathbb{C}_{cp}]^{-1}$, see (4.26); whereby $\mathbb{C}_{cp} = \mathbb{R}_{cp}(t=0)$ is the homogenized elastic stiffness of cement paste. Conclusively, we are minimizing the error between the model-predicted viscous part of the uniaxial creep function in the LC space, $J_{v,cp}^{mod,*}(p)$, and its experimentally measured counterpart, $J_{v,cp}^{exp,*}(p)$; in mathematical terms,

$$\sum_{i=1}^{n_{w/c}} \sum_{j=1}^{n_{\xi}} \sum_{k=1}^{n_p} \left[J_{v,cp}^{mod,*}(p) - J_{v,cp}^{exp,*}(p) \right]^2 \rightarrow \min. \tag{4.31}$$

In Eq. (4.31), the sum over $n_{w/c} = 3$ indicates that three different cement paste mixes exhibiting $w/c \in \{0.42, 0.45, 0.50\}$ are tested, the sum over $n_\xi = 167$ indicates that 167 creep tests were performed on each cement composition for different maturity states, and the sum over $n_p = 20$ indicates that 20 complex LC “time” values $p \in [10^{-6}, 10^{-4}]$ are considered. The optimization problem (4.31) is solved in MATLAB (2013), by means of a quasi-Newtonian solver, and this provides the optimal creep parameters for well-saturated hydrates as

$$\mu_{c,hyd} = 20.93 \text{ GPa}, \quad \beta_{hyd} = 0.251. \quad (4.32)$$

These optimal hydrate creep parameters indeed allow for satisfactory representation of the experimental results in the time domain, see Fig. 4.3. The agreement between model prediction and experiment is quantified through the mean error, defined as the sum of the absolute values of the difference between model-predicted and experimentally measured uniaxial viscous creep function, resolved for $n_t = 180$ steps within the three-minute-long creep tests $t_k \in [1, 180]$, and averaged with respect to the number of creep tests ($n_{w/c} n_\xi \approx 500$) and the number of time steps n_t , reading as

$$\epsilon = \frac{\sum_{i=1}^{n_{w/c}} \sum_{j=1}^{n_\xi} \sum_{k=1}^{n_t} |J_{v,cp}^{mod}(t_k) - J_{v,cp}^{exp}(t_k)|}{n_{w/c} n_\xi n_t}. \quad (4.33)$$

This error amounts to $0.768 \cdot 10^{-6}$ /MPa. This supports the idea that the (visco-)elastic properties of well-saturated hydrates neither change during the aging of cement paste nor upon composition change of the cement paste. Accordingly, the varying creep potential of cement pastes arises solely from varying volume dosages of the hydrates, as predicted by Powers’ hydration model.

4.3.2 Confirmation of hydrate creep properties by data from weeks-long creep test on 30-year-old cement paste

The question arises whether the intrinsic (i.e. mixture- and maturity-independent) creep properties of well-saturated hydrates as identified here from three-minutes creep tests on different early-age cement pastes, may be also relevant for longer creep durations, and for more mature pastes. In this context, we consider the results of Tamtsia and Beaudoin (2000), who performed a 30-day-long uniaxial compressive creep test on a 30-year-old Portland cement paste sample with $w/c=0.50$, stored continuously under water. Given its age, the sample can be considered to be completely hydrated; thus, also in this case, it is appropriate to consider aging effects as negligible during the test period. An estimate for the hydration degree which corresponds to full hydration of cement paste, can be obtained from the empirical relationship of Lin and Meyer (2009). Accordingly, a water-to-cement mass ratio of $w/c=0.50$ and a typical Blaine fineness of $340 \text{ m}^2/\text{kg}$ (Tamtsia et al., 2004) relate to a final hydration degree of $\xi = 0.87$. The corresponding model-predicted creep function, i.e. that relating to $w/c=0.50$, $\xi = 0.87$, and to the hydrate properties according to (4.2) and (4.32), agrees remarkably well with the aforementioned experimental results, see Fig. 4.4. This result shows that it is the intrinsic viscous behavior of the hydrate needles, which drives the basic creep of cement paste for time intervals ranging from a few seconds, up to several weeks. Moreover, this corroborates that the viscous behavior of well-saturated hydrates does not change.

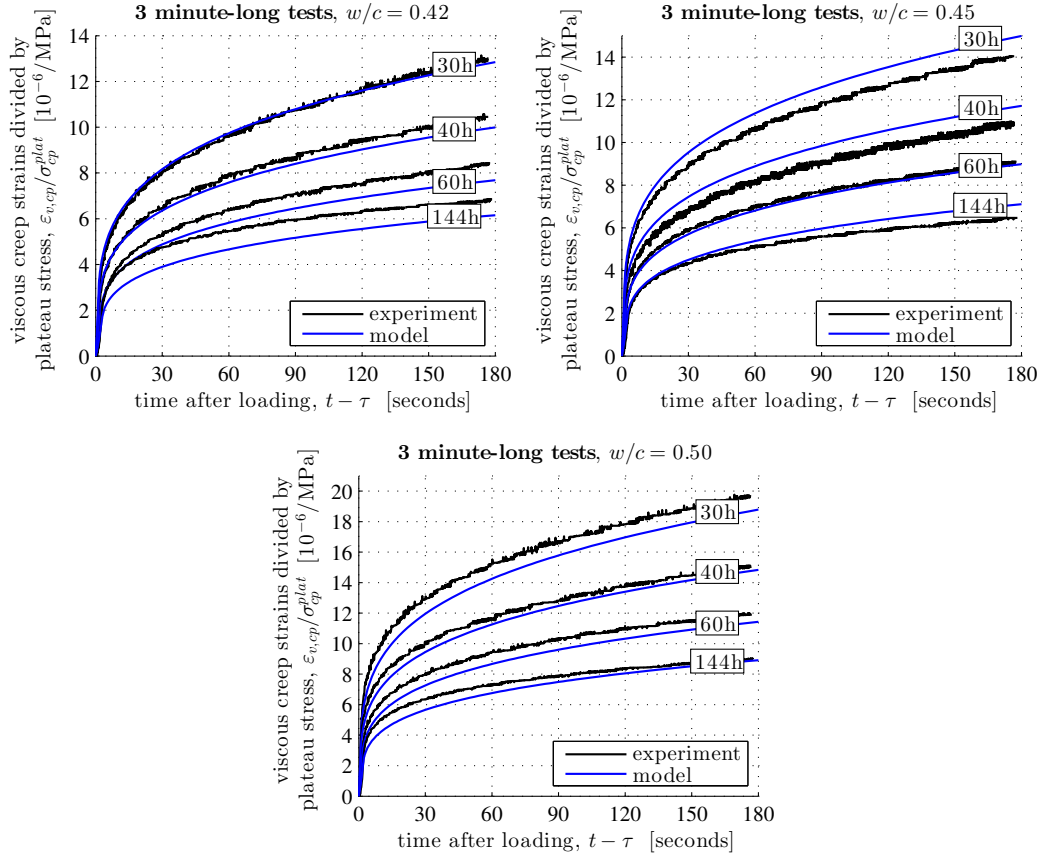


Figure 4.3: Comparison of the experimentally determined and model-predicted viscous strains of cement pastes aged 30, 40, 60, and 144 hours, respectively; the relation between material age and hydration degree is taken from Irfan-ul-Hassan et al. (2016)

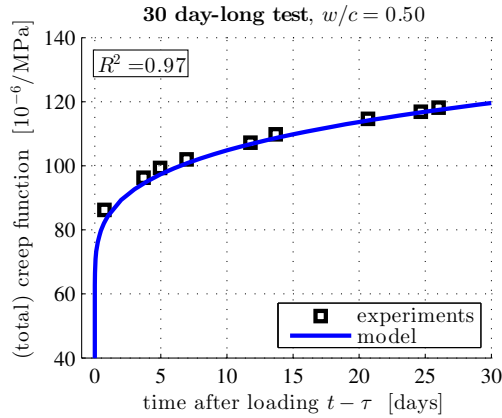


Figure 4.4: Comparison of experimental data (Tamtsia and Beaudoin, 2000) for (total) creep functions of 30-year-old cement paste samples with $w/c = 0.50$, with corresponding model predictions

4.4 General characteristics of the creep of well-saturated hydrates

The good agreements in Figs. 4.3 to 4.4 motivate deeper study of the features of the homogenized creep behavior of cement paste. Therefore, we represent the viscous part of the model-predicted uniaxial creep functions of cement paste very accurately, see Fig. 4.5, by means of a power function,

$$J_{v,cp}^{mod}(t - \tau) = \frac{1}{E_{c,cp}^{mod}} \left(\frac{t - \tau}{t_{ref}} \right)^{\beta_{cp}^{mod}}, \quad (4.34)$$

with $E_{c,cp}^{mod}$ denoting the model-predicted creep modulus, and β_{cp}^{mod} representing the model-predicted creep exponent. Notably, the total model-predicted creep function then reads as

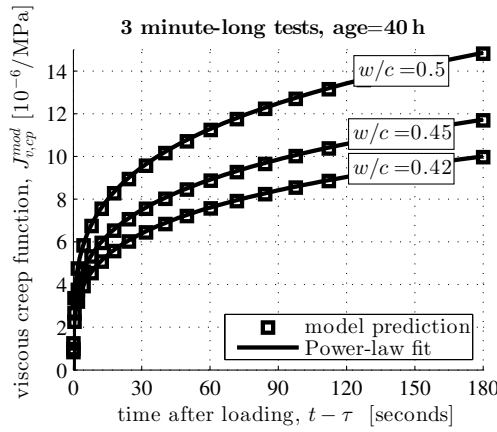


Figure 4.5: Viscous part of the uniaxial creep function of 40 h old cement paste with $w/c \in \{0.42, 0.45, 0.50\}$: point-wisely obtained model predictions and corresponding power-law fits according to Eq. (4.27), with quadratic correlations coefficients $R^2 > 99.9\%$

$J_{cp}^{mod} = J_{v,cp}^{mod} + 1/E_{cp}^{mod}$ with E_{cp}^{mod} denoting the model-predicted Young's elastic modulus. It turns out that the elastic and creep modulus are strongly composition-dependent; they increase with increasing ξ and decreasing w/c , see Fig. 4.6. In contrast, the creep exponent appears as virtually composition- and maturity-independent quantity, being constant around $\beta \approx 0.252$ for $w/c \in [0.2, 1]$ and $\xi \in [0, 1]$. This value is even close to the hydrate creep exponent of Eq. (4.32); i.e. it is hardly effected by the upscaling scheme.

4.5 Discussion and conclusion

Concerning the invariant hydrate creep properties, expressed by Eq. (4.32) and Figs. 4.3-4.4, it is important to note that the herein investigated cement samples were all characterized by $w/c \geq 0.42$, that they were tested within the first week after production, and that they were continuously covered, in order to avoid drying. Consequently, these samples (and the hydrates within them) were well saturated, and our statement on the invariance of hydrate creep properties is valid for well saturated hydrates.

Change of this saturated state, i.e. drying, is known to significantly influence the macroscopic creep behavior of cement paste (Acker and Ulm, 2001; Tamtsia and Beaudoin, 2000),

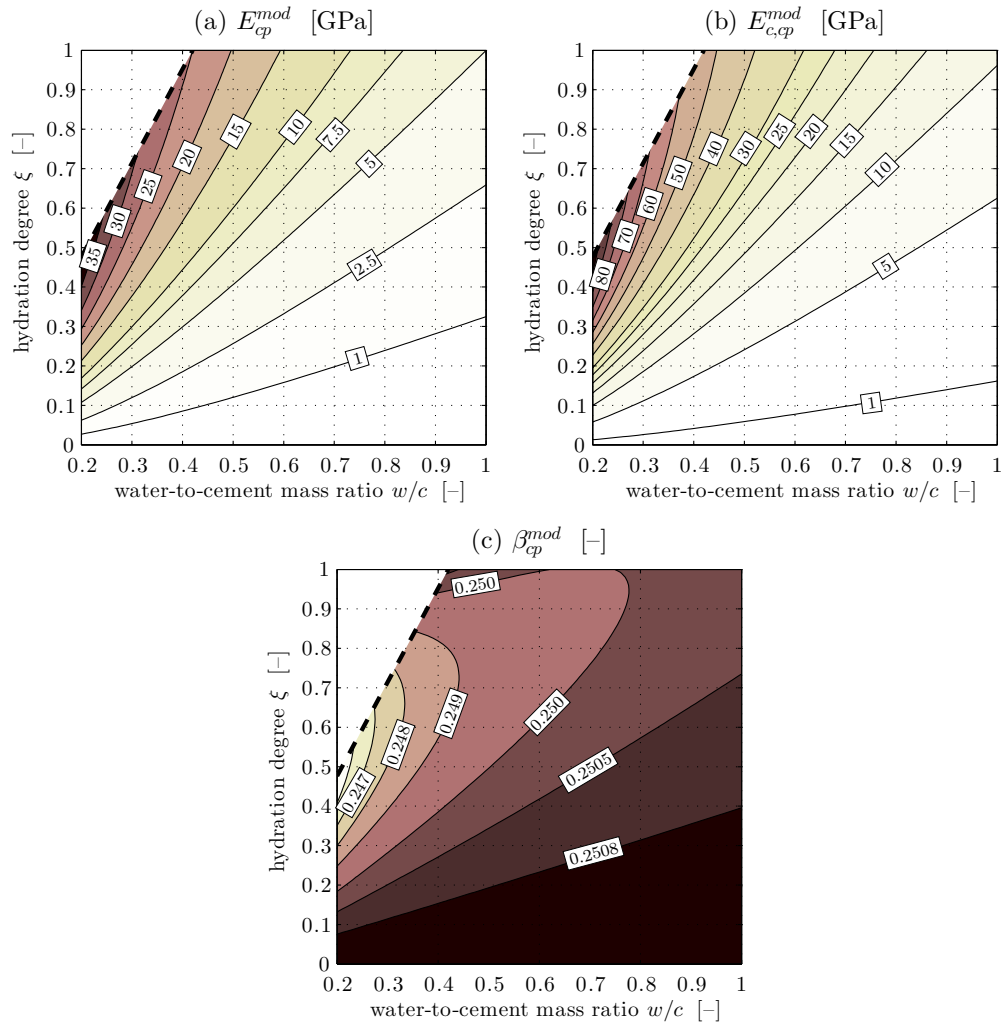


Figure 4.6: Model-predicted elastic and creep properties for hydrating cement pastes with hydration degrees $\xi \in [0, 1]$ and exhibiting water-to-cement mass ratios $w/c \in [0.2, 1]$: (a) Young's elastic modulus, (b) Young's creep modulus, (c) dimensionless creep exponent

and of other hydrated nanolayered material systems, such as clay (Carrier et al., 2016). It is very probable that drying also changes the hydrate creep behavior itself, e.g. through reduction of so-called creep sites within the hydrate phases (Thomas and Jennings, 2006). The same authors report NMR studies which show that even under constant hydro-thermal conditions, the polymerization state within the hydrates changes, and they propose that this so-called “chemical aging of C-S-H” might also change the hydrate creep properties. More recent research results, however, seem to relativize this proposition: indeed, polymerization leads to an enlargement of the non-spherical nanoscaled solid elements within the hydrates, while the actual source of hydrate creep lies in the layered (confined) water sheets *between* these solid elements (Manzano et al., 2012, 2013; Shahidi et al., 2014, 2015c). Hence, as long as the amount of the latter “creep sites” does not change, it makes sense to expect invariant creep properties of the hydrate phases as introduced in Fig. 4.2 (b).

Fig. 4.6 and Eq. (4.34) illustrate that upscaling of a power-law creep function from needle-shaped hydrates up to the scale of cement paste results in a power-law creep function. In other words, the herein performed scale transitions do not alter the shape of the creep function, a fact that was also found for upscaling the asymptotically reached creep rates “seen” in nano- and microindentation tests (Vandamme and Ulm, 2013; Zhang et al., 2014). Pursuing this argument to the scale of concrete, one will also end up with a creep function which virtually follows a power function. However, concrete creep tests or monitoring activities spanning over time periods of years, have revealed a transition to a logarithmic creep behavior (Bažant et al., 2011). Conclusively, the validity range of the hydrate creep properties identified through Eq. (4.2) and (4.32) is constrained to creep periods of weeks to months (see Fig. 4.4). During such time periods, creep of cement paste indeed follows a power-law function (Tamtsia and Beaudoin, 2000; Irfan-ul-Hassan et al., 2016). Extension of the formulation (4.1) towards ultralong creep periods is beyond the scope of the present manuscript.

The quantification of the hydrate creep function according to (4.26) and (4.28)-(4.31) rests on the assumption of isochoric creep according to (4.2), implying that creeping hydrates would exhibit a time-invariant volume. This assumption is motivated by a suggestion of Bernard et al. (2003a), by results of an earlier creep micromechanics model (Scheiner and Hellmich, 2009), and by theoretical considerations concerning the upscaling of sliding processes of viscous interfaces within hydrated calcium silicate (Shahidi et al., 2014, 2015a,b,c). These viscous interfaces are located within the hydrate nanoparticles, such as solid C-S-H, see Fig. 4.7 (c). The needle-shaped hydrate phases considered in the present work are defined at a level well above the aforementioned nanoparticles: our hydrate phases are actually built up by these nanoparticles as well as by the gel porosity in between. Such nanocomposites are also referred to as “C-S-H gel” (Sanahuja and Dormieux, 2010; Manzano et al., 2013). Accordingly, the isochoric creep function of the nanoparticles would actually scale up to a hydrate gel-related creep function also including volumetric creep strains (Sanahuja and Dormieux, 2010). Hence, the question arises whether consideration of such volumetric creep strains occurring at the level of hydrate gel [i.e. that of the needle-shaped hydrate phases in Fig. 4.2 (b)] would have a remarkable effect on the results of the downscaling-based hydrate creep identification process described further above. In order to answer this question, we here repeat this process, but now based on the popular concept of a constant (elastic and creep) Poisson’s ratio as proposed

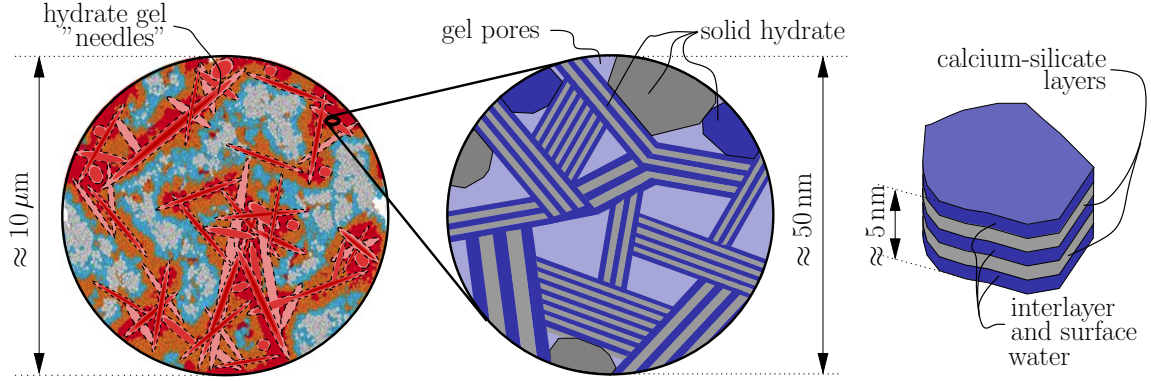


Figure 4.7: Nanoscopic downscaling from hydrate foam microstructure introduced in Fig. 4.2 (b): (a) Hybrid Molecular Dynamics - Grand Canonical Monte Carlo simulations suggest emergence of elongated morphological features at the level of the hydrate foam (a); these needles, represented by the needle-shaped hydrate phases shown in Fig. 4.2 (b), are made up of hydrate gel (b), consisting itself of gel pores and solid hydrates (c); the latter are built from calcium silicate layers separated or covered by films of confined water

by Bažant and L'Hermite (1988). Accordingly, we consider

$$\begin{aligned} \mathbb{J}_{hyd}(t - \tau) = & \left[\frac{1 - 2\nu_{hyd}}{E_{hyd}} + \frac{1 - 2\nu_{hyd}}{E_{c,hyd}} \left(\frac{t - \tau}{t_{ref}} \right)^{\beta_{hyd}} \right] \mathbb{I}^{vol} \\ & + \left[\frac{1 + \nu_{hyd}}{E_{hyd}} + \frac{1 + \nu_{hyd}}{E_{c,hyd}} \left(\frac{t - \tau}{t_{ref}} \right)^{\beta_{hyd}} \right] \mathbb{I}^{dev} \end{aligned} \quad (4.35)$$

whereby E_{hyd} denotes Young's elastic modulus, $E_{c,hyd}$ denotes Young's creep modulus, and ν_{hyd} denotes Poisson's ratio. The latter follows from the elastic bulk and shear moduli of isotropic hydrates (see also Table 4.1), as $\nu_{hyd} = 0.24$. The alternative hydrate creep tensor function (4.35) is then upscaled to the level of cement paste, as described in Section "Micromechanics of creeping cement pastes". Thereafter, the hydrate creep properties $E_{c,hyd}$ and β_{hyd} are identified by means of minimizing Eq. (4.31). The resulting prediction error ϵ according to Eq. (4.33) is, in good approximation, equal to the one obtained under the assumption of isochoric creep, see Table 4.2. Very remarkably, virtually the *same* Young's creep modulus of

Table 4.2: Comparison of hydrate creep properties of Eq. (4.2) and (4.35), identified by means of downscaling 500 macroscopic creep tests on cement pastes: isochoric creep vs. creep at constant Poisson's ratio; prediction error ϵ according to Eq. (4.33)

assumption	$E_{c,hyd}$ [GPa]	β_{hyd}	ϵ [10^{-6} /MPa]
isochoric	62.8 ^a	0.251	0.768
constant Poisson's ratio	62.4	0.250	0.765

^aThe Young's creep modulus $E_{c,hyd}$ follows from the shear creep modulus identified in Eq. (4.32) as $E_{c,hyd} = 3\mu_{c,hyd}$

hydrates, and the *same* power-law creep exponent of hydrates are obtained, irrespective of whether isochoric creep or creep at constant Poisson's ratio is considered. The underlying

reason seems to lie in the elongated (non-spherical) shape of the hydrate phases building up kind of a “framework”, with the capillary porosity playing the role of the “free spaces” in between. In such a “framework”, the individual needles (or “beams”) are predominantly loaded in terms of uniaxial stress states, irrespective of potential lateral deformations which remain insignificant for the overall load carrying behavior. A very similar result has been obtained in the context of homogenizing the elastic properties of various types of ceramic porous polycrystals with non-spherical (needle- or disc-shaped) solid phases (Fritsch et al., 2013), as was confirmed by very many experiments as well as by full 3D Finite Element simulations of corresponding microstructures (Sanahuja et al., 2010). In this context, we note that the morphology with non-spherical hydrate phase shapes, as depicted in Fig. 4.2 (b), was validated by various experimental sources (Pichler et al., 2009; Pichler and Hellmich, 2011; Pichler et al., 2013a). Moreover, this morphology has been, only very recently, further confirmed by a hybrid Molecular Dynamics – Grand Canonical Monte Carlo simulation (MD-GCMC) scheme (Ioannidou et al., 2016), see Fig. 4.7 (a).

Appendix A: Analytical expressions facilitating upscaling in LC space

Upscaling of the hydrate creep behavior, up to the larger scales of the hydrate foam and of the cement paste, respectively, is performed in the LC space, according to the analytical formulae described next. Thereby, we consider that an isotropic fourth-order tensor, \mathbb{G} , can be decomposed into a volumetric part and a deviatoric part as $\mathbb{G} = G^{vol}\mathbb{I}^{vol} + G^{dev}\mathbb{I}^{dev}$, where G^{vol} and G^{dev} , respectively, are the (scalar) volumetric and deviatoric components of the fourth-order tensor \mathbb{G} , and where \mathbb{I}^{vol} and \mathbb{I}^{dev} are the volumetric and deviatoric parts of the symmetric fourth-order identity tensor, as introduced below Eq. (4.2). They satisfy $\mathbb{I}^{vol} : \mathbb{I}^{vol} = \mathbb{I}^{vol}$, $\mathbb{I}^{dev} : \mathbb{I}^{dev} = \mathbb{I}^{dev}$, and $\mathbb{I}^{vol} : \mathbb{I}^{dev} = \mathbb{I}^{dev} : \mathbb{I}^{vol} = 0$. In addition, the isotropic average of a transversally isotropic tensor \mathbb{F} can be written as (Torquato, 2013; Sadowski et al., 2015)

$$\int_0^{2\pi} \int_0^\pi \mathbb{F}(\varphi, \vartheta) \frac{\sin \vartheta}{4\pi} d\vartheta d\varphi = \sum_{i=1}^3 \sum_{j=1}^3 \left[\frac{1}{3} F_{iijj} \mathbb{I}^{vol} + \frac{1}{5} \left(F_{ijij} - \frac{1}{3} F_{iijj} \right) \mathbb{I}^{dev} \right], \quad (4.36)$$

provided that the tensor \mathbb{F} exhibits the symmetries $F_{ijkl} = F_{jikl} = F_{ijlk} = F_{jilk}$.

We start our collection of analytical formulae with the LC-transformed Hill tensors occurring in concentration and stiffness expressions of Eqs. (4.24)-(4.26). Given the organization of cement paste according to Fig. 4.2, the inclusions in the corresponding Eshelby problems are all embedded in an infinite hydrate foam matrix with quasi-elastic “stiffness” \mathbb{R}_{hf}^* . For material phases with spherical shape ($j = sph$), i.e. for air, water, and cement clinker, and for cylindrical hydrates ($j = cyl$) the Hill tensor reads as

$$\mathbb{P}_j^{hf,*}(p) = \mathbb{S}_j^{hf,*}(p) : \left[\mathbb{R}_{hf}^*(p) \right]^{-1} \quad \forall j \in \{sph, cyl\}, \quad (4.37)$$

whereby $\mathbb{S}_j^{hf,*}$ denotes the LC-transformed Eshelby tensor. As for a spherical inclusion embedded in an infinite hydrate foam matrix, the LC-transformed Eshelby tensor $\mathbb{S}_{sph}^{hf,*}$ is isotropic, and its volumetric and deviatoric components read as (Eshelby, 1957; Zaoui, 2002)

$$S_{sph}^{hf,*,vol}(p) = \frac{3k_{hf}^*(p)}{3k_{hf}^*(p) + 4\mu_{hf}^*(p)}, \quad S_{sph}^{hf,*,dev}(p) = \frac{6k_{hf}^*(p) + 2\mu_{hf}^*(p)}{5(3k_{hf}^*(p) + 4\mu_{hf}^*(p))}. \quad (4.38)$$

As for a cylindrical hydrate orientated in \underline{e}_3 -direction and embedded in an infinite hydrate foam matrix, the non-zero components of the LC-transformed Eshelby tensor $\mathbb{S}_{cyl}^{hf,*}$ read as (Eshelby, 1957; Hellmich et al., 2004)

$$\begin{aligned}
S_{cyl,1111}^{hf,*}(p) &= S_{cyl,2222}^{hf,*}(p) = \frac{9}{4} \frac{k_{hf}^*(p) + \mu_{hf}^*(p)}{3k_{hf}^*(p) + 4\mu_{hf}^*(p)}, \\
S_{cyl,1122}^{hf,*}(p) &= S_{cyl,2211}^{hf,*}(p) = \frac{1}{4} \frac{3k_{hf}^*(p) - 5\mu_{hf}^*(p)}{3k_{hf}^*(p) + 4\mu_{hf}^*(p)}, \\
S_{cyl,1133}^{hf,*}(p) &= S_{cyl,2233}^{hf,*}(p) = \frac{1}{2} \frac{3k_{hf}^*(p) - 2\mu_{hf}^*(p)}{3k_{hf}^*(p) + 4\mu_{hf}^*(p)}, \\
S_{cyl,1212}^{hf,*}(p) &= \frac{1}{4} \frac{3k_{hf}^*(p) + 7\mu_{hf}^*(p)}{3k_{hf}^*(p) + 4\mu_{hf}^*(p)}, \\
S_{cyl,1313}^{hf,*} &= S_{cyl,2323}^{hf,*} = \frac{1}{4},
\end{aligned} \tag{4.39}$$

whereby $\mathbb{S}_{cyl}^{hf,*}$ exhibits symmetries $S_{cyl,ijkl}^{hf,*} = S_{cyl,jikl}^{hf,*} = S_{cyl,ijlk}^{hf,*} = S_{cyl,jilk}^{hf,*}$.

Next, we discuss the expressions for the homogenized quasi-elastic “stiffness” tensor \mathbb{R}_{hf}^* , see Section “Homogenization of cement paste properties”. As for hydrate foam, insertion of the LC-transformed Eshelby tensor expressions (4.38) and (4.39) into (4.37), and further insertion of the thus obtained Hill tensors, together with the vanishing quasi-elastic “stiffnesses” of air and water (see Table 4.1) and the quasi-elastic “stiffness” of hydrates (4.20), into the expression for the quasi-elastic “stiffness” of the homogenized hydrate foam (4.25), yields scalar expressions for the LC-transformed bulk and shear moduli, reading as

$$\begin{aligned}
k_{hf}^*(p) &= f_{hyd}^{hf} k_{hyd} A_{\infty,hyd}^{*,vol}(p) \left[\left(f_{air}^{hf} + f_{H_2O}^{hf} \right) A_{\infty,pore}^{*,vol}(p) + f_{hyd}^{hf} A_{\infty,hyd}^{*,vol}(p) \right]^{-1}, \\
\mu_{hf}^*(p) &= f_{hyd}^{hf} \mu_{hyd}^*(p) A_{\infty,hyd}^{*,dev}(p) \left[\left(f_{air}^{hf} + f_{H_2O}^{hf} \right) A_{\infty,pore}^{*,dev}(p) + f_{hyd}^{hf} A_{\infty,dev}^{*,vol}(p) \right]^{-1},
\end{aligned} \tag{4.40}$$

with $A_{\infty,pore}^{*,vol}$, $A_{\infty,pore}^{*,dev}$, $A_{\infty,hyd}^{*,vol}$, and $A_{\infty,hyd}^{*,dev}$ denoting the LC-transformed volumetric and deviatoric components of the Eshelby problem-related strain concentration tensors for the pores (air and water) and for the hydrates, reading as

$$\begin{aligned}
A_{\infty,pore}^{*,vol}(p) &= \left[1 - S_{sph}^{hf,*,vol}(p) \right]^{-1}, \\
A_{\infty,pore}^{*,dev}(p) &= \left[1 - S_{sph}^{hf,*,dev}(p) \right]^{-1},
\end{aligned} \tag{4.41}$$

so that, according to (4.36), we finally have

$$\begin{aligned}
A_{\infty,hyd}^{*,vol}(p) &= \frac{3k_{hf}^*(p) + \mu_{hyd}^*(p) + 3\mu_{hf}^*(p)}{3k_{hyd} + \mu_{hyd}^*(p) + 3\mu_{hf}^*(p)}, \\
A_{\infty,hyd}^{*,dev}(p) &= \left\{ 9k_{hyd} [\mu_{hyd}^*(p)]^2 k_{hf}^*(p) + 64 [\mu_{hf}^*(p)]^4 + \right. \\
&\quad \left[63k_{hyd} + 84k_{hf}^*(p) + 184\mu_{hyd}^*(p) \right] [\mu_{hf}^*(p)]^3 + \\
&\quad \left[156k_{hyd} \mu_{hyd}^*(p) + 120k_{hf}^*(p) \mu_{hyd} + 72 [\mu_{hyd}^*(p)]^2 + 81k_{hyd} k_{hf}^*(p) \right] [\mu_{hf}^*(p)]^2 + \\
&\quad \left[36k_{hf}^*(p) [\mu_{hyd}^*(p)]^2 + 21k_{hyd} [\mu_{hyd}^*(p)]^2 + 90k_{hf}^*(p) k_{hyd} \mu_{hyd}^*(p) \right] \mu_{hf}^*(p) \Big\} \\
&\quad \left(5 \left\{ [\mu_{hf}^*(p)]^2 + [7\mu_{hyd}^*(p) + 3k_{hf}^*(p)] \mu_{hf}^*(p) + 3k_{hf}^*(p) \mu_{hyd}^*(p) \right\} \right. \\
&\quad \left. [\mu_{hf}^*(p) + \mu_{hyd}^*(p)] [3k_{hyd} + \mu_{hyd}^*(p) + 3\mu_{hf}^*(p)] \right)^{-1}.
\end{aligned} \tag{4.42}$$

As for cement paste, insertion of LC-transformed Eshelby tensor expression (4.38) into (4.37), and further insertion of the thus obtained Hill tensor, together with the quasi-elastic “stiffnesses” of cement clinker (see Table 4.1) and of hydrate foam (4.40), into the expression for the quasi-elastic “stiffness” of the homogenized cement paste (4.26), yields scalar expressions for the LC-transformed bulk and shear moduli, reading as

$$\begin{aligned}
k_{cp}^*(p) &= \left[f_{hf}^{cp} k_{hf}^*(p) + f_{clin}^{cp} k_{clin} A_{\infty,clin}^{*,vol}(p) \right] \left[f_{hf}^{cp} + f_{clin}^{cp} A_{\infty,clin}^{*,vol}(p) \right]^{-1}, \\
\mu_{cp}^*(p) &= \left[f_{hf}^{cp} \mu_{hf}^*(p) + f_{clin}^{cp} \mu_{clin} A_{\infty,clin}^{*,dev}(p) \right] \left[f_{hf}^{cp} + f_{clin}^{cp} A_{\infty,clin}^{*,dev}(p) \right]^{-1},
\end{aligned} \tag{4.43}$$

with $A_{\infty,clin}^{*,vol}$, $A_{\infty,clin}^{*,dev}$ denoting the LC-transformed volumetric and deviatoric components of the Eshelby problem-related strain concentration tensor for clinker inclusions, reading as

$$\begin{aligned}
A_{\infty,clin}^{*,vol}(p) &= \left[1 + S_{sph}^{hf,*,vol}(p) \frac{k_{clin} - k_{hf}^*(p)}{k_{hf}^*(p)} \right]^{-1}, \\
A_{\infty,clin}^{*,dev}(p) &= \left[1 + S_{sph}^{hf,*,dev}(p) \frac{\mu_{clin} - \mu_{hf}^*(p)}{\mu_{hf}^*(p)} \right]^{-1}.
\end{aligned} \tag{4.44}$$

Appendix B: Notation

The following symbols are used in this paper:

$A_{\infty,j}^{*,vol}$, $A_{\infty,j}^{*,dev}$ = LC-transformed volumetric and deviatoric components of Eshelby problem-related strain concentration tensor of phase j ;

\mathbb{A}_j^* = LC transform of strain concentration tensor of phase j ;

\mathbb{C}_j = elastic stiffness tensor of phase j ;

$clin$ = cement clinker;

cp = cement paste;
 cyl = cylindrical (needle-shaped);
 div = divergence operator;
 E_{cp}^{exp} = experimentally determined Young's elastic modulus of cement paste;
 $E_{c,cp}^{exp}, E_{c,cp}^{mod}$ = experimentally determined and model-predicted Young's creep modulus of cement paste;
 E_{hyd} = Young's elastic modulus of the hydrates;
 $E_{c,hyd}$ = Young's creep modulus of the hydrates;
 exp = experimentally determined;
 \mathbb{F} = auxiliary anisotropic fourth-order tensor;
 f_j^{hf} = hydrate foam-related volume fraction of phase j , $j \in \{air, H_2O, hyd\}$;
 f_j^{cp} = cement paste-related volume fraction of phase j , $j \in \{clin, hf\}$;
 \mathbb{G} = auxiliary isotropic fourth-order tensor;
 G^{vol}, G^{dev} = volumetric and deviatoric components of \mathbb{G} ;
 H_2O = water;
 hf = hydrate foam;
 hyd = hydrates;
 \mathbb{I} = fourth-order identity tensor;
 $\mathbb{I}^{vol}, \mathbb{I}^{dev}$ = volumetric and deviatoric parts of fourth-order identity tensor;
 J_j = uniaxial creep function of phase j ;
 $J_{cp}^{exp}, J_{cp}^{mod}$ = experimentally determined and model-predicted uniaxial creep function of cement paste;
 $J_{e,cp}^{exp}$ = elastic part of J_{cp}^{exp} ;
 $J_{v,cp}^{exp}, J_{v,cp}^{mod}$ = viscous parts of J_{cp}^{exp} and J_{cp}^{mod} ;
 J_{hyd} = uniaxial elastic creep function of cement paste;
 $J_{e,hyd}$ = elastic part of J_{hyd} ;
 $J_{v,hyd}$ = viscous part of J_{hyd} ;
 \mathbb{J}_j = fourth-order creep tensor function of phase j ;
 $\mathbb{J}_{v,cp}^{mod,*}$ = model-predicted viscous part of the creep tensor function of cement paste in the LC space;
 k_j = bulk modulus of phase j ;
 ℓ = length of needle-shaped hydrates;
 M = number of precision digits for computations in the LC space;
 mod = model-predicted;
 \underline{n} = unit normal vector perpendicular to ∂V_{hf} ;
 $n_p, n_{w/c}, n_\xi$ = numbers over which sums in the optimization problem (4.31) extend;
 $\mathbb{P}_j^{hf,*}$ = LC-transformed Hill tensor of an inclusion with shape j , embedded in an infinite hydrate foam matrix, $j \in \{sph, cyl\}$;
 p = complex variable in the LC domain;
 por = pores;
 \mathbb{R}_j = fourth-order relaxation tensor function of phase j ;
 $\mathbb{S}_j^{hf,*}$ = LC-transformed Eshelby tensor of an inclusion with shape j embedded in an infinite hydrate foam matrix, $j \in \{sph, cyl\}$;
 $S_j^{hf,*,vol}, S_j^{hf,*,dev}$ = volumetric and deviatoric components of $\mathbb{S}_j^{hf,*}$;
 sph = spherical;
 \underline{T} = traction vector acting at ∂V_{hf} ;
 t = chronological time;

t_{ref} = reference time, $t_{ref} = 1 \text{ d} = 86\,400 \text{ s}$;
 V_{hf} = volume of RVE of hydrate foam;
 ∂V_{hf} = boundary of RVE of hydrate foam;
 W_{hf}^{ext} = external work density, done on the boundary of the RVE of hydrate foam;
 w/c = initial water-to-cement mass ratio;
 \underline{x} = position vector labeling positions inside V_{hf} as well as at the boundary ∂V_{hf} ;
 $\beta_{cp}^{exp}, \beta_{cp}^{mod}$ = experimentally determined and model-predicted power-law exponent in the creep function of cement paste;
 β_{hyd} = power-law exponent of hydrates;
 δ_{ij} = Kronecker delta;
 $\Gamma(\cdot)$ = gamma function of real quantity (\cdot) ;
 ϵ = mean error between model-predicted and experimentally measured uniaxial viscous creep functions;
 $\boldsymbol{\varepsilon}$ = second-order strain tensor;
 $\boldsymbol{\varepsilon}_j$ = second-order strain tensor of phase j ;
 $\varepsilon_{c,cp}$ = viscous cement paste strain component in loading direction;
 ϑ = zenith angle;
 μ_j = shear modulus of phase j ;
 $\mu_{c,hyd}$ = shear creep modulus of the hydrates;
 ν_{hyd} = Poisson's ratio of the hydrates;
 ξ = hydration degree;
 $\boldsymbol{\xi}$ = displacement vector;
 $\boldsymbol{\sigma}$ = second-order stress tensor;
 $\boldsymbol{\sigma}_j$ = second-order stress tensor of phase j ;
 σ_{cp} = cement paste stress component in loading direction;
 σ_{cp}^{plat} = applied uniaxial stress in creep experiment;
 τ = time instant of loading;
 φ = azimuth angle;
 $\mathbf{1}$ = second-order identity tensor;
 $(\cdot)^*$ = Laplace-Carson transform of quantity (\cdot) ;
 $(\hat{\cdot})$ = Laplace transform of quantity (\cdot) ;
 \cdot = inner product;
 $:$ = second-order tensor contraction;
 \otimes = dyadic product;
 ∇ = nabla operator.

Chapter 5

How water-aggregate interactions affect concrete creep: a multiscale analysis

Authored by: Muhammad Irfan-ul-Hassan, Markus Königsberger, Roland Reihnsner, Bernhard Pichler, and Christian Hellmich

Publication outlook: At the time of finalizing this thesis, this paper is under review for possible publication in the *Journal of Nanomechanics and Micromechanics*

Abstract: Customary micromechanics models for the poroelasticity, creep, and strength of concrete restrict the domain affected by the hydration reaction, to the cement paste volume; considering the latter as thermodynamically closed system with respect to the (chemically inert) aggregates. Accordingly, the famous Powers hydration model appears as a natural choice for the determination of clinker, cement, water, and aggregates volume fractions entering such micromechanical models. The situation changes once internal curing occurs, i.e. once part of the present water is absorbed initially by the aggregates, and then soaked “back” to the cement paste during the hydration reaction. For this case, we here develop an extended hydration model, introducing water uptake capacity of the aggregates on the one hand, and paste void filling extent on the other, as additional quantities. Based on constant values for just these two new quantities, and on previously determined creep properties of cement pastes as functions of an effective water-to-cement mass ratio (i.e. that associated to the cement paste domain, rather than to the entire concrete volume), a series of ultrashort-term creep tests on different mortars and concretes can indeed be very satisfactorily predicted by a standard micro-viscoelastic mathematical model. This further extends the applicability range of micromechanics modeling in cement and concrete research.

Contribution: Bernhard Pichler and Christian Hellmich set up the overall strategy for bottom-up prediction of creep properties of mortars and concretes, based on a new hydration model considering (i) initial water uptake by aggregates and (ii) autogeneous shrinkage-driven suction of water “back” to the cement paste matrix. They supervised the research progress, checked key results, and supported the documentation process. Muhammad Irfan-ul-Hassan produced the mortar and concrete specimens and carried out hourly-repeated three-minute creep experiments supported by the technical staff of the laboratory. He incorporated the new hydration model into a Maple code for two-scale creep homogenization of mortars and

concretes. He used the code for identification (i) of the water uptake capacity of the used aggregates, and (ii) of the filling extent of shrinkage-induced voids by water. He carried out model validation and documented the research results. Markus Königsberger developed the Maple code for creep homogenization, contributed to both the discussion processes and the documentation of research results, and helped proof reading the paper. Roland Reihnsner operated the testing machine and the deformation measurement equipment.

Keywords: creep homogenization, continuum micromechanics, correspondence principle, cement paste, upscaling, internal curing

5.1 Introduction

Concrete hydration is generally regarded as a process from which the aggregates, being chemically inert, are fully excluded, and which is therefore taking place exclusively in the cement paste, where water reacts with cement grains, so as to form hydrates. Correspondingly, concrete hydration models such as the famous Powers-Acker model (Powers and Brownyard, 1947; Acker, 2001) are typically built on evolving volume fractions of cement clinker, water, and hydrates in the cement paste; and considering the cement paste compartment as a thermodynamically closed system, all these volume fractions can be traced back to the hydration degree and to the (initial) water-to-cement mass ratio. By contrast, the volume fractions of cement paste and aggregates remain constant at the hierarchical level of concrete. Besides other applications, such hydration models have been a particularly appropriate basis for the development of multiscale mechanics models for concrete, be they related to elasticity (Bernard et al., 2003b; Hellmich and Ulm, 2005; Sanahuja et al., 2007) to poroelasticity (Ulm and Heukamp, 2004; Ghabezloo, 2010) to viscoelasticity (Scheiner and Hellmich, 2009) or to strength (Pichler and Hellmich, 2011; Pichler et al., 2013a).

All these models have been experimentally validated up to different levels of precision, so that on the one hand, multiscale continuum mechanics has become a well accepted theoretical tool in cement and concrete research; while on the other hand, the field is still open for improvements. The latter is true in particular for the very challenging topic of concrete creep, which spans several orders of time magnitude, starting from the scale of minutes (Vandamme and Ulm, 2009; Delsaute et al., 2012; Boulay et al., 2012; Vandamme and Ulm, 2013; Zhang et al., 2014; Irfan-ul-Hassan et al., 2016) to that of several days (Bažant et al., 1976; Tamtsia et al., 2004; Rossi et al., 2011), weeks (Tamtsia and Beaudoin, 2000; Laplante, 2003; Atrushi, 2003; Briffaut et al., 2012), months (Rossi et al., 1994; Zhang et al., 2014), or even years (Bažant et al., 2011, 2012; Zhang et al., 2014).

In the present paper, we show that the challenge in the multiscale modeling of concrete creep probably does not lie so much in finding the appropriate micromechanical representation of the material, but rather in the reliable estimation of the evolving volume fractions of the material constituents, entering the corresponding micromechanics models as input. In this context, we abandon the aforementioned assumption of the cement paste being a thermodynamically closed system, and we explicitly introduce water migration from the inter-aggregates spaces into the aggregates, as well as back-suction of water from the aggregates into the hydrating (and therefore water-consuming) cement paste.

Accordingly, the paper is organized as follows: A simple mathematical model for water migration into and from the aggregates is formulated in Section 5.2. Based on the initial water-to-cement mass ratio, on the hydration degree, and on two newly introduced quantities, namely the water uptake capacity of the aggregates and the water filling extent of the cement

paste voids, this model provides the volume fractions of water, cement clinker, hydrates, and aggregates within concretes and mortars with water-absorbing aggregates. These volume fractions then enter a micromechanical model for mortar and concrete creep, upscaling cement paste behavior, as quantified in the recent ultrashort-term tests of Irfan-ul-Hassan et al. (2016), to the mortar and concrete level, as detailed in Section 5.3. Corresponding micromechanical model predictions are then compared to a total of 32 newly performed ultrashort-term creep tests at two different mortars (made from aggregates type I - „Normensand Quartz”) and two different concretes (made from aggregates type II - „Pannonia Kies”), which are all made from the same cement, but differ in water-to-cement and aggregate-to-cement mass ratios, see Section 5.4. It is checked whether this comparison would allow for identification of one value each for (i) the water uptake capacity of aggregates; and (ii) the cement-specific void filling extent by water soaked out from the aggregates. Also, air entrapment between aggregates and cement paste is considered. Thereafter, the paper is terminated by a conclusion section.

5.2 Modeling hydration-dependent water migration to and from the aggregates

We consider that during the mixing of concrete or mortar, i.e. before the hydration reaction, a significant amount of water may be taken up by the aggregates. This is the case with oven-dried quartz aggregates, on which we focus throughout the present paper. Accordingly, we decompose the total mass of water, w , into that of the water residing inside the cement paste, w_{cp} , and that which is absorbed within the open porosity of quartz, w_a ,

$$w = w_{cp}(\xi) + w_a(\xi). \quad (5.1)$$

During the hydration reaction, however, part of the water which has been initially absorbed into the aggregates, is soaked back into the inter-aggregates space, which is then occupied by the cement paste. This is because the hydration products fill less volume than their unreacted counterparts. In more detail, the volume reduction during cement paste hydration [also called autogenous shrinkage (Powers and Brownyard, 1947; Acker, 2001)] leads to the formation of air voids, which are partially refilled by the additional water extracted from the aggregates. Such a process driven by water supply from the aggregates is sometimes called internal curing (Bentz et al., 2005; Jensen and Lura, 2006; Wyrzykowski et al., 2011; Zhutovsky and Kovler, 2012; Justs et al., 2015). Maintaining the philosophy of the Powers model to identify linear relations between chemical reactants and products on the one hand, and the degree of hydration on the other hand, we envision that the amount of aggregate-extracted water increases (linearly) with the volume of voids. The latter increases (linearly) with the mass of hydrates formed, which then increases, again linearly, with the degree of hydration. Hence, the water content in the cement paste is linearly linked to the hydration degree as well, which is mathematically expressed as follows

$$\frac{w_{cp}(\xi)}{c} = d + k \xi \quad (5.2)$$

In this context, it needs to be emphasized that $w_{cp}(\xi)$ comprises the mass of *all* the water in the cement paste in the most general understanding, i.e. both the unreacted water *and* that which is chemically combined to the cement clinker; in the same sense, c denotes the *total* mass of cement, including both the unreacted cement and that which is chemically combined to water. The material constants in (5.2), d and k , are the initial value of the water-to-cement

mass ratio which is effective at the cement paste level, and the hydration-dependent (linear) increase of this effective mass ratio. The former constant can be linked to the water mass which is initially uptaken by the aggregates, $w_a(0)$. This quantity is normalized by the mass of the aggregates, a , yielding the initial water-to-aggregate mass ratio in the form $w_a(0)/a$. Namely, when splitting the (nominal) water-to-cement mass ratio into a cement paste-specific and an aggregate-specific portion, the respective mathematical expression can be readily solved for d , according to

$$\frac{w}{c} = \frac{w_{cp}(0)}{c} + \frac{w_a(0)}{a} \frac{a}{c} \quad \Rightarrow \quad d = \frac{w_{cp}(0)}{c} = (w/c) - \frac{w_a(0)}{a} (a/c) \quad (5.3)$$

Concerning the soaking of water, from the aggregates back to the inter-aggregate spaces, then occupied by cement paste, we introduce a cement-specific void-filling extent α between 0 and 1, with zero referring to no water filling of air voids formed during autogeneous shrinkage of the cement paste, while 1 relates to complete filling of the air voids by water. Thereby, the voids themselves evolve linearly with the hydration degree, as seen in Fig. 5.1. This void filling

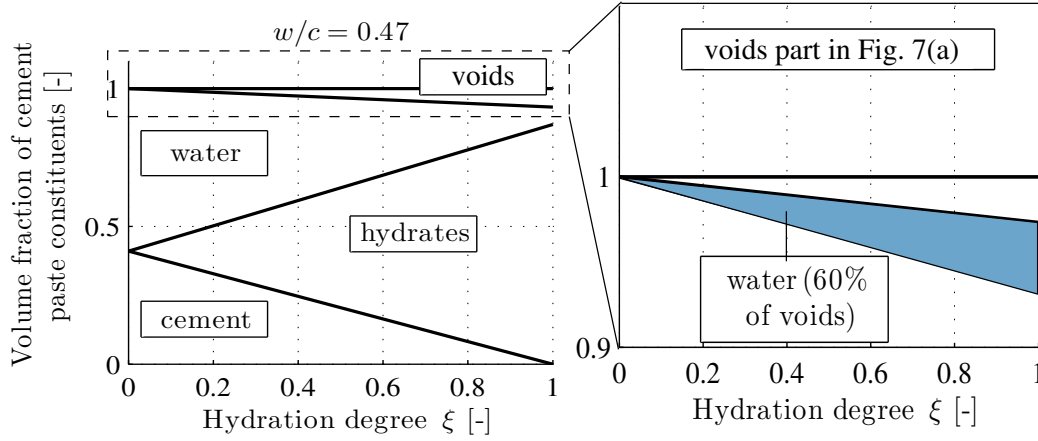


Figure 5.1: Hydration-driven evolution of volume fractions of cement paste constituents (cement, water, hydrates, and voids) according to Powers-Acker's hydration model: (a) complete phase volume evolution diagram according to (Powers and Brownyard, 1947; Acker, 2001); (b) detail illustrating void filling extent α , concerning partial void filling by water that is soaked from the open porosity of quartz into the cement paste matrix

extent α can be related to the back-soaking-related parameter k , by deriving an expression for the hydration-dependent water mass which was soaked into the cement paste, through combination of Eqs. (5.2) and (5.3), yielding

$$w_{cp}(\xi) - w_{cp}(0) = c k \xi \quad (5.4)$$

and by expressing this mass as the volume of voids, times the void filling extent α , times the mass density of water, yielding

$$c k \xi = V_{void} \alpha \rho_{H_2O} \quad (5.5)$$

We are left with relating the void volume V_{void} to the initial composition of the cement paste and to the hydration degree. To this end, the void volume is considered to be equal to the volume of cement paste, V_{cp} , times the cement paste-related volume fraction of voids, f_{void}^{cp}

$$V_{void} = V_{cp} f_{void}^{cp} \quad (5.6)$$

The volume of cement paste is equal to the initial volumes of cement and water, i.e. V_c and V_w , which can be expressed by the masses of cement and water as well as by the related mass densities as

$$V_{cp} = V_c + V_w = \frac{c}{\rho_{clin}} + \frac{w_{cp}(0)}{\rho_{H_2O}} \quad (5.7)$$

Finally, the volume fraction of shrinkage-induced voids in cement paste is considered to increase proportionally to the hydration degree, as quantified through the Powers-Acker hydration model (Powers and Brownyard, 1947; Acker, 2001), evaluated for the effective initial composition of the cement paste matrix, quantified in terms of the effective initial water-to-cement mass fraction $w_{cp}(0)/c$, compare Eq. (15.4) of (Pichler et al., 2009):

$$f_{void}^{cp} = \frac{\left(1 + 0.42 \frac{\rho_{clin}}{\rho_{H_2O}} - 1.42 \frac{\rho_{clin}}{\rho_{hyd}}\right) \xi}{1 + \frac{\rho_{clin}}{\rho_{H_2O}} (w_{cp}(0)/c)} = \frac{3.31 \xi}{20 + 63 \frac{w_{cp}(0)}{c}} \quad (5.8)$$

with $\rho_{clin} = 3.150 \text{ kg/dm}^3$ (Acker and Ulm, 2001), $\rho_{H_2O} = 1.000 \text{ kg/dm}^3$, and $\rho_{hyd} = 2.073 \text{ kg/dm}^3$ (Barthélémy and Dormieux, 2003), denoting the mass densities of cement clinker grains, water, and hydrates, respectively. The sought relation between the constant k and the void filling extent by water, α , follows from specialization of Eq. (5.5) for Eqs. (5.6), (5.7), and (5.8), as well as from solving the resulting expression for k , yielding

$$k = \left[\frac{\rho_{H_2O}}{\rho_{clin}} + \frac{w_{cp}(0)}{c} \right] \frac{3.31 \alpha}{20 + 63 \frac{w_{cp}(0)}{c}} \quad (5.9)$$

Eq. (5.9) underlines that k , the hydration degree-related rate of the effective water-to-cement mass fraction of the cement paste matrix, see Eq. (5.2), is directly proportional to α , the extent up to which the shrinkage-induced voids in the cement paste are filled by water.

With respect to the classical Powers-Acker model, the herein developed hydration model which considers also internal curing, contains two additional quantities: (i) the water uptake capacity of the aggregates, $w_a(0)/a$, and (ii) the void filling extent by water, α . The former quantity is involved in the expression for the initial value of the effective water-to-cement mass fraction, see Eq. (5.3), while α is involved in the mathematical expression for the evolution of the water-to-cement mass ratio which is effective in the cement paste; and this expression is obtained by specializing Eq. (5.2) for d and k according to (5.3) and (5.9), respectively, and from consideration of the mass densities $\rho_{clin} = 3.150 \text{ kg/dm}^3$ and $\rho_{H_2O} = 1.000 \text{ kg/dm}^3$, as

$$\begin{aligned} \frac{w_{cp}(\xi)}{c} &= (w/c) - \frac{w_a(0)}{a} (a/c) + \left(\left[\frac{\rho_{H_2O}}{\rho_{clin}} + \frac{w_{cp}(0)}{c} \right] \frac{3.31 \alpha}{20 + 63 \frac{w_{cp}(0)}{c}} \right) \xi \\ &= (w/c) - \frac{w_a(0)}{a} (a/c) + \left[\frac{1.051 + 3.31 [(w/c) - \frac{w_a(0)}{a} (a/c)]}{20 + 63 [(w/c) - \frac{w_a(0)}{a} (a/c)]} \right] \alpha \xi \end{aligned} \quad (5.10)$$

This is the water-to-cement mass ratio which is effective at the cement paste level, and which governs the hydration reaction taking place there.

Its initial value needs to be considered when quantifying the volume fractions of cement paste and aggregates in a material volume of concrete or mortar with water absorbing aggregates; except for the use of this effective water-to-cement mass ratio, the latter quantification

follows the standard relation given in (Bernard et al., 2003b; Pichler et al., 2009) , which finally yields

$$\begin{aligned} f_{cp}^{no-air} &= \frac{\frac{\rho_{agg}}{\rho_{clin}} + \frac{\rho_{agg}}{\rho_{H_2O}} (w_{cp}(0)/c)}{\frac{\rho_{agg}}{\rho_{clin}} + \frac{\rho_{agg}}{\rho_{H_2O}} (w_{cp}(0)/c) + (a/c)} = \frac{0.8406 + 2.648 [(w/c) - \frac{w_a(0)}{a} (a/c)]}{0.8406 + 2.648 [(w/c) - \frac{w_a(0)}{a} (a/c)] + (a/c)} \\ f_{agg}^{no-air} &= \frac{(a/c)}{\frac{\rho_{agg}}{\rho_{clin}} + \frac{\rho_{agg}}{\rho_{H_2O}} (w_{cp}(0)/c) + (a/c)} = \frac{(a/c)}{0.8406 + 2.648 [(w/c) - \frac{w_a(0)}{a} (a/c)] + (a/c)} \end{aligned} \quad (5.11)$$

with $\rho_{agg} = 2.648 \text{ kg/dm}^3$ as the mass density of quartz aggregates, considered throughout the present paper. However, it often occurs during mixing that small amounts of air get entrapped into the cement paste matrix as well. Denoting the corresponding air volume fraction by f_{air} , the volume fractions at the concrete or mortar level can be derived from the relations

$$f_{cp} + f_{agg} + f_{air} = 1 \quad \frac{f_{cp}}{f_{agg}} = \frac{f_{cp}^{no-air}}{f_{agg}^{no-air}} \quad (5.12)$$

which imply that

$$f_{cp} = \frac{1 - f_{air}}{1 + f_{agg}^{no-air} / f_{cp}^{no-air}}, \quad f_{agg} = \frac{1 - f_{air}}{1 + f_{cp}^{no-air} / f_{agg}^{no-air}}, \quad (5.13)$$

The relevance of this new water migration model and its effect on concrete composition will now be tested through a creep upscaling analysis from the cement paste level to the concrete or mortar level.

5.3 Creep homogenization of mortars and concretes

The relevance of the effective water-to-cement mass ratio according to Eq. (5.10) and of the cement paste and aggregates volume fractions according to Eq. (5.11) and (5.13), both depending on the void filling extent α and the water uptake capacity of the aggregates, $w_a(0)/a$, will now be checked by using Eq. (5.10), (5.11), and (5.13) and the quantities appearing therein, within a creep upscaling analysis from the cement paste to the mortar and concrete level.

Thereby, the question is tackled whether the experimental results of numerous creep tests performed at the level of cement paste made from *only one* type of cement, and at the level of mortars and concretes made from *the same* type of cement, but with two different types of aggregates, can be predicted by a micromechanical model, which is based on *only one* value for the cement-specific void filling capacity α , and of *only two* aggregate-specific values for the water absorption capacity $w_a(0)/a$.

The creep tests considered in this context all follow the protocol recently reported by Irfan-ul-Hassan et al. (2016): Accordingly, three-minute creep tests on the same cement paste, mortar, or concrete samples are hourly repeated. The key idea behind this protocol is that three minutes are short enough for the microstructure to remain practically *invariant* throughout each individual test. Within one hour, on the other hand, the hydration process in early-age cementitious systems goes on in a significant manner, such that two subsequent three-minute long creep tests refer to already remarkably *different* microstructures. Hence, an upscaling analysis concerning cement paste, mortar, and concrete samples tested according to the aforementioned protocol can be performed in the theoretical framework of classical,

non-aging micro-viscoelasticity (Read Jr, 1950; Sips, 1951; Laws and McLaughlin, 1978; Beurthey and Zaoui, 2000).

Choosing, in this context, a standard micromechanical representation for mortar and concrete (Scheiner and Hellmich, 2009; Baweja et al., 1998; Bernard et al., 2003b; Hellmich and Ulm, 2005), namely that of a composite material consisting of a (viscoelastic) cement paste matrix with (elastic) aggregate inclusions and with (potentially occurring) air inclusions, as seen in Fig. 5.2, the (homogenized) relaxation tensor at the concrete/mortar scale, \mathbf{R}_{hom} ,

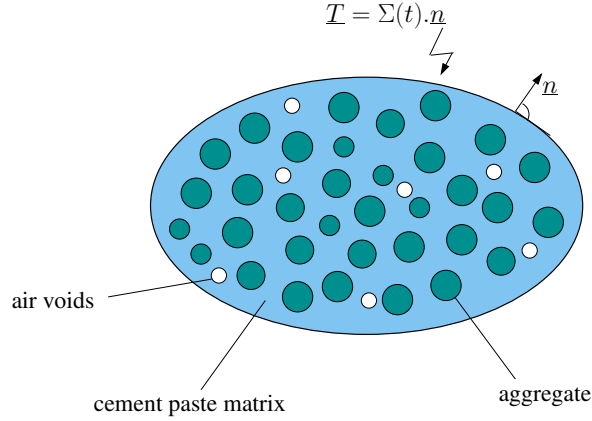


Figure 5.2: Micromechanical representation of mortar and concrete: 2D sketch of 3D matrix-inclusion composites comprising a continuous cement paste matrix with embedded spherical inclusions representing quartz aggregates and air pores

follow from those at the cement paste scale, \mathbf{R}_{cp} , as well as from the volume fractions of cement paste, of aggregates, and of (potentially occurring) air, as (Scheiner and Hellmich, 2009)

$$\begin{aligned}
 \mathbf{R}_{hom}^*(p) &= 3 k_{hom}^*(p) \mathbb{I}_{vol} + 2 \mu_{hom}^*(p) \mathbb{I}_{dev} = \\
 &\left(f_{cp} \mathbf{R}_{cp}^* + f_{agg} \mathbf{R}_{agg}^* : \left\{ \mathbb{I} + \mathbb{P}_{sph}^*(p) : \left[\mathbf{R}_{agg}^* - \mathbf{R}_{cp}^*(p) \right] \right\}^{-1} \right. \\
 &\quad \left. + f_{air} \mathbf{R}_{air}^* : \left\{ \mathbb{I} + \mathbb{P}_{sph}^*(p) : \left[\mathbf{R}_{air}^* - \mathbf{R}_{cp}^*(p) \right] \right\}^{-1} \right) \\
 &: \left(f_{cp} \mathbb{I} + f_{agg} \left\{ \mathbb{I} + \mathbb{P}_{sph}^*(p) : \left[\mathbf{R}_{agg}^* - \mathbf{R}_{cp}^*(p) \right] \right\}^{-1} \right. \\
 &\quad \left. + f_{air} \left\{ \mathbb{I} + \mathbb{P}_{sph}^*(p) : \left[\mathbf{R}_{air}^* - \mathbf{R}_{cp}^*(p) \right] \right\}^{-1} \right)^{-1}
 \end{aligned} \tag{5.14}$$

where the star-indicated properties refer to the Laplace Carson (LC) transforms of the originally time-dependent quantities occurring in the standard convolution integrals of linear viscoelasticity [“correspondence principle” (Read Jr, 1950; Sips, 1951; Laws and McLaughlin, 1978; Beurthey and Zaoui, 2000)]

$$f^*(p) = p \hat{f}(p) = p \int_0^\infty f(t) \exp(-pt) dt, \tag{5.15}$$

and back-transformation of (5.14) from the Laplace Carson domain back to the time domain may be performed by the Gaver-Wynn-Rho algorithm (Scheiner and Hellmich, 2009; Gaver, 1966). Mathematical details on the LC-transformed homogenized bulk and shear moduli, k_{hom}^* and μ_{hom}^* , on the fourth-order unity tensor \mathbb{I} with its volumetric and deviatoric parts, \mathbb{I}_{vol} and \mathbb{I}_{dev} , and on the morphology tensor \mathbb{P}_{sph}^* can be found in the Appendix. The relaxation tensors \mathbb{R}_{cp}^* correspond to a power-law-type creep behavior characterized by an elastic modulus E_{cp} , a Poisson's ratio ν_{cp} , a creep modulus $E_{c,cp}$, and a creep exponent β_{cp} ; hence they read as

$$\begin{aligned} \mathbb{R}_{cp}^*(p) &= 3 k_{cp}^*(p) \mathbb{I}_{vol} + 2 \mu_{cp}^*(p) \mathbb{I}_{dev} \\ &= \left[\frac{1 - 2\nu_{cp}}{E_{cp}} + \frac{1 - 2\nu_{cp}}{E_{c,cp}} \left(\frac{1}{t_{ref}} \right)^{\beta_{cp}} \Gamma(\beta_{cp} + 1) p^{-\beta_{cp}} \right]^{-1} \mathbb{I}_{vol} \\ &\quad + \left[\frac{1 + \nu_{cp}}{E_{cp}} + \frac{1 + \nu_{cp}}{E_{c,cp}} \left(\frac{1}{t_{ref}} \right)^{\beta_{cp}} \Gamma(\beta_{cp} + 1) p^{-\beta_{cp}} \right]^{-1} \mathbb{I}_{dev}. \end{aligned} \quad (5.16)$$

The aforementioned material characteristics at the cement paste level all depend on the (here effective) water-to-cement mass ratio and the hydration degree, as identified in the more than 500 creep tests on cement paste reported by Irfan-ul-Hassan et al. (2016), see Fig. 5.3. For considering (effective) water-to-cement mass ratios between those which were

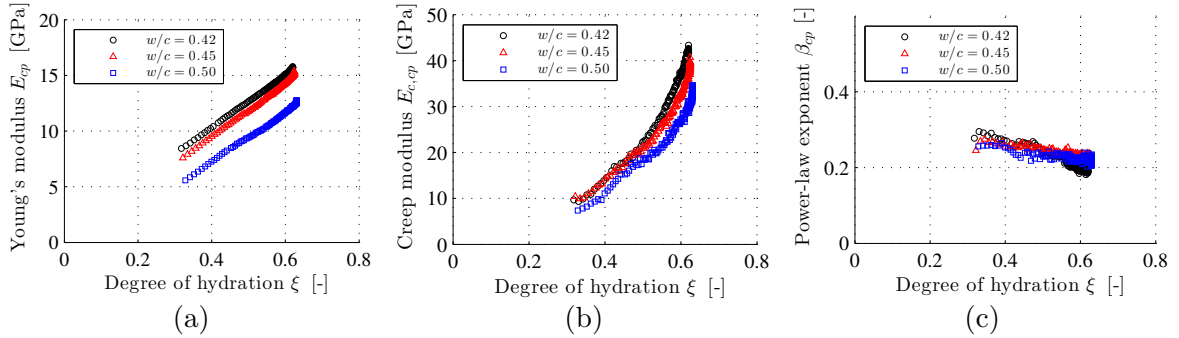


Figure 5.3: Results from hourly-repeated three-minute creep testing on cement pastes with initial water-to-cement mass ratios amounting to 0.42, 0.45, and 0.50, respectively: (a) elastic modulus E_{cp} , (b) creep modulus $E_{c,cp}$, and (c) creep exponent β_{cp} ; as functions of hydration degree, see (Irfan-ul-Hassan et al., 2016)

explicitly tested, we resort to quadratic interpolation, as exemplified in Fig. 5.4. For the quantification of Poisson's ratio, we use a validated multiscale model (Pichler et al., 2008; Pichler and Hellmich, 2011) for establishment of a relation between the latter and the elastic modulus, see Fig. 5.5.

Our present study is devoted to aggregates consisting of quartz, with elastic bulk and shear moduli amounting to (Bass, 2013),

$$k_{agg} = 37.8 \text{ GPa}, \quad \mu_{agg} = 44.3 \text{ GPa} \quad \Rightarrow \quad \mathbb{R}_{agg}^* = 3 k_{agg} \mathbb{I}_{vol} + 2 \mu_{agg} \mathbb{I}_{dev} \quad (5.17)$$

while the air inclusions (if existing) dispose over only negligible elastic stiffness,

$$k_{air} = \mu_{air} = 0 \text{ GPa}, \quad \Rightarrow \quad \mathbb{R}_{air}^* = 0. \quad (5.18)$$

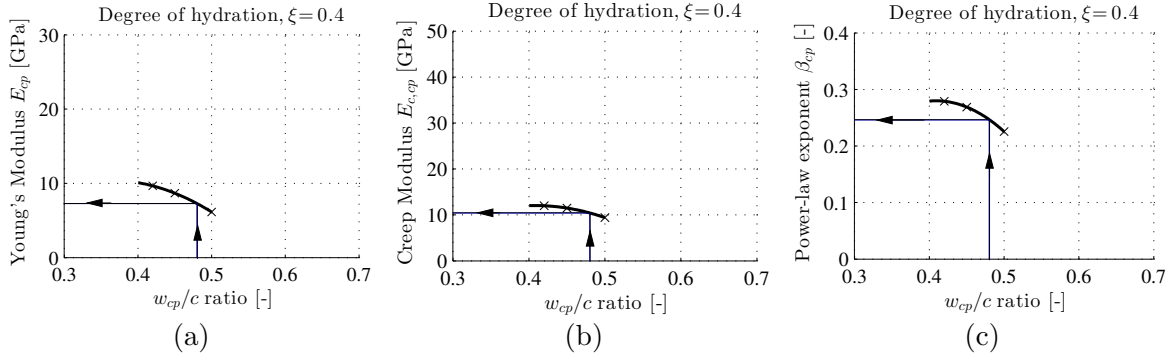


Figure 5.4: Quantification of effective viscoelastic properties of the cement paste matrix as a function of the effective water-to-cement mass fraction w_{cp}/c , by means of quadratic interpolation between creep test results on plain cement pastes with $w/c \in [0.42, 0.45, 0.50]$: (a) elastic modulus E_{cp} , (b) creep modulus $E_{c,cp}$, and (c) creep exponent β_{cp} ; at degree of hydration $\xi = 0.40$

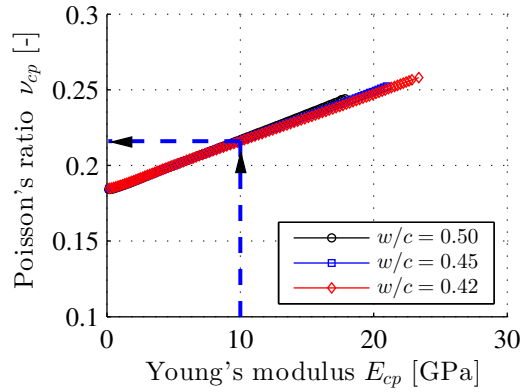


Figure 5.5: Relation between elastic modulus and Poisson's ratio of cement pastes with initial water-to-cement mass ratios amounting to 0.42, 0.45, and 0.50, respectively; predictions of the validated multiscale model of Pichler et al. (2009) and Pichler and Hellmich (2011)

5.4 Comparison of ultrashort creep experiments and corresponding micromechanics predictions – identification of water absorption capacities of quartz aggregates and of paste void filling extent

5.4.1 Experimental campaign on the mortar/concrete level

In order to assess the relevance of the newly introduced quantities, the paste void filling extent α and the water absorption capacity of aggregates, $w_a(0)/a$, expressed in corresponding creep homogenization results as described in the previous section, the latter results need to be compared to experimental data at the level of mortar and concrete. To this end, a series of three minute-long creep tests on two mortars and two concretes was performed:

Thereby, all four materials exhibited the same nominal volume fractions of quartz aggregates and of cement paste, respectively, namely amounting to 0.58 and to 0.42, respectively, see

Table 5.1. Mortar #1 and Concrete #1 exhibited the same nominal composition in terms of $w/c = 0.50$ and $a/c = 3.0$. Mortar #2 and Concrete #2, in turn, exhibited $w/c = 0.42$ and $a/c = 2.7$. All four materials were produced from a commercial cement of type CEMI 42.5 N and distilled water, i.e. with the same raw materials that were also used for the production of the cement pastes discussed in Irfan-ul-Hassan et al. (2016). In addition, we used oven-dried aggregates made of quartz. The two mortars contain standard sand of the company “Normensand” as per standard DIN EN-196-1, consisting of rounded sand grains with diameters being smaller or equal to $d_{max} = 2$ mm. The two concretes contain aggregates of the Austrian company “Pannonia Kies”, consisting of quartz gravels with diameters being smaller or equal to $d_{max} = 8$ mm.

Table 5.1: Nominal composition of tested mortars and concretes

Material	w/c	a/c	f_{cp}^{nom}	f_{agg}^{nom}	d_{max}
Mortar #1	0.50	3.0	0.42	0.58	2 mm
Mortar #2	0.42	2.7	0.42	0.58	2 mm
Concrete #1	0.50	3.0	0.42	0.58	8 mm
Concrete #2	0.42	2.7	0.42	0.58	8 mm

The early-age testing protocol is identical to the one used to characterize cement paste [see Irfan-ul-Hassan et al. (2016)], i.e. the mortar and concrete specimens with dimensions (70 mm diameter and 300 mm height) were hourly subjected to three-minute long creep tests under uniaxial stress conditions, see Fig. 5.6 (a) for the stress history in a specific three-minute long creep test. For each test, the load plateau was selected such that induced compressive stresses were smaller than 15 % of the expected compressive strength, see Fig. 5.6 (b). Using the calorimetry results described by Irfan-ul-Hassan et al. (2016), sample ages were “translated” into equivalent hydration degrees.

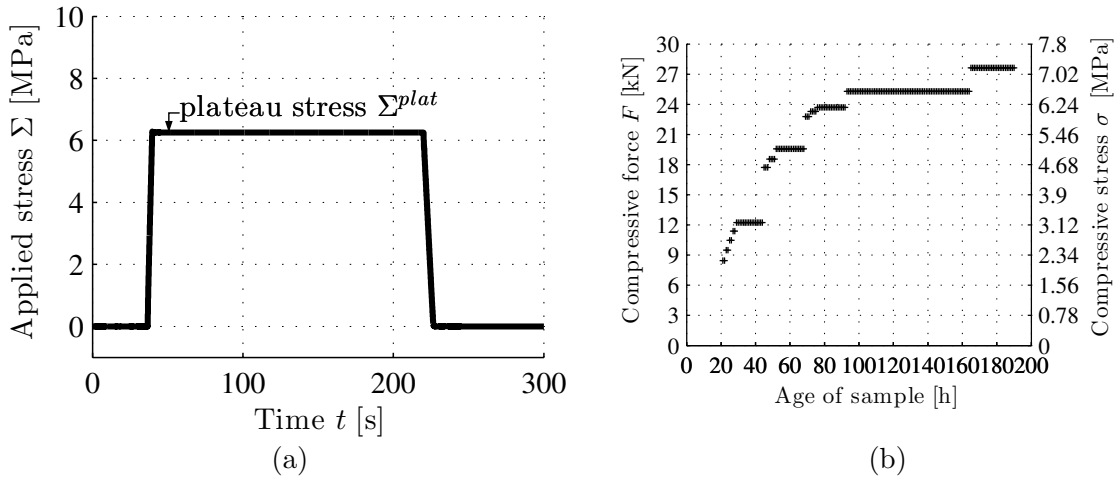


Figure 5.6: Three-minute creep tests on mortars and concretes: (a) force history during creep testing carried out at an age of 100 h on Mortar #1; and (b) prescribed load levels chosen to be smaller than or equal to 15 % of the expected compressive strength

Each tested specimen was subjected to 168 three-minute creep tests. Out of this database,

we focus on the tests carried out at hydration degrees amounting to

$$\xi \in [0.32, 0.35, 0.40, 0.45, 0.50, 0.55, 0.60, 0.63] \quad (5.19)$$

The plateau stresses of Fig. 5.6, which correspond to the hydration degrees of Eq. (5.19), were

$$\Sigma_{plat} = [2.08, 2.32, 3.0, 3.0, 4.37, 4.83, 6.25, 6.25] \text{ MPa} \quad (5.20)$$

The correspondingly measured normal strains in loading direction, $E(t)$, were divided by the applied plateau stress Σ_{plat} , see Fig. 5.6, so as to arrive at a convenient illustration of the test results, as shown in Fig. 5.7

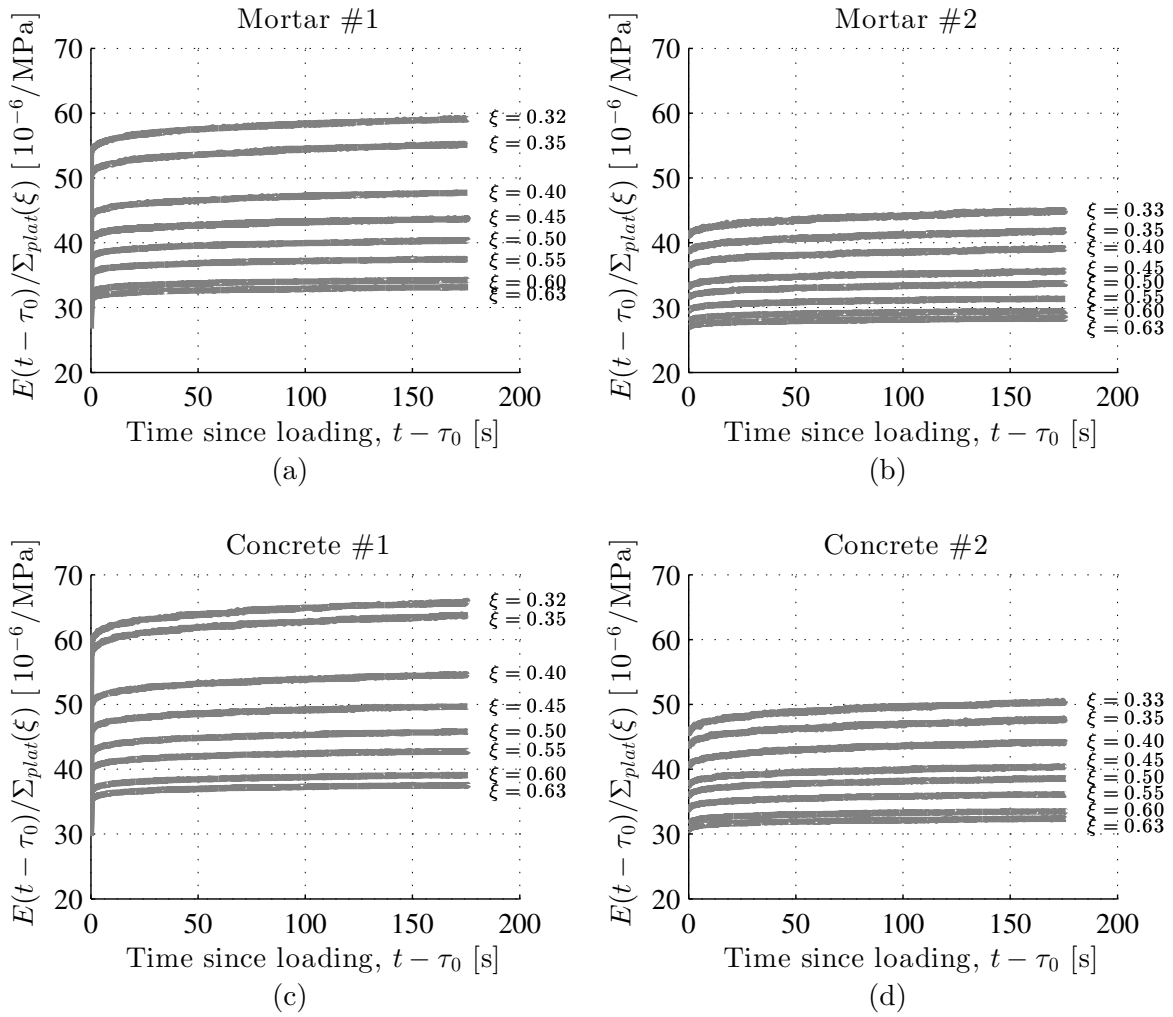


Figure 5.7: Plateau stress-normalized strains obtained from three minute-long creep tests on mortars and concretes, at the hydration degrees given in Eq. (5.19), and the corresponding load plateaus according to Eq. (5.20): (a) Mortar #1: $w/c = 0.50, a/c = 3.00$, (b) Mortar #2: $w/c = 0.42, a/c = 2.70$, (c) Concrete #1: $w/c = 0.50, a/c = 3.00$, (d) Concrete #2: $w/c = 0.42, a/c = 2.70$

5.4.2 Micromechanical predictions of experimental data

For micromechanically predicting the creep test results of Fig. 5.7, the relaxation functions of Eq. (5.14) are transformed to creep functions according to

$$\begin{aligned}\mathbb{J}_{hom}^*(p) &= \mathbb{R}_{hom}^*(p)^{-1} \\ \mathbf{E}^*(p) &= \mathbb{J}_{hom}^*(p) : \boldsymbol{\Sigma}^*(p)\end{aligned}\tag{5.21}$$

and this result is then back-transformed into the time-domain, yielding

$$\mathbf{E}(\xi, t) = \int_0^t \mathbb{J}_{hom}(\xi, t - \tau) : \dot{\boldsymbol{\Sigma}}(\tau) d\tau\tag{5.22}$$

This Boltzmann convolution integral is then evaluated for the volume fractions of Eqs. (5.11) and (5.13), for the cement paste properties of Fig. 5.4, and for the loading history of Fig. 5.6. These evaluations comprise two quantities which are not known *a priori*, but which are identified from a series of creep results at the concrete and mortar levels. This is described next.

Also, it needs to be emphasized that consideration of the load history of Fig. 5.6 as a continuous function, rather than as a step function, and corresponding use of the continuous form of the Boltzmann integral (5.22), is mandatory for arriving at reliable results. This is because a ramp loading as indicated in Fig. 5.6, does not only provoke elastic, but also viscoelastic strains, as was explicitly evidenced by Irfan-ul-Hassan et al. (2016).

5.4.3 Identification of water uptake capacity of “Normensand” quartz aggregates and of the paste void filling extent, from experimental data concerning Mortar #1

The water uptake capacity of quartz, $w_a(0)/a$, and the paste void filling extent α , are identified from a very large set of numerical values making up the following "search intervals"

$$\begin{aligned}w_a(0)/a &\in [0.000, 0.0001, 0.0002, \dots, 0.0199, 0.0200] \\ \alpha &\in [0.000, 0.001, 0.002, \dots, 0.999, 1.000].\end{aligned}\tag{5.23}$$

For all data pairs $[w_a(0)/a, \alpha]$ composed from the values given in Eq. (5.23), the micromechanics model of Eqs. (5.14)–(5.18), together with Eqs. (5.3), (5.10), and (5.11) evaluated for $w/c = 0.50$ and $a/c = 3.0$, see Table 5.1, with the interpolation scheme of Fig. 5.4, and with the loading history of Fig. 5.6 entering Eq. (5.22), is used to predict the creep functions arising from the eight creep tests conducted on Mortar #1, as seen in Fig. 5.7(a). Eight hydration degree-specific model predictions of the normal strain histories E^{pred} , represented by 180 discrete values each, are compared to the corresponding experimentally determined strains normalized by plateau stress E^{exp} ; and the corresponding prediction error is quantified through

$$\mathcal{E} = \frac{1}{8 \times 180} \sum_{i=1}^8 \frac{1}{\Sigma_{plat}(\xi_i)} \sum_{j=1}^{180} \left| E^{pred}(\xi_i, t_j) - E^{exp}(\xi_i, t_j) \right|\tag{5.24}$$

whereby all strain values were normalized with respect to the plateau stresses Σ_{plat} . The smallest prediction error $\mathcal{E} = 1.55 \times 10^{-7} \text{ MPa}^{-1}$ (see Table 5.2) is obtained for the following

Table 5.2: Prediction Errors \mathcal{E} (MPa⁻¹) according to Eq. (5.24)

Material	\mathcal{E} from nominal composition	\mathcal{E} from water migration model
Mortar #1	4.50×10^{-6}	1.55×10^{-7}
Mortar #2	1.50×10^{-6}	2.90×10^{-7}
Concrete #1	5.50×10^{-6}	1.50×10^{-7}
Concrete #2	1.23×10^{-6}	1.30×10^{-7}

values of the water uptake capacity of quartz and of the water filling extent of shrinkage-induced voids:

$$\frac{w_a(0)}{a} = 0.0099 \quad \alpha = 0.603 \quad (5.25)$$

see Fig. 5.8 (a) for the comparison of measured and modeled creep functions. The identified material constants (5.25) imply (i) that 1 kilogram of quartz takes up 9.9 gram of water during mixing of the raw materials, and (ii) that shrinkage-induced voids of the cement paste matrix soak water from the open porosity of quartz such that these voids are water-filled to an extent of 60.3 percent.

The identified material constants (5.25) provide access to the effective composition of the cement paste of Mortar #1. The initial value of the effective water-to-cement mass fraction of the cement paste matrix, for instance, follows from specialization of Eq. (5.3) for $w_a(0)/a$ from (5.25) and for the mix-related water-to-cement and quartz-to-cement mass ratios $w/c = 0.50$ and $a/c = 3.0$ as:

$$\frac{w_{cp}(0)}{c} = 0.4703 \quad (5.26)$$

This is remarkably smaller than the (nominal) mix-related water-to-cement mass ratio $w/c = 0.50$. The evolution of the effective water-to-cement mass fraction of the cement paste matrix follows from specialization of Eq. (5.10) for (5.25), $w/c = 0.50$, and $a/c = 3.0$ as

$$\frac{w_{cp}(\xi)}{c} = 0.4703 + 0.0317 \xi \quad (5.27)$$

see also Fig. 5.8 (b). The actual volume fractions of the cement paste matrix and of quartz follow from specialization of Eqs. (5.11) for Eq. (5.26), $w/c = 0.50$, and $a/c = 3.0$ as

$$f_{cp} = 0.4101, \quad f_{agg} = 0.5899. \quad (5.28)$$

5.4.4 Confirmation of the water uptake capacity of "Normensand" quartz aggregates and of the paste void filling extent, through experimental data concerning Mortar #2

Since Mortar #1 and Mortar #2 are produced with the same raw materials, the identified material constants given in Eqs. (5.25) are not only valid for Mortar #1, but they must also hold for Mortar #2, i.e. the strain evolutions measured during creep testing of Mortar #2 must be predictable, and this is checked next. To this end, the initial value of the effective water-to-cement mass fraction of the cement paste matrix follows from specialization of Eq. (5.3)

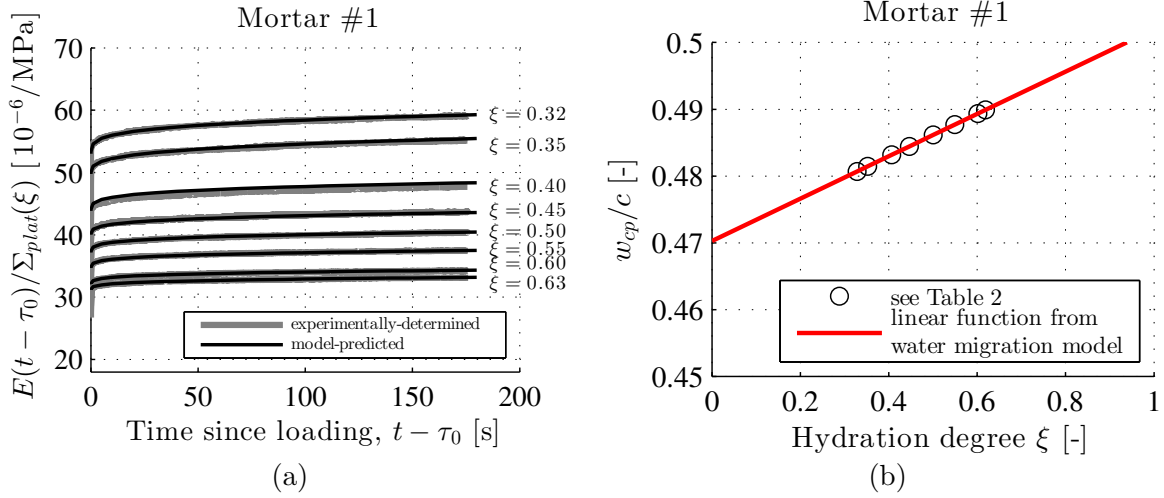


Figure 5.8: Application of the water migration model according to Eq. (5.10) to Mortar #1, with a mix-related (nominal) composition given through $w/c = 0.50$ and $a/c = 3.0$, as well as water uptake capacity of quartz and void water-filling extent according to Eq. (5.25): (a) Comparison of experimentally-determined and model-predicted plateau stress-normalized strains, at the hydration degrees given in Eq. (5.19) and the corresponding load plateaus according to Eq. (5.20); (b) evolution of the effective water-to-cement mass fraction of the cement paste matrix, as a function of degree of hydration; for the complete set of material properties of cement paste, see Table 5.3

for $w_a(0)/a$ from (5.25) and for the mix-related water-to-cement and quartz-to-cement mass ratios $w/c = 0.42$ and $a/c = 2.7$ as:

$$\frac{w_{cp}(0)}{c} = 0.3933 \quad (5.29)$$

This is significantly smaller than the mix-related water-to-cement mass ratio $w/c = 0.42$. The evolution of the effective water-to-cement mass fraction of the cement paste matrix follows from specialization of Eq. (5.10) for (5.25), $w/c = 0.42$, and $a/c = 2.7$ as

$$\frac{w_{cp}(\xi)}{c} = 0.3933 + 0.0317 \xi \quad (5.30)$$

see also Fig. 5.9 (b). The actual volume fractions of the cement paste matrix and of quartz follow from specialization of Eq. (5.11) for Eq. (5.29), $w/c = 0.42$, and $a/c = 2.7$ as

$$f_{cp} = 0.4107, \quad f_{agg} = 0.5893. \quad (5.31)$$

Viscoelastic properties of the cement paste matrix – valid for effective water-to-cement mass fractions from Eq. (5.30), evaluated for all hydration degrees of interest given in Eq. (5.19) – are quantified by means of interpolation; as described in the previous subsection, see also Fig. 5.4.

Model-predicted creep functions for Mortar #2 agree well with measured creep functions, as quantified by prediction error $\mathcal{E} = 2.90 \times 10^{-7} \text{ MPa}^{-1}$ (see Table 5.2) evaluated according to Eq. (5.24), see also Fig. 5.9 (a). This underlines not only the satisfactory predictive capabilities of the developed water migration model, see Eq. (5.10), but also the significance of the identified values of the water uptake capacity of quartz and of the water filling extent of shrinkage-induced voids, see Eqs. (5.25).

Table 5.3: Input quantities for creep homogenization of Mortar #1 with mix-related (nominal) composition quantified through $w/c = 0.50$ and $a/c = 3.0$: effective water-to-cement mass fractions of the cement paste matrix according to Eqs. (5.10) and (5.25), as well as corresponding viscoelastic properties of the cement paste matrix found by means of interpolation (see Fig. 5.4), for hydration degrees listed in Eq. (5.19)

ξ [-]	$w_{cp}(\xi)/c$ [-]	E_{cp} [GPa]	ν_{cp} [-]	$E_{c,cp}$ [GPa]	β_{cp} [-]
0.32	0.480	6.529	0.205	9.218	0.269
0.35	0.481	7.041	0.206	8.562	0.267
0.40	0.483	8.223	0.210	13.220	0.242
0.45	0.484	9.172	0.214	15.775	0.228
0.50	0.486	10.236	0.217	19.270	0.219
0.55	0.487	11.274	0.221	23.640	0.210
0.60	0.489	12.442	0.225	29.012	0.209
0.63	0.490	12.843	0.226	30.774	0.208

Table 5.4: Input quantities for creep homogenization of Mortar #2 with mix-related (nominal) composition quantified through $w/c = 0.42$ and $a/c = 2.7$: effective water-to-cement mass fractions of the cement paste matrix according to Eqs. (5.10) and (5.25), as well as corresponding viscoelastic properties of the cement paste matrix found by means of interpolation (see Fig. 5.4), for hydration degrees listed in Eq. (5.19)

ξ [-]	$w_{cp}(\xi)/c$ [-]	E_{cp} [GPa]	ν_{cp} [-]	$E_{c,cp}$ [GPa]	β_{cp} [-]
0.32	0.403	8.623	0.211	9.719	0.322
0.35	0.404	9.864	0.215	11.857	0.290
0.40	0.405	10.693	0.218	14.872	0.270
0.45	0.407	12.175	0.222	19.312	0.260
0.50	0.409	13.189	0.225	23.055	0.244
0.55	0.410	14.369	0.229	30.780	0.222
0.60	0.412	15.417	0.232	38.460	0.196
0.62	0.413	16.146	0.234	44.927	0.192

5.4.5 Identification of water uptake capacity of "Pannonia Kies" aggregates and of entrapped air content, from experimental data concerning Concrete #1

When it comes to model prediction of the creep strain evolutions measured in three-minutes creep tests on Concrete #1, it is important to emphasize that both concretes were produced with quartz gravel of type "Pannonia Kies", i.e. the corresponding water-uptake capacity is unknown and needs to be identified. Notably, this is not enough for obtaining a satisfactory agreement between model-predicted and measured creep functions, because the model-predicted creep functions turn out to underestimate the measured creep functions, particularly because the elastic stiffness is overestimated. In order to improve the situation, we consider that air was mixed into concrete during production. Since all eight considered creep tests were carried out on the *same* specimen, just one entrapped air content, as appearing in Eq. (5.13) needs to be identified.

Similar to the identification process described for Mortar #1, the water uptake capacity

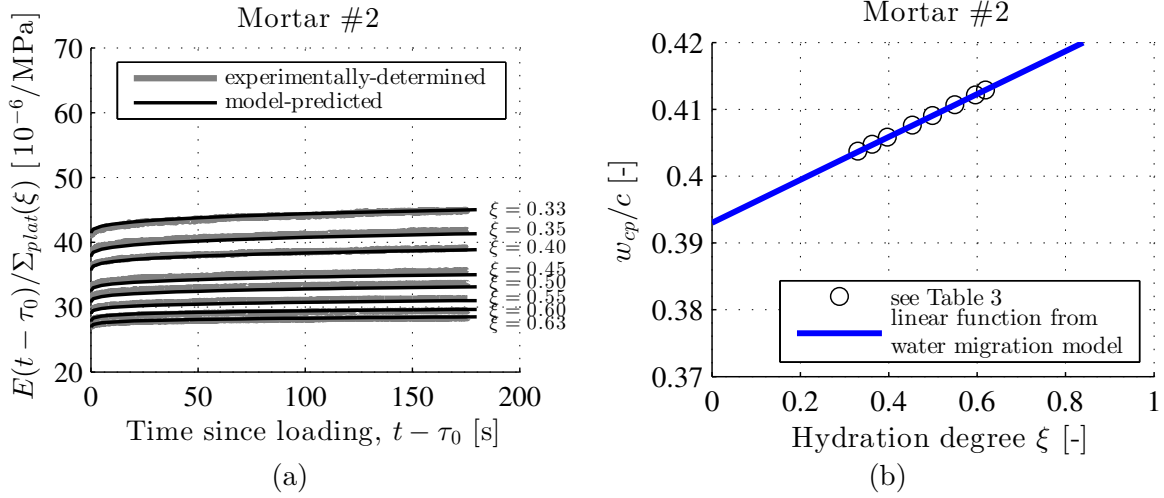


Figure 5.9: Application of the water migration model according to Eq. (5.10) to Mortar #2, with a mix-related (nominal) composition given through $w/c = 0.42$ and $a/c = 2.7$, as well as water uptake capacity of quartz and void water-filling extent according to Eq. (5.25): (a) Comparison of experimentally-determined and model-predicted plateau stress-normalized strains, at the hydration degrees given in Eq. (5.19) and the corresponding load plateaus according to Eq. (5.20); (b) evolution of effective water-to-cement mass fraction of the cement paste matrix, as a function of degree of hydration; for the complete set of material properties of cement paste, see Table 5.4

of “Pannonia Kies” quartz and the entrapped air content are identified from the following search intervals:

$$\begin{aligned} w_a(0)/a &\in [0.000, 0.0001, 0.0002, \dots, 0.0199, 0.0200] \\ f_{air} &\in [0.000, 0.001, 0.002, \dots, 0.049, 0.050] \end{aligned} \quad (5.32)$$

The identified void filling extent α according to Eq. (5.25), in turn, is treated as being also applicable to both concretes.

Accordingly, for all data pairs $[w_a/a(0), f_{air}]$ composed from the values given in Eq. (5.32), the micromechanics model of Eqs. (5.14)–(5.18), together with Eqs. (5.3), (5.10), and (5.11) evaluated for $\alpha = 0.603$, as well as for $w/c = 0.50$ and $a/c = 3.0$, see Table 5.1, with the interpolation scheme of Fig. 5.4 and with the loading history of Fig. 5.6 entering Eq. (5.22), is used to predict the creep functions arising from the eight creep tests conducted on Concrete #1, as seen in Fig. 5.7 (c). Model-predicted creep functions are compared to measured creep functions, and model prediction errors are quantified according to Eq. (5.24). The smallest prediction error amounts to $\mathcal{E} = 1.5 \times 10^{-7} \text{ MPa}^{-1}$ (see Table 5.2), and the corresponding values of the water uptake capacity and of the air volume fraction read as

$$\frac{w_a(0)}{a} = 0.0089 \quad f_{air} = 0.026 \quad (5.33)$$

see Fig. 5.10 (a) for the comparison of measured and model-predicted creep functions. The identified water uptake capacity given in (5.33) implies that 1 kilogram of “Pannonia Kies” quartz takes up 8.9 gram of water during mixing of the raw materials. The corresponding initial value of the effective water-to-cement mass fraction of the cement paste matrix follows

from specialization of Eq. (5.3) for $w_a(0)/a$ from (5.33) and for the mix-related water-to-cement and quartz-to-cement mass ratios $w/c = 0.50$ and $a/c = 3.0$ as:

$$\frac{w_{cp}(0)}{c} = 0.4733 \quad (5.34)$$

This is significantly smaller than the mix-related water-to-cement mass ratio $w/c = 0.50$. The evolution of the effective water-to-cement mass fraction of the cement paste matrix follows from specialization of Eq. (5.10) for α from (5.25), for $w_a(0)/a$ from (5.33), for $w/c = 0.50$, and for $a/c = 3.0$, as

$$\frac{w_{cp}(\xi)}{c} = 0.4733 + 0.0317 \xi \quad (5.35)$$

see also Fig. 5.10 (b). Finally, the actual volume fractions of the cement paste matrix and of quartz follow from Eqs. (5.33), (5.34), $w/c = 0.50$, $a/c = 3.0$, (5.11), and (5.13) as:

$$f_{cp} = 0.4004, \quad f_{agg} = 0.5736. \quad (5.36)$$

The satisfactory agreement between between model-predicted and measured creep functions further corroborates the developed water migration model, see Eq. (5.10), and the void water-filling extent α given in Eq. (5.25).

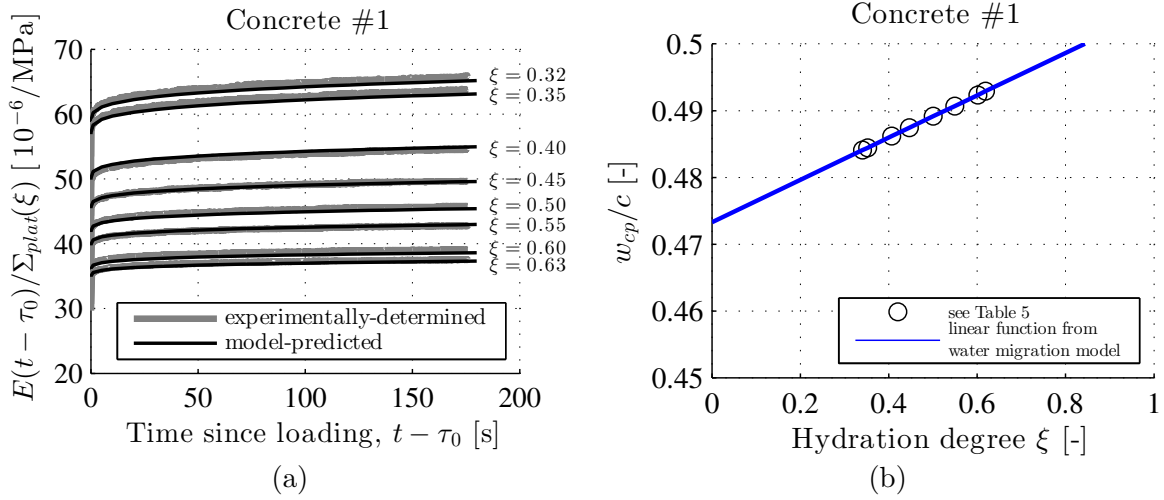


Figure 5.10: Application of the water migration model according to Eq. (5.10) to Concrete #1, with a mix-related (nominal) composition given through $w/c = 0.50$ and $a/c = 3.0$, with void water-filling extent according to Eqs. (5.25), as well as with water uptake capacity of quartz and entrapped air volume fraction according to Eq. (5.33): (a) Comparison of experimentally-determined and model-predicted plateau stress-normalized strains, at the hydration degrees given in Eq. (5.19) and the corresponding load plateaus according to Eq. (5.20); (b) evolution of effective water-to-cement mass fraction of the cement paste matrix, as a function of degree of hydration; for the complete set of material properties of cement paste, see Table 5.5

5.4.6 Confirmation of water uptake capacity of "Pannonia Kies" aggregates, through experimental data concerning Concrete #2

Since Concretes #1 and #2 were produced with the same quartz gravel, the water uptake capacity is already known, see Eq. (5.33). Also, the void water-filling ratio α is already

Table 5.5: Input quantities for creep homogenization of Concrete #1 with mix-related (nominal) composition quantified through $w/c = 0.50$ and $a/c = 3.0$: effective water-to-cement mass fractions of the cement paste matrix according to Eqs. (5.10), with void water-filling extent according to Eq. (5.25), and with water uptake capacity of quartz and entrapped air volume fraction according to Eq. (5.33), as well as corresponding viscoelastic properties of the cement paste matrix found by means of interpolation (see Fig. 5.4), for hydration degrees listed in Eq. (5.19)

ξ [-]	$w_{cp}(\xi)/c$ [-]	E_{cp} [GPa]	ν_{cp} [-]	$E_{c,cp}$ [GPa]	β_{cp} [-]
0.33	0.484	6.720	0.205	9.096	0.262
0.35	0.4845	6.927	0.206	9.531	0.257
0.40	0.486	7.966	0.210	12.332	0.244
0.44	0.487	8.900	0.213	15.582	0.240
0.50	0.489	9.940	0.216	18.548	0.232
0.55	0.490	10.884	0.219	21.911	0.227
0.60	0.492	12.115	0.224	27.777	0.215
0.63	0.493	12.569	0.225	30.116	0.218

identified, see Eq. (5.25). However, Concrete #2 was tested on a specific specimen, and the related air volume fraction is to be identified. By analogy to the previously described identification processes, the entrapped air volume fraction is found as

$$f_{air} = 0.027 \quad (5.37)$$

The initial value of the effective water-to-cement mass fraction of the cement paste matrix follows from specialization of Eq. (5.3) for $w_a(0)/a$ from (5.33) and for the mix-related water-to-cement and quartz-to-cement mass ratios $w/c = 0.42$ and $a/c = 2.7$ as:

$$\frac{w_{cp}(0)}{c} = 0.3960 \quad (5.38)$$

This is significantly smaller than the mix-related water-to-cement mass ratio $w/c = 0.42$. The evolution of the effective water-to-cement mass fraction of the cement paste matrix follows from specialization of Eq. (5.10) for α from (5.25), for $w_a(0)/a$ from (5.33), for $w/c = 0.42$, and for $a/c = 2.7$, as

$$\frac{w_{cp}(\xi)}{c} = 0.3960 + 0.0317 \xi \quad (5.39)$$

see also Fig. 5.11 (b). Finally, the actual volume fractions of the cement paste matrix and of quartz follow from Eqs. (5.33), (5.38), $w/c = 0.42$, $a/c = 2.7$, (5.11), and (5.13) as:

$$f_{cp} = 0.4005, \quad f_{agg} = 0.5725. \quad (5.40)$$

The satisfactory agreement between model-predicted and measured creep functions, as quantified by prediction error $\mathcal{E} = 1.30 \times 10^{-7} \text{ MPa}^{-1}$ (see Table 5.2) further corroborates the developed water migration model, see Eq. (5.10), evaluated according to Eq. (5.24) the void water-filling extent α given in Eq. (5.25), and the water uptake capacity $w_a(0)/a$ given in Eqs. (5.33).

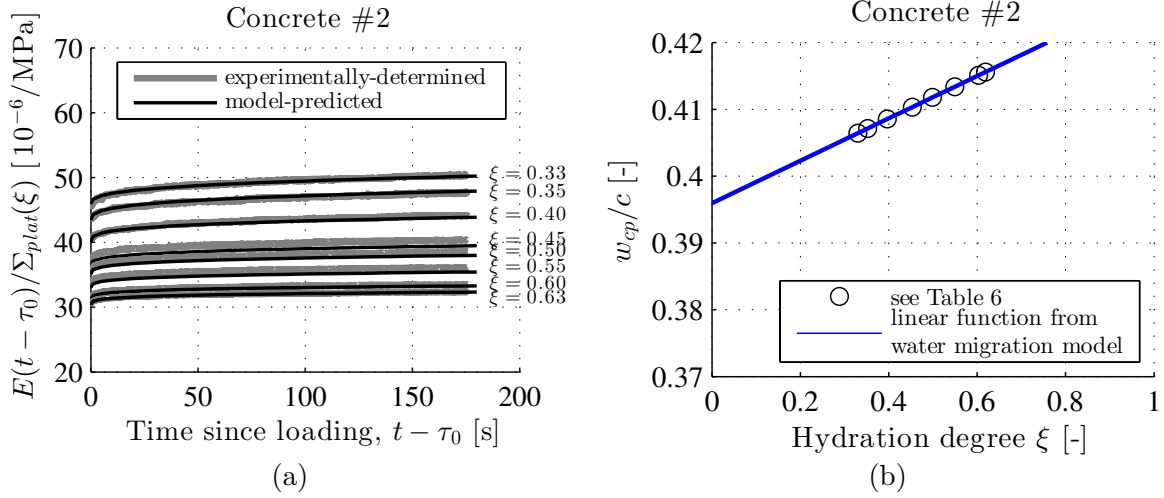


Figure 5.11: Application of the water migration model according to Eq. (5.10) to Concrete #2, with a mix-related (nominal) composition given through $w/c = 0.42$ and $a/c = 2.7$, with void water-filling extent according to Eq. (5.25), with water uptake capacity of quartz according to Eqs. (5.33) and with entrapped air volume fraction according to Eq. (5.37): (a) Comparison of experimentally-determined and model-predicted plateau stress-normalized strains, at the hydration degrees given in Eq. (5.19) and the corresponding load plateaus according to Eq. (5.20); (b) evolution of effective water-to-cement mass fraction of the cement paste matrix, as a function of degree of hydration; for the complete set of material properties of cement paste, see Table 5.6

5.5 Conclusions

We here presented an extension of the classical Powers hydration model with respect to internal curing, and checked the relevance of the latter through micromechanical upscaling of effective water-to-cement mass ratio-dependent cement paste creep functions, up to the levels of mortar/concrete. Remarkably, internal curing can be considered in terms of only two additional quantities: an aggregate-specific uptake capacity, and a cement-paste specific void filling extent. Identifying these quantities herein for two types of oven-dried quartz aggregates, and for one type of cement, allowed for satisfactory prediction of numerous ultrashort-term creep tests on two mortars and two concretes, see Figs. 5.8 to 5.11. Such creep tests directly deliver the hydration-dependent (non-aging) creep properties, also valid for medium-term creep tests on very old pastes, see (Irfan-ul-Hassan et al., 2016). Neglecting internal curing effects, i.e. initial water uptake through the aggregates followed by "back-soaking" of this water from the aggregates domain to that of the maturing cement paste, would clearly *not* allow for satisfactory micromechanical prediction of the creep properties at the mortar and concrete level, as is quantified in Table 5.2 and illustrated in Fig. 5.12, showing predictions based on $w_a(0)/a = \alpha = f_{air} = 0$, while keeping all other input variables as defined earlier in this paper. Obviously, the creep response predicted by the micromechanical model of Fig. 5.2 would be too soft under these conditions. It is also illustrative to quantify the degree of hydration when the "back-suction" of water from aggregates to the cement paste is finished, simply because no water is left any more in the aggregates. To this end, $w_{cp}(\xi)/c$ in Eq. (5.10) is set equal to

Table 5.6: Input quantities for creep homogenization of Concrete #2 with mix-related (nominal) composition quantified through $w/c = 0.42$ and $a/c = 2.7$: effective water-to-cement mass fractions of the cement paste matrix according to Eq. (5.10), with void water-filling extent according to Eq. (5.25), with water uptake capacity of quartz according to Eqs. (5.33), and with entrapped air volume fraction according to Eq. (5.37), as well as corresponding viscoelastic properties of the cement paste matrix found by means of interpolation (see Fig. 5.4), for hydration degrees listed in Eq. (5.19)

ξ [-]	$w_{cp}(\xi)/c$ [-]	E_{cp} [GPa]	ν_{cp} [-]	$E_{c,cp}$ [GPa]	β_{cp} [-]
0.33	0.406	8.519	0.211	9.597	0.312
0.35	0.407	9.268	0.213	10.701	0.286
0.40	0.408	10.477	0.217	14.669	0.265
0.45	0.410	11.921	0.221	19.020	0.255
0.50	0.411	12.791	0.224	22.434	0.238
0.55	0.413	13.940	0.228	29.692	0.218
0.60	0.415	15.153	0.231	38.407	0.195
0.62	0.415	15.672	0.233	43.084	0.191

w/c , and the resulting expression is solved for hydration degree ξ . This delivers

$$\xi^* = \frac{\frac{w_a(0)}{a} (a/c) \left\{ 20 + 63 \left[w/c - \frac{w_a(0)}{a} (a/c) \right] \right\}}{\alpha \left\{ 1.051 + 3.31 \left[w/c - \frac{w_a(0)}{a} (a/c) \right] \right\}} \quad (5.41)$$

Notably, the creep tests which were analyzed herein refer to hydration degrees smaller than ξ^* , see Figs. 5.8 (b), 5.9 (b), 5.10 (b), and 5.11 (b).

The method described herein, showing how to integrate internal curing events into micromechanical modeling of concrete, in particular concerning creep, can be straightforwardly extended to aging creep behavior, based on earlier contributions such as those of Scheiner and Hellmich (2009) or Sanahuja (2013a).

Another obvious extension concerns the deeper reasons for the dependencies of the creep properties of cement paste, on the water-to-cement mass ratio as depicted in Fig. 5.4, which may be deciphered through micromechanical resolution down to the level of the hydrates (Königsberger et al., 2016b), or even, down to the level of lubricating water layers between calcium silicate sheets, (Pellenq et al., 2009; Sanahuja and Dormieux, 2010; Shahidi et al., 2014, 2015a; Vandamme et al., 2015; Shahidi et al., 2015b).

Acknowledgment

We cordially thank for valuable help of the laboratory staff of the Institute of Mechanics of Materials and Structures, TU Wien – Vienna University of Technology. The first author also wishes to thank the Higher Education Commission (HEC) Pakistan and the University of Engineering and Technology, Lahore, Pakistan, for their support.

Appendix A: Analytical expressions facilitating upscaling in LC space

Upscaling of the creep behavior, up to the larger scales of mortar or concrete, is performed in the LC space, according to the analytical formulae described next. Thereby, we consider that an isotropic fourth-order tensor, \mathbb{G} , can be decomposed into a volumetric part and a deviatoric part as $\mathbb{G} = G^{vol}\mathbb{I}^{vol} + G^{dev}\mathbb{I}^{dev}$, where G^{vol} and G^{dev} , respectively, are the (scalar) volumetric and deviatoric components of the tensor. \mathbb{I}^{vol} and \mathbb{I}^{dev} are the volumetric and deviatoric parts of the fourth-order identity tensor \mathbb{I} , defined as $I_{ijkl} = 1/2(\delta_{ik}\delta_{jl} + \delta_{il}\delta_{jk})$, $\mathbb{I}^{vol} = 1/3(\mathbf{1} \otimes \mathbf{1})$, and $\mathbb{I}^{dev} = \mathbb{I} - \mathbb{I}^{vol}$, respectively, whereby $\mathbf{1}$ denotes the second-order identity tensor with components equal to the Kronecker delta δ_{ij} , namely $\delta_{ij} = 1$ for $i = j$, and 0 otherwise. They satisfy $\mathbb{I}^{vol} : \mathbb{I}^{vol} = \mathbb{I}^{vol}$, $\mathbb{I}^{dev} : \mathbb{I}^{dev} = \mathbb{I}^{dev}$, and $\mathbb{I}^{vol} : \mathbb{I}^{dev} = \mathbb{I}^{dev} : \mathbb{I}^{vol} = 0$.

We start our collection of analytical formulae with the LC-transformed Hill tensors for spherical inclusions embedded in an infinite cement matrix with quasi-elastic “stiffness” \mathbb{R}_{cp}^* , occurring in concentration and stiffness expressions of (5.14). The Hill tensor reads as

$$\mathbb{P}_{sph}^*(p) = \mathbb{S}_{sph}^*(p) : [\mathbb{R}_{cp}^*(p)]^{-1} \quad (5.42)$$

In Eq. (4.37), \mathbb{S}_{sph}^* denotes the LC-transformed Eshelby tensor of a spherical inclusion embedded in an infinite cement paste matrix. The LC-transformed Eshelby tensor \mathbb{S}_{sph}^* is isotropic, and its volumetric and deviatoric components read as (Zaoui, 2002; Hellmich et al., 2004)

$$S_{sph}^{*,vol}(p) = \frac{3k_{cp}^*(p)}{3k_{cp}^*(p) + 4\mu_{cp}^*(p)}, \quad S_{sph}^{*,dev}(p) = \frac{6}{5} \frac{k_{cp}^*(p) + 2\mu_{cp}^*(p)}{3k_{cp}^*(p) + 4\mu_{cp}^*(p)}. \quad (5.43)$$

Next, we discuss the expressions for the homogenized quasi-elastic “stiffness” tensor \mathbb{R}_{hom}^* . As for mortar or concrete, insertion of the LC-transformed Eshelby tensor expressions (5.43) into (5.42), and further insertion of the obtained Hill tensor, together with the vanishing quasi-elastic “stiffnesses” of air and the available quasi-elastic “stiffness” of quartz (5.16), into the expression for the quasi-elastic “stiffness” of the homogenized mortar or concrete (5.14), yields scalar expressions for the LC-transformed bulk and shear moduli, reading as

$$\begin{aligned} k_{hom}^*(p) &= [f_{cp}k_{cp}^*(p) + f_{agg}A_{\infty,agg}^{*,vol}(p)] \left[f_{cp}\mathbb{I} + f_{agg}A_{\infty,agg}^{*,vol}(p) + f_{air}A_{\infty,air}^{*,vol}(p) \right]^{-1}, \\ \mu_{hom}^*(p) &= [f_{cp}\mu_{cp}^*(p) + f_{agg}\mu_{agg}A_{\infty,agg}^{*,dev}(p)] \left[f_{cp}\mathbb{I} + f_{agg}A_{\infty,agg}^{*,dev}(p) + f_{air}A_{\infty,air}^{*,dev}(p) \right]^{-1}, \end{aligned} \quad (5.44)$$

with $A_{\infty,agg}^{*,vol}$, $A_{\infty,agg}^{*,dev}$, $A_{\infty,air}^{*,vol}$, and $A_{\infty,air}^{*,dev}$ denoting the LC-transformed volumetric and deviatoric components of the Eshelby problem-related strain concentration tensors for quartz aggregates and air. As for air, the volumetric and deviatoric components of the strain concentration tensor can be written as

$$\begin{aligned} A_{\infty,air}^{*,vol}(p) &= \left[1 - S_{sph}^{*,vol}(p) \right]^{-1}, \\ A_{\infty,air}^{*,dev}(p) &= \left[1 - S_{sph}^{*,dev}(p) \right]^{-1}, \end{aligned} \quad (5.45)$$

As for quartz, they read as

$$\begin{aligned} A_{\infty,agg}^{*,vol}(p) &= \left[1 + S_{sph}^{*,vol}(p) \frac{k_{agg} - k_{cp}^*(p)}{k_{cp}^*(p)} \right]^{-1}, \\ A_{\infty,agg}^{*,dev}(p) &= \left[1 + S_{sph}^{*,dev}(p) \frac{\mu_{agg} - \mu_{cp}^*(p)}{\mu_{cp}^*(p)} \right]^{-1}. \end{aligned} \quad (5.46)$$

Appendix B: Nomenclature

Symbols:

$A_{\infty,agg}^{*,vol}$	LC-transformed volumetric component of Eshelby problem-related strain concentration tensor of aggregates
$A_{\infty,agg}^{*,dev}$	LC-transformed deviatoric component of Eshelby problem-related strain concentration tensor of aggregates
$A_{\infty,air}^{*,vol}$	LC-transformed volumetric component of Eshelby problem-related strain concentration tensor of air
$A_{\infty,air}^{*,dev}$	LC-transformed deviatoric component of Eshelby problem-related strain concentration tensor of air
a	mass of aggregates
a/c	aggregate-to-cement mass ratio
α	water filling extent of shrinkage induced voids in cement paste
β_{cp}	power-law creep exponent for cement paste
c	mass of cement paste
d	a material constant equal to $w_{cp}(0)/c$
d_{max}	maximum diameter of aggregates
δ_{ij}	Kronecker delta
E	macroscopic uniaxial strain
\mathbf{E}	macroscopic strain tensor
E^{exp}	experimentally-determined macroscopic uniaxial strain
E^{pred}	model-predicted macroscopic uniaxial strain
E_{cp}	Young's elastic modulus of cement paste
$E_{c,cp}$	Young's creep modulus of cement paste
\mathcal{E}	prediction error
F_{plat}	plateau force
f_{cp}	volume fraction of the cement paste
f_{agg}	volume fraction of the aggregates
f_{air}	volume fraction of the air
f_{agg}^{no-air}	volume fraction of aggregates without entrapped air
f_{cp}^{no-air}	volume fraction of cement paste without entrapped air
f_{void}^{cp}	cement paste-related volume fraction of voids
\mathbb{G}	auxiliary isotropic fourth-order tensor
G^{vol}, G^{dev}	volumetric and deviatoric components of \mathbb{G}
\mathbb{I}	fourth-order identity tensor
$\mathbf{1}$	second-order identity tensor
$\mathbb{I}^{vol}, \mathbb{I}^{dev}$	volumetric and deviatoric parts of \mathbb{I}
\mathbb{J}_{hom}	homogenized fourth-order tensorial creep function

k	a material constant equal to rate of w_{cp}/c
k_{agg}	bulk modulus of aggregates
k_{air}	bulk modulus of air
k_{cp}	bulk modulus of cement paste
k_{hom}	bulk modulus of mortar or concrete
LC	Laplace-Carson
μ_{agg}	shear modulus of aggregates
μ_{air}	shear modulus of air
μ_{cp}	shear modulus of cement paste
μ_{hom}	shear modulus of mortar or concrete
ν_{cp}	Poisson's ratio of cement paste
p	complex variable in the LC domain
\mathbb{P}_{sph}^*	LC-transformed Hill tensor of spherical inclusions, embedded in an infinite cement paste matrix
\mathbb{R}_{agg}^*	LC-transformed fourth-order relaxation tensor function of aggregates
\mathbb{R}_{air}^*	LC-transformed fourth-order relaxation tensor function of air
\mathbb{R}_{cp}^*	LC-transformed fourth-order relaxation tensor function of cement paste
\mathbb{R}_{hom}^*	LC-transformed fourth-order relaxation tensor function of mortar or concrete
ρ_{agg}	mass density of aggregates
ρ_{clin}	mass density of cement clinker
ρ_{H_2O}	mass density of water
ρ_{hyd}	mass density of hydrates
Σ	macroscopic stress tensor
Σ_{plat}	plateau stress
\mathbb{S}_{sph}^*	LC-transformed Eshelby tensor of spherical inclusion, embedded in an infinite cement paste matrix
$S_{sph}^{*,vol}, S_{sph}^{*,dev}$	volumetric and deviatoric components of \mathbb{S}_{sph}^*
t	chronological time
τ	time instant during creep test
τ_0	time instant at start of the loading ramp
t_{ref}	reference time, $t_{ref} = 1 \text{ d} = 86\,400 \text{ s}$
V_c	volume of cement
V_{cp}	volume of cement paste
V_{void}	volume of voids
V_w	volume of water
w	total water mass
w_a	water absorbed into the aggregates
$w_a(0)/a$	initial water-to-aggregate mass ratio
w_{cp}	water residing inside the cement paste
w_{cp}/c	effective water-to-cement mass ratio
$w_{cp}(0)/c$	initial value of the effective water-to-cement mass ratio
w/c	(nominal) water-to-cement mass ratio
ξ	hydration degree
ξ^*	hydration degree at which all aggregates-absorbed water is soaked to cement paste
<i>Operators:</i>	
$(.)^*$	Laplace-Carson transform of quantity $(.)$
\cdot	inner product

$\hat{(\cdot)}$	Laplace transform of quantity (\cdot)
\times	multiplication
$:$	second-order tensor contraction
$\Gamma(\cdot)$	gamma function of real quantity (\cdot)
$\dot{(\cdot)}$	time derivative of quantity (\cdot)

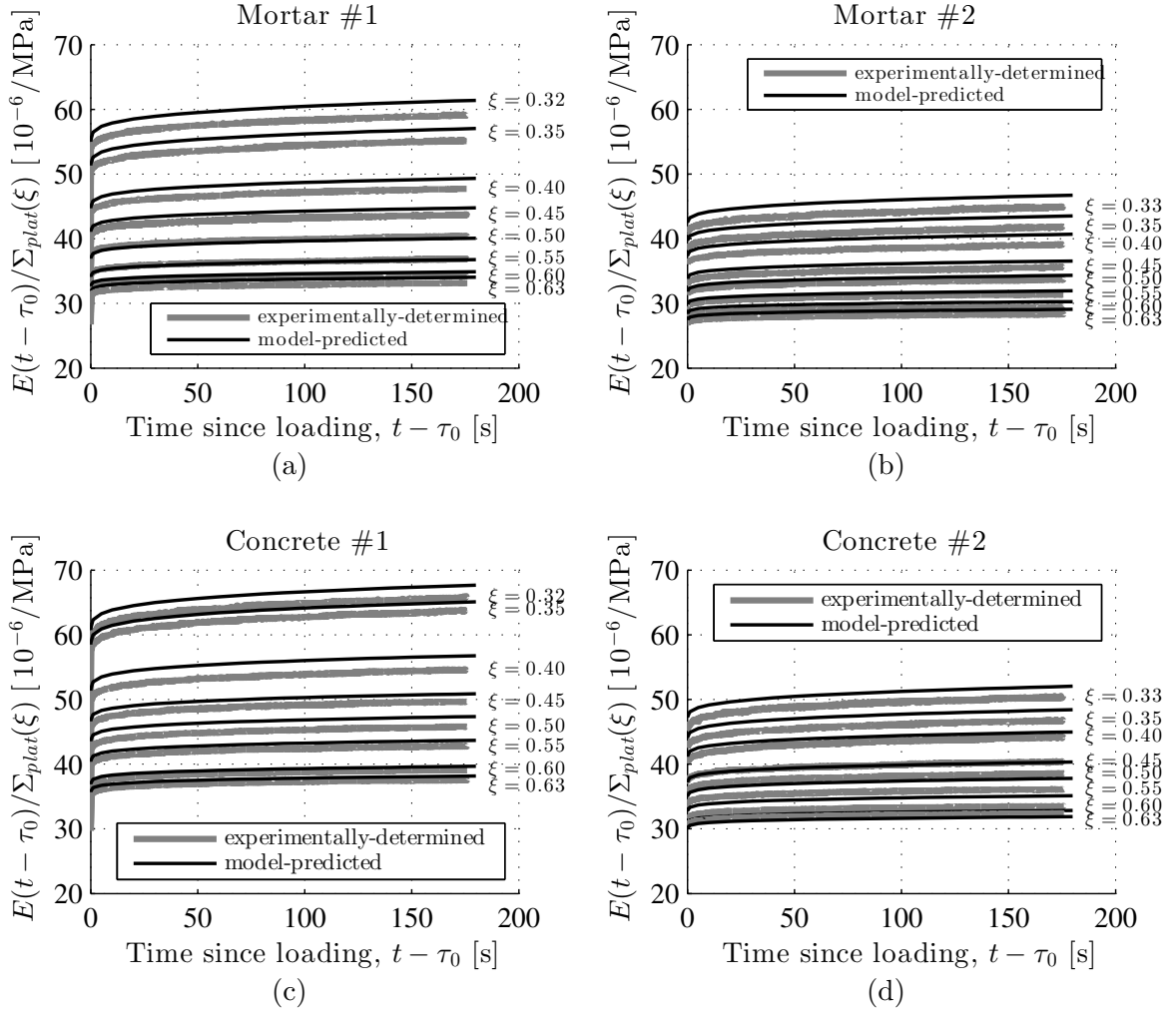


Figure 5.12: Comparison of experimentally-determined and model-predicted plateau stress-normalized strains, using nominal compositions as input, see Table 5.1, at the hydration degrees given in Eq. (5.19) and the corresponding load plateaus according to Eq. (5.20); For (a) Mortar #1, (b) Mortar #2, (c) Concrete #1, and (d) Concrete #2: Model predicted strains overestimate the experimentally measured strains; see also Table 5.2

Chapter 6

Densification of C-S-H is mainly driven by available precipitation space, as quantified through an analytical cement hydration model based on NMR data

Published in: *Cement and Concrete Research*, 88:170–183, 2016

The final publication is available at:

<http://ascelibrary.org/doi/abs/10.1061/%28ASCE%29EM.1943-7889.0001169>

<http://www.sciencedirect.com/science/article/pii/S0008884616303374>

Authored by: Markus Königsberger, Christian Hellmich, and Bernhard Pichler

Abstract: NMR relaxometry (Muller et al., 2012, 2013) quantifies the mass fractions of differently bound water in cement paste, as functions of hydration degree and water-to-cement ratio. We here reduce these findings to a single explanation: the density of C-S-H gel is solely governed by the specific precipitation space, across three “hydration regimes”: In regime I, solid C-S-H platelets (without gel porosity) precipitate on clinker surfaces. In regime II, C-S-H starts to include gel porosity. The forming gel densifies linearly with decreasing precipitation space. Thereby, regime III starts once the C-S-H gel has completely filled the capillary porosity. These findings allow for developing an analytical hydration model. It provides expressions for C-S-H gel densification and for the evolution of the volume fractions of clinker, of solid hydrates, as well as of the gel and capillary porosities, as functions of the water-to-cement ratio and the hydration degree; consistently representing published experimental data.

Contribution: Bernhard Pichler and Christian Hellmich set up the overall research strategy, supervised the research progress, checked key results, and supported the documentation process. Markus Königsberger developed the mathematical model, performed all computations, studied the sensitivity of key results, and documented research results.

Keywords: cement paste, calcium-silicate-hydrate (C-S-H), hydration, modeling, phase volume fractions

6.1 Introduction

After water, cement is the most frequently used material on the planet (Wray and Scrivener, 2012). Given the significant amounts of carbon dioxide released during cement production, great efforts are nowadays made to minimize the cement content in mortars and concretes, while preserving their mechanical properties. This calls specifically for careful analysis of cement paste, the binder of all cementitious materials – from the atomistic scale up to the homogenized material scale.

In recent years, the development of several multiscale models allowed for describing the microstructural evolution of hydrating cement paste, see e.g. (Bentz, 2000; Van Breugel, 1995b,a; Bishnoi and Scrivener, 2009; Thomas et al., 2011), and for microstructure-based prediction of early-age mechanical properties of cement pastes, including stiffness (Bernard et al., 2003b; Constantinides and Ulm, 2004; Sanahuja et al., 2007; Stefan et al., 2010; Bary, 2011; Venkovic et al., 2013), compressive strength (Pichler et al., 2009; Pichler and Hellmich, 2011), and creep (Scheiner and Hellmich, 2009; Sanahuja and Dormieux, 2010; Sanahuja, 2013b), to name just a few. Thereby, quantitative information on the hydration-driven evolution of material microstructures concerns in particular the volume fractions of the individual material constituents (i.e. those of “cement”, “water”, and “hydrates”) per volume of cement paste. Such volume fractions are customarily estimated by means of Powers’ 1946/1957 hydration model (Powers and Brownyard, 1947; Powers, 1958), which was developed on the basis of water vapor sorption isotherms. Powers’ model provides access to the volumes of cement, water, and hydrates for any composition in terms of the initial water-to-cement mass ratio w/c , and for any maturity in terms of the hydration degree ξ ; see also (Hansen, 1986; Acker, 2001) for compact descriptions. Most importantly, all phase volumes are *linear* functions of the hydration degree, and the “hydrate phase” includes not only solid matter [calcium-silicate-hydrates, calcium hydroxide, alumina-ferric oxide-monosulfate – AFm, as inferred from nitrogen sorption experiments (Jennings and Tennis, 1994)], but also water-filled gel pores. The linearity of the hydration model stems from the assumption that the density of all formed hydrates is *constant*. This constant hydration density, together with the constant chemical composition of the hydrates’ elementary components, would imply a constant gel porosity of all the hydrates.

This viewpoint was considerably challenged by recent nuclear magnetic resonance (NMR) measurements of Muller et al. (2012, 2013), which provide – for the first time in cement research – access to the relative amounts of water in different confinement states, and this allows for distinguishing water chemically bound in solids, such as in calcium-silicate-hydrates (weak chemical bonding) or in other types of hydrates (strong chemical bonding), from liquid water filling capillary pores (weak confinement) and gel pores (strong confinement). It turns out that much of the water that according to classical hydration models, would fill capillary pores, is actually residing as gel water *within* the porous calcium-silicate-hydrates (C-S-H) (Muller et al., 2012, 2013). This indicates evolving (rather than constant) porosity of the C-S-H gel, and calls for careful re-thinking of the assumptions underlying Powers’ hydration model.

Such re-thinking process is the topic of the present contribution: On the one hand, Powers’ assumption of constant hydrate density needs to be replaced by a more appropriate statement; while on the other hand, the appealing simplicity of Powers’ linear relations should be kept to the maximum degree possible. Therefore, we here develop new analytical mathematical expressions, comprising an only linear dependency of the hydrate mass density on a new state variable describing the hydration degree- and water-to-cement ratio-dependent microstructure

of cement paste: this new variable is called specific precipitation space. The new mathematical model, based on a minimum of involved physical quantities with very simple mutual relations, will be shown to be able to account for a collection of recent experimental data from NMR concerning (i) the density of C-S-H gel as it evolves with ongoing hydration; and (ii) the simultaneous evolution of phase volume fractions in white cement pastes with different initial water-to-cement ratios. The former mathematical expressions are referred to as “C-S-H densification model” and the latter as “phase volume evolution model”. Together, they form a new analytical hydration model for cement pastes which are chemically similar to the white cement pastes tested by Muller et al. (2013). Like Powers’ model, the new phase volume evolution model will provide access to the volumes of cement, water, and hydrates; for any initial water-to-cement mass ratio w/c , and for any maturity in terms of the hydration degree ξ .

The paper is structured as follows: Based on the NMR experiments of Muller et al. (2012, 2013); Muller (2014), the C-S-H gel density is shown to vary with time and with the initial water-to-cement-mass ratio (Sections 6.2.1 and 6.2.2). In order to explain this variation, we introduce a new quantity called specific precipitation space, defined as the volume ratio of water-filled (gel and capillary) pores over the sum of these pore spaces and the solid C-S-H. The evolution of the C-S-H gel density with respect to this new quantity turns out to be independent of the w/c -ratio (Section 6.2.3), in a highly nonlinear fashion. The corresponding relation suggests three distinct hydration regimes with typical morphologies seen in Scanning Electron Micrographs (SEM). It is explained by subdividing the C-S-H gel into two classes: one of constant mass density (class A) and one of varying density (class B), see Sections 6.2.4 and 6.2.5. This finding enters an analytical hydration model which allows for quantitative consideration of effects stemming from different w/c -ratios (Section 6.3). It comprises a reaction equation for the main clinker phases of typical Portland cement pastes and contains three fitting parameters: the precipitation space thresholds between the aforementioned hydration regimes, and the density increase per lost precipitation space. These model parameters are identified and analytical expressions for phase volumes of hydrating cement pastes are given. After discussing several aspects of the new hydration model, including several sensitivity analyses (Section 6.4), the paper closes with conclusions (Section 6.5).

6.2 C-S-H gel densification quantified from NMR water mass fractions

6.2.1 NMR quantification of water mass fractions in hydrating Portland cement pastes

Applying ^1H nuclear magnetic resonance (NMR) relaxometry, Muller et al. (2012, 2013); Muller (2014) characterized white cement pastes at different ages and corresponding maturity stages, using quadrature and CPMG (Carr-Purcell-Meiboom-Gill) echos for resolving the water phases in cement pastes. The measured spin-spin relaxation times of water molecules, which are the smaller, the more bound (i.e. the less mobile) the molecules (Valori et al., 2013), delivered the amounts (i) of chemically strongly bonded water in solids such as portlandite and ettringite, (ii) of chemically weakly bonded water within solid C-S-H (interlayer water), (iii) of water strongly confined in gel pores (strong physical bond), and (iv) of water weakly confined in capillary pores (weak physical bond in inter-hydrate pores). Notably, the NMR signal fractions I_j quantify the mass fraction of specific water types $m_{H_2O}^j$ relative to the total

mass of water m_{H_2O}

$$I_j(t) = \frac{m_{H_2O}^j(t)}{m_{H_2O}}, \quad j \in \{PE, sCSH, gpor, cpor\}, \quad (6.1)$$

where PE refers to portlandite and ettringite, $sCSH$ to solid C-S-H, $gpor$ to gel water, and $cpor$ to capillary water. The sum of all signal fractions is equal to one, $I_{PE}(t) + I_{sCSH}(t) + I_{gpor}(t) + I_{cpor}(t) = 1$. Because of hydration, signal fractions according to Eq. (6.1) evolve with increasing material age t , where $t=0$ refers to the time instant where cement gets in contact with water. We here evaluate NMR signal fractions measured on white cement pastes with initial water-to-cement mass ratios $w/c \in \{0.32, 0.40, 0.48\}$, and cured at 20 °C, see (Muller, 2014) and Fig. 6.1.

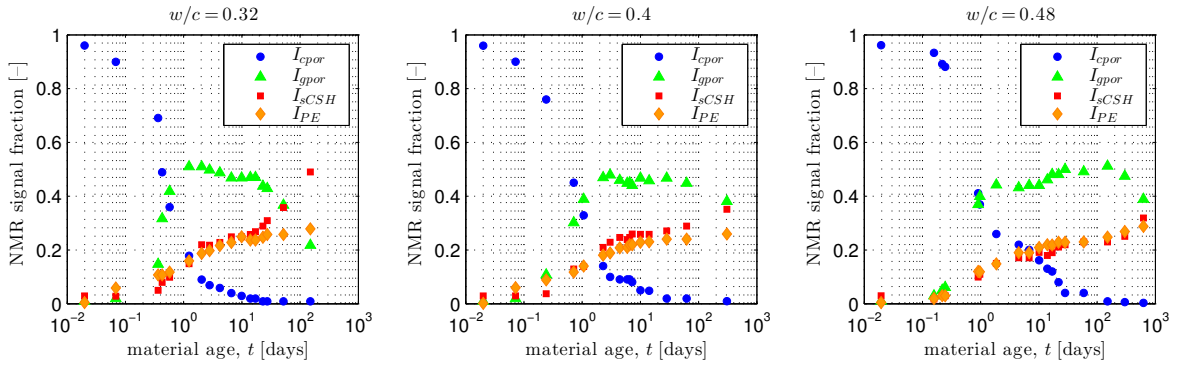


Figure 6.1: NMR signal fractions of three white cement pastes cured at 20 °C, as function of material age; after (Muller, 2014)

6.2.2 Evolution of C-S-H gel density with time

In order to quantify the evolution of C-S-H gel density based on the NMR signal fractions of (Muller, 2014) (see Fig. 6.1), we consider that C-S-H gel density is the sum of the masses of solid C-S-H and of gel water, divided by their volumes, the latter labeled as V_{sCSH} and V_{gpor} , respectively:

$$\rho_{gel}(t) = \frac{m_{sCSH}(t) + m_{H_2O}^{gpor}(t)}{V_{sCSH}(t) + V_{gpor}(t)} = \frac{\rho_{sCSH} V_{sCSH}(t) + \rho_{H_2O} V_{gpor}(t)}{V_{sCSH}(t) + V_{gpor}(t)}, \quad (6.2)$$

where mass densities of solid C-S-H and of water, respectively, amount to (Allen et al., 2007)

$$\rho_{sCSH} = 2.604 \text{ g/cm}^3, \quad \rho_{H_2O} = 1 \text{ g/cm}^3. \quad (6.3)$$

This mass density value for solid C-S-H was derived from combining small-angle neutron and X-ray scattering data, and by exploiting the hydrogen/deuterium neutron isotope effect both in water and methanol, see (Allen et al., 2007) for more details. More recent studies based on NMR (Muller et al., 2012, 2013) revealed that this mass density might actually slightly depend on the hydration degree. The effect of this variational subtlety on the results of our analysis is studied in more detail in the Discussion, see Section 6.4.3. In order to link the solid C-S-H volume to the NMR signal fraction I_{sCSH} , we express the mass of solid C-S-H, m_{sCSH} ,

as the mass of water which is chemically bound inside solid C-S-H, $m_{H_2O}^{sCSH}$, see Eq. (6.1), divided by the mass fraction of water within solid C-S-H, $\mu_{H_2O}^{sCSH}$,

$$m_{sCSH}(t) = \frac{m_{H_2O}^{sCSH}(t)}{\mu_{H_2O}^{sCSH}}. \quad (6.4)$$

The water mass fraction $\mu_{H_2O}^{sCSH}$ follows from the chemical composition of solid C-S-H, quantified as $1.7 \text{ CaO} \cdot \text{SiO}_2 \cdot 1.8 \text{ H}_2\text{O}$ from small angle scattering techniques (Allen et al., 2007), as well as from the molar masses of water and solid C-S-H, amounting to 18.01 g/mol and to 187.8 g/mol, respectively. This results in

$$\mu_{H_2O}^{sCSH} = \frac{1.8 \times 18.01}{187.8} = 0.1726. \quad (6.5)$$

The sought relation between solid C-S-H volume V_{sCSH} and the corresponding NMR signal fraction $I_{sCSH}(t)$ follows under consideration of Eqs. (6.1) and (6.4) as

$$V_{sCSH}(t) = \frac{m_{sCSH}(t)}{\rho_{sCSH}} = \frac{m_{H_2O}}{\mu_{H_2O}^{sCSH} \rho_{sCSH}} I_{sCSH}(t). \quad (6.6)$$

As for the gel pore volume V_{gpor} , we consider the gel pores to be water-saturated. Therefore, V_{gpor} is directly proportional to the NMR signal fraction $I_{gpor}(t)$, and it follows under consideration of Eq. (6.1) as

$$V_{gpor}(t) = \frac{m_{H_2O}^{gpor}(t)}{\rho_{H_2O}} = \frac{m_{H_2O}}{\rho_{H_2O}} I_{gpor}(t). \quad (6.7)$$

The evolution of the C-S-H gel density as a function of material age follows from specialization of the C-S-H gel density according to Eq. (6.2) for phase volumes according to Eqs. (6.6) and (6.7), for the constants given in Eqs. (6.3) and (6.5), as well as for the signal fractions of the three cement paste mixes (see Fig. 6.1) as

$$\rho_{gel}(t) = \frac{\rho_{sCSH} \rho_{H_2O} [I_{sCSH}(t) + \mu_{H_2O}^{sCSH} I_{gpor}(t)]}{\rho_{H_2O} I_{sCSH}(t) + \rho_{sCSH} \mu_{H_2O}^{sCSH} I_{gpor}(t)}. \quad (6.8)$$

Interestingly, the obtained C-S-H gel densities *decrease* during the first few hours of hydration, followed by progressive C-S-H gel *densification* (Fig. 6.2). At mature ages, the C-S-H gel density is the larger, the smaller the initial water-to-cement mass ratio w/c . The reason for the w/c -dependent density evolutions is analyzed next.

6.2.3 Specific precipitation space controls C-S-H gel density

We now check whether there may be a w/c -independent relationship between the gel densities and the space which is available for new solid C-S-H to precipitate. In this context, we quantify the precipitation space as the porosity γ of a *C-S-H foam* consisting of solid C-S-H as well as of water filling gel *and* capillary pores:

$$\gamma(t) = \frac{V_{H_2O}(t)}{V_{sCSH}(t) + V_{H_2O}(t)}, \quad (6.9)$$

where V_{H_2O} is the volume of water filling the gel and capillary pores, and V_{sCSH} is the volume filled by solid C-S-H. In the sequel, γ is referred to as specific precipitation space. It is equal to

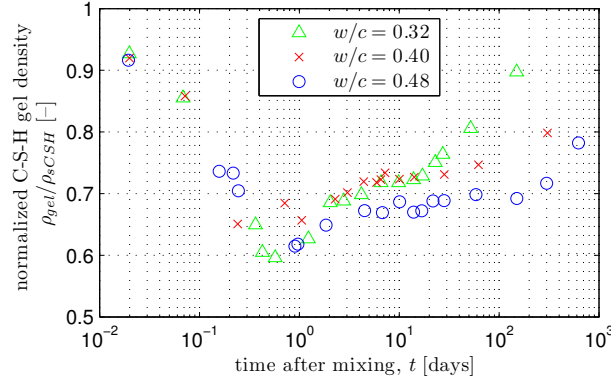


Figure 6.2: Normalized C-S-H gel density of three white cement pastes cured at 20 °C, as function of material age; quantified from NMR signal fractions of Fig. 6.1, together with Eqs. (6.2)-(6.8)

1 at the time instant of mixing cement and water, $\gamma(t=0) = 1$, it decreases during hydration, and it reaches zero once all initially available water is chemically combined with clinker.

Translating NMR signal fractions (Fig. 6.1) into a parameter plot showing C-S-H gel density $\rho_{gel}(t)$ over specific precipitation space $\gamma(t)$ requires the quantification of the right-hand-side of Eq. (6.9) based on time-dependent NMR signal fractions. The expression for $V_{sCSH}(t)$ is given in Eq. (6.6). As for $V_{H_2O}(t)$, we consider effective drying prevention, such that the liquid water-occupied volume V_{H_2O} is equal to the sum of gel and capillary pore volumes, following by analogy to Eq. (6.7) as

$$V_{H_2O}(t) = V_{gpor}(t) + V_{cpor}(t) = \frac{m_{H_2O}}{\rho_{H_2O}} [I_{gpor}(t) + I_{cpor}(t)]. \quad (6.10)$$

The sought expressions of the specific precipitation space as a function of the time-dependent NMR signal fractions is obtained from specialization of Eq. (6.9) for Eqs. (6.6) and (6.10), and reads as

$$\gamma(t) = \frac{\mu_{H_2O}^{sCSH} \rho_{sCSH} [I_{gpor}(t) + I_{cpor}(t)]}{\rho_{H_2O} I_{sCSH}(t) + \mu_{H_2O}^{sCSH} \rho_{sCSH} [I_{gpor}(t) + I_{cpor}(t)]}. \quad (6.11)$$

Finally, the $\rho_{gel}(t)$ - $\gamma(t)$ diagram is obtained from combining $\rho_{gel}(t)$ according to Eq. (6.8), with the evolution $\gamma(t)$ according to Eq. (6.11), under consideration of the numerical values given in Eqs. (6.3) and (6.5). Very remarkably, this indicates the existence of a w/c -independent master curve (Fig. 6.3). This corroborates that space confinement indeed controls the evolution of the C-S-H gel density.

In order to clarify why the C-S-H gel density evolves *nonlinearly* with decreasing precipitation space (Fig. 6.3), we now deal with the partition of the total water volume $V_{H_2O}(t)$ into the gel pores and the capillary pores, respectively. To this end, we introduce a capillary pore fraction φ_{cpor} and a gel pore fraction φ_{gpor} , which add up to 1, i.e. $\varphi_{cpor} + \varphi_{gpor} = 1$. They are defined as

$$\begin{aligned} \varphi_{cpor}(t) &= \frac{V_{cpor}(t)}{V_{cpor}(t) + V_{gpor}(t)} = \frac{I_{cpor}(t)}{I_{cpor}(t) + I_{gpor}(t)}, \\ \varphi_{gpor}(t) &= \frac{V_{gpor}(t)}{V_{cpor}(t) + V_{gpor}(t)} = \frac{I_{gpor}(t)}{I_{cpor}(t) + I_{gpor}(t)}. \end{aligned} \quad (6.12)$$

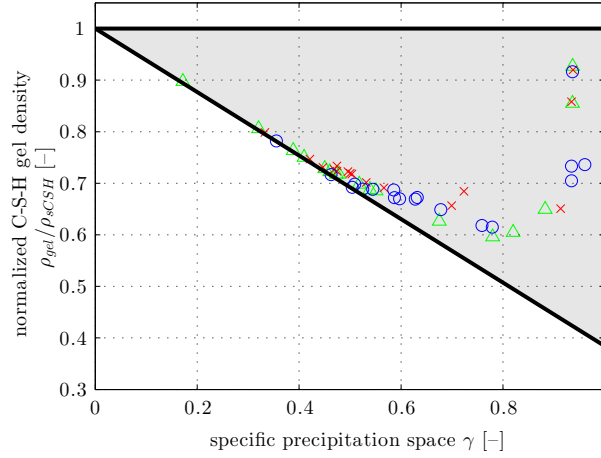


Figure 6.3: Normalized C-S-H gel density of three white cement pastes cured at 20 °C (triangles, crosses, and circles refer to $w/c=0.32$, $w/c=0.40$, and $w/c=0.48$, respectively), as function of the specific precipitation space; quantified from NMR signal fractions of Fig. 6.1, together with Eqs. (6.3), (6.5), (6.8), and (6.11); solid lines are upper and lower bounds described in Section 6.2.4

A parameter plot showing $\varphi_{cpor}(t)$ and $\varphi_{gpor}(t)$ over the specific precipitation space $\gamma(t)$ is obtained from combining Eqs. (6.3), (6.5), (6.11), and (6.12) with the NMR signal fractions given in Fig. 6.1, see Fig. 6.4. At very early ages, i.e. in the vicinity of $\gamma = 1$, virtually all pores are capillary pores, thus $\varphi_{cpor} \approx 1$ and $\varphi_{gpor} \approx 0$. At quite mature ages, i.e. for $\gamma \leq 0.43$, virtually all capillary pores have vanished, thus $\varphi_{cpor} \approx 0$ and $\varphi_{gpor} \approx 1$ (Fig. 6.4). In between, a quite dense data cloud describes a smooth and w/c -independent transition from the initial limiting case (vanishing gel porosity) to the final limiting case (vanishing capillary porosity). This provides the motivation for introducing three hydration regimes and two classes of C-S-H, as is discussed next.

6.2.4 Interpretation of gel densification: introduction of two C-S-H classes and three hydration regimes

Hydration regime I covers the first few hours after mixing cement and water, during which reaction products with vanishing gel porosity precipitate. This is consistent with Scanning Electron Micrographs – SEM (Garraut et al., 2005; Ylmén et al., 2009), showing “platelets” of ordered C-S-H on electrically charged clinker surfaces (Nachbaur et al., 1998), see Fig. 6.5(a). We here refer to this type of precipitation products as class A C-S-H. In hydration regime I, the “gel” volume is equal to the volume of solid C-S-H and the “gel” density is equal to the solid C-S-H density, $\rho_{gel} = \rho_{sCSH}$, see also the upper bound in Fig. 6.3 ($\rho_{gel}/\rho_{sCSH} = 1$).

Hydration regime II starts a few hours after mixing, once the formation of ordered class A C-S-H comes to an end and *less ordered calcium-silicate-hydrates* (class B C-S-H) start to grow such that gel pores are enclosed (Ylmén et al., 2009; Scrivener and Nonat, 2011), see Fig. 6.5(b). In hydration regime II, we envision two precipitation mechanisms to happen simultaneously on two different length scales: (i) on two different length scales related to capillary and gel pores, respectively: gel porous calcium silicate hydrates precipitate out of the supersaturated water filling both (i) the interstitial capillary pore spaces and (ii) the gel pores themselves. The latter process leads to a progressive densification of the C-S-H gel itself.

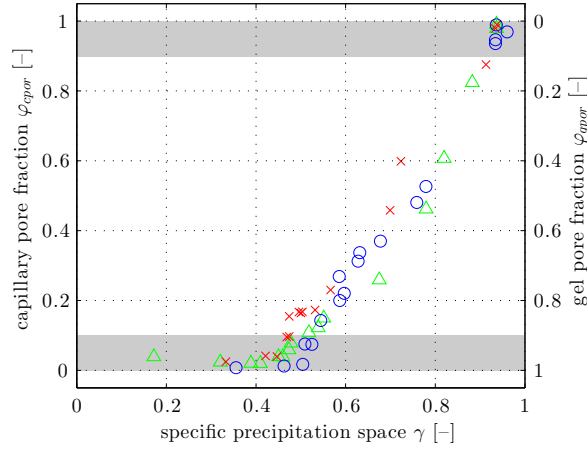


Figure 6.4: Capillary as well as gel pore fractions of three white cement pastes cured at 20 °C (triangles, crosses, and circles refer to $w/c=0.32$, $w/c=0.40$, and $w/c=0.48$, respectively), as functions of the specific precipitation space; quantified from NMR signal fractions of Fig. 6.1, together with Eqs. (6.3), (6.5), (6.11), and (6.12); data points between the gray areas at the top and the bottom of the graph belong to hydration regime II

Hydration regime II ends, once the gel porous hydrates have completely filled the interstitial space, so that the water-filled capillary porosity vanishes.

In the final hydration regime III, C-S-H precipitates only inside the gel pores. Since capillary porosity has vanished, the water volume is equal to the gel pore volume, $V_{H_2O} = V_{gpor}$. Consequently, the specific precipitation space is equal to the porosity of the C-S-H gel, and the relationship between the C-S-H gel density according Eq. (6.2), and the specific precipitation space according to Eq. (6.9) follows as

$$\rho_{gel}(\gamma) = \rho_{sCSH} (1 - \gamma) + \rho_{H_2O} \gamma, \quad (6.13)$$

see also the lower bound in Fig. 6.3.

6.2.5 Nonlinear gel density evolution in hydration regime II results from linear densification of class B C-S-H gel

Focusing on hydration regime II, we now quantify the density of class B C-S-H as a function of the specific precipitation space, based on the time-dependent NMR signal fractions (see Fig. 6.1 and (Muller, 2014)). To this end, we consider that the nonlinear evolution of the overall gel density $\rho_{gel}(\gamma)$, see Fig. 6.3, results from the interplay of *constant* class A C-S-H volume V_{ACSH} exhibiting solid C-S-H density ρ_{sCSH} , see Eq. (6.3), and *growing* class B C-S-H gel volume $V_{Bgel}(\gamma)$ exhibiting an *evolving* mass density $\rho_{Bgel}(\gamma)$, i.e.

$$\rho_{gel}(\gamma) = \frac{\rho_{sCSH} V_{ACSH} + \rho_{Bgel}(\gamma) V_{Bgel}(\gamma)}{V_{ACSH} + V_{Bgel}(\gamma)}. \quad (6.14)$$

Solving Eq. (6.14) for $\rho_{Bgel}(\gamma)$, delivers the following expression for the mass density of the class B C-S-H gel, as a function of the specific precipitation space:

$$\rho_{Bgel}(\gamma) = \frac{\rho_{gel}(\gamma) \times [V_{ACSH} + V_{Bgel}(\gamma)] - \rho_{sCSH} V_{ACSH}}{V_{Bgel}(\gamma)}. \quad (6.15)$$

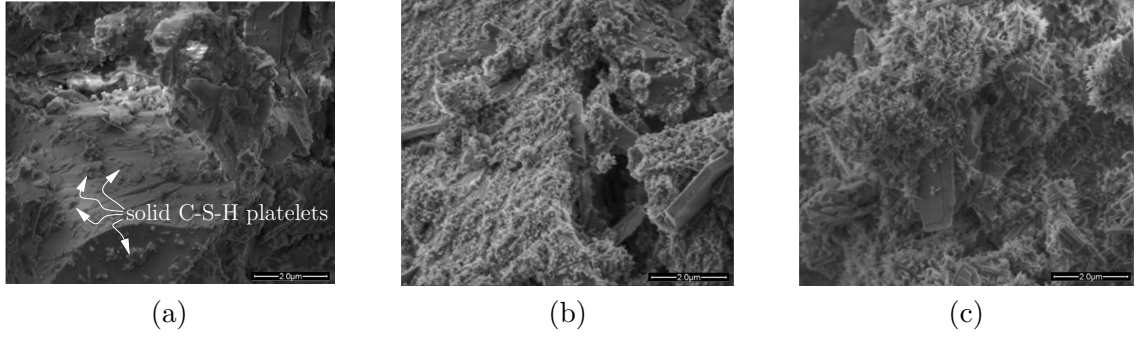


Figure 6.5: Morphology of C-S-H gel at clinker surfaces in Portland cement pastes as observed by SEM: (a) 120 min after mixing, solid C-S-H platelets grow at grain surfaces, (b) 240 min after mixing, C-S-H starts to cluster, i.e. to enclose gel pores, and (c) 480 min after mixing, C-S-H gel occupies a lot of the available precipitation space, after Ylmén et al. (2009); permission to reproduce the figures is granted by Elsevier

In Eq. (6.15), the volume of class A C-S-H is equal to the volume of solid C-S-H “platelets” at the end of hydration regime I. Introducing γ_{I-II} as the (unknown) specific precipitation space marking the transition from hydration regime I to II, volume V_{ACSH} follows as

$$V_{ACSH} = V_{sCSH}(\gamma_{I-II}). \quad (6.16)$$

The volume of class B C-S-H gel is equal to the volumes of the solid C-S-H and of the gel pores forming in hydration regime II

$$V_{Bgel}(\gamma) = V_{sCSH}(\gamma) - V_{sCSH}(\gamma_{I-II}) + V_{gpor}(\gamma). \quad (6.17)$$

The sought parameter plot between the mass density of class B C-S-H gel $\rho_{Bgel}(t)$ and specific precipitation space $\gamma(t)$ requires a relation between $\rho_{Bgel}(t)$ and the time-dependent NMR signal fractions (see Fig. 6.1 and (Muller, 2014)). This relation is gained as follows: Eqs. (6.16) and (6.17) are inserted into Eq. (6.15); this results in an expression which is then specialized for (6.6) and (6.7), yielding

$$\rho_{Bgel}(t) = \frac{\rho_{gel}(t) \times [\rho_{H_2O} I_{sCSH}(t) + \rho_{sCSH} \mu_{H_2O}^{sCSH} I_{gpor}(t)] - \rho_{sCSH} \rho_{H_2O} I_{sCSH}(\gamma_{I-II})}{\rho_{H_2O} [I_{sCSH}(t) - I_{sCSH}(\gamma_{I-II})] + \rho_{sCSH} \mu_{H_2O}^{sCSH} I_{gpor}(t)}. \quad (6.18)$$

As for the quantification of the right-hand-side of Eq. (6.18), the expression for $\rho_{gel}(t)$ in terms of NMR signal fractions is given in Eq. (6.8); the NMR signal fractions $I_{sCSH}(t)$ and $I_{gpor}(t)$ are given in Fig. 6.1; and the numerical values for the mass densities ρ_{sCSH} and ρ_{H_2O} as well as for the water mass fraction $\mu_{H_2O}^{sCSH}$ are given in Eq. (6.3) and (6.5), respectively. However, the NMR signal fraction of solid C-S-H at the transition point from hydration regime I to hydration regime II, denoted as $I_{sCSH}(\gamma_{I-II})$ in Eq. (6.18), is unknown, because the boundary between hydration regimes I and II cannot be identified clearly in Fig. 6.4. Similarly, also the boundary between hydration regimes II and III cannot be clearly identified in Fig. 6.4. While a sophisticated (and therefore more expensive) solution of this problem is reserved for Section 6.3 in the form of a new hydration model, we here present a more basic access to the nature of class B gel densification, by excluding points which are potentially close or even beyond the I-II and the II-III hydration regime boundaries, respectively. More precisely, as boundary I-II relates to vanishing gel porosity, and boundary II-III relates to vanishing

capillary porosity, we exclude data points with any (gel or capillary) porosity value below 10 %, as indicated by the grey shaded areas in Fig. 6.4. In addition, we estimate $I_{sCSH}(\gamma_{I-II})$ based on the average of solid C-S-H signal fractions of all data points which exhibit $\varphi_{gpor} < 0.1$, see the top gray area in Fig. 6.4, resulting in $I_{sCSH}(\gamma_{I-II}) \approx 0.028$.

On this basis, we combine temporal evolutions of $\rho_{Bgel}(t)$ according to Eq. (6.18) with the evolutions of the specific precipitation space $\gamma(t)$ according to Eq. (6.11), yielding a parameter plot ρ_{Bgel} over γ , see Fig. 6.6. It illustrates the remarkable result that class B C-S-H gel densifies in hydration regime II – in very good approximation – *linearly* with decreasing precipitation space. The corresponding linear regression function reads as

$$\rho_{Bgel}(\gamma) = (0.925 - 0.457 \gamma) \rho_{sCSH}, \quad \gamma \in \text{hydration regime II}, \quad (6.19)$$

and the respective coefficient of determination amounts to $R^2 = 0.94$.

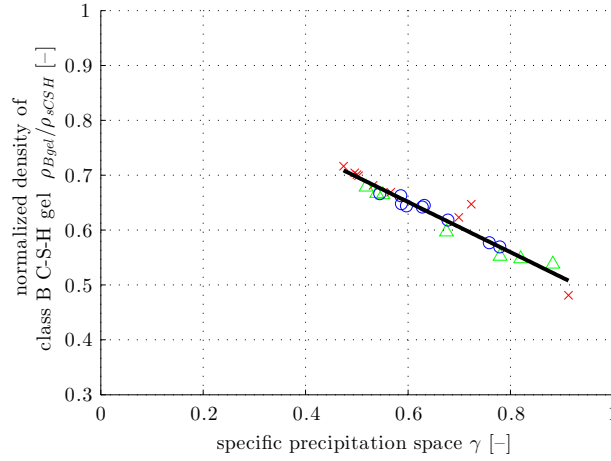


Figure 6.6: Normalized density evolution of class B C-S-H gel of three white cement pastes cured at 20 °C (triangles, crosses, and circles refer to $w/c=0.32$, $w/c=0.40$, and $w/c=0.48$, respectively), as function of the specific precipitation space; quantified from NMR signal fractions of Fig. 6.1, together with Eqs. (6.3), (6.5) and (6.8), as well as from $I_{sCSH}(\gamma_{I-II}) \approx 0.028$ (see Section 6.2.5 for details on this estimation); the linear regression function given in Eq. (6.19) exhibits $R^2 = 0.94$

This remarkable linear relation between class B C-S-H gel density and the specific precipitation space will now be combined with basic cement chemistry, so as to come up with a simple hydration model delivering phase volume fractions as functions of w/c -ratio and hydration degree. This is described in Section 6.3, where we also identify the values of the specific precipitation space at the transition points from hydration regime I to hydration regime II, γ_{I-II} , and from hydration regime II to hydration regime III, γ_{II-III} . Then, the value for γ_{I-II} will allow us to identify $I_{sCSH}(\gamma_{I-II})$ more precisely than through the estimate of $I_{sCSH}(\gamma_{I-II}) \approx 0.028$, as given above.

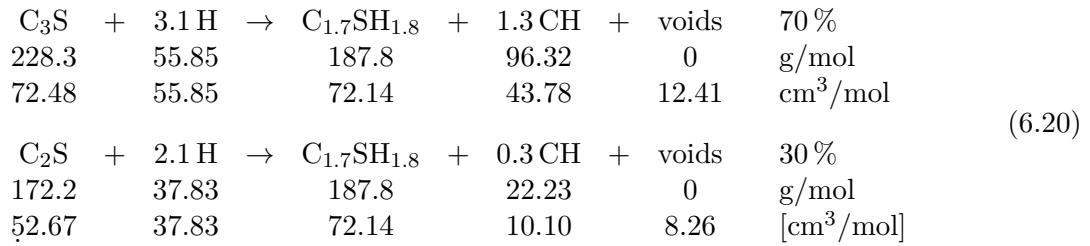
6.3 Development of a mathematical hydration model for C-S-H gel densification

We here develop a mathematical hydration model for white cement pastes, based on the observation that the C-S-H density varies during hydration. In this sense, the new model may

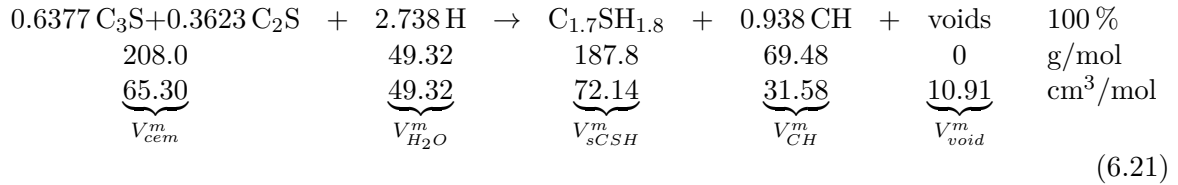
qualify as an alternative to Powers' famous hydration model (Powers and Brownnyard, 1947), where the C-S-H density is assumed to be constant. The new model comprises two parts: the first part concerns *C-S-H densification* in terms of mathematical functions quantifying the densification of C-S-H gel. They are the basis for the second part: a *phase evolution model* defined in terms of functions quantifying the hydration-driven evolution of phase volume fractions. Our aim is to develop *analytical* mathematical functions which can be evaluated for any initial water-to-cement mass ratio w/c and any hydration degree ξ . Accounting for the observation that the C-S-H gel density varies during the hydration, this will provide an alternative to the Powers model. The C-S-H densification model will provide continuous functions for the point-wisely resolved relations shown in Figs. 6.3 and 6.4, and it will in particular allow for precise *identification* of the NMR signal fraction at the transition between hydration regimes I and II, $I_{sCSH}(\gamma_{I-II})$. This will be done by considering a specific reaction chemistry, as described next.

6.3.1 Hydration chemistry of typical Portland cement pastes

Typical Portland cement clinker consists of 70 % (per mass) tricalcium silicate C_3S ("alite") and 30 % dicalcium silicate C_2S ("belite") (Neville, 1995), whereby we use the standard abbreviations of cement chemistry: $C = CaO$, $S = SiO_2$, $H = H_2O$, and $CH = Ca(OH)_2$. Hydration of these two main clinker types produces essentially C-S-H and calcium hydroxide CH ("portlandite"), as quantified by the following reaction equations (Odler, 1998), see also Table 6.1



For the sake of simplicity, it is assumed that both reactions take place simultaneously and up to the same extent, i.e. C_3S and C_2S are consumed proportionally to their initial mass fractions. Noting that the initial mass fractions $m_{C_3S} : m_{C_2S} = 70 : 30$, see above, relate to molar fractions $63.77 : 36.23$, the combined reaction equation for one mol of cement reads as



where V_{cem}^m , $V_{H_2O}^m$, V_{sCSH}^m , V_{CH}^m , V_{void}^m denote phase volumes per one mole of cement. Notably, the mass density of cement follows from dividing its molar mass, 208 g/mol, by its molar volume, $65.3 \text{ cm}^3/\text{mol}$, see Eq. (6.21), as

$$\rho_{cem} = 3.185 \text{ g/cm}^3. \tag{6.22}$$

Table 6.1: Mass densities and molar masses of clinker and hydrates

	mass density g/cm ³	molar mass g/mol
C ₃ S	3.15 (Bye, 1999)	228.3
C ₂ S	3.27 (Bye, 1999)	172.2
H ₂ O	1.00	18.01
C _{1.7} SH _{1.8}	2.604 (Muller et al., 2012)	187.8
CH	2.20 (Muller et al., 2012)	74.09

6.3.2 Phase volumes as functions of hydration degree

Next, we derive, from reaction equation (6.21), how the volumes of each of the phases (cement clinker, water, C-S-H, CH, and voids) depend on the hydration degree ξ , on the initial water-to-cement ratio w/c , and on the molar volumes given in Eq. (6.21). To this end, we recall that the hydration degree ξ is defined as the volume of hydrated cement over the initially available volume of cement $V_{cem}(t=0)$. Denoting the volume of unhydrated cement available at time t as $V_{cem}(t)$, the definition of the hydration degree reads as

$$\xi(t) = \frac{V_{cem}(t=0) - V_{cem}(t)}{V_{cem}(t=0)}. \quad (6.23)$$

In order to use hydration degree ξ rather than time t as the parameter for our further developments, we consider the bijective relation between ξ and t in order to re-formulate Eq. (6.23) as

$$\xi = \frac{V_{cem}(\xi=0) - V_{cem}(\xi)}{V_{cem}(\xi=0)}. \quad (6.24)$$

It will turn out to be useful to express all phase volumes as functions of the initially available cement volume. Therefore, we solve (6.24) for $V_{cem}(\xi)$, yielding

$$V_{cem}(\xi) = (1 - \xi) V_{cem}(\xi=0). \quad (6.25)$$

Next, we focus on the phase volume evolution of water, which is equal to the initial amount of water, $V_{H_2O}(\xi=0)$, minus the volume of chemically consumed water, $\Delta V_{H_2O}(\xi)$, i.e.

$$V_{H_2O}(\xi) = V_{H_2O}(\xi=0) - \Delta V_{H_2O}(\xi). \quad (6.26)$$

The initial water volume $V_{H_2O}(\xi=0)$ can be related to the initial water-to-cement mass ratio $w/c = m_{H_2O}(\xi=0)/m_{cem}(\xi=0)$. When expressing these masses as products of volumes times mass densities, w/c reads as

$$w/c = \frac{\rho_{H_2O} V_{H_2O}(\xi=0)}{\rho_{cem} V_{cem}(\xi=0)}. \quad (6.27)$$

Solving Eq. (6.27) for $V_{H_2O}(\xi=0)$ delivers the sought expression for the initial water volume as

$$V_{H_2O}(\xi=0) = w/c \frac{\rho_{cem}}{\rho_{H_2O}} V_{cem}(\xi=0). \quad (6.28)$$

The volume of chemically consumed water, $\Delta V_{H_2O}(\xi)$, in turn, is proportional to the volume of chemically consumed cement, $\Delta V_{cem}(\xi) = \xi V_{cem}(\xi=0)$, see Eq. (6.25), and the proportionality

factor is the initial water-to-cement ratio of molar volumes, see hydration reaction equation (6.21),

$$\Delta V_{H_2O}(\xi) = \frac{V_{H_2O}^m}{V_{cem}^m} \xi V_{cem}(\xi=0). \quad (6.29)$$

The phase volume evolution of water follows from specifying Eq. (6.26) for Eqs. (6.28) and (6.29), as

$$V_{H_2O}(\xi) = \left(w/c \frac{\rho_{cem}}{\rho_{H_2O}} - \frac{V_{H_2O}^m}{V_{cem}^m} \xi \right) V_{cem}(\xi=0). \quad (6.30)$$

Finally, the phase volume evolutions of solid C-S-H, CH, and voids (related to autogenous shrinkage) follow by analogy to Eq. (6.29) as

$$V_i(\xi) = \frac{V_i^m}{V_{cem}^m} \xi V_{cem}(\xi=0), \quad i \in [sCSH, CH, void]. \quad (6.31)$$

Eqs. (6.25), (6.30), and (6.31) provide access to the phase volume evolutions of cement, water, solid C-S-H, CH, and voids, as functions of the hydration degree ξ . The transition from hydration degree ξ to specific precipitation space γ is discussed next.

6.3.3 Relation between hydration degree and specific precipitation space

Specifying the definition of the specific precipitation space according to Eq. (6.9), for the phase volumes of water, see Eq. (6.30), and of solid C-S-H, see Eq. (6.31), delivers the following expression for the specific precipitation space γ as a function of the hydration degree ξ

$$\gamma(\xi) = \frac{w/c \frac{\rho_{cem}}{\rho_{H_2O}} - \frac{V_{H_2O}^m}{V_{cem}^m} \xi}{w/c \frac{\rho_{cem}}{\rho_{H_2O}} + \frac{V_{sCSH}^m - V_{H_2O}^m}{V_{cem}^m} \xi}. \quad (6.32)$$

The inverse relationship, i.e. hydration degree ξ expressed as a function of the specific precipitation space γ , is obtained from solving Eq. (6.32) for the hydration degree

$$\xi(\gamma) = \frac{w/c \frac{\rho_{cem}}{\rho_{H_2O}} (1 - \gamma)}{\frac{\gamma V_{sCSH}^m + V_{H_2O}^m (1 - \gamma)}{V_{cem}^m}}. \quad (6.33)$$

6.3.4 Partition of total water volume into gel and capillary pore volumes

Reaction equation (6.21) provides access to the evolution of the *total* water volume, see Eq. (6.30), which is now partitioned between the gel and capillary pore volumes. This is simple in hydration regimes I and III, because gel porosity vanishes in regime I

$$V_{gpor}(\gamma) = 0 \quad V_{cpor}(\gamma) = V_{H_2O}(\gamma) \quad 1 \geq \gamma \geq \gamma_{I-II}, \quad (6.34)$$

and capillary porosity vanishes in regime III

$$V_{gpor}(\gamma) = V_{H_2O}(\gamma) \quad V_{cpor}(\gamma) = 0 \quad \gamma_{II-III} \geq \gamma \geq 0, \quad (6.35)$$

with γ_{II-III} as the specific precipitation space marking the transition from hydration regime II to III. We are left with the intermediate hydration regime II.

The key to partitioning water volume between gel and capillary pore volumes in hydration regime II is the density of class B C-S-H gel. On the one hand, evaluation of NMR experiments

has shown that ρ_{Bgel} increases in a linear manner, with decreasing precipitation space, see Fig. 6.6 and Eq. (6.19), and this is now modeled as

$$\rho_{Bgel}(\gamma) = \rho_{Bgel}(\gamma_{II-III}) - \left| \frac{d\rho_{Bgel}}{d\gamma} \right|^II (\gamma - \gamma_{II-III}) \quad \forall \gamma_{II-III} \leq \gamma \leq \gamma_{I-II}, \quad (6.36)$$

with three fitting parameters, $\left| \frac{d\rho_{Bgel}}{d\gamma} \right|^II$, γ_{I-II} , and γ_{II-III} , which need to be identified. $\rho_{Bgel}(\gamma_{II-III})$ depends on the three fitting parameters, i.e. its numerical value follows from considering that the total C-S-H gel density is continuous at the transition from hydration regime II to III, i.e. that Eqs. (6.13) and (6.14) deliver the same density for $\gamma = \gamma_{II-III}$. On the other hand, ρ_{Bgel} can be expressed through the volumes of solid C-S-H and gel pores formed in hydration regime II, as well as the mass densities of solid C-S-H and water

$$\rho_{Bgel}(\gamma) = \frac{\rho_{sCSH} [V_{sCSH}(\gamma) - V_{sCSH}(\gamma_{I-II})] + \rho_{H_2O} V_{gpor}(\gamma)}{V_{sCSH}(\gamma) - V_{sCSH}(\gamma_{I-II}) + V_{gpor}(\gamma)}. \quad (6.37)$$

The sought gel pore volume evolution in hydration regime II follows from solving Eq. (6.37) for V_{gpor} as

$$V_{gpor}(\gamma) = \frac{[\rho_{sCSH} - \rho_{Bgel}(\gamma)] [V_{sCSH}(\gamma) - V_{sCSH}(\gamma_{I-II})]}{\rho_{Bgel}(\gamma) - \rho_{H_2O}}. \quad (6.38)$$

Specifying Eq. (6.38) for $V_{sCSH}(\gamma)$ according to Eqs. (6.31) and (6.33), for the mass densities given in Table 6.1, and for $\rho_{Bgel}(\gamma)$ according to Eq. (6.36), delivers the gel porosity as a function of the specific precipitation space, in hydration regime II. The corresponding capillary pore volume follows as the difference between the total water volume and the gel pore volume

$$V_{cpor}(\gamma) = V_{H_2O}(\gamma) - V_{gpor}(\gamma). \quad (6.39)$$

Combination of the precipitation space-dependent pore volumes according to (6.38) and (6.39) with Eq. (6.32) yields (w/c) - and hydration degree-dependent pore volumes, in analogy to the format given for the constituent volumes of Eq. (6.25), (6.30), and (6.31). Thus, the C-S-H densification model is completed, whereby its key equations are (6.25), (6.30), and (6.31); as well as (6.38) and (6.39) in combination with Eq. (6.32).

6.3.5 Identification of fitting parameters

The three fitting parameters of the densification model, namely $\left| \frac{d\rho_{Bgel}}{d\gamma} \right|^II$, γ_{I-II} , and γ_{II-III} , see Eq. (6.36), are identified by minimizing the sum of the squared modeling errors regarding capillary and gel pore fractions according to Eq. (6.12)

$$\sum_{i=1}^{51} [\varphi_{cpor,i}^{\exp} - \varphi_{cpor,i}^{\text{mod}}]^2 = \sum_{i=1}^{51} [\varphi_{gpor,i}^{\exp} - \varphi_{gpor,i}^{\text{mod}}]^2 \rightarrow \min, \quad (6.40)$$

where $\varphi_{cpor,i}^{\exp}$ and $\varphi_{gpor,i}^{\exp}$ are two times 51 NMR-derived values, see Fig. 6.4, and where $\varphi_{cpor,i}^{\text{mod}}$ and $\varphi_{gpor,i}^{\text{mod}}$ are two times 51 modeled values of capillary and gel pore fractions. The equal sign in Eq. (6.40) stems from the fact that the entire water-filled pore space is composed of two pore fractions only; $\varphi_{cpor} + \varphi_{gpor} = 1$. Hence, any gel fraction modeling error, $(\varphi_{gpor,i}^{\exp} - \varphi_{gpor,i}^{\text{mod}})$ is always equal to the corresponding capillary fraction modeling error multiplied by minus one, $(\varphi_{cpor,i}^{\exp} - \varphi_{cpor,i}^{\text{mod}})$; and hence the squared errors are identical. As for quantification of $\varphi_{cpor,i}^{\text{mod}}$ and $\varphi_{gpor,i}^{\text{mod}}$ values, we combine Eqs. (6.12), (6.30)-(6.36), (6.38), (6.39), and the numerical

Table 6.2: Numerical values of constants involved in the developed mathematical model

ρ_{sCSH}	2.604 g/cm ³	Eq. (6.3)
ρ_{H_2O}	1.000 g/cm ³	Eq. (6.3)
$\mu_{H_2O}^{sCSH}$	0.1726	Eq. (6.5)
ρ_{cem}	3.185 g/cm ³	Eq. (6.22)
$\left \frac{d\rho_{Bgel}}{d\gamma} \right ^II$	1.07 g/cm ³	Eq. (6.41)
γ_{I-II}	0.942	Eq. (6.41)
γ_{II-III}	0.426	Eq. (6.41)
$\rho_{Bgel}(\gamma_{II-III})$	1.89 g/cm ³	Eq. (6.41)

values summarized in Table 6.2. Error minimization according to Eq. (6.40) on the basis of capillary or gel pore fractions, rather than on the basis of mass densities, is motivated by the pronounced uncertainty propagation from the measured NMR signals to the mass density values derived therefrom, particularly so at the beginning of hydration regime II (for details see Section 6.4.1). The optimal fitting parameters as well as the resulting value of $\rho_{Bgel}(\gamma_{II-III})$ are identified as

$$\left| \frac{d\rho_{Bgel}}{d\gamma} \right|^II = 1.07 \text{ g/cm}^3, \quad \gamma_{I-II} = 0.942, \quad \gamma_{II-III} = 0.426, \quad \rho_{Bgel}(\gamma_{II-III}) = 1.89 \text{ g/cm}^3. \quad (6.41)$$

The resulting fit, characterized by a quadratic correlation coefficient of $R^2 = 98\%$, is of very satisfactory quality, see Fig. 6.7, suggesting that the partition of water volume into gel and capillary porosity is slightly nonlinear in hydration regime II.

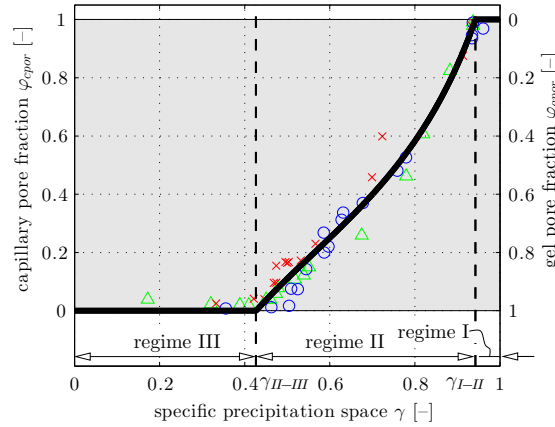


Figure 6.7: Capillary and gel pore fractions according to Eqs. (6.12), as functions of the specific precipitation space according to Eq. (6.9): comparison of best model fit (thick solid line) with NMR-derived data (triangles, crosses, and circles refer to $w/c=0.32$, $w/c=0.40$, and $w/c=0.48$, respectively); see Eq. (6.41) for optimal model parameters

6.3.6 Model consistency: quantification of C-S-H gel densification

The mathematical expression describing the densification of class B-C-S-H in hydration regime II is obtained from inserting the identified quantities according to Eq. (6.41), into the

linear density evolution model of Eq. (6.36), yielding

$$\rho_{Bgel}(\gamma) = (0.901 - 0.411\gamma) \rho_{sCSH}, \quad 0.426 \leq \gamma \leq 0.942. \quad (6.42)$$

The coefficients in Eq. (6.42) are quite similar to the ones given in Eq. (6.19), which underlines the relevance of the much simpler estimate for $\rho_{Bgel}(\gamma)$ described in Section 6.2. However, the more sophisticated optimization problem of Eq. (6.36) has also delivered values for the specific precipitation space at the interval boundaries between the three hydration regimes, γ_{I-II} and γ_{II-III} , see Eq. (6.41). This allows for identification of the solid C-S-H signal fraction at the transition from regime I to regime II, $I_{sCSH}(\gamma_{I-II})$. It follows from combination of Eqs. (6.6), (6.27), (6.31), and (6.33) under consideration of the relation $m_{H_2O} = V_{H_2O} \rho_{H_2O}$ resulting in

$$I_{sCSH}(\gamma_{I-II}) = \frac{\mu_{H_2O}^{sCSH} \rho_{sCSH} V_{sCSH}^m (1 - \gamma_{I-II})}{\rho_{H_2O} [\gamma_{I-II} V_{sCSH}^m + V_{H_2O}^m (1 - \gamma_{I-II})]} = 0.0266, \quad (6.43)$$

where numerical values of phase volumes V_{sCSH}^m and $V_{H_2O}^m$ according to Eq. (6.21), densities according to Eq. (6.3), and $\mu_{H_2O}^{sCSH}$ according to Eq. (6.5) were considered. The linear densification model for class B C-S-H gel forming in hydration regime II, see Eq. (6.42), very satisfactorily represents the densities of class B-C-S-H gel considering $I_{sCSH}(\gamma_{I-II}) = 0.0266$ according to Eq. (6.43), see Fig. 6.8. The increased scatter of NMR-derived values at the beginning of hydration regime II, i.e. in the vicinity of $\gamma_{I-II} = 0.942$, is a consequence of the small signal fractions I_{sCSH} and their considerable dispersion at very early ages, see Fig. 6.1 and Section 6.4.1 for more details.

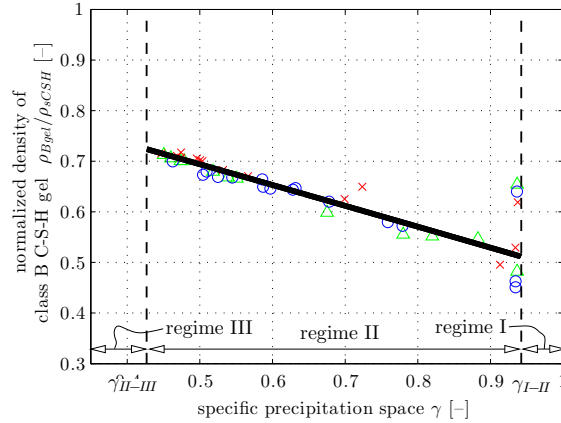


Figure 6.8: Normalized density evolution of class B C-S-H gel according to Eq. (6.42), as function of the specific precipitation space according to Eq. (6.9) in hydration regime II: comparison of model (thick solid line) with NMR signal fractions of Fig. 6.1, together with Eqs. (6.3), (6.5) and (6.8), as well as from $I_{sCSH}(\gamma_{I-II}) = 0.0266$ (triangles, crosses, and circles refer to $w/c=0.32$, $w/c=0.40$, and $w/c=0.48$, respectively)

The C-S-H densification model reproduces the NMR-derived evolution of the total C-S-H gel density also very reliably, see Fig. 6.9. At the beginning of hydration regime II, i.e. in the vicinity of $\gamma_{I-II} = 0.942$, gel density decreases with decreasing precipitation space, because gel-porous class B C-S-H gel grows so quickly into the interstitial space that the associated generation of new gel porosity outperforms the densification of this gel. The minimum total C-S-H gel density is reached around $\gamma = 0.84$, and this corresponds to material

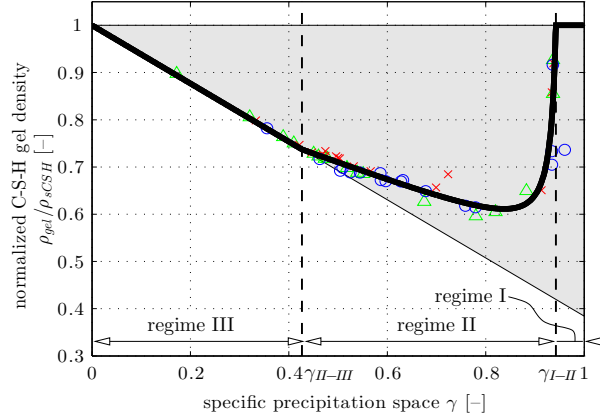


Figure 6.9: Normalized C-S-H gel density according to Eq. (6.2), as function of the specific precipitation space according to Eq. (6.9): comparison of model (thick solid line) with NMR-derived data (triangles, crosses, and circles refer to $w/c=0.32$, $w/c=0.40$, and $w/c=0.48$, respectively)

ages of approximately 10 hours. This implies that the minimum C-S-H gel density is reached somewhere around (but not exactly at) the maximum heat release rate, which marks the transition from the acceleration period to the deceleration period (Bullard et al., 2011). After that, hydration kinetics are well known to decelerate significantly (Scrivener and Nonat, 2011), such that densification of already formed class B C-S-H gel outperforms the generation of new gel porosity associated with the new production of class B C-S-H gel. Our model suggests that capillary porosity vanishes at $\gamma_{II-III} = 0.426$, and this corresponds to material ages ranging from approximately 20 days ($w/c=0.32$), to 50 days ($w/c=0.40$), and to 400 days ($w/c=0.48$), given a hydration temperature amounting to 20 °C.

6.3.7 Phase volume fraction evolutions derived from new C-S-H densification model

Herein, we provide closed-form expressions for the phase volume fractions of cement paste, as functions of the hydration degree ξ and of the initial water-to-cement mass ratio w/c . To this end, we now explicitly consider the numerical values for the phase densities, as given in Tables 6.1 and 6.2, the molar volumes involved in reaction equation (6.21), and the optimal densification parameters according to Eqs. (6.41).

At first, we quantify the hydration degrees which mark the transition from one hydration regime to the following, i.e. ξ_{I-II} and ξ_{II-III} . They follow from specialization of Eq. (6.33) for the corresponding precipitation spaces γ_{I-II} and γ_{II-III} from Eqs. (6.41) as

$$\xi_{I-II} = 0.170 w/c, \quad \xi_{II-III} = 2.022 w/c. \quad (6.44)$$

Eqs. (6.44) express that hydration degrees at transition points between hydration regimes increase linearly with increasing initial water-to-cement mass ratio (Fig. 6.10).

Cement paste-related phase volume fractions, f_i^{cp} , are defined as the phase volumes $V_i(\xi)$ divided by the total cement paste volume $V_{cp}(\xi)$:

$$f_i^{cp}(\xi) = \frac{V_i(\xi)}{V_{cp}(\xi)}, \quad i \in [cem, H_2O, sCSH, CH, void, gpor, cpor, gel], \quad (6.45)$$

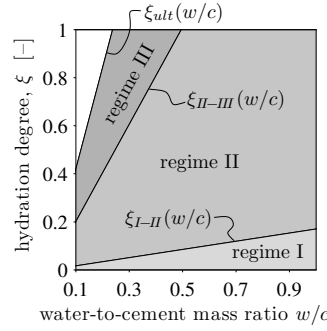


Figure 6.10: Hydration regimes I, II, and III defined in terms of hydration degree ξ and initial water-to-cement mass ratio w/c ; for theoretically reachable ultimate hydration degrees see Section 6.4.6

for phase volumes of cement, water, solid C-S-H, CH, voids, as well as gel and capillary pores, see Eqs. (6.25), (6.30), (6.31), and (6.38) in combination with Eq. (6.10). The total cement paste volume $V_{cp}(\xi)$ is traditionally set equal to its initial value, see (Powers and Brownyard, 1947; Acker, 2001), such that it can be expressed, under consideration of (6.28), as

$$V_{cp}(\xi) = V_{cem}(\xi=0) + V_{H_2O}(\xi=0) = \left(1 + w/c \frac{\rho_{cem}}{\rho_{H_2O}}\right) V_{cem}(\xi=0). \quad (6.46)$$

The sought expressions for the phase volume fractions follow from specialization of Eqs. (6.45) for (6.25), for (6.30), for (6.31), for (6.38) combined with (6.10) and with (6.32), and for (6.46) – under consideration of the aforementioned numerical input parameters – as

$$f_{cem}^{cp} = \frac{1 - \xi}{1 + 3.185 w/c} \geq 0, \quad (6.47)$$

$$f_{CH}^{cp} = \frac{0.484 \xi}{1 + 3.185 w/c}, \quad (6.48)$$

$$f_{sCSH}^{cp} = \frac{1.105 \xi}{1 + 3.185 w/c}, \quad (6.49)$$

$$f_{gpor}^{cp} = \begin{cases} 0 & 0 \leq \xi \leq \xi_{I-II}, \\ \frac{-0.799 (w/c)^2 + 4.824 w/c \xi - 0.793 \xi^2}{(1 + 3.185 w/c) (0.864 w/c + 1.278 \xi)} & \xi_{I-II} < \xi < \xi_{II-III}, \\ \frac{3.185 w/c - 0.755 \xi}{1 + 3.185 w/c} \geq 0 & \xi_{II-III} \leq \xi \leq 1, \end{cases} \quad (6.50)$$

$$f_{cpor}^{cp} = \frac{3.185 w/c - 0.755 \xi}{1 + 3.185 w/c} - f_{gpor}^{cp} \geq 0, \quad (6.51)$$

$$f_{void}^{cp} = \frac{0.167 \xi}{1 + 3.185 w/c}. \quad (6.52)$$

It turns out that the phase volume fractions of cement, solid hydrates (CH and solid C-S-H), and voids are obtained as *linear* functions of the hydration degree, similar to the case encountered with Powers' model (Powers and Brownyard, 1947; Powers, 1958). On the other hand, phase volume fractions of gel and capillary pores are *nonlinear* functions of the hydration degree in hydration regime II.

We proceed with comparing the phase volume fraction evolutions according to Eqs. (6.47)-(6.52) to data of Muller et al. (2012), who combined ^1H nuclear magnetic resonance relaxometry, Rietveld analyses of X-ray diffraction patterns, thermal gravimetric analysis (TGA), and chemical shrinkage measurements, in order to identify the phase volume fraction evolutions of cement pastes with initial water-to-cement mass ratios of 0.32, 0.40, and 0.48, respectively. The comparison regarding unhydrated cement, solid hydrates (= solid C-S-H + CH), gel porosity, capillary porosity, and voids with experimental data from Muller et al. (2012) underlines the coherence of the developed model (Fig. 6.11). It is particularly appealing that the model reliably foresees hydration degrees ξ_{II-III} at which water in capillary pores is completely consumed by the chemical reaction, so that the continued hydration of cement is limited to water in gel pores. In addition, the model can be evaluated for any paste composition in terms

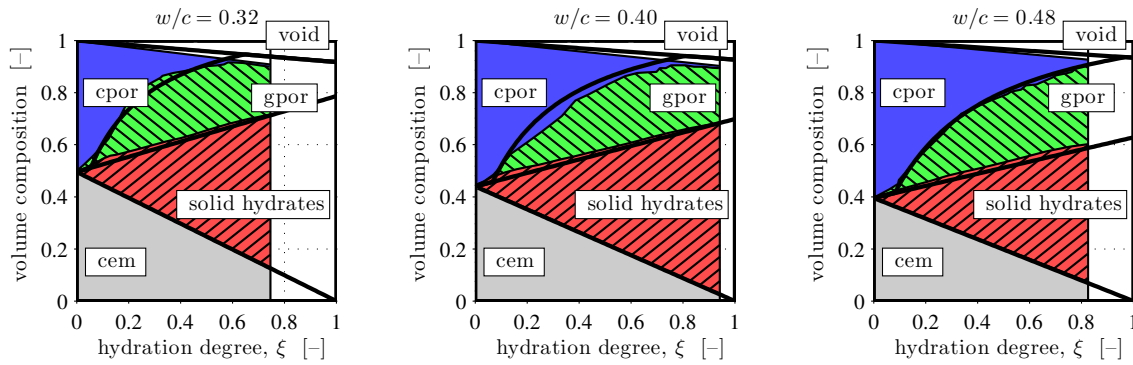


Figure 6.11: Comparison of modeled phase volume fraction evolutions (thick black lines), see (6.47)-(6.52), with experimental data from Muller et al. (2012) (colored areas)

of the initial water-to-cement mass ratio w/c , and for any maturity in terms of hydration degree ξ , see Fig. 6.12.

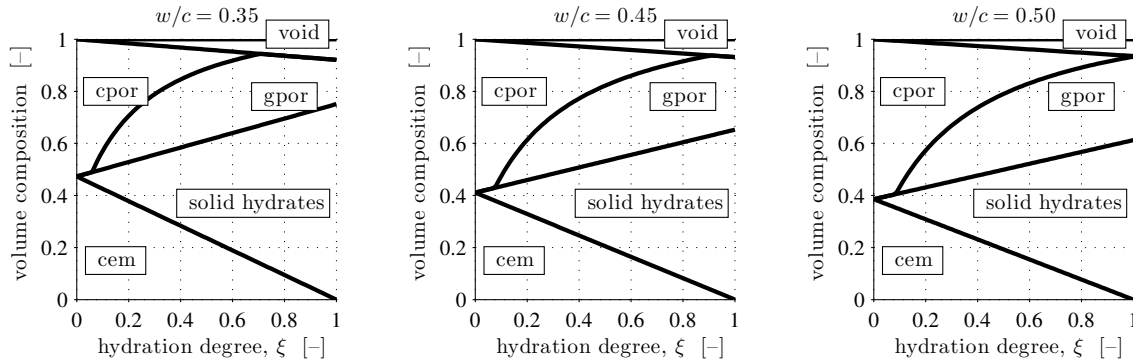


Figure 6.12: Phase volume fraction evolutions for pastes with $w/c \in \{0.35, 0.45, 0.50\}$, according to the mathematical model defined by Eqs. (6.47)-(6.52)

6.4 Discussion

We here discuss five major issues: (i) the influence of the metrological uncertainty associated with NMR tests, on the quantities involved in the C-S-H densification model, (ii) the relation between existing C-S-H classifications (e.g. inner/outer products low/high density C-S-H) and

the newly introduced class A C-S-H and class B C-S-H, (iii) the density of solid C-S-H, (iv) the model sensitivities with respect to changes of the solid C-S-H density and of the reaction kinetics, as well as (v) theoretically reachable ultimate hydration degrees.

6.4.1 Assessment of uncertainty regarding NMR signal fractions

So far, NMR signal fractions were treated as *deterministic values*, but since measurements are unavoidably characterized by uncertainty, it is interesting to note that Muller (2014) estimate their measured NMR signal fractions to exhibit a metrological dispersion amounting to $\pm 2\%$. This raises the question how this uncertainty would affect quantities which are derived from the NMR fractions, such as the specific precipitation space, the density of class B C-S-H, the capillary pore fraction, and the gel pore fraction.

Herein, we derive upper and lower bounds for the mass density of class B C-S-H gel ρ_{Bgel} , as well as for the capillary pore fraction φ_{cpor} and for the gel pore fraction φ_{gpor} , as these bounds arise from the C-S-H densification model [Eqs. (6.12), (6.14)-(6.17), (6.30)-(6.36), (6.38), (6.39), and the numerical values summarized in Table 6.2] when specialized for NMR fraction values which are increased or decreased by 2%, respectively, see Figs. 6.13 (a) and (b). The uncertainty interval of ρ_{Bgel} is rather wide at the beginning of hydration regime II, and it decreases significantly with decreasing specific precipitation space, see Fig. 6.13 (a). The uncertainty interval of the pore ratios φ_{cpor} and φ_{gpor} , in turn, exhibits an almost constant width in hydration regime II, see Fig. 6.13 (b). This clarifies, *a posteriori*, the motivation to identify the four model parameters listed in Eq. (6.41) through minimizing errors regarding the capillary and gel pore fractions, see Eq. (6.40), rather than minimizing errors regarding the density of class B C-S-H gel.

6.4.2 Relation between existing C-S-H classifications and the new categories “class A/class B C-S-H”

The presented model is based on two classes of C-S-H: class A C-S-H and class B C-S-H. This is reminiscent of traditional approaches in cement and concrete research, where *two* distinct classes of C-S-H are distinguished:

1. *Inner products* and *outer products* were introduced by Taplin (1959). They refer to C-S-H forming either within or outside the initial clinker boundaries.
2. *Phenograin* and *groundmass* were introduced by Diamond and Bonen (1993). They refer to either visible or invisible microporosity in backscattered electron micrographs.
3. *Low-density C-S-H* and *high-density C-S-H* were introduced by Jennings (2000); Tennis and Jennings (2000). They refer to C-S-H which is penetrable or impenetrable by nitrogen in sorption experiments.

Deconvolution of frequency plots regarding indentation modulus and indentation hardness, obtained from nanoindentation grid indentation studies (Qomi et al., 2014; Constantinides and Ulm, 2004, 2007), revealed two characteristic peaks which can be associated with low and high density C-S-H. Since both probability distribution functions exhibit a considerable spread, C-S-H gel could also be seen as a *polymorph* material exhibiting a widespread density distribution (Juenger and Jennings, 2001; Muller et al., 2012, 2013).

The question arises how the two newly introduced C-S-H classes are related to the existing C-S-H classifications. Class A C-S-H refers to *solid C-S-H*, being free of gel pores, such that

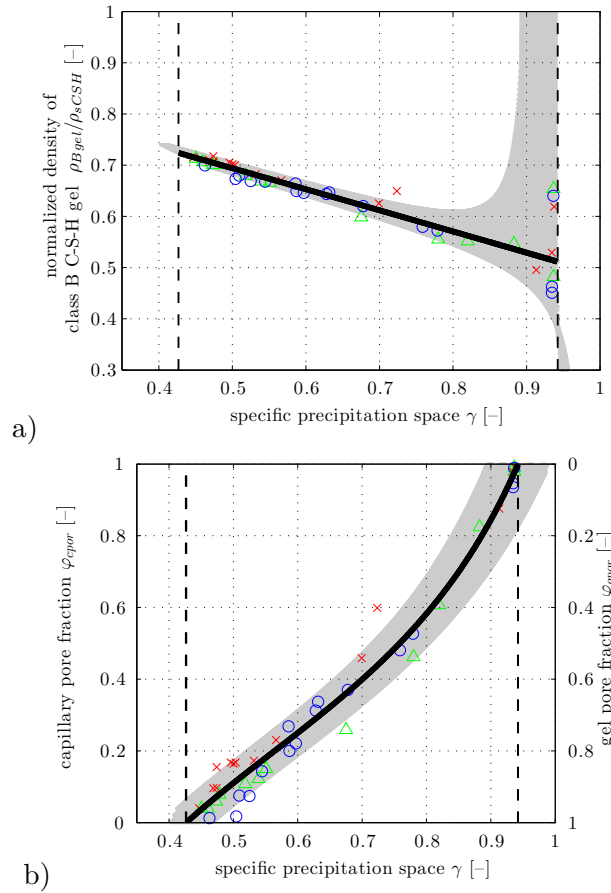


Figure 6.13: (a) Normalized density of class B C-S-H gel according to Eq. (6.15) as well as (b) capillary and gel pore fractions according to Eqs. (6.12), respectively, as functions of the specific precipitation space according to Eq. (6.9): gray areas refer to uncertainty intervals related to a metrological dispersion of $\pm 2\%$ of the underlying NMR signal fractions

expected density fluctuations of class A C-S-H are very small, see Fig. 6.14. This classification is new, given that all existing C-S-H classifications (see above) contain at least some gel pores. Class B C-S-H, in turn, refers to *C-S-H gel* exhibiting a widespread density distribution. The herein introduced *density of class B C-S-H gel* refers to the *average* of the underlying density distribution. NMR experiments, namely, provide access to the average density, while details regarding the underlying density distribution function remain inaccessible. In other words, also class B C-S-H is a new classification, referring to C-S-H including both inner products and outer products, as well as both low-density C-S-H and high-density C-S-H.

6.4.3 Is the density of solid C-S-H indeed constant?

We have followed the diffraction data-derived suggestion of Allen et al. (2007), that the solid C-S-H density $\rho_{s\text{CSH}}$ may be regarded as an invariant material property. However, NMR experiments of Muller et al. (2012, 2013) propose a (slight) decrease of the solid C-S-H density with increasing hydration degree, particularly so for hydration degrees exceeding 80 %, see Fig. 6.14. This slight decrease of density may be due to the formation of larger C-S-H compounds comprising more alternating calcium/silicate and water layers (Valori et al., 2013):

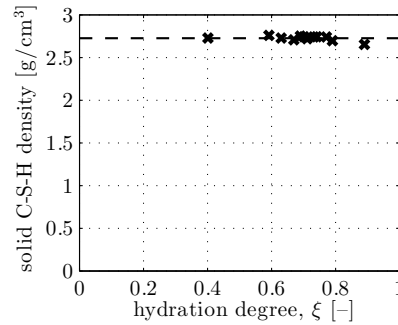


Figure 6.14: NMR-derived solid C-S-H density (points) for white cement paste with $w/c = 0.4$, as function of the hydration degree ξ , after (Muller et al., 2013); the dashed line represents the mean value amounting to $\rho_{sCSH} = 2.73 \text{ g/cm}^3$

As the two outermost layers are always made of calcium/silicate, such an increase of layers entails an increasing water volume fraction of the “calcium/silicate-water-nanocompound”. Still, these effects are of really subtle nature, so that Fig 6.14 actually supports the idea of an approximately constant solid C-S-H density, in particular so at early ages.

6.4.4 Sensitivity of the presented models, with respect to the density of solid C-S-H

The presented models for C-S-H gel densification and for phase volume evolutions were based on the density of solid C-S-H, $\rho_{sCSH} = 2.604 \text{ g/cm}^3$, which was quantified by means of small angle scattering techniques (Allen et al., 2007). Notably, this value is by 4.6 % smaller than the value of $\rho_{sCSH} = 2.73 \text{ g/cm}^3$, which was quantified from NMR experiments, see (Muller et al., 2013) and Fig. 6.14. This difference provides the motivation to study the sensitivity of the presented models with respect to the uncertainty regarding the density of solid C-S-H.

In order to quantify the sensitivity of the C-S-H densification model, we repeat the aforementioned computations, whereby we now use the NMR-related density $\rho_{sCSH} = 2.73 \text{ g/cm}^3$, rather than $\rho_{sCSH} = 2.604 \text{ g/cm}^3$. The results are almost identical to those obtained for $\rho_{sCSH} = 2.604 \text{ g/cm}^3$, as is underlined by fits which are in both cases characterized by a quadratic correlation coefficient amounting to $R^2 = 98 \%$, while the corresponding numbers for fitting parameters of Eq. (6.40) vary slightly, see Table 6.3. This underlines that the presented mathematical description of densification of C-S-H gel is very robust with respect to uncertainties regarding knowledge of the density of solid C-S-H – the latter is known to lie somewhere between 2.604 g/cm^3 (as derived from diffraction experiments (Allen et al., 2007)) and 2.73 g/cm^3 (as derived from NMR experiments (Muller et al., 2012, 2013)).

In order to quantify the sensitivity of the model-predicted phase volume evolutions, we re-evaluate the corresponding expressions, whereby we now use the NMR-related density $\rho_{sCSH} = 2.73 \text{ g/cm}^3$ rather than $\rho_{sCSH} = 2.604 \text{ g/cm}^3$. This increase of the density of solid C-S-H essentially manifests itself in an increase of autogeneous shrinkage, compare the V_{void}^m values given in Table 6.3. Still, the shrinkage-related reduction in volume is small in both cases, such that the phase volume evolutions change only marginally, compare Fig. 6.15 with Fig. 6.11. This underlines that also the presented mathematical description of phase volume evolutions is very robust with respect to uncertainties regarding the density of solid C-S-H.

In general, consideration of an evolving C-S-H gel density results in *nonlinear* evolutions of capillary and gel pore volume fractions. This is a notable difference to Powers’ *linear* phase

Table 6.3: Sensitivity of numerical values involved in the presented models with respect to changes in solid C-S-H density

ρ_{sCSH} [g/cm ³]	2.604	2.73
$\left \frac{d\rho_{Bgel}}{d\gamma} \right ^{\text{II}}$ [g/cm ³]	1.07	1.16
$\gamma_{\text{I-II}}$	0.942	0.945
$\gamma_{\text{II-III}}$	0.426	0.438
$\rho_{Bgel}(\gamma_{\text{II-III}})$ [g/cm ³]	1.89	1.94
V_{void}^m [cm ³ /mol]	10.91	14.24

volume evolutions, resulting from consideration of a constant C-S-H gel density (see Fig. 6.15).

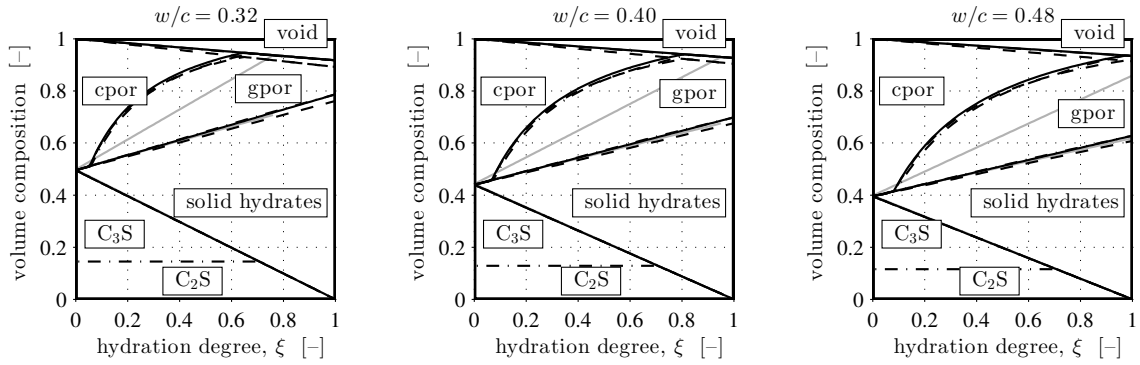


Figure 6.15: Comparison of phase volume fraction evolutions: continuous black lines refer to derivations described in Section 6.3, i.e. to $\rho_{sCSH} = 2.604$ g/cm³; dashed lines refer to same derivations, but evaluated for $\rho_{sCSH} = 2.73$ g/cm³; dashdotted lines refer to consideration of C₃S hydration prior to C₂S hydration; and gray solid lines refer to the Powers' hydration model (Powers and Brownyard, 1947; Hansen, 1986)

6.4.5 Sensitivity of model-predicted phase volume evolutions with respect to reaction rates of tricalcium silicate and dicalcium silicate

While tricalcium silicate (C₃S) actually reacts faster than dicalcium silicate (C₂S), see, e.g., (Odler, 1998), the phase volume evolution model presented here is based on the assumption of *identical* reaction rates, see Eq. (6.21). The resulting underestimation of the reaction kinetics of C₃S and overestimation of the reaction kinetics of C₂S motivates a sensitivity analysis on the model-predicted phase volume fractions, with respect the reaction rates of C₃S and C₂S. To this end, we now analyze the limit case of *sequential* hydration of C₃S and C₂S, i.e. hydration is considered to start with the consumption of C₃S only, and consumption of C₂S only starts once the C₃S is completely hydrated. This overestimates the reaction kinetics of C₃S and underestimates the reaction kinetics of C₂S. Therefore, the actual hydration rates will obviously fall within the two considered limit cases, sequential hydration versus simultaneous hydration at identical rates.

Actually, these two limit case computations deliver very similar results, see Fig. 6.15. This underlines that the presented model for phase volume evolutions is very robust with respect to uncertainties regarding knowledge on actual reaction rates of C₃S and C₂S.

Although it may seem conceptually desirable to use realistic hydration kinetics models such as the Avrami model, see (Bernard et al., 2003b), or thermodynamics approaches (Lothenbach and Winnefeld, 2006), such models would significantly increase the complexity of the analytical mathematical expressions for the phase volume evolutions, while they, most probably, would not significantly increase their reliability for Portland cement pastes. The presented expressions given in Eqs. (6.47) to (6.52), in turn, appear to be appealing because they are comparably simple, and at the same time, they turn out to be robust enough for many practical purposes. In this context, it appears as interesting future task to use the presented phase volume evolution expressions as input for improved versions of multiscale models for elasticity, creep, and strength of cementitious materials, continuing the line of research documented in (Sanahuja et al., 2007; Stefan et al., 2010; Scheiner and Hellmich, 2009; Pichler et al., 2009; Pichler and Hellmich, 2011), which so far, has been based on the original Powers' model.

6.4.6 Theoretically reachable ultimate hydration degrees

Finally, we here discuss theoretically reachable ultimate hydration degrees. Noting that 208.0 g/mol of clinker require only 49.32 g/mol of water for complete hydration, see Eq. (6.21), every composition exhibiting an initial water-to-cement mass ratio larger than $(w/c)_{lim} = 49.32/208.0 = 0.237$ contains (at least theoretically) enough water for complete hydration of cement, hence the ultimate hydration degree $\xi_{ult} = 1$ (Fig. 6.10). Sub-stoichiometric compositions, $w/c < (w/c)_{lim}$, do not contain enough water for complete hydration and the ultimate hydration degree decreases proportionally to w/c , i.e. $\xi_{ult} = (w/c)/(w/c)_{lim} = 4.217 w/c$, see Fig. 6.10.

6.5 Conclusion

We here studied the hydration-induced evolution of the C-S-H gel density, based on data from ^1H nuclear magnetic resonance relaxometry carried out on three different Portland cement pastes with initial water-to-cement mass ratios $w/c \in \{0.32, 0.40, 0.48\}$, curing at 20°C , see (Muller et al., 2012) and Fig. 6.1. Our analysis considers two C-S-H composites containing nanometer-sized solid C-S-H and pores of different sizes: *C-S-H gel* consists of solid C-S-H and gel pores, while *C-S-H foam* consists of solid C-S-H as well as gel *and* capillary pores. The results of our analyses suggest the following conclusions:

- C-S-H gel density is a w/c -independent function of the specific precipitation space (Fig. 6.3). The latter is the porosity of the C-S-H foam. This corroborates the nowadays widely discussed expectation that C-S-H gel density would be controlled by the available precipitation space.
- The total C-S-H gel density evolves nonlinearly during hydration: it is practically equal to the solid C-S-H density at very early ages, then it decreases quickly by some 40 %, and after this minimum, the density increases again. Cement paste with $w/c = 0.32$, for instance, reaches 90 % of the solid C-S-H density a few months after production. This underlines that the *total* C-S-H gel density is *not* progressively densifying.
- The nonlinear evolution of total C-S-H gel density can be traced back to three underlying successive hydration regimes, and to two classes of C-S-H:

- Hydration regime I covers the first few hours after mixing cement and water. *Ordered calcium-silicate-hydrates* (class A C-S-H) precipitate on electrically charged clinker surfaces (Nachbaur et al., 1998) without forming any gel porosity. Consequently, at that stage, the “gel” density is equal to the solid C-S-H density.
 - Hydration regime II starts a few hours after mixing, once formation of ordered class A C-S-H comes to an end and *less ordered calcium-silicate-hydrates* (class B C-S-H) form, this time enclosing gel pores. Thereby, two precipitation mechanisms are happening simultaneously at two different length scales: (i) at the larger length scale of the capillary porosity, class B C-S-H gel grows into the interstitial space, and (ii) at the smaller length scale of the gel pores, the gel gradually densifies because calcium-silicate-hydrates precipitate also out of the supersaturated water which fills the gel pores.
 - Hydration regime III starts once class B C-S-H gel has completely filled the interstitial space, such that the water-filled capillary porosity vanishes and the precipitation of calcium-silicate-hydrates is restricted to the gel pores only. This manifests itself in a linear increase of the total C-S-H gel density with decreasing specific precipitation space.
- The nonlinear evolution of total C-S-H gel density in hydration regime II results from the terminated formation of the “totally compact” class A C-S-H and the new formation of class B C-S-H gel which densifies linearly with decreasing specific precipitation space. At the beginning of hydration regime II, the total C-S-H gel density decreases with decreasing precipitation space, because class A C-S-H is no longer produced and class B C-S-H gel grows so quickly into the interstitial space that production of new gel porosity outperforms its densification. The minimum of total C-S-H gel density is reached somewhere around (but not exactly at) the maximum heat release rate marking the transition from the acceleration period of hydration to the deceleration period. In the latter period, the hydration kinetics are well known to decelerate significantly, such that the densification of already formed class B C-S-H gel outperforms the generation of new gel porosity associated with the new production of class B C-S-H gel. Consequently, the total C-S-H gel density increases with decreasing precipitation space.
 - Combining the described precipitation theory with traditional reaction equations for typical Portland cement pastes allows for deriving analytical expressions linking the phase volumes to the initial water-to-cement mass ratio w/c and to the hydration degree ξ , see in particular Eqs. (6.25), (6.30), and (6.31); as well as (6.38) and (6.39) in combination with (6.32). The new hydration model suggests that the nonlinear C-S-H gel density evolution in the central hydration regime II relates to gel and capillary porosities which depend *nonlinearly* on the hydration degree. Also, the new model describes continued hydration in hydration regime III, where the capillary porosity does not exist anymore. The model considers that hydrates precipitate out of the supersaturated water filling the gel pores, resulting in progressive densification of the C-S-H gel.
 - The new hydration model appears as interesting alternative to Powers’ model (which assumes constant C-S-H gel density) and is expected to translate straightforwardly NMR-provided insight concerning C-S-H gel densification, into quantitative input for multiscale models predicting the poromechanical properties of hydrating Portland cement pastes.

Appendix A: Nomenclature

Abbreviations

<i>ACSH</i>	Class A C-S-H
<i>Bgel</i>	Class B C-S-H gel
CH	Calcium Hydroxide, Portlandite
<i>cpor</i>	Capillary pores, capillary water
C-S-H	Calcium Silicate Hydrate
<i>gel</i>	C-S-H gel
<i>gpor</i>	Gel pores, gel water
H ₂ O	Water
NMR	Nuclear Magnetic Resonance
<i>PE</i>	Portlandite and Ettringite
<i>sCSH</i>	Solid C-S-H
<i>void</i>	Voids

Mathematical symbols

f_j^{cp}	Cement paste-related volume fraction of material phase j
I_j	NMR-based signal fraction of phase j
m_j	Mass of phase j
$m_{H_2O}^j$	Mass of water fraction in phase j
t	Material age
V_j	Volume of phase j
V_j^m	Volume of phase j after hydration of 1 mole of typical Portland cements
w/c	Initial water-to-cement mass ratio
$(w/c)_{lim}$	Initial water-to-cement mass ratio w/c required for full hydration of typical Portland cements
$\mu_{H_2O}^{sCSH}$	Mass fraction of water within solid C-S-H
γ	Specific precipitation space
γ_{I-II}	γ at the transition point from hydration regime I to II
γ_{II-III}	γ at the transition point from hydration regime II to III
ΔV_j	Chemically consumed volume of phase j during hydration
ξ	Hydration degree
ξ_{I-II}	Hydration degree ξ at the transition from hydration regime I to II
ξ_{II-III}	Hydration degree ξ at the transition from hydration regime II to III
ξ_{ult}	Ultimate hydration degree
ρ_j	Mass density of phase j
φ_{cpor}	Capillary pore fraction (capillary pore volume divided by total water-filled pore volume)
φ_{gpor}	Gel pore fraction (gel pore volume divided by total water-filled pore volume)
$\varphi_{cpor}^{exp}, \varphi_{gpor}^{exp}$	NMR-derived values of φ_{cpor} and φ_{gpor}
$\varphi_{cpor}^{mod}, \varphi_{gpor}^{mod}$	Model-predicted values of φ_{cpor} and φ_{gpor}

Molecular-to-continuum poroelasticity upscaling of hydrating cement pastes, considering progressive C-S-H gel densification

Authored by: Markus Königsberger, Christian Hellmich, and Bernhard Pichler

Publication outlook: At the time of finalizing this thesis, it is planned to submit this mature paper draft – after incorporation of further improvements – for publication to *Cement and Concrete Research*.

Abstract: We here bridge the molecular-to-continuum gap in cement poroelasticity, providing a multiscale poro-micromechanical representation allowing for predictive upscaling of elasticity properties of nanoscopic solid C-S-H blocks, as determined from statistical physics (Manzano et al., 2012), to poroelastic properties at the cement paste and the capillary pore-hosting hydrate foam scale, as obtained from resonance frequency, ultrasonic, or quasi-static unloading tests. The success of the novel predictive model stems from explicit consideration of (i) densification of the C-S-H gel during the hydration process, i.e. of C-S-H basic blocks with gel porosity in-between, as evidenced by recent nuclear magnetic resonance relaxometry experiments (Muller et al., 2012) and cast in a mathematical evolution rule thereafter (Königsberger et al., 2016a), and of (ii) the shape of the basic C-S-H units, precipitating as plate-type features at early hydration stages (Garraut et al., 2005), but showing a variety of shapes with ongoing chemical reactions at more mature stages (Chiang et al., 2012). At the cement paste scale, elastic moduli increase with increasing hydration degree and decreasing initial water-to-cement mass ratio; while within the C-S-H gel, the hydration characteristics results in non-monotonous relationships. The same is also true for the Biot coefficients and moduli.

Contribution: Bernhard Pichler and Christian Hellmich set up the overall research strategy, supervised the research progress, checked key results, and supported the documentation process. Markus Königsberger developed the microstructural model, performed continuum micromechanics-based poroelasticity upscaling, validated the model based on stiffness data

from the literature, and documented research results.

Keywords: micromechanics, poromechanics, cement paste, Calcium-Silicate-Hydrates (C-S-H), hydration, multiscale modeling

7.1 Introduction

A rigorous material mechanics framework for hydrating cement paste and concrete poses great challenges, as the material is chemically active and therefore exhibits elastic, viscoelastic, and strength properties, which evolve with time. This has kept the material mechanics community busy over decades, developing more and more precise and physically sound mathematical formulations. Important steps thereby are thermodynamics-based formulations (Ulm and Coussy, 1995, 1996; Sercombe et al., 2000) introducing the degree of hydration and the reaction kinetics into material mechanics; and micromechanics formulations (Bernard et al., 2003b; Ulm and Heukamp, 2004; Sanahuja et al., 2007; Scheiner and Hellmich, 2009; Pichler and Hellmich, 2011) resolving the material into non-reactive basic components: unhydrated clinker, water, air, aggregate, and one or several types of hydrates (the hydration products between water and clinker). Invariant mechanical properties of these basic components have thereby been estimated from nanoindentation (Constantinides et al., 2003; Constantinides and Ulm, 2004; Sorelli et al., 2008) or from top-down back-analyses based on very many experiments on the composite material level (Pichler et al., 2013a; Königsberger et al., 2016b; Irfan-ul Hassan et al., 2016).

There is still a gap between such basic mechanical properties, and those found, by a bottom-up approach based on statistical physics methods (Pellenq et al., 2009; Manzano et al., 2012; Ioannidou et al., 2016), at an even smaller level of the fundamental calcium-silicate-hydrate (C-S-H) building block (Allen et al., 2007). The present contributions seeks to close this remaining gap, by carefully investing into an appropriate representation of the complex hierarchical nano- and microstructure of cement paste and concrete, and its physical properties. In fact, two features which hitherto have remained ignored in the pertinent literature on the topic so far, are explicitly considered here: (i) densification of the C-S-H gel during the hydration process, i.e. of C-S-H basic blocks with gel porosity in-between, as evidenced by recent nuclear magnetic resonance (NMR) relaxometry experiments (Halperin et al., 1994; Muller et al., 2012, 2013; Valori et al., 2013) and cast in a mathematical evolution rule thereafter (Königsberger et al., 2016a), and (ii) the shape of the basic C-S-H units, precipitating as plate-type features at early hydration stages (Garraut et al., 2005), but showing a variety of shapes with ongoing chemical reactions at more mature stages (Chiang et al., 2012). The corresponding material description is cast in the framework of micro-poromechanics (Dormieux et al., 2006), making in particular use of an extended form of the so-called transformation field analysis (Dvorak and Benveniste, 1992; Pichler and Hellmich, 2010) allowing for eigenstress upscaling from arbitrarily oriented and shaped material phases, to the scale of homogenized poroelastic media.

Accordingly, the remainder of this paper is structured as follows: First, the homogenization concept is explained and the microstructural representation of hydrating cement pastes is introduced, see Sec. 7.2. This is followed by discussing the volume evolutions of the cement paste constituents considering the NMR-derived densification, see Sec. 7.2. Next, the poromechanical behavior is scaled up throughout the different observation scales, see Sec. 7.4-7.6. In Sec. 7.7, the pore pressures are determined based on the macroscopic loading. This yields macroscopic poromechanics state equations and an expression for the undrained stiffness of cement paste, see Sec. 7.8. Careful model validation based on independent experimental

data is carried out in Sec. 7.9. The paper is closed with discussions on pore pressure-induced stiffening effects and on the dependencies of the predicted poroelastic properties with respect to maturity and composition; and finally with concluding remarks, see Sec. 7.10.

7.2 Homogenization of poromechanical properties and micromechanical representation of hydrating cement paste

We consider cement paste as a macro-homogeneous, but micro-heterogeneous matter filling a representative volume element (RVE), (Zaoui, 2002; Hill, 1963), fulfilling the separation of scales principle, reading as

$$d \ll \ell \ll \mathcal{L} \quad (7.1)$$

Inequalities (7.1) imply that the characteristic size ℓ of an RVE is considerably larger than the characteristic size d of the heterogeneities contained inside the RVE and, at the same time, ℓ is considerably smaller than characteristic size \mathcal{L} of the structure containing the RVE. Notably, the aforementioned requirements of “much larger” (\gg) and “much smaller” (\ll), respectively, have been shown to be already satisfied if the respective characteristic lengths are separated by a factor of two to three, and five to ten, respectively (Drugan and Willis, 1996; Kohlhauser and Hellmich, 2013). Inside such RVEs, the morphological details are represented in the form of homogeneous subdomains called phases. Then, the shape of these phases, their poro-mechanical properties and their volume fractions are used for estimating the overall (“homogenized”) mechanical properties of the RVE: therefore, homogeneous deformation or traction boundary conditions, related to “macroscopic” strains or pore pressures, are enforced at the external and internal boundaries of the RVE, while the virtual power equivalence of “macroscopic” and “microscopic” (phase-specific) physical quantities is maintained (Germain, 1973; Dormieux et al., 2006). The mechanical properties of the phases may arise from yet another homogenization process across another RVE, of size $\ell_2 \leq d$ and $\ell_2 \gg d_2$; and this leads to the introduction of multiscale homogenization schemes as described in (Fritsch and Hellmich, 2007), involving a sequence of characteristic sizes; fulfilling in the case of three such schemes

$$\mathcal{L} \gg \ell \gg d \geq \ell_2 \gg d_2 \geq \ell_3 \gg d_3. \quad (7.2)$$

In the case of cement paste, we indeed employ such a sequence of three RVEs, as depicted in Fig. 7.1. An RVE of cement paste sized around 1 mm [see Fig. 7.1(a)] consists of the phases “(unhydrated) clinker”, “portlandite”, and “C-S-H foam”. The mechanical properties of the latter are approximated from homogenization over yet another RVE [see Fig. 7.1(b)], which consists of the phases “C-S-H gel”, “capillary pores”, and “air voids”. Gel and capillary pores not only relate different length scales (Muller et al., 2012), but also to different physical characteristics: gel water is strongly influenced by surface forces, while capillary water is not. The mechanical properties of C-S-H gel are obtained from a third homogenization step [see Fig. 7.1(c)], involving the phases called “gel pores” and “solid C-S-H crystals” (the properties of which are those resulting from the bottom-up statistical physics approach of Manzano et al. (2012), alluded to already in the Introduction). Besides the remaining elastic phase properties, i.e. that of the pores, of portlandite, and of unhydrated clinker, the volume fractions are the key input parameters involved in the three-level scheme depicted in Fig. 7.1. They are derived from latest results in NMR research, as described next.

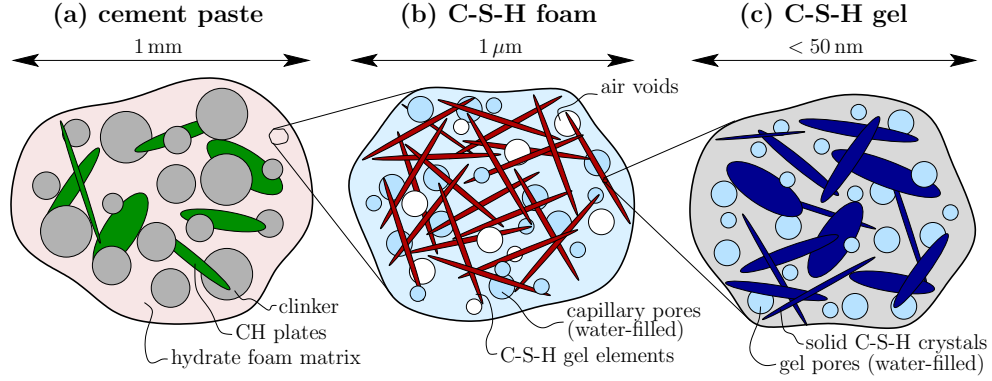


Figure 7.1: Three-scale representation of cement paste: (a) single millimeter-sized RVE of cement paste: clinker grains and portlandite crystals embedded in a C-S-H foam matrix; (b) single micrometer-sized RVE of C-S-H foam: C-S-H gel needles intermixed with capillary pores; (c) 50 nm-sized RVE of C-S-H gel: solid C-S-H building blocks with gel pores in between

7.3 Phase volume evolutions considering progressive C-S-H gel densification

In order to quantify the hydration-driven phase volume evolution, existing micromechanics models (see e.g. (Sanahuja et al., 2007; Scheiner and Hellmich, 2009; Pichler and Hellmich, 2011)) typically rest on the Powers' hydration model (Powers and Brownayard, 1947; Powers, 1958). However, NMR relaxometry measurements on white cement pastes, performed by Muller et al. (Muller et al., 2012, 2013), have shown that C-S-H gel densifies during hydration, rather than maintaining a constant mass density, as assumed by Powers and Brownayard (1947). The NMR-evidenced gel densification has been translated into a mathematical evolution rule by Königsberger et al. (2016a), and the resulting, alternative hydration model is used hereafter.

This model is based on the idea that it is the confinement of space in the water-filled pores, which governs the densification of the C-S-H gel. This confinement is quantified by means of the specific precipitation space γ . Denoting the volume occupied by solid C-S-H as V_{sCSH} , the volume occupied by gel porosity as V_{gpor} , and the volume occupied by capillary porosity as V_{cpor} , the specific precipitation space is defined as (Königsberger et al., 2016a)

$$\gamma = \frac{V_{gpor} + V_{cpor}}{V_{sCSH} + V_{gpor} + V_{cpor}}, \quad 0 \leq \gamma \leq 1. \quad (7.3)$$

This way, γ suitably quantifies the available space where solid C-S-H crystals can precipitate, and thus characterizes the confinement state in the water-filled pore space. Remarkably, the relation between the NMR-derived C-S-H gel density ρ_{gel} and the precipitation space is fully independent of the material composition as quantified by the initial water-to-cement mass ratio w/c , see Fig. 7.2. The obtained relation also reveals that the hydration process – the progress of which is customarily described by a hydration degree ξ (defined as the volume of already hydrated cement clinker over the initially available clinker volume) – comprises three characteristic precipitation regimes (Königsberger et al., 2016a):

- Regime I ($0 \leq \xi \leq \xi_{I-II}$), is characterized by precipitation of C-S-H solids without entrapment of any gel porosity.
- In regime II ($\xi_{I-II} < \xi < \xi_{II-III}$), C-S-H precipitates as gel with entrapped gel pores, and

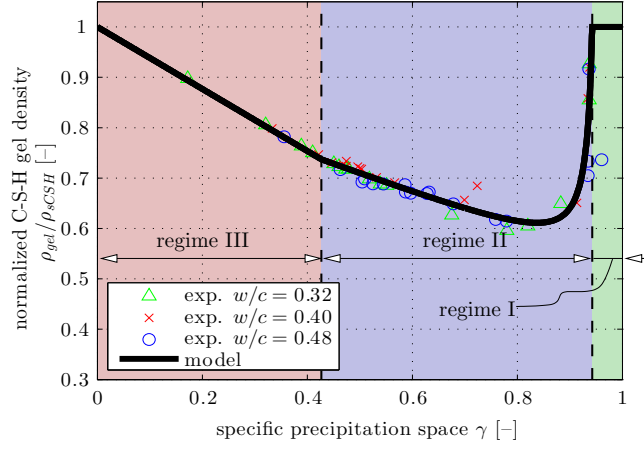


Figure 7.2: C-S-H gel density (normalized with respect to the solid C-S-H density $\rho_{sCSH} = 2.604 \text{ g/cm}^3$, see (Allen et al., 2007)) as function of the specific precipitation space: experimental points from NMR relaxometry for three different cement pastes exhibiting $w/c \in \{0.32, 0.40, 0.48\}$, as provided by Muller et al. (2012, 2013); and model-predicted density evolution according to Königsberger et al. (2016a)

which exhibits a density increasing linearly with decreasing precipitation space. This process is accompanied by a progressive reduction of the capillary porosity as the water residing there drives the hydration process.

- Once all capillary pore water is consumed, hydration regime III ($\xi_{II-III} \leq \xi \leq 1$) starts. Further precipitation is forced to happen on the expense of the water in the gel pores. This leads to a further densification of the C-S-H gel.

Stoichiometric equations for the hydration of alite and belite in combination with the assumption that the considered clinker phases dissolve proportionally to their initial extend allows for predicting, from the modeled C-S-H gel densification behavior, the volumes of the cement paste constituents, as functions of the hydration degree ξ and of the water-to-cement mass ratio w/c . Dividing the individual phase volumes by the total cement paste volume, we end up with cement paste-related phase volume fractions, labeled as f_i^{cp} with i standing for cement clinker (abbreviated as *cem*), portlandite crystals (*CH*), solid C-S-H crystals (*sCSH*), gel pores (*gpor*), capillary pores (*cpor*), and voids (*void*), reading as (Königsberger et al.,

2016a)

$$f_{cem}^{cp} = \frac{1 - \xi}{1 + 3.185 w/c} \geq 0 \quad (7.4)$$

$$f_{CH}^{cp} = \frac{0.484 \xi}{1 + 3.185 w/c} \quad (7.5)$$

$$f_{sCSH}^{cp} = \frac{1.105 \xi}{1 + 3.185 w/c} \quad (7.6)$$

$$f_{gpor}^{cp} = \begin{cases} 0 & \forall 0 \leq \xi \leq \xi_{I-II} \\ \frac{-0.799 (w/c)^2 + 4.824 w/c \xi - 0.793 \xi^2}{(1 + 3.185 w/c) (0.864 w/c + 1.278 \xi)} & \forall \xi_{I-II} < \xi < \xi_{II-III} \\ \frac{3.185 w/c - 0.755 \xi}{1 + 3.185 w/c} & \forall \xi_{II-III} \leq \xi \leq 1 \end{cases} \quad (7.7)$$

$$f_{cpor}^{cp} = \frac{3.185 w/c - 0.755 \xi}{1 + 3.185 w/c} - f_{gpor}^{cp} \quad (7.8)$$

$$f_{void}^{cp} = \frac{0.167 \xi}{1 + 3.185 w/c} \quad (7.9)$$

The three precipitation regimes are bounded, for the white cement paste studied from Muller et al. (2013), by the hydration degrees (Königsberger et al., 2016a)

$$\xi_{I-II} = 0.170 w/c \quad \xi_{II-III} = 2.022 w/c. \quad (7.10)$$

Theoretically, hydration either stops if all clinker is consumed, $\xi \leq 1$, or if – focusing on sealed conditions – all mixing water is consumed. The latter implies that $\xi \leq 4.217 w/c$, see (Königsberger et al., 2016a). We can simultaneously represent both conditions through introduction of an ultimate hydration degree $\xi_{ult} \geq \xi$, reading as

$$\xi_{ult} = \min \{4.217 w/c; 1\}. \quad (7.11)$$

However, once regime III is reached, the water necessary for further hydration exclusively comes from the gel water, i.e. the water in the nanometer-sized gel pores. Consequently, further hydration slows down significantly, so that the ultimate hydration degree may be reached only after a very long time.

The hydration model was derived on the basis of the experimental densification characteristics determined on white cement paste samples. Given the chemical analogy between white cement paste and Portland cement paste (Neville, 1995), the model is expected to reasonably approximate the volume evolutions of Portland cement pastes as well.

7.4 Microporoelasticity of cement paste

In the following, a micro-poromechanics approach considering eigenstresses in arbitrarily shaped phases (Pichler and Hellmich, 2010) will be applied for upscaling pore pressures and elastic properties from the phase level to the RVE level, based on the microstructural representation of hydrating cement pastes, depicted in Fig. 7.1. We start from the largest observation scale, i.e. the scale of cement paste [see Fig. 7.1(a)], and subsequently we move to the C-S-H foam [see Fig. 7.1(b)], and thereafter to the C-S-H gel [see Fig. 7.1(c)].

In an RVE of cement paste, we consider the following bulk material phases: an unhydrated clinker phase of approximately spherical shape (indicated by subscript “*cem*”), infinitely many disc-shaped portlandite phases which are uniformly oriented in all space directions (indicated by subscript “*CH*”), and a C-S-H foam phase (indicated by subscript “*foam*”), see Fig. 7.1(a). Portlandite crystals are considered as phase on the cement paste scale because they precipitate as crystals with diameters up to 50 microns (Pratt et al., 1983) in the first hours of hydration, which is comparable to typical clinker grain sizes (Sun et al., 2007). This is in accordance with earlier micromechanics models (Bernard et al., 2003b; Venkovic et al., 2013). The spherical disc-like shape of these crystal phases is approximately consistent with observations from environmental scanning electron microscopy (Meredith et al., 1995), showing the precipitation of thin hexagonal platelets in particular at early age. The orientations of the individual crystal phases are quantified through the normal vectors \underline{n}_{CH} aligned with the axes of rotational symmetry of the crystals, see Fig. 7.11 in Appendix A.

The elastic properties of the unhydrated clinker phase are isotropic, quantified in terms of bulk modulus $k_{cem} = 116.7$ GPa and shear modulus $\mu_{cem} = 53.8$ GPa, see (Velez et al., 2001; Pichler and Hellmich, 2011). Accordingly, the phase stiffness tensor of cement clinker \mathbb{C}_{cem} reads as

$$\mathbb{C}_{cem} = 3k_{cem}\mathbb{I}_{vol} + 2\mu_{cem}\mathbb{I}_{dev} \quad (7.12)$$

with \mathbb{I}_{vol} and \mathbb{I}_{dev} standing for the volumetric and the deviatoric part of the fourth-order unity tensor \mathbb{I} , respectively. They are defined as $\mathbb{I}_{vol} = 1/3(\mathbf{1} \otimes \mathbf{1})$, and $\mathbb{I}_{dev} = \mathbb{I} - \mathbb{I}_{vol}$, whereby the components of \mathbb{I} read as $I_{ijkl} = 1/2(\delta_{ik}\delta_{jl} + \delta_{il}\delta_{jk})$, and where $\mathbf{1}$ denotes the second-order identity tensor with components equal to the Kronecker delta δ_{ij} , namely $\delta_{ij} = 1$ for $i = j$, and 0 otherwise. Portlandite crystals exhibit a layered structure and therefore an intrinsic anisotropy (Speziale et al., 2008). Holuj et al. (1985b) measured their stiffness by Brillouin spectroscopy and found stiffness tensor components (in Kelvin-Mandel notation (Cowin and Mehrabadi, 1992), see also Appendix A) reading as

$$\mathbb{C}_{CH} = \begin{bmatrix} 99.3 & 36.2 & 29.7 & 0 & 0 & 0 \\ 36.2 & 102 & 29.7 & 0 & 0 & 0 \\ 29.7 & 29.7 & 32.6 & 0 & 0 & 0 \\ 0 & 0 & 0 & 19.7 & 0 & 0 \\ 0 & 0 & 0 & 0 & 19.7 & 0 \\ 0 & 0 & 0 & 0 & 0 & 70.0 \end{bmatrix} \text{ GPa}, \quad (7.13)$$

$\underline{e}_\theta, \underline{e}_\varphi, \underline{e}_r$

whereby the components are given in a local CH crystal-related base frame with base vectors \underline{e}_θ and \underline{e}_φ defining planes being parallel to the crystal and with $\underline{e}_r = \underline{n}_{CH}$ representing the axis of rotational symmetry. The stiffness tensor of the C-S-H foam phase evolves during the hydration process. Consequently, it follows from homogenization over lower-scale RVEs, determined in Sec. 7.5. Furthermore, the C-S-H foam is the only phase in the RVE of cement paste, which exhibits eigenstresses $\sigma_{foam}^{hom,E} = -p_{foam}\mathbf{1}$, whereby p_{foam} is the pressure exerted by the foam to the adjacent matter within the RVE. These eigenstresses are obtained by means of homogenization over the RVE of C-S-H foam, as described in Sec. 7.5.

Based on the aforementioned elastic properties and eigenstresses, homogenization theory (Dormieux et al., 2006; Pichler and Hellmich, 2010) provides the first poromechanical state equation in the form

$$\sigma_{cp} = \mathbb{C}_{cp}^{hom} : \varepsilon_{cp} + \sigma_{cp}^{hom,E}, \quad (7.14)$$

where σ_{cp} and ε_{cp} denote macrostresses and macrostrains at the scale of cement paste, while \mathbb{C}_{cp}^{hom} and $\sigma_{cp}^{hom,E}$ denote the isotropic homogenized stiffness and the homogenized eigenstress

of cement paste. The isotropic cement paste stiffness reads as (Benveniste, 1987; Fritsch et al., 2006, 2010)

$$\begin{aligned} \mathbb{C}_{cp}^{hom} = & f_{cem}^{cp} \mathbb{C}_{cem} : \mathbb{A}_{cem} + f_{CH}^{cp} \int_0^{2\pi} \int_0^\pi \mathbb{C}_{CH}(\underline{n}_{CH}) : \mathbb{A}_{CH}(\underline{n}_{CH}) \frac{\sin \vartheta}{4\pi} d\vartheta d\varphi \\ & + f_{foam}^{cp} \mathbb{C}_{foam}^{hom} : \mathbb{A}_{foam}, \end{aligned} \quad (7.15)$$

whereby the uniform orientation of the CH crystals is captured by means of integration along the unit sphere in terms of azimuth angle φ and zenith angle ϑ , respectively, which determine the orientation of the orientation vector \underline{n}_{CH} , see Appendix A and in particular Fig. 7.11(a) for more details. Cement paste-related volume fractions f_{cem}^{cp} , f_{CH}^{cp} , and f_{foam}^{cp} are directly provided by the hydration model [see (7.4)-(7.9) in Sec. 7.3], whereby the foam volume fraction is obtained as

$$f_{foam}^{cp} = f_{sCSH}^{cp} + f_{gpor}^{cp} + f_{cpor}^{cp} + f_{void}^{cp}. \quad (7.16)$$

Moreover, \mathbb{A}_{cem} , \mathbb{A}_{CH} , and \mathbb{A}_{foam} denote the phase strain concentration tensors, see Appendix C for details. These strain concentration tensors reflect the mechanical interaction of the phases within an RVE of cement paste, namely that clinker and CH inclusions are embedded into a C-S-H foam matrix. A homogenization approach related to such a mode of interaction is normally called Mori-Tanaka scheme (Mori and Tanaka, 1973). The homogenized eigenstresses, in turn, follow from Levin's theorem and read as (Levin, 1967; Zaoui, 2002; Dormieux et al., 2006)

$$\boldsymbol{\sigma}_{cp}^{hom,E} = f_{foam}^{cp} \boldsymbol{\sigma}_{foam}^{hom,E} : \mathbb{A}_{foam}. \quad (7.17)$$

The second state equation of poromechanics relates macrostrains and phase eigenstresses to phase strains (in particular pore space changes). Homogenization theory provides access via the so-called transformation field analyses (Dvorak and Benveniste, 1992; Pichler and Hellmich, 2010), so that the RVE of cement paste is characterized by

$$\boldsymbol{\varepsilon}_{cem} = \mathbb{A}_{cem} : \boldsymbol{\varepsilon}_{cp} - \mathbb{Q}_{cem,foam} : \boldsymbol{\sigma}_{foam}^{hom,E}, \quad (7.18)$$

$$\boldsymbol{\varepsilon}_{CH}(\underline{n}_{CH}) = \mathbb{A}_{CH}(\underline{n}_{CH}) : \boldsymbol{\varepsilon}_{cp} - \mathbb{Q}_{CH,foam}(\underline{n}_{CH}) : \boldsymbol{\sigma}_{foam}^{hom,E}, \quad (7.19)$$

$$\boldsymbol{\varepsilon}_{foam} = \mathbb{A}_{foam} : \boldsymbol{\varepsilon}_{cp} - \mathbb{Q}_{foam,foam} : \boldsymbol{\sigma}_{foam}^{hom,E}, \quad (7.20)$$

where $\mathbb{Q}_{j,foam}$ denote the phase eigenstress influence tensors, relating the homogenized eigenstress of C-S-H foam, $\boldsymbol{\sigma}_{foam}^{hom,E}$, to the average strains of phase j , $\boldsymbol{\varepsilon}_j$. Analytical expressions for all eigenstress influence tensors $\mathbb{Q}_{j,foam}$ are given in Appendix C.

7.5 Microporoelasticity of C-S-H foam

In an RVE of C-S-H foam [see Fig. 7.1(b)], we consider the following phases: two spherical phases representing air voids (subscript “*void*”) and water-filled capillary porosity (subscript “*cpor*”), and infinitely many, needle-shaped phases oriented in all space directions, representing C-S-H gel elements (subscript “*gel*”). Thereby the orientation of the individual C-S-H gel phases is indicated by the orientation vector \underline{n}_{gel} , see Appendix A and Fig. 7.11(b). The considered morphology of C-S-H gel elements follows from experimental observation by means of Scanning Electron Microscopy (SEM), secondary SEM (Pratt et al., 1983; Williamson,

1972), environmental SEM (Meredith et al., 1995), backscatter-mode SEM (Scrivener, 2004; Diamond, 2004; Kjellsen and Justnes, 2004), transition electron microscopy (TEM) (Jennings et al., 1981; Richardson and Groves, 1993; Richardson, 1999) and atomic force microscopy (AFM) (Garraut et al., 2005). It is described as strongly heterogeneous material with fibrillar (Jennings et al., 1981; Kjellsen and Justnes, 2004), reticular, foil-like (Kjellsen and Justnes, 2004), flaky or plate-like (Jennings et al., 1981; Garraut et al., 2005; Chiang et al., 2012), or amorphous morphology, varying with age (Kjellsen and Justnes, 2004), cement composition (Scrivener and Nonat, 2011), temperature (Kjellsen et al., 1991), and with the position of precipitation (inside or outside the shell around clinker grains) (Pratt et al., 1983). Herein, we focus on plain Portland cement, which predominately exhibits fibrillar gel morphologies (Scrivener and Nonat, 2011). Following Pichler and Hellmich (Pichler and Hellmich, 2011), we use infinitely many needles, oriented uniformly in all space directions, to represent this fibrillar morphology of the C-S-H gel in our micromechanics model. The micromechanical combination of isotropically oriented needles with spheres, in a self-consistent setting, has been endured as the optimal choice for representing a disordered network of needle-shaped elements with pore space in between (Sanahuja et al., 2010).

Only gel phases exhibit a non-zero stiffness tensor, which evolves during hydration, and is therefore obtained from homogenization over a lower-scale RVE, as described in Sec. 7.6. On the other hand, the C-S-H gel elements also exhibit orientation-specific eigenstresses $\sigma_{gel}^{hom,E}(\underline{n}_{gel})$, which also follows from homogenization over a lower-scale RVE, as described in Sec. 7.6. In addition, also the capillary porosity exhibit eigenstresses, which are related to the capillary pore pressure p_{cpor} and accordingly read as $\sigma_{cpor}^E = -p_{cpor} \mathbf{1}$. As it was the case in Sec. 7.4, microporomechanics provides the theoretical means to translate the aforementioned morphological and mechanical information into the first state equation of poromechanics related to the RVE of C-S-H foam,

$$\sigma_{foam} = \mathbb{C}_{foam}^{hom} : \varepsilon_{foam} + \sigma_{foam}^{hom,E}, \quad (7.21)$$

with RVE-related C-S-H foam stresses σ_{foam} and strains ε_{foam} . The homogenized stiffness at the C-S-H foam scale, \mathbb{C}_{foam}^{hom} follows from the self-consistent scheme (Hershey, 1954; Kröner, 1958; Hill, 1965) as

$$\mathbb{C}_{foam}^{hom} = f_{gel}^{foam} \int_0^{2\pi} \int_0^\pi \mathbb{C}_{gel}^{hom} : \mathbb{A}_{gel}(\underline{n}_{gel}) \frac{\sin \vartheta}{4\pi} d\vartheta d\varphi. \quad (7.22)$$

C-S-H foam-related volume fractions of voids and capillary pores and C-S-H gel (f_{void}^{foam} , f_{cpor}^{foam} , and f_{gel}^{foam} , respectively) follow from the cement paste-related volume fractions see (7.4)-(7.9) and (7.16), and they read as

$$f_j^{foam} = \frac{f_j^{cp}}{f_{foam}^{cp}}, \quad j = \{cpor, void, gel\}, \quad (7.23)$$

whereby $f_{void}^{foam} + f_{cpor}^{foam} + f_{gel}^{foam} = 1$. The latter volume fractions enter the homogenized eigenstresses at the C-S-H foam scale, $\sigma_{foam}^{hom,E}$, reading in analogy to (7.17) as

$$\sigma_{foam}^{hom,E} = f_{gel}^{foam} \int_0^{2\pi} \int_0^\pi \sigma_{gel}^{hom,E}(\underline{n}_{gel}) : \mathbb{A}_{gel}(\underline{n}_{gel}) \frac{\sin \vartheta}{4\pi} d\vartheta d\varphi - f_{cpor}^{foam} p_{cpor} \mathbf{1} : \mathbb{A}_{cpor}. \quad (7.24)$$

The second poromechanical state equation at the scale of the C-S-H foam concerns the porosity change of the capillary pores, reading as

$$\Delta\phi_{cpor}^{foam} = f_{cpor}^{foam} \mathbf{1} : \boldsymbol{\varepsilon}_{cpor} , \quad (7.25)$$

where $\boldsymbol{\varepsilon}_{cpor}$ denotes the average phase strains of the capillary pores. By analogy to the phase strain concentration at the cement paste scale, see Eqs. (7.18)-(7.20), the orientation-dependent phase strains of gel needles, $\boldsymbol{\varepsilon}_{gel}(\underline{n}_{gel})$, as well as the strains within capillary pores, $\boldsymbol{\varepsilon}_{cpor}$, and the ones in the voids, $\boldsymbol{\varepsilon}_{void}$, respectively, are linearly linked to the C-S-H foam strains and to the phase eigenstresses. They read as

$$\begin{aligned} \boldsymbol{\varepsilon}_{cpor} = & \mathbb{A}_{cpor} : \boldsymbol{\varepsilon}_{foam} - \int_0^{2\pi} \int_0^\pi \mathbb{Q}_{cpor,gel}(\underline{n}_{gel}) : \boldsymbol{\sigma}_{gel}^{hom,E}(\underline{n}_{gel}) \frac{\sin \vartheta}{4\pi} d\vartheta d\varphi \\ & + \mathbb{Q}_{cpor,cpor} : \mathbf{1} p_{cpor} , \end{aligned} \quad (7.26)$$

$$\begin{aligned} \boldsymbol{\varepsilon}_{gel}(\underline{n}_{gel}) = & \mathbb{A}_{gel}(\underline{n}_{gel}) : \boldsymbol{\varepsilon}_{foam} - \int_0^{2\pi} \int_0^\pi \mathbb{Q}_{gel,gel}(\underline{n}_{gel}, \underline{n}_{gel}^*) : \boldsymbol{\sigma}_{gel}^{hom,E}(\underline{n}_{gel}^*) \frac{\sin \vartheta^*}{4\pi} d\vartheta^* d\varphi^* \\ & + \mathbb{Q}_{gel,cpor}(\underline{n}_{gel}) : \mathbf{1} p_{cpor} , \end{aligned} \quad (7.27)$$

$$\begin{aligned} \boldsymbol{\varepsilon}_{void} = & \mathbb{A}_{void} : \boldsymbol{\varepsilon}_{foam} - \int_0^{2\pi} \int_0^\pi \mathbb{Q}_{void,gel}(\underline{n}_{gel}) : \boldsymbol{\sigma}_{gel}^{hom,E}(\underline{n}_{gel}) \frac{\sin \vartheta}{4\pi} d\vartheta d\varphi \\ & + \mathbb{Q}_{void,cpor} : \mathbf{1} p_{cpor} . \end{aligned} \quad (7.28)$$

Given that eigenstresses occur in the capillary pore phase and in the infinitely many gel needles (with particular orientation \underline{n}_{gel}), all respective eigenstress influences on phase strains have to be considered. This way, Eqs. (7.26)-(7.28) involve infinitely many influence tensors. Notably, in Eq. (7.27), gel orientation vector \underline{n}_{gel}^* is moving along the surface of the unit sphere in order to account for gel eigenstresses from all possible directions, while \underline{n}_{gel} is fixed. Again, analytical expressions of all concentration and influence tensors can be found in Appendix C.

7.6 Microporoelasticity of C-S-H gel

Finally, we deal with the RVE of C-S-H gel [see Fig. 7.1(c)], consisting of a spherical pore phase, and of infinitely many, oblate spheroidal phases, with axes of rotational symmetry functioning as orientation vectors \underline{n}_{sCSH} ; these orientation vectors are uniformly oriented in all space directions. The corresponding gel pores (subscript “*gpor*”) are intermixed with solid C-S-H crystals (subscript “*sCSH*”), i. e. with the primary hydration products of the chemical reaction between Portland cement clinker and water, which represent the smallest microstructural building blocks of cementitious materials; this interpretation of phases will be represented by a self-consistent homogenization approach, as it was the case in Sec. 7.5.

Solid C-S-H crystals exhibit characteristic dimensions ranging from a few single nanometers to several tens of nanometers. Therefore, characterization is typically carried out based on scattering spectroscopy experiments (Allen et al., 2007; Chiang et al., 2012; Brisard and Levitz, 2013), NMR (Muller et al., 2012), atomic force microscopy (Garrault et al., 2005), and atomistic modeling (Pellenq et al., 2009). At the very early material age of 4 hours, atomic force microscopy shows that solid C-S-H crystals typically exhibit platy shapes, with

dimensions of $60 \text{ nm} \times 30 \text{ nm} \times 5 \text{ nm}$, see (Garraut et al., 2005). At an age of 40 days, small angle neutron scattering experiments propose that solid C-S-H crystals exhibit a disk-like shape, whereby (i) in-plane dimensions range from 13 nm to 18 nm and (ii) out-of-plane thicknesses exhibiting a wide distribution with averages around $5\text{-}12 \text{ nm}$, see (Chiang et al., 2012). More qualitative evidence for age-specific C-S-H crystal dimensions was provided from Valori et al. (2013), who concluded, based on NMR measurements, that the number of layers in the solid C-S-H crystals increases with hydration. Based on these experimental findings, solid C-S-H crystals are considered as oblate spheroids with age-specific aspect ratios, denoted as X_{sCSH} . In this context, by analogy to the C-S-H gel density (see Sec. 7.3), also the solid C-S-H crystal morphology is assumed to be driven by space confinements in the C-S-H foam, expressed in terms of the precipitation space parameter γ according to (7.3). In the limit case of $\gamma = 1$, flat discs exhibiting $X_{sCSH} = 0$ precipitate in the unconfined pore space. Solid C-S-H crystals precipitating in the next densification increment $\Delta\gamma$ exhibit larger aspect ratios $X_{sCSH} > 0$, see Fig. 7.3. Finally, spherical crystals exhibiting $X_{sCSH} = 1$ precipitate in the

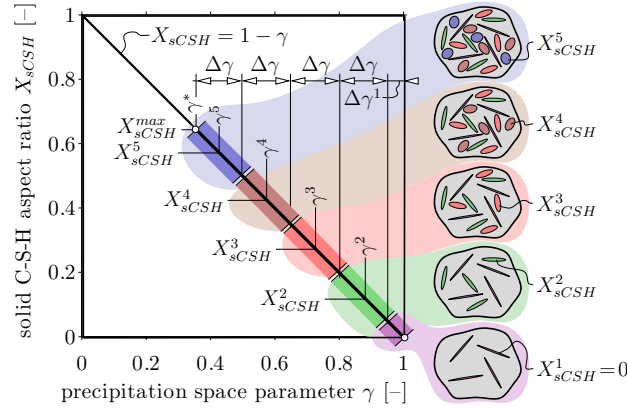


Figure 7.3: Maximum solid C-S-H aspect ratio as a function of the specific precipitation space including schematically the discretization process: the earlier a solid C-S-H crystal precipitate, the closer is its shape to a plate, the later it precipitates, the closer is its shape to a sphere; depicted volume elements schemtatically show the shape dependence in 2D; more details can be found in Appendix B

fully confined pore space, corresponding to the limit case $\gamma = 0$. Linear interpolation between the described limit cases allows for calculating the space limitation-dependent maximal aspect ratio in the RVE,

$$X_{sCSH}^{max} = 1 - \gamma. \quad (7.29)$$

Thus, at a particular densification state of the gel γ^* , the RVE contains solid C-S-H crystal phases which are uniformly distributed within the aspect ratio interval $X_{sCSH} \in [0; X_{sCSH}^{max}]$. Appendix B provides additional details on the numerical discretization of this aspect ratio distribution. Conclusively, an RVE of C-S-H gel is modeled as a polycrystal of spherical gel pores and disc-like C-S-H crystal phases which are uniformly oriented in all space directions, see also Fig. 7.1(c). The individual orientation of a single C-S-H crystal is described by the normal vector \underline{n}_{sCSH} , aligned with the axis of rotational symmetry with the C-S-H oblates, see Fig. 7.11(a) in Appendix A.

The layered structure of the C-S-H crystal (Allen et al., 2007; Muller et al., 2012; Chiang et al., 2012) implies an intrinsic anisotropy considered in full detail here. Quantitative information on the elasticity tensor is provided by atomistic models (Pellenq et al., 2009;

Manzano et al., 2012). Accordingly, the stiffness tensor of solid C-S-H is transversely isotropic, and its components read (in Kelvin-Mandel notation (Cowin and Mehrabadi, 1992), see also Appendix A) as (Manzano et al., 2012):

$$\mathbb{C}_{sCSH} = \begin{bmatrix} 91.2 & 33.2 & 29.8 & 0 & 0 & 0 \\ 33.2 & 91.2 & 29.8 & 0 & 0 & 0 \\ 29.8 & 29.8 & 72.6 & 0 & 0 & 0 \\ 0 & 0 & 0 & 42.4 & 0 & 0 \\ 0 & 0 & 0 & 0 & 42.4 & 0 \\ 0 & 0 & 0 & 0 & 0 & 58.0 \end{bmatrix} \text{ GPa}, \quad (7.30)$$

$\underline{e}_\vartheta, \underline{e}_\varphi, \underline{e}_r$

whereby the components are given in a local material base frame with base vectors \underline{e}_ϑ and \underline{e}_φ defining planes being parallel to the crystal layers and with $\underline{e}_r = \underline{n}_{sCSH}$ being equal to the representing the axis of rotational symmetry. The solid C-S-H phases do not exhibit any eigenstresses, while no stiffness is assigned to the gel pores. The latter, however, exhibit eigenstresses in the form of a gel pore pressure p_{gpor} , namely $\sigma_{gpor}^E = -p_{gpor}\mathbf{1}$. This pore pressure, however, depends on the orientation of the phase within the higher-scale RVE of C-S-H foam of Fig. 7.1(b), hence $\sigma_{gpor}^E(\underline{n}_{gel}) = -p_{gpor}(\underline{n}_{gel})\mathbf{1}$.

As in the preceding sections, the first poromechanical state equation, i.e. the relation between C-S-H gel stresses σ_{gel} and strains ε_{gel} , follows from homogenization theory, and reads as

$$\sigma_{gel}(\underline{n}_{gel}) = \mathbb{C}_{gel}^{hom} : \varepsilon_{gel}(\underline{n}_{gel}) + \sigma_{gel}^{hom,E}(\underline{n}_{gel}), \quad (7.31)$$

whereby the homogenized gel stiffness \mathbb{C}_{gel}^{hom} is isotropic (gel orientation-independent), while the homogenized eigenstress $\sigma_{gel}^{hom,E}$ does depend on the C-S-H gel orientation \underline{n}_{gel} . The corresponding self-consistent expression for the homogenized stiffness (Hershey, 1954; Kröner, 1958; Hill, 1965) has to account (i) for the orientation of the solid C-S-H crystals (expressed by the normal vector \underline{n}_{sCSH}), and (ii) for the aspect ratio distribution of the solid C-S-H crystals (which is characterized by the aspect ratio X_{sCSH}). Thus, we end up with surface integral expressions over the surface of a unit sphere accounting for all space directions, and an additional integral over the aspect ratio distribution with $X_{sCSH} \in \{0, X_{sCSH}^{max}\}$, whereby X_{sCSH}^{max} follows from (7.29), reading as

$$\mathbb{C}_{gel}^{hom} = f_{sCSH}^{gel} \int_1^{1-\gamma} \int_0^{2\pi} \int_0^\pi \mathbb{C}_{sCSH}(\underline{n}_{sCSH}) : \mathbb{A}_{sCSH}(\underline{n}_{sCSH}, X_{sCSH}) \frac{\sin \vartheta}{4\pi} d\vartheta d\varphi dX_{sCSH}, \quad (7.32)$$

where C-S-H gel-related volume fractions of solid C-S-H f_{sCSH}^{gel} and of gel pores f_{gpor}^{gel} follow from the cement paste-related gel volume fraction

$$f_{gel}^{cp} = f_{sCSH}^{cp} + f_{gpor}^{cp}, \quad (7.33)$$

given in (7.6) and in (7.7), respectively, and read as

$$f_j^{gel} = \frac{f_j^{cp}}{f_{gel}^{cp}}, \quad j = \{sCSH, gpor\}. \quad (7.34)$$

Mathematical details on the strain concentration tensor \mathbb{A}_{sCSH} are found in Appendix C. By analogy to the previous scales, the strain concentration tensors also allow for deriving the homogenized gel eigenstresses from the phase eigenstresses as

$$\sigma_{gel}^{hom,E}(\underline{n}_{gel}) = -f_{gpor}^{gel} p_{gpor}(\underline{n}_{gel}) \mathbf{1} : \mathbb{A}_{gpor}. \quad (7.35)$$

The second poroelastic state equation at the C-S-H gel scale links the the change of the gel porosity within the gel RVE with orientation \underline{n}_{gel} , denoted as $\Delta\phi_{gpor}^{gel}(\underline{n}_{gel})$, to the gel orientation-dependent gel pore strains, and reads as

$$\Delta\phi_{gpor}^{gel}(\underline{n}_{gel}) = f_{gpor}^{gel} \mathbf{1} : \boldsymbol{\varepsilon}_{gpor}(\underline{n}_{gel}). \quad (7.36)$$

Strain concentration relations provide access to the strains in gel pores, $\boldsymbol{\varepsilon}_{gpor}(\underline{n}_{gel})$, and also to strains in the solid C-S-H crystals $\boldsymbol{\varepsilon}_{sCSH}(\underline{n}_{gel}, \underline{n}_{sCSH}, X_{sCSH})$,

$$\boldsymbol{\varepsilon}_{gpor}(\underline{n}_{gel}) = \mathbb{A}_{gpor} : \boldsymbol{\varepsilon}_{gel}(\underline{n}_{gel}) + \mathbb{Q}_{gpor,gpor} : \mathbf{1} p_{gpor}(\underline{n}_{gel}), \quad (7.37)$$

$$\begin{aligned} \boldsymbol{\varepsilon}_{sCSH}(\underline{n}_{gel}, \underline{n}_{sCSH}, X_{sCSH}) &= \mathbb{A}_{sCSH}(\underline{n}_{sCSH}, X_{sCSH}) : \boldsymbol{\varepsilon}_{gel}(\underline{n}_{gel}) \\ &+ \mathbb{Q}_{sCSH,gpor}(\underline{n}_{sCSH}, X_{sCSH}) : \mathbf{1} p_{gpor}(\underline{n}_{gel}). \end{aligned} \quad (7.38)$$

For the sake of clarification, $\mathbb{Q}_{sCSH,gpor}$ relates the gel pore pressure of gel needle with orientation \underline{n}_{gel} to the solid C-S-H body of orientation \underline{n}_{sCSH} and aspect ratio X_{sCSH} . Notably, phase strain concentration \mathbb{A}_i and eigenstress influence tensors $\mathbb{Q}_{j,i}$ are equivalent for all C-S-H gel RVEs [argument (\underline{n}_{gel}) is not necessary]. Analytical expressions of these tensors are given in Appendix C.

7.7 Pore pressure determination for drained and undrained conditions

We are interested in the potential stiffening effect of water in gel and capillary pores in hydrating cement paste samples. This is why we distinguish between drained and undrained conditions. Under drained conditions, all pore pressures vanish:

$$p_{gpor}(\underline{n}_{gel}) = p_{cpor} = 0 \quad (7.39)$$

As undrained conditions we here refer to fully saturated and sealed gel and capillary pore spaces, so as to obtain an upper bound for the hydraulic stiffening effect. In this context, water is considered to be trapped in either the gel or the capillary pore phases, i.e. we neither consider any interaction between the different pore pressures in gel needle-specific gel pore families, nor any interactions between gel and capillary pore pressures. These assumption allows us to find a functional relation between the pore pressures and the macrostrains, as described next.

Gel pore volume changes, which are given in (7.36), can be written as

$$\Delta\phi_{gpor}^{gel}(\underline{n}_{gel}) = f\left(\boldsymbol{\varepsilon}_{cp}^{hom}, p_{gpor}(\forall \underline{n}_{gel}), p_{cpor}\right), \quad (7.40)$$

i.e. they are a function of macrostrains, of gel pore pressures of gel needles oriented in all space directions, and of the capillary pore pressure. By analogy, capillary volume changes, see (7.25), read as

$$\Delta\phi_{cpor}^{foam}(\underline{n}_{gel}) = f\left(\boldsymbol{\varepsilon}_{cp}^{hom}, p_{gpor}(\forall \underline{n}_{gel}), p_{cpor}\right). \quad (7.41)$$

In addition, if no mass transport of water out of the different pore spaces occurs, the porosity changes can be also obtained from the elastic behavior of the fluid filling the pore space (Coussy, 2004), which allows us to obtain gel porosity changes at the C-S-H gel RVE of orientation \underline{n}_{gel} with respect to the C-S-H gel scale as

$$\Delta\phi_{gpor}^{gel}(\underline{n}_{gel}) = f_{gpor}^{gel} \frac{p_{gpor}(\underline{n}_{gel})}{k_{H_2O}}, \quad (7.42)$$

whereby $k_{H_2O} = 2.3 \text{ GPa}$ is the bulk modulus of water. By analogy, changes of the capillary porosity referring to the C-S-H foam scale read as

$$\Delta \phi_{cpor}^{foam} = -f_{cpor}^{foam} \frac{p_{cpor}}{k_{H_2O}} \quad (7.43)$$

Setting equal (7.40) with (7.42), as well as (7.41) with (7.43), provides the sought relation between pore pressures and macrostrains for undrained conditions, reading as

$$p_{gpor}(\underline{n}_{gel}) = \mathbf{L}_{gpor}^{cp}(\underline{n}_{gel}) : \boldsymbol{\varepsilon}_{cp} \quad \text{and} \quad p_{cpor} = \mathbf{L}_{cpor}^{cp} : \boldsymbol{\varepsilon}_{cp}. \quad (7.44)$$

As for the computation of the second-order auxiliary tensors $\mathbf{L}_{gpor}^{cp}(\underline{n}_{gel})$ and \mathbf{L}_{cpor}^{cp} , we have to distinguish between the three hydration regimes introduced in Sec. 7.3. Since there are no gel pores in regime I ($0 \leq \xi \leq \xi_{I-II}$), all gel pore pressures must vanish, while in regime II and III nonzero gel pore pressures exist. Thus, the gel pore-related tensors $\mathbf{L}_{gpor}^{cp}(\underline{n}_{gel})$ read as

$$\mathbf{L}_{gpor}^{cp}(\underline{n}_{gel}) = \begin{cases} 0 & \forall 0 \leq \xi \leq \xi_{I-II} \\ \text{see Appendix C} & \forall \xi_{I-II} < \xi \leq 1 \end{cases} \quad (7.45)$$

By analogy, capillary pores vanish in regime III ($\xi_{II-III} < \xi \leq 1$), implying

$$\mathbf{L}_{cpor}^{cp} = \begin{cases} \text{see Appendix C} & \forall 0 \leq \xi < \xi_{II-III} \\ 0 & \forall \xi_{II-III} < \xi \leq 1 \end{cases} \quad (7.46)$$

7.8 Macroscopic poromechanics state equations and undrained stiffness of cement paste

So far, we presented our derivations in the framework of the transformation field or the eigenstress influence tensor concept (Dvorak and Benveniste, 1992; Pichler and Hellmich, 2010). We now turn towards more classical poromechanical quantities, such as the Biot tensors and the Biot moduli, and rewrite the macroscopic poromechanical state equation. This way, the first state equation follows from stepwise insertion of the C-S-H gel eigenstress $\boldsymbol{\sigma}_{gel}^{hom,E}$ [see (7.35)] into the C-S-H foam eigenstress $\boldsymbol{\sigma}_{foam}^{hom,E}$ [see (7.24)], further insertion of the result into the cement paste eigenstress $\boldsymbol{\sigma}_{cp}^{hom,E}$ [see (7.17)], and finally, insertion of the result into the cement paste-related stress-strain relation (7.14), resulting in

$$\boldsymbol{\sigma}_{cp} = \mathbb{C}_{cp}^{hom} : \boldsymbol{\varepsilon}_{cp} - \int_0^{2\pi} \int_0^\pi \mathbb{B}_{gpor}^{cp}(\underline{n}_{gel}) p_{gpor}(\underline{n}_{gel}) \frac{\sin \vartheta}{4\pi} d\vartheta d\varphi - \mathbb{B}_{cpor}^{cp} p_{cpor} \quad (7.47)$$

Therein, \mathbf{B}_{gpor}^{cp} and \mathbf{B}_{cpor}^{cp} denote cement paste-related Biot tensor for the gel pore phases and for the capillary pore phase, whereby the former tensor is a function of the orientation of the C-S-H gel needle, in which the gel pores reside, and the latter tensor is isotropic $\mathbf{B}_{cpor}^{cp} = B_{cpor}^{cp} \mathbf{1}$. They read as

$$\mathbf{B}_{gpor}^{cp}(\underline{n}_{gel}) = f_{foam}^{cp} f_{gel}^{foam} f_{gpor}^{gel} \mathbf{1} : \mathbb{A}_{gpor} : \mathbb{A}_{gel}(\underline{n}_{gel}) : \mathbb{A}_{foam} \quad (7.48)$$

$$\mathbf{B}_{cpor}^{cp} = f_{foam}^{cp} f_{cpor}^{foam} \mathbf{1} : \mathbb{A}_{cpor} : \mathbb{A}_{foam} \quad (7.49)$$

Stepwise insertion of the C-S-H foam strains, $\boldsymbol{\varepsilon}_{foam}$, according to (7.20), into the expression of the strains of gel phase $\boldsymbol{\varepsilon}_{gel}$, according to (7.27), and further insertion of the result into

the expression of the strains of gel pores in C-S-H gel RVE, $\boldsymbol{\varepsilon}_{gpor}$ according to (7.37), yields – under consideration of the homogenized eigenstresses $\boldsymbol{\sigma}_{gel}^{hom,E}$, $\boldsymbol{\sigma}_{foam}^{hom,E}$, according to (7.35) and (7.24), and after combination with the porosity change relation (7.36) – the so-called second state equation of poromechanics in the more classical setting of

$$\Delta\phi_{gpor}^{cp}(\underline{n}_{gel}) = \mathbf{B}_{gpor}^{cp}(\underline{n}_{gel}) : \boldsymbol{\varepsilon}_{cp} + \int_0^{2\pi} \int_0^\pi \frac{p_{gpor}(\underline{n}_{gel}^*)}{N_{gpor,gpor}^{cp}(\underline{n}_{gel}, \underline{n}_{gel}^*)} \frac{\sin \vartheta^*}{4\pi} d\vartheta^* d\varphi^* + \frac{p_{cpor}}{N_{gpor,cpor}^{cp}}. \quad (7.50)$$

Notably, \underline{n}_{gel} is the fixed orientation vector, while \underline{n}_{gel}^* is moving along the surface of a unit sphere. In Eq. (7.50), $N_{gpor,gpor}^{cp}$ and $N_{gpor,cpor}^{cp}$ ¹ denote cement paste-related solid Biot moduli relating gel and capillary pore pressures to gel porosity changes, and they read as

$$\begin{aligned} \frac{1}{N_{gpor,gpor}^{cp}(\underline{n}_{gel}, \underline{n}_{gel}^*)} &= f_{foam}^{cp} f_{gel}^{foam} f_{gpor}^{gel} \mathbf{1} : \\ &\left[f_{gel}^{foam} f_{gpor}^{gel} \mathbb{A}_{gpor} : \mathbb{A}_{gel}(\underline{n}_{gel}) : \mathbb{Q}_{foam,foam} : \mathbb{A}_{gel}(\underline{n}_{gel}^*) \right. \\ &: \mathbf{1} : \mathbb{A}_{gpor} + f_{cpor}^{foam} \mathbb{A}_{gpor} : \mathbb{Q}_{gel,gel}(\underline{n}_{gel}, \underline{n}_{gel}^*) \\ &: \mathbf{1} : \mathbb{A}_{gpor} + \delta(\underline{n}_{gel}, \underline{n}_{gel}^*) \mathbb{Q}_{gpor,gpor} : \mathbb{Q}_{gpor,gpor} \mathbf{1} \left. \right] \end{aligned} \quad (7.51)$$

$$\begin{aligned} \frac{1}{N_{gpor,cpor}^{cp}} &= f_{foam}^{cp} f_{gel}^{foam} f_{gpor}^{gel} \mathbf{1} : \mathbb{A}_{gpor} : \\ &\left[f_{cpor}^{foam} \mathbb{A}_{gel}(\underline{n}_{gel}) : \mathbb{Q}_{foam,foam} : \mathbf{1} : \mathbb{A}_{cpor} + \mathbb{Q}_{gel,cpor}(\underline{n}_{gel}) : \mathbf{1} \right] \end{aligned} \quad (7.52)$$

with $\delta(\underline{n}_{gel}, \underline{n}_{gel}^*)$ denoting the tensorial Kronecker-Delta, with $\delta(\underline{n}_{gel}, \underline{n}_{gel}^*) = \mathbf{1}$ for $\underline{n}_{gel} = \underline{n}_{gel}^*$, and $\delta(\underline{n}_{gel}, \underline{n}_{gel}^*) = 0$ for $\underline{n}_{gel} \neq \underline{n}_{gel}^*$. By analogy, we find the macrostrain-to-capillary porosity change concentration relation by inserting both the C-S-H foam strains, $\boldsymbol{\varepsilon}_{foam}$, according to (7.20), as well as the expression for the homogenized eigenstrains of the C-S-H gel needles, $\boldsymbol{\sigma}_{gel}^{hom,E}$, according to (7.35), into the expression of capillary pore strains, $\boldsymbol{\varepsilon}_{cpor}$, according to (7.26) – after insertion of the result into (7.25) – as

$$\Delta\phi_{cpor}^{cp} = \mathbf{B}_{cpor}^{cp} : \boldsymbol{\varepsilon}_{cp} + \int_0^{2\pi} \int_0^\pi \frac{p_{gpor}(\underline{n}_{gel})}{N_{cpor,gpor}^{cp}} \frac{\sin \vartheta}{4\pi} d\vartheta d\varphi + \frac{p_{cpor}}{N_{cpor,cpor}^{cp}}. \quad (7.53)$$

Therein, $N_{cpor,gpor}^{cp}$ and $N_{cpor,cpor}^{cp}$ denote cement paste-related solid Biot moduli relating gel pore pressure and capillary pore pressure to the capillary porosity change, respectively, and they read as

$$N_{cpor,gpor}^{cp} = N_{gpor,cpor}^{cp}, \quad (7.54)$$

$$\frac{1}{N_{cpor,cpor}^{cp}} = f_{foam}^{cp} f_{cpor}^{foam} \mathbf{1} : \left(\mathbb{Q}_{cpor,cpor} : \mathbf{1} + f_{cpor}^{foam} \mathbb{A}_{cpor} : \mathbb{Q}_{foam,foam} : \mathbf{1} : \mathbb{A}_{cpor} \right). \quad (7.55)$$

¹ $N_{gpor,cpor}^{cp}$ translates the capillary pore pressure into gel porosity changes and since capillary pore pressures are isotropic $N_{gpor,cpor}^{cp}$ is gel orientation independent. For energetic reasons, $N_{ij} = N_{ji}$ (Dormieux et al., 2006). Thus, also $N_{gpor,gpor}^{cp}$ is gel orientation independent and the argument (\underline{n}_{gel}) can be omitted.

The link (7.44) between the macrostrains and pore pressures, finally allows us to derive the undrained stiffness tensor of cement paste. Insertion of the pore pressures according to (7.44) into the macrostress expression (7.47) and comparison with the (undrained) elastic law on the cement paste scale

$$\boldsymbol{\sigma}_{cp} = \mathbb{C}_{cp}^{hom,u} : \boldsymbol{\varepsilon}_{cp} \quad (7.56)$$

finally yields the undrained stiffness of cement paste as

$$\mathbb{C}_{cp}^{hom,u} = \mathbb{C}_{cp}^{hom} - \int_0^{2\pi} \int_0^{\pi} \mathbf{B}_{gpor}^{cp}(\underline{n}_{gel}) \otimes \mathbf{L}_{gpor}^{cp}(\underline{n}_{gel}) \frac{\sin \vartheta}{4\pi} d\vartheta d\varphi - \mathbf{B}_{cpor}^{cp} \otimes \mathbf{L}_{cpor}^{cp}, \quad (7.57)$$

whereby the symbol \otimes denotes a dyadic product. Having predicted the (drained) homogenized cement paste stiffness, see (7.15), as well as the undrained homogenized cement paste stiffness (7.57), we now compare our predictions to experimental results.

7.9 Model validation

Herein, the poroelastic model predictions are presented and compared to several independent experimentally determined elastic properties. Stiffnesses of (almost) fully hydrated cement pastes exhibiting $w/c \in [0.25, 0.85]$ obtained by resonance frequency measurements from Helmuth and Turk (Helmuth and Turk, 1966) and from Haecker et. al. (Haecker et al., 2005) are compared to corresponding model predictions in Subsec. 7.9.1. Experimentally determined evolutions of elastic properties with respect to the hydration degree, measured by mechanical and ultrasonic testing at Vienna University of Technology (Karte et al., 2015; Wasserbauer, 2014), are compared to corresponding model predictions in Subsec. 7.9.2.

7.9.1 Fully hydrated cement paste

Two experimental datasets are used for validation of mature cement pastes, shortly summarized next. Helmuth and Turk (Helmuth and Turk, 1966) studied thin samples (80 by 15 by 1-2 mm) of cement paste (Portland cement with Blaine fineness of 342 and 447 m²/kg, respectively) exhibiting w/c ranging from 0.35 to 0.85 after several months of water curing at 25° Celsius. They measured the flexural and torsional fundamental resonance frequency, the specimen mass and specimen dimensions, and back-calculated the Young's modulus and the shear modulus of the paste. A similar approach was used from Haecker et. al. (Haecker et al., 2005), who studied 2 month old water-stored samples of different cement pastes exhibiting w/c ranging from 0.25 to 0.60.

The model for fully hydrated cement paste $\xi = \xi_{ult}$ according to (7.11) beautifully predicts the experimental data, see Fig. 7.4. The difference between drained (black line in Fig. 7.4) and undrained (blue line) is remarkably small for both the homogenized Young's and, in particular, for the homogenized shear modulus. Clearly, the smaller w/c the smaller is the pore pressure-induced stiffening effect, since in low- w/c -pastes, only a small pore volume fraction remains at complete hydration $\xi = \xi_{ult}$. The relatively large deviation between the model and experiment for $w/c < 0.35$ probably stems from the fact that specimens of Haecker et al. (2005) are only two months old, and at very low w/c the hydration process far from complete (Juenger and Jennings, 2001). In such specimen, capillary water is likely to have vanished completely due to hydration, while gel water might still be present. Thus, the poroelastic model prediction for the hydration degree ξ_{II-III} according to (7.10), can be seen as a lower bound for the elastic properties, see Fig. 7.4. Haecker et al. (2005) also noted that

they observe some bleeding for pastes exhibiting $w/c > 0.5$, implying that the real w/c for such pastes is definitely smaller. This might explain why the stiffness values for pastes exhibiting $w/c > 0.5$, as measured by Haecker et al. (2005), are slightly higher than the ones obtained from Helmuth and Turk (1966) – and also slightly higher than the model-predicted ones.

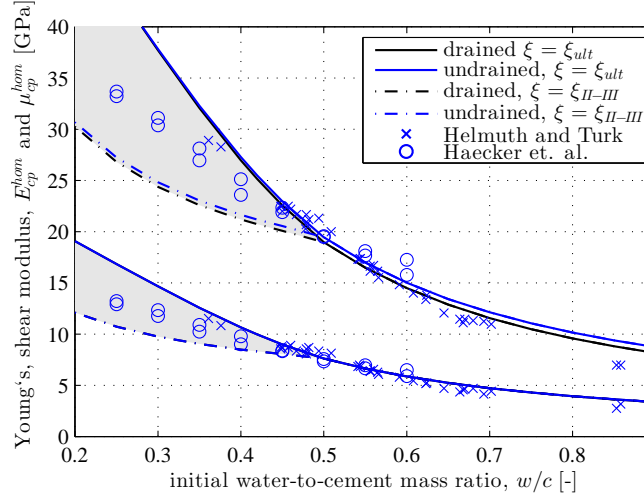


Figure 7.4: Young’s modulus and shear modulus, respectively, as a function of the initial water-to-cement ratio of mature pastes; drained and fully undrained model predictions and test data from Helmuth and Turk (1966) and Haecker et al. (2005) measured by resonance frequency methods; gray areas indicate limits for elastic properties (see text)

7.9.2 Early age cement paste

Next, we compare our predictions to early age elastic properties measured at Vienna University of Technology (Wasserbauer, 2014; Karte et al., 2015). Two mixes ($w/c \in \{0.42; 0.50\}$) of commercially available CEMI 42.5 N were tested at 20° C by means of a mechanical unloading tests and by means of ultrasonic testing. The mechanical tests were conducted in parallel to the hydration process with close-to-centric loads causing stresses well below the critical 30 % of the material strength. Five LVDTs, evenly distributed around the perimeter of the specimen, are used for deformation measurements. Ultrasonic tests deliver longitudinal and transversal wave velocities, respectively, which allow for the back calculation of the so-called *dynamic* elastic stiffness components. Notably, the ultrasonic frequency amounting to 250 kHz ensures that the wavelength is, at any time, larger than 4 mm, i.e. significantly larger than the characteristic size of the RVE of cement paste, see Fig. 7.1. Hence, scale separation $\ell \ll \mathcal{L}$ according to inequalities (7.1) is fulfilled. In order to relate sample ages to hydration degrees, isothermal differential calorimetry measurements were performed.

Comparing the model-predicted Young’s and shear moduli evolution to mechanical test results as well as to ultrasonic test results, shows, in general, an excellent agreement between predictions and test results, see Fig. 7.5. The model predicted drained Young’s moduli agree remarkably well with the values obtained by mechanical testing. The model-predicted undrained Young’s moduli are only slightly larger than the drained model results during the whole hydration regime $0 \leq \xi \leq 1$. The Young’s moduli determined by means of ultrasonic measurements are marginally higher than the undrained model predictions and thus also only slightly higher than the results from the mechanical test campaign. The stiffening effect due

to pore pressures is negligible for the homogenized shear moduli, in Fig. 7.5, the undrained predictions overlap the drained ones. Hence, the fact that water does not resist any shear stresses, reflects itself also at the macroscopic scale, despite the mutual interactions of the pore water with all the other solid phases throughout the three observation scales. The agreement between the experimentally determined shear moduli and the model results is outstanding. While this impressively shows the predictive capabilities of the presented model, we are left with discussing the pore-pressure induced increase of other elastic properties, as it is done next.

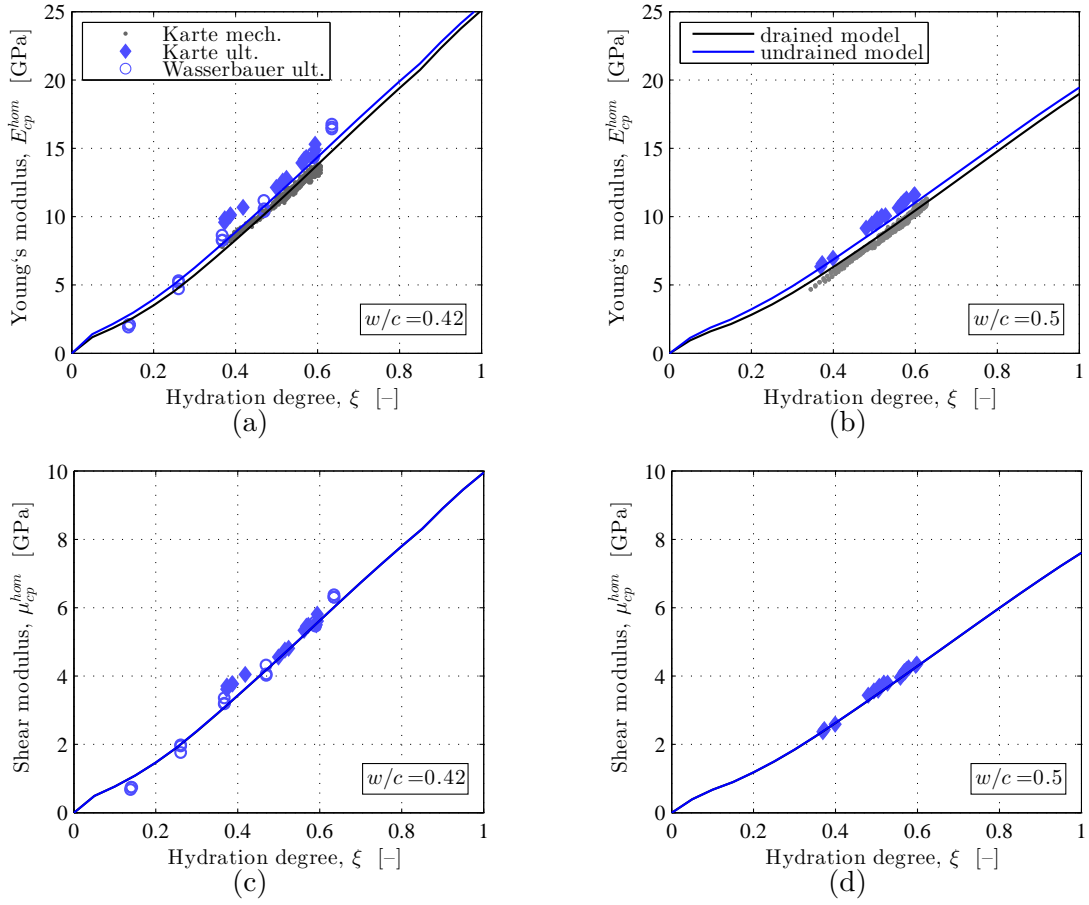


Figure 7.5: Comparison of drained and undrained model predictions with experimental data from TU Wien (ultrasonic (Wasserbauer, 2014; Karte et al., 2015) and mechanical testing (Karte et al., 2015)) for cement pastes exhibiting $w/c \in \{0.42, 0.50\}$: (a)+(b) Young's modulus; (c)+(d) shear modulus

7.10 Discussion and conclusion

In order to discuss the poromechanical stiffening effect during the hydration-induced hardening in more detail, we study the evolution of two other homogenized elasticity quantities herein, namely the homogenized Poisson's ratio and the 1111-component of the homogenized stiffness tensor of cement paste. The difference between drained and undrained homogenized Poisson's ratio is much more pronounced than the difference between drained and undrained moduli, see

Fig. 7.6. The Poisson's ratio for drained conditions amounts to ≈ 0.2 initially and it increases during ongoing hydration. In the undrained case, however, the initial value of the Poisson's ratio amounts to 0.5, and it decreases during ongoing hydration, and thus corroborates results obtained from Bernard et al. (2003b). This shows that pore pressure-induced stiffening effects might play a considerable role for characterizing the full elastic behavior of cement paste, in particular at very early ages. The experimentally determined Poisson's ratios (back-calculated from longitudinal and shear wave velocity as measured by ultrasonics) agree reasonably well with the undrained model predictions, demonstrating that ultrasonic pulses activate pore pressures. The mechanical tests of Karte et al. (2015) allow for measuring the Young's

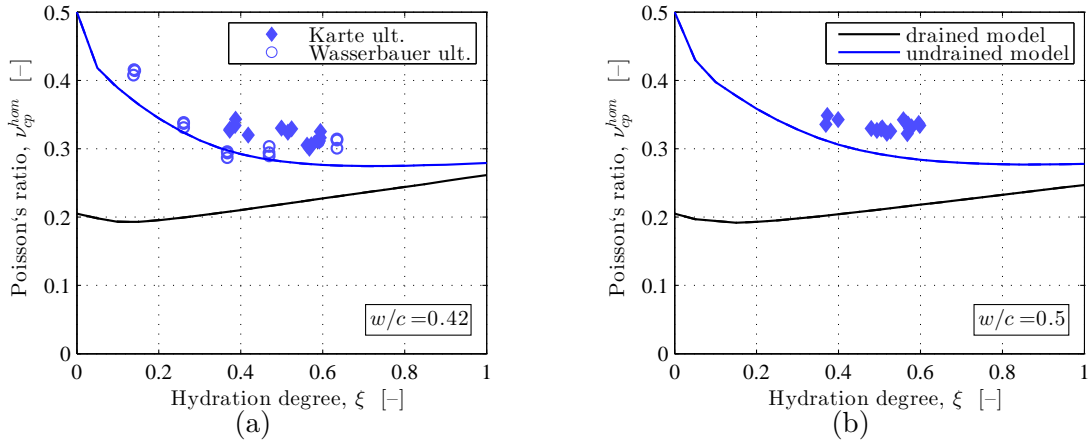


Figure 7.6: Comparison of the drained and undrained model-predicted Poisson's ratio with experimental data from TU Wien (ultrasonic (Wasserbauer, 2014; Karte et al., 2015)) for cement pastes exhibiting (a) $w/c=0.42$ and (b) $w/c=0.50$

moduli only, rendering similar conclusions regarding the activation of pore pressures in such mechanical tests impossible.

As for the 1111-component of the homogenized stiffness tensor of cement paste again, undrained predictions are much larger than the drained counterpart, see Fig. 7.7. Given a typical cement paste used in construction engineering with $w/c = 0.60$, the 1111-component of the undrained stiffness is by approximately 30 % larger than the drained counterpart at an hydration degree of $\xi = 0.50$, and still approximately 10 % larger at ultimate hydration $\xi = 1$. Our model also allows us to quantify the stiffening effect of gel and capillary porosity separately. By evaluating the model for the case of drained capillary porosity ($p_{cpor} = 0$), but undrained gel porosity ($p_{gpor} \neq 0$), it is shown that the stiffening effect of the porosity scales with its volume fractions: in early ages, the capillary pore pressures stiffen the material, while later on, the gel pore pressures are responsible for the material stiffening.

The good agreements between model predictions and experimental results motivate deeper study of the poroelastic behavior of cement paste, namely its evolution of as a function of the hydration degree ξ and its dependence on the initial water-to-cement mass ratio w/c , see Fig. 7.8-7.10. The drained Young's modulus of cement paste increases with increasing hydration degree, and decreases with increasing water-to-cement mass ratio, see Fig. 7.8(a). A similar dependence is observed at the scale of the C-S-H foam, which, however, is always softer than the corresponding cement paste. Respective factors vary between 1.1 (at $w/c=0.3$) and 2.7 (at $w/c=1.0$) for complete hydration $\xi=1.0$, while they typically amount to 5 at early ages, see Fig. 7.8(b). This demonstrates the reinforcing effect of the clinker grains, which is

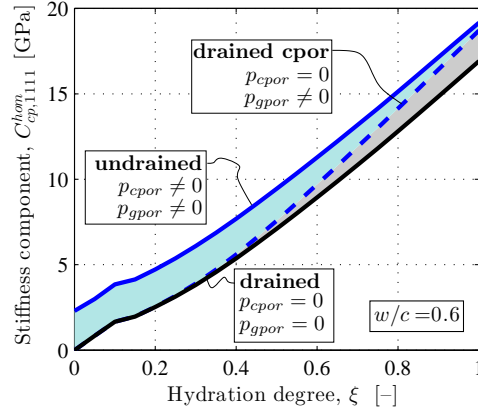


Figure 7.7: Model-predicted stiffness tensor component C_{1111} of cement paste exhibiting $w/c = 0.60$ as a function of the hydration degree ξ for drained, undrained and partially drained conditions

particular effective at early ages. A difference emerges at the C-S-H gel scale where, with increasing hydration degree, the elastic Young's modulus first rapidly *decreases*, and then starts to increase only with hydration degree between 0.2 and 0.6. In more detail, the C-S-H scale-related Young's modulus is constant and amounts to 63.6 GPa in hydration regime I ($\xi \leq \xi_{I-II}$), since no gel pores are present. If hydration proceeds, the gel pore stiffness sharply drops to minimum values of ≈ 5.5 GPa and then continually increases again, see Fig. 7.8(c). As for the Poisson's ratio of the C-S-H gel, the constant value in hydration regime I amounts to 0.28, and the initial decrease at the scale of the gel further translates itself to the larger scales of the C-S-H foam and the cement paste, see Fig. 7.8(d)-(f). While the undrained Young's modulus very much agrees with the drained counterpart [see Fig. 7.9(a) and compare with Fig. 7.8(a)], the undrained Poisson's ratio, unlike the drained one, decreases, from initial values of 0.5, with increasing hydration degree in most of the studied w/c interval, see Fig. 7.9(b).

Next, we discuss the Biot tensors and the Biot moduli. The isotropic Biot tensor for the capillary pores $\mathbf{B}_{cpor}^{cp} = B_{cpor}^{cp} \mathbf{1}$ is equal to one for $\xi = 0$, it smoothly decreases with increasing hydration degree, and reaches zero for $\xi = \xi_{II-III}$; and in hydration regime III, it does not exist anymore as the capillary pore space has vanished, see Fig. 7.10(a). This shows, that capillary pore pressures affect the macroscopic stresses, according to the first poromechanical state equation (7.47), in particular at early ages. The gel pore-related Biot tensors do not exist in hydration regime I, and they amount to zero at the $\xi = \xi_{I-II}$. We visualize these anisotropic tensors for C-S-H gel needle oriented in \underline{e}_z -direction so that $\mathbf{B}_{gpor}^{cp} = B_{gpor,t}^{cp}(\underline{e}_x \otimes \underline{e}_x + \underline{e}_y \otimes \underline{e}_y) + B_{gpor,l}^{cp} \underline{e}_z \otimes \underline{e}_z$. The longitudinal and transversal component, $B_{gpor,l}^{cp}$ and $B_{gpor,t}^{cp}$, exhibit similar dependencies with respect to ξ and w/c , see Fig. 7.10(b)-(c), whereby $B_{gpor,l}^{cp} > B_{gpor,t}^{cp}$; they increase, for increasing hydration degree, from $\xi = \xi_{I-II}$ continuously up to approximately $\xi = \xi_{II-III}$, and afterwards, they decrease sharply due to the sharply decreasing gel pore volume fraction. The Biot moduli, in turn, relate the pore pressures to the pore volume changes, see the poroelastic state equations (7.42) and (7.43). Again, studying their dependencies as function of ξ and w/c strongly reflects the three hydration regimes of Fig. 7.2. The Biot modulus $N_{cpor,cpor}^{cp}$ rapidly goes to infinity for $\xi \rightarrow \xi_{II-III}$, see Fig. 7.10(d), demonstrating that capillary pore pressures in the end of hydration regime II hardly affect the capillary pore volume, due to the vanishing capillary porosity. The Biot

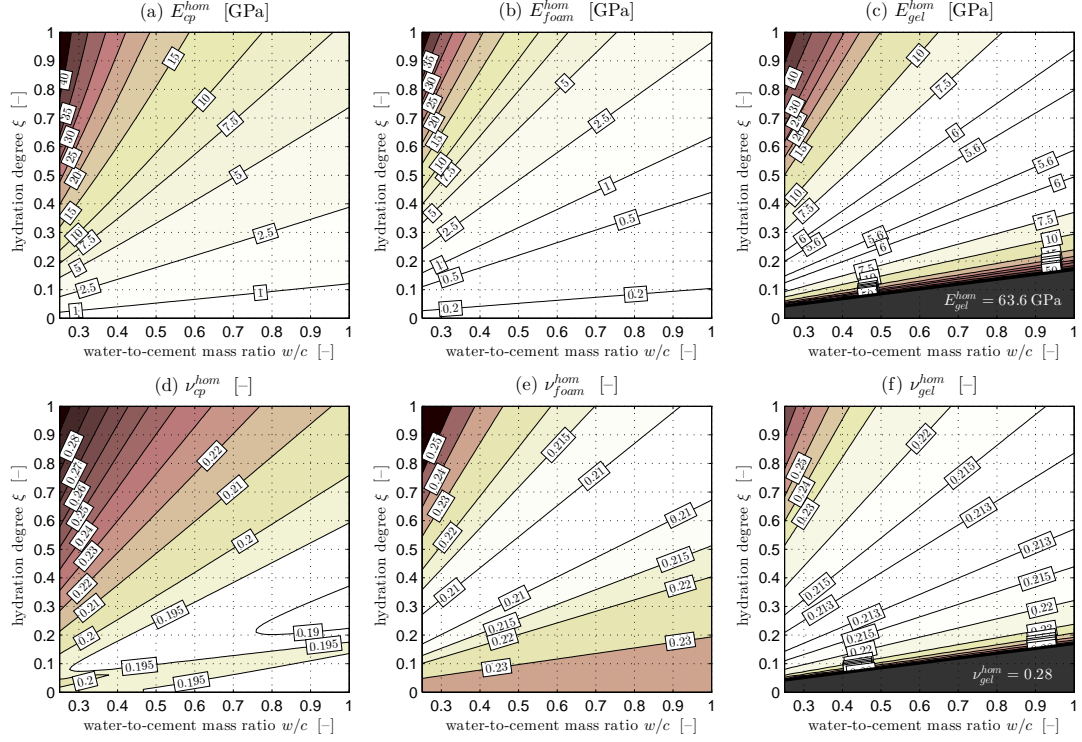


Figure 7.8: Drained RVE-specific homogenized Young's moduli (a)-(c) and Poisson's ratios (d)-(f), as functions of w/c and ξ

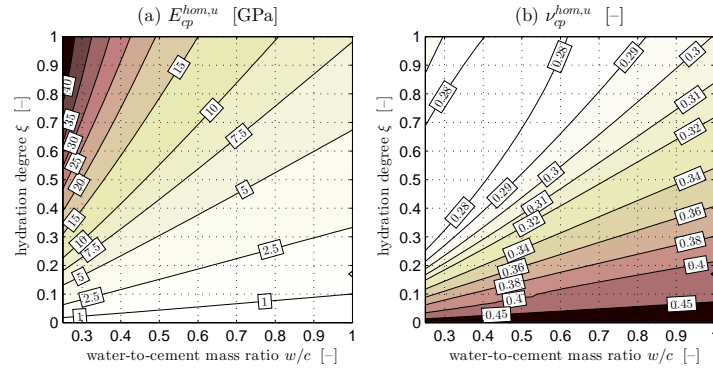


Figure 7.9: Undrained cement paste-related Young's moduli (a) and Poisson's ratios (b), as functions of w/c and ξ

moduli $N_{gpor, cpor}^{cp} = N_{cpor, gpor}^{cp}$ exist neither in hydration regime III, nor in hydration regime I, see Fig. 7.10(e), and they are negative in hydration regime II. Hence, capillary pore pressures increase the gel pore volume, and gel pore pressures increase the capillary pore volume. In order to visualize the C-S-H gel orientation dependent Biot moduli $N_{gpor, gpor}^{cp}(n_{gel}, n_{gel}^*)$, we focus on its maximum value which occurs for the case of $n_{gel} = n_{gel}^*$, which does not depend on the C-S-H gel orientation anymore. Its dependencies on ξ and w/c are reminiscent of those encountered at the cement paste scale, see Fig. 7.10(f).

In summary, by developing a novel representation of the cement pastes' nano- and microstructure, taking into account latest findings regarding the densification of C-S-H and

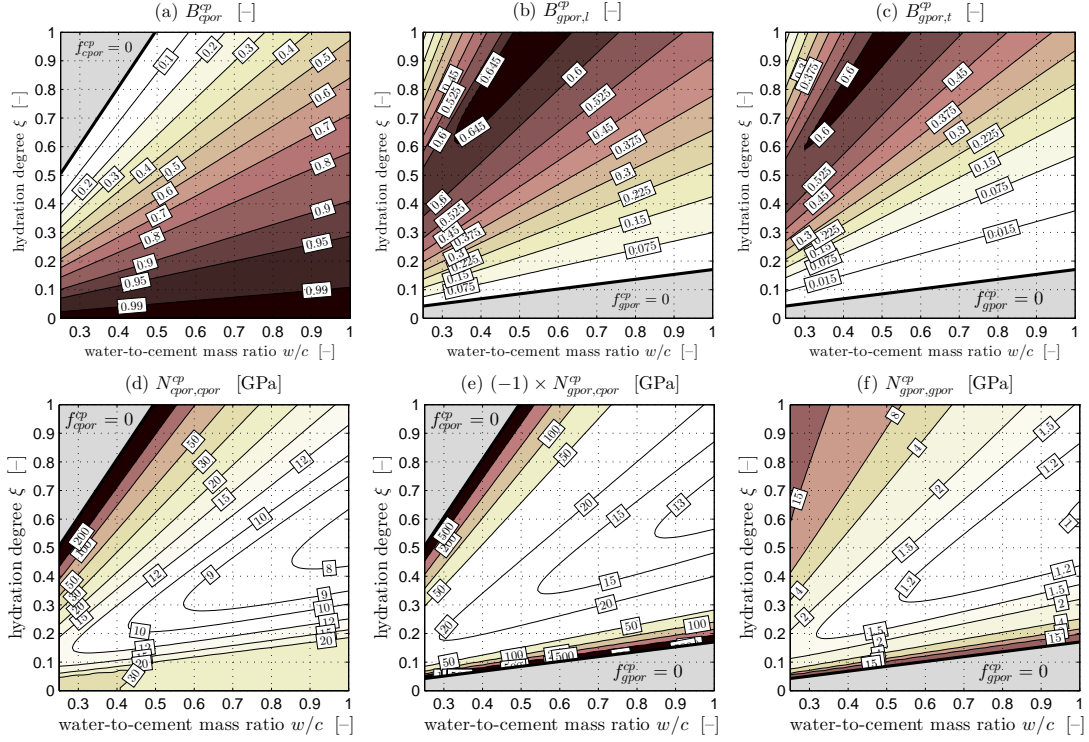


Figure 7.10: Cement paste-related Biot tensor components (a)-(c) and Biot moduli (d)-(f), as functions of w/c and ξ ; note that: $\mathbf{B}_{cpor}^{cp} = B_{cpor}^{cp} \mathbf{1}$ is isotropic; \mathbf{B}_{gpor}^{cp} is shown for the needle aligned with \underline{e}_z implying $\mathbf{B}_{gpor}^{cp} = B_{gpor,t}^{cp}(\underline{e}_x \otimes \underline{e}_x + \underline{e}_y \otimes \underline{e}_y) + B_{gpor,l}^{cp} \underline{e}_z \otimes \underline{e}_z$; the Biot moduli $N_{gpor,gpor}^{cp}(n_{gel}, n_{gel}^*)$ are shown for the case of $n_{gel} = n_{gel}^*$ for which they do not depend on the C-S-H gel orientation

regarding the morphology and stiffness of the solid C-S-H nanoparticles, we developed a micromechanical multiscale model for poroelastic nano-to-macro homogenization. Remarkably, the model does not introduce any parameters which have to be calibrated from macroscopic experiments. All mechanical input quantities either stem from physically sound experimental methods, or from yet another model at the atomistic scale (Manzano et al., 2012) for the elastic stiffness the nanometer-large solid C-S-H particles. The volume evolution of the cement paste constituents, in turn, are predicted based on a recently developed and validated hydration model (Königsberger et al., 2016a). This allows for model validation in a very strict sense, by comparing the *blind* stiffness predictions to experimental results from four different comprehensive testing campaigns conducted in three different laboratories by means of three different testing principles (resonance frequency methods, ultrasonics, and mechanical testing). Surviving all these falsification attempts demonstrates the reliability of the presented micromechanical model and the underlying microstructural representation. Moreover, we can conclude that the homogenized Young's modulus and the homogenized shear modulus for the case of drained and undrained pore spaces are very close to each other, which agrees very well with recent experimental insights (Karte et al., 2015; Irfan-ul-Hassan et al., 2016). However, a very significant pore pressure-induced increase of the homogenized Poisson's ratio or the homogenized 1111 stiffness tensor component is found, in particular so at early ages.

Appendix A: Base frames and numerical integration over the surface of a unit sphere

Use of different base frames enables the computational handling of material phases which are oriented in all space directions (solid C-S-H crystals, C-S-H gel needles, and CH crystals), see Fig. 7.1. The orientation of these needles can be described based on the link between the global (RVE-related) and the local (phase-related) base frame. Therefore, we recall the transformation rules for fourth-order tensors. Finally, the present section addresses the numerical integration scheme used for computing the integrals over the surface of a unit sphere in terms of zenith angle ϑ and azimuth angle φ .

We consider, apart from the global Cartesian base frame $\underline{e}_x, \underline{e}_y, \underline{e}_z$, a local base frame $\underline{e}_\vartheta, \underline{e}_\varphi, \underline{e}_r$ moving along along the surface of a unit sphere, see Fig. 7.11. The zenith angle ϑ

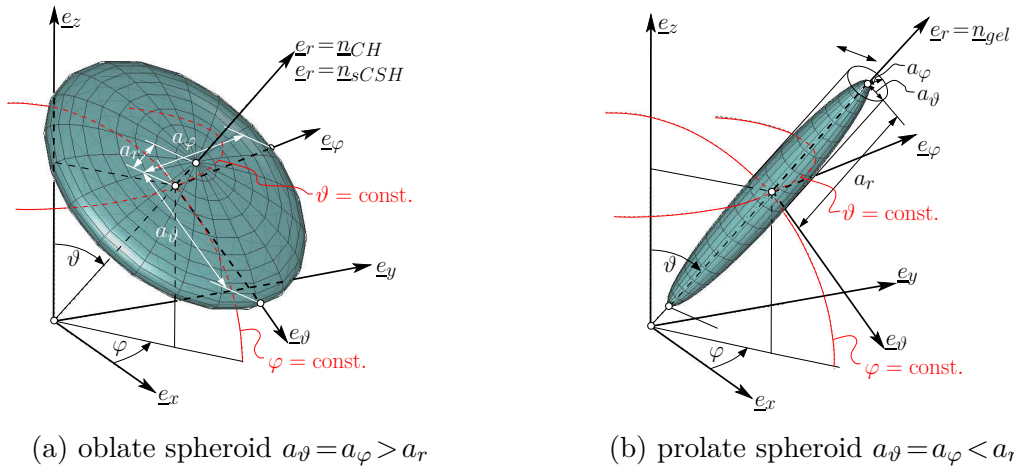


Figure 7.11: Global Cartesian base frame $\underline{e}_1, \underline{e}_2, \underline{e}_3$ and local spherical base frame $\underline{e}_\vartheta, \underline{e}_\varphi, \underline{e}_r$; and characterization of the orientation of oblate solid C-S-H crystals and of disc shaped CH crystals (a), and of needle shaped C-S-H gel needles (b), by the unit normal vector in the axis of rotational symmetry \underline{n}_{sCSH} , \underline{n}_{CH} , and \underline{n}_{gel} , respectively, which corresponds to the base vector \underline{e}_r

and the azimuth angle φ allow for characterization of the position on the surface of a unit sphere. Moreover, they also allow us to describe the orientation of the non-spherical phases considered in our multiscale micromechanics model. Solid C-S-H element orientation is given by the unit normal vector \underline{n}_{sCSH} which is orthogonal to the plane of isotropy, and is therefore aligned with the axis of rotational symmetry of the oblate spheroid. Notably, \underline{n}_{sCSH} coincides with the base vector \underline{e}_r , see Fig. 7.11(a). By analogy, the orientation of the needle-shaped C-S-H gel needles is characterized by the unit normal vector \underline{n}_{gel} , see Fig. 7.11(b), and the orientation of penny-shaped CH element is characterized by the unit normal vector \underline{n}_{CH} , see again Fig. 7.11(a).

Next, the transformation rules for fourth-order tensor components are shortly recalled. A fourth-order tensor \mathbb{T} with components T_{ijkl} (exhibiting minor symmetry, $T_{ijkl} = T_{ijlk} = T_{jilk} = T_{jikl}$) given in the local spherical base $\underline{e}_\vartheta, \underline{e}_\varphi, \underline{e}_r$ is introduced. The transformation of components referring to this local base, to components referring to the global Cartesian base

reads as

$$\begin{pmatrix} T_{xxxx} & T_{xxyy} & T_{xxzz} & \sqrt{2}T_{xxyz} & \sqrt{2}T_{xxxz} & \sqrt{2}T_{xxxy} \\ T_{yyxx} & T_{yyyy} & T_{yyzz} & \sqrt{2}T_{yyyz} & \sqrt{2}T_{yyxz} & \sqrt{2}T_{yyxy} \\ T_{zzxx} & T_{zzyy} & T_{zzzz} & \sqrt{2}T_{zzyz} & \sqrt{2}T_{zzxz} & \sqrt{2}T_{zzxy} \\ \sqrt{2}T_{yzxx} & \sqrt{2}T_{yzyy} & \sqrt{2}T_{yzzz} & 2T_{yzyz} & 2T_{yzxz} & 2T_{yzxy} \\ \sqrt{2}T_{zxxx} & \sqrt{2}T_{zxyy} & \sqrt{2}T_{zxzz} & 2T_{xzyz} & 2T_{xzxz} & 2T_{xzxxy} \\ \sqrt{2}T_{xyxx} & \sqrt{2}T_{xyyy} & \sqrt{2}T_{xyzx} & 2T_{xyyz} & 2T_{xyxz} & 2T_{xyxy} \end{pmatrix}_{\mathbf{e}_x, \mathbf{e}_y, \mathbf{e}_z} = \mathcal{Q}^T \times \begin{pmatrix} T_{\vartheta\vartheta\vartheta\vartheta} & T_{\vartheta\vartheta\varphi\varphi} & T_{\vartheta\vartheta rr} & \sqrt{2}T_{\vartheta\vartheta\varphi r} & \sqrt{2}T_{\vartheta\vartheta\vartheta r} & \sqrt{2}T_{\vartheta\vartheta\vartheta\varphi} \\ T_{\varphi\varphi\vartheta\vartheta} & T_{\varphi\varphi\varphi\varphi} & T_{\varphi\varphi rr} & \sqrt{2}T_{\varphi\varphi\varphi r} & \sqrt{2}T_{\varphi\varphi\vartheta r} & \sqrt{2}T_{\varphi\varphi\vartheta\varphi} \\ T_{rr\vartheta\vartheta} & T_{rr\varphi\varphi} & T_{rrrr} & \sqrt{2}T_{rr\varphi r} & \sqrt{2}T_{rr\vartheta r} & \sqrt{2}T_{rr\vartheta\varphi} \\ \sqrt{2}T_{\varphi r\vartheta\vartheta} & \sqrt{2}T_{\varphi r\varphi\varphi} & \sqrt{2}T_{\varphi rrr} & 2T_{\varphi r\varphi r} & 2T_{\varphi r\vartheta r} & 2T_{\varphi r\vartheta\varphi} \\ \sqrt{2}T_{\vartheta r\vartheta\vartheta} & \sqrt{2}T_{\vartheta r\varphi\varphi} & \sqrt{2}T_{\vartheta rrr} & 2T_{\vartheta r\varphi r} & 2T_{\vartheta r\vartheta r} & 2T_{\vartheta r\vartheta\varphi} \\ \sqrt{2}T_{\vartheta\varphi\vartheta\vartheta} & \sqrt{2}T_{\vartheta\varphi\varphi\varphi} & \sqrt{2}T_{\vartheta\varphi rr} & 2T_{\vartheta\varphi\varphi r} & 2T_{\vartheta\varphi\vartheta r} & 2T_{\vartheta\varphi\vartheta\varphi} \end{pmatrix}_{\mathbf{e}_\vartheta, \mathbf{e}_\varphi, \mathbf{e}_r} \times \mathcal{Q} \quad (7.58)$$

whereby \mathcal{Q} denotes a 6×6 transformation matrix with elements reading as

$$\mathcal{Q} = \begin{pmatrix} Q_{11}^2 & Q_{12}^2 & Q_{13}^2 & \sqrt{2}Q_{12}Q_{13} & \sqrt{2}Q_{11}Q_{13} & \sqrt{2}Q_{11}Q_{12} \\ Q_{21}^2 & Q_{22}^2 & Q_{23}^2 & \sqrt{2}Q_{22}Q_{23} & \sqrt{2}Q_{21}Q_{23} & \sqrt{2}Q_{21}Q_{22} \\ Q_{31}^2 & Q_{32}^2 & Q_{33}^2 & \sqrt{2}Q_{32}Q_{33} & \sqrt{2}Q_{31}Q_{33} & \sqrt{2}Q_{31}Q_{32} \\ \sqrt{2}Q_{21}Q_{31} & \sqrt{2}Q_{22}Q_{32} & \sqrt{2}Q_{23}Q_{33} & Q_{22}Q_{33} + Q_{23}Q_{32} & Q_{21}Q_{33} + Q_{23}Q_{31} & Q_{21}Q_{32} + Q_{22}Q_{31} \\ \sqrt{2}Q_{11}Q_{31} & \sqrt{2}Q_{12}Q_{32} & \sqrt{2}Q_{13}Q_{33} & Q_{12}Q_{33} + Q_{13}Q_{32} & Q_{11}Q_{33} + Q_{13}Q_{31} & Q_{11}Q_{32} + Q_{12}Q_{31} \\ \sqrt{2}Q_{11}Q_{21} & \sqrt{2}Q_{12}Q_{22} & \sqrt{2}Q_{13}Q_{23} & Q_{12}Q_{23} + Q_{13}Q_{22} & Q_{11}Q_{23} + Q_{13}Q_{21} & Q_{11}Q_{22} + Q_{12}Q_{21} \end{pmatrix} \quad (7.59)$$

and Q_{ij} are the elements of the 3×3 transformation matrix \mathbf{Q} reading as

$$\mathbf{Q} = \begin{pmatrix} Q_{11} & Q_{12} & Q_{13} \\ Q_{21} & Q_{22} & Q_{23} \\ Q_{31} & Q_{32} & Q_{33} \end{pmatrix} = \begin{pmatrix} \cos \vartheta \cos \varphi & \cos \vartheta \sin \varphi & -\sin \vartheta \\ -\sin \varphi & \cos \varphi & 0 \\ \sin \vartheta \cos \varphi & \sin \vartheta \sin \varphi & \cos \vartheta \end{pmatrix} \quad (7.60)$$

Transformation rule (7.58) allows for e.g. transformation of local spherical components of the transversely isotropic stiffness tensors given in (7.30) and (7.13), to the global Cartesian ones, in order to account for the element orientation.

We are left with discussing the integration of a tensorial quantity \mathbb{T} over the surface of a unit sphere. This enables us to account for phases which are oriented in all space directions (solid C-S-H crystals, C-S-H gel needles and CH discs). Since analytical integration is out of reach for the surface integrals encountered herein, a discretized approach is employed. Herein, we use a 15-point numerical integration rule (Stroud, 1971). Thus, the integration over an infinite amount of orientations is approximated by a summation over 15 orientation as follows

$$\int_0^{2\pi} \int_0^\pi \mathbb{T}(\vartheta, \varphi) \frac{\sin \vartheta}{4\pi} d\vartheta d\varphi, \approx \frac{1}{15} \sum_{i=1}^{15} \mathbb{T}(\vartheta_i, \varphi_i) \quad (7.61)$$

whereby ϑ_i and φ_i are the position angles referring to integration point i (see (Pichler et al., 2009) or (Stroud, 1971) for numerical values), and the factor $1/15$ is the uniform weight at each point and can therefore be taken out from the sum. Notably, this numerical integration method is exact for integration of polynomials with degrees up to 5 (Stroud, 1971). Thus, it also represents a very good approximation for the integration of the gel orientation-dependent gel pore pressures $p_{gpor}(\underline{n}_{gel})$.

Appendix B: Discretized aspect ratio distribution

Herein, we discuss the discretization of the aspect ratio distribution of solid C-S-H crystals, introduced in Sec. 7.6. We first recall that aspect ratios of solid C-S-H crystals are a function of the available precipitation space γ , see Fig. 7.3. Given our interest in a model capable of predicting poroelastic properties as a function of hydration degree ξ and water-to-cement mass ratio w/c , a link between precipitation space and hydration degree is required. This link was derived in the Königsberger et al. (2016a) and it reads as

$$\gamma = \frac{3.185 w/c - 0.755 \xi}{3.185 w/c + 0.349 \xi} \quad (7.62)$$

Next, we can give details on the discretization. In the first precipitation increment $\Delta\gamma^{(1)}$, a crystal family exhibiting aspect ratio $X_{sCSH}^{(1)}$ precipitates, implying immediate non-zero stiffness at the level of the RVE of C-S-H gel. The crystals precipitating in this first increment are chosen to be penny-shaped infinite long with aspect ratio $X_{sCSH}^{(1)} = 0$. The increment is chosen to cover a very small precipitation space range: $\Delta\gamma^{(1)} = 10^{-3}$. Next, the remaining precipitation space interval $\gamma \in [\gamma^*, 1 - \Delta\gamma^{(1)}]$ is subdivided into $(n_f - 1)$ precipitation increments $\Delta\gamma$, with n_f denoting the number of aspect ratio families considered. Further hydration in terms of $\gamma \in [1 - \Delta\gamma^{(1)}, 1 - \Delta\gamma^{(1)} - \Delta\gamma]$ results in precipitation of solid C-S-H crystals of aspect ratio $X_{sCSH}^{(2)}$, which follows from the mean precipitation space value in the current interval, $\gamma^{(2)}$, according the linear relation (7.29) as $X_{sCSH} = 1 - \gamma^{(2)}$. Within the third precipitation increment $\gamma \in [1 - \Delta\gamma^{(1)} - \Delta\gamma, 1 - \Delta\gamma^{(1)} - 2\Delta\gamma]$, crystals with aspect ratio X_{sCSH}^3 precipitate, whereby the aspect ratio X_{sCSH}^3 , by analogy to increment two, follows from the mean precipitation space value γ^3 as $X_{sCSH}^3 = 1 - \gamma^3$. This procedure is repeated up to the last precipitation increment $\gamma \in [\gamma^* + \Delta\gamma, \gamma^*]$. We are left with assigning, to the i -th family, volume fractions f_i^{sCSH} , with $i = 1 \dots n_f$, whereby $\sum_{i=1}^{n_f} f_i^{sCSH} = 1$. Since the volume fraction is proportional to the length of the precipitation increment, and since the increment length is chosen to be constant for all increments after the first one, the volume fractions are also constant, $f_2^{sCSH} = f_3^{sCSH} = \dots f_{n_f}^{sCSH} = \Delta\gamma / (1 - \gamma^*)$. The volume fraction of the first family, however, follows as $f_1^{sCSH} = \Delta\gamma^{(1)} / (1 - \gamma^*)$. In summary, we deal, at a particular maturity state in terms of the precipitation space parameter γ^* , with a C-S-H gel RVE with n_f aspect ratio families exhibiting uniformly distributed aspect ratios. Thereby, each aspect ratio family consists of crystal phases, which are oriented in 15 particular space directions (see Appendix A).

As for the computation, we consider, that RVE at all maturity states exhibit the same amount of aspect ratio families. Therefore, the increment lengths $\Delta\gamma$ increase with decreasing precipitation space γ . This procedure avoids kinks in the results since the aspect ratio discretization is smoothly running in the interval which has to be covered. Keeping the precipitation increment length constant would lead to an increasing aspect ratio family number which, in turn, would lead to a kink in the results when a new family starts to evolve. It turns out that considering $n_f = 20$ aspect ratio families, already delivers a convergent solution.

Appendix C: Computational implementation based on 15 element orientations and 20 aspect ratio families

Herein, we provide full details on the computational implementation of the poro-micromechanical homogenization and the poromechanics at all involved scales discussed in Sec. 7.4-7.6. Thereby, we use the 15 point numerical integration scheme (7.61) to account for the orientation of solid C-S-H crystals, of C-S-H gel elements, and of CH crystals, as it was described in Appendix A. Moreover, we consider the discretized aspect ratio distribution involving 20 aspect ratio families, see Appendix B. We start the derivation at the smallest scale.

Within an RVE of C-S-H gel, we now deal with spherical gel pores and 20 aspect ratio families of solid C-S-H crystals with aspect ratio $X_{sCSH} = X_{sCSH}^{(1)} \dots X_{sCSH}^{(20)}$, whereby each family is oriented in 15 space directions described by normal vectors $\underline{n}_{sCSH}^{(1)} \dots \underline{n}_{sCSH}^{(15)}$. Thus, in total the RVE contains $15 \times 20 + 1 = 301$ material phases. The phase strains at the solid C-S-H scale stem from the strains in the solid C-S-H gel and from the gel pore pressure, see (7.38) and (7.37), respectively. These equations involve phase strain concentration \mathbb{A}_{sCSH} as well as \mathbb{A}_{gpor} , and eigenstress influence tensors $\mathbb{Q}_{sCSH,gpor}$ as well as $\mathbb{Q}_{gpor,gpor}$, discussed next. The phase strain concentration tensors read as

$$\mathbb{A}_{sCSH}(\underline{n}_{sCSH}^{(i)}, X_{sCSH}^{(j)}) = \mathbb{A}_{\infty,sCSH}(\underline{n}_{sCSH}^{(i)}, X_{sCSH}^{(j)}) : \left(\sum_{r=1}^{301} f_r^{gel} \mathbb{A}_{\infty,r} \right)^{-1} \quad (7.63)$$

$$\mathbb{A}_{gpor} = \mathbb{A}_{\infty,gpor} : \left(\sum_{r=1}^{301} f_r^{gel} \mathbb{A}_{\infty,r} \right)^{-1}, \quad (7.64)$$

with $\mathbb{A}_{\infty,j}$ as Eshelby problem-related strain concentration tensors, assigning remote matrix strains to inclusion strains in the corresponding Eshelby problems (Eshelby, 1957). Due to the polycrystalline nature of the RVE of C-S-H gel, the stiffness of the infinite matrix in the underlying matrix-inclusion problems, \mathbb{C}_{∞} , is chosen to be equal to the homogenized stiffness of the gel RVE. Considering $\mathbb{C}_{\infty} = \mathbb{C}_{gel}^{hom}$ yields the Eshelby problem-related strain concentration tensors as

$$\mathbb{A}_{\infty,sCSH}(\underline{n}_{sCSH}^{(i)}, X_{sCSH}^{(j)}) = \left[\mathbb{I} + \mathbb{P}_{sCSH}(\underline{n}_{sCSH}^{(i)}, X_{sCSH}^{(j)}) : \left(\mathbb{C}_{sCSH}(\underline{n}_{sCSH}^{(i)}) - \mathbb{C}_{gel}^{hom} \right) \right]^{-1} \quad (7.65)$$

$$\mathbb{A}_{\infty,gpor} = (\mathbb{I} - \mathbb{S}_{gpor})^{-1}, \quad (7.66)$$

whereby in the latter Eq. we take advantage of the vanishing pore stiffness. Aspect ratio family-specific and orientation-specific Hill Tensors \mathbb{P}_{sCSH} and Eshelby tensor of the spherical gel pores \mathbb{S}_{gpor} are discussed in Appendix D. Also the transversely isotropic stiffness tensor of the solid C-S-H crystals [for components related to the local base frame $\underline{e}_{\vartheta}, \underline{e}_{\varphi}, \underline{e}_r$ see (7.30)] is a function of the orientation \underline{n}_{sCSH} , see also Fig. 7.11. Orientation-dependent tensors follow from transformation of local components to global ones, see (7.58), whereby the angles ϑ^i, φ^i which describe the orientation vector $\underline{n}_{sCSH}^{(i)}$ of the solid C-S-H crystals (see Fig. 7.11) are used to construct transformation matrices \mathbb{Q} and \mathbb{Q} , see (7.60) and (7.59), respectively. The sum in (7.63) and (7.64) comprise all solid C-S-H phases (20 considered aspect ratio families with 15 orientations in each family) and also includes the gel pore phase – thus, index r runs

from 1 to 301 – allowing for rewriting the sum as

$$\sum_{r=1}^{301} f_r^{gel} \mathbb{A}_{\infty,r} = \frac{1}{15} f_{sCSH}^{gel} \sum_{i=1}^{15} \sum_{j=1}^{20} f_j^{sCSH} \mathbb{A}_{\infty,sCSH}(\underline{n}_{sCSH}^{(i)}, X_{sCSH}^{(j)}) + f_{gpor}^{gel} \mathbb{A}_{\infty,gpor} \quad (7.67)$$

whereby the family volume fraction related to the total solid C-S-H volume f_j^{sCSH} is given in Appendix B, and the gel-related volume fraction of solid C-S-H and of gel pores can be found in Sec. 7.6. Phase eigenstress influence tensor are derived next. Since the homogenized eigenstress of the infinite matrix is chosen to be equal to the homogenized eigenstress, $\boldsymbol{\sigma}_{\infty}^E = \boldsymbol{\sigma}_{gel}^{hom,E}$, the eigenstress influence tensor $\mathbb{Q}_{gpor,gpor}$ then read as (Pichler and Hellmich, 2010)

$$\begin{aligned} \mathbb{Q}_{gpor,gpor} = & \left[\mathbb{I} - f_{gpor}^{gel} \mathbb{A}_{gpor} \right] : \mathbb{A}_{\infty,gpor} : \mathbb{P}_{gpor} + \\ & \left[\mathbb{A}_{gpor} : \sum_{r=1}^{301} f_r^{gel} \mathbb{A}_{\infty,r} : \mathbb{P}_r - \mathbb{A}_{\infty,gpor} : \mathbb{P}_{gpor} \right] : f_{gpor}^{gel} \mathbb{A}_{gpor}^T \end{aligned} \quad (7.68)$$

$$\begin{aligned} \mathbb{Q}_{sCSH,gpor}(\underline{n}_{sCSH}^{(i)}, X_{sCSH}^{(j)}) = & - \mathbb{A}_{sCSH}(\underline{n}_{sCSH}^{(i)}, X_{sCSH}^{(j)}) : f_{gpor}^{gel} \mathbb{A}_{\infty,gpor} : \mathbb{P}_{gpor} + \\ & \left[\mathbb{A}_{gpor} : \sum_{r=1}^{301} f_r^{gel} \mathbb{A}_{\infty,r} : \mathbb{P}_r - \mathbb{A}_{\infty,gpor} : \mathbb{P}_{gpor} \right] : f_{gpor}^{gel} \mathbb{A}_{gpor}^T \end{aligned} \quad (7.69)$$

with the sum being equal to

$$\begin{aligned} \sum_{r=1}^{301} f_r^{gel} \mathbb{A}_{\infty,r} : \mathbb{P}_r = & \frac{1}{15} f_{sCSH}^{gel} \sum_{i=1}^{15} \sum_{j=1}^{20} f_j^{sCSH} \mathbb{A}_{\infty,sCSH}(\underline{n}_{sCSH}^{(i)}, X_{sCSH}^{(j)}) : \mathbb{P}_{sCSH}(\underline{n}_{sCSH}^{(i)}, X_{sCSH}^{(j)}) \\ & + f_{gpor}^{gel} \mathbb{A}_{\infty,gpor} : \mathbb{P}_{gpor} \end{aligned} \quad (7.70)$$

The homogenized (drained) isotropic stiffness \mathbb{C}_{gel}^{hom} follows from (7.32), which can be rewritten in discretized fashion as

$$\mathbb{C}_{gel}^{hom} = \frac{1}{15} f_{sCSH}^{gel} \sum_{i=1}^{15} \sum_{j=1}^{20} f_j^{sCSH} \mathbb{C}_{sCSH}(\underline{n}_{sCSH}^{(i)}) : \mathbb{A}_{sCSH}(\underline{n}_{sCSH}^{(i)}, X_{sCSH}^{(j)}) . \quad (7.71)$$

The homogenized eigenstress is C-S-H orientation-dependent, see (7.35) – in discretized form, we get the homogenized eigenstress of the RVE of gel oriented in $\underline{n}_{gel}^{(i)}$ direction as

$$\boldsymbol{\sigma}_{gel}^{hom,E}(\underline{n}_{gel}^{(i)}) = -f_{gpor}^{gel} p_{gpor}(\underline{n}_{gel}^{(i)}) \mathbf{1} : \mathbb{A}_{gpor} , \quad (7.72)$$

whereby herein, we deal with 15 orientations $\underline{n}_{gel}^{(1)} \dots \underline{n}_{gel}^{(15)}$.

Within the polycrystalline nature of the RVE of C-S-H foam, C-S-H gel needles in 15 particular orientations $\underline{n}_{gel}^{(1)} \dots \underline{n}_{gel}^{(15)}$ and spherical water-filled capillary pores as well as voids, are intermixed. The phase strains follow from (7.27)-(7.28), whereby the double integral over the unit sphere surface is replaced by the sum over the 15 considered orientations $\underline{n}_{gel}^{(1)} \dots \underline{n}_{gel}^{(15)}$, see (7.61). We need analytical access to phase strain concentration tensors for gel needles

oriented in direction $\underline{n}_{gel}^{(i)}$, \mathbb{A}_{gel} , for capillary pores \mathbb{A}_{cpor} , and for voids, \mathbb{A}_{void} . They read as

$$\mathbb{A}_{gel}(\underline{n}_{gel}^{(i)}) = \mathbb{A}_{\infty,gel}(\underline{n}_{gel}^{(i)}) : \left(\sum_{r=1}^{17} f_r^{foam} \mathbb{A}_{\infty,r} \right)^{-1} \quad (7.73)$$

$$\mathbb{A}_{cpor} = \mathbb{A}_{\infty,cpor} : \left(\sum_{r=1}^{17} f_r^{foam} \mathbb{A}_{\infty,r} \right)^{-1} \quad (7.74)$$

$$\mathbb{A}_{void} = \mathbb{A}_{\infty,void} : \left(\sum_{r=1}^{17} f_r^{foam} \mathbb{A}_{\infty,r} \right)^{-1}, \quad (7.75)$$

whereby the sum comprises the 15 gel phases with orientations $\underline{n}_{gel}^{(i)}$, the capillary pores, and the voids. The involved Eshelby problem-related strain concentration tensors follow from the underlying matrix-inclusion problem. Due to the polycrystalline nature of the RVE, the stiffness of the infinite matrix in the matrix-inclusion problem is chosen to be equal to the homogenized stiffness of the C-S-H foam RVE, $\mathbb{C}_{\infty} = \mathbb{C}_{foam}^{hom}$. Thus, the Eshelby problem-related strain concentration tensors read as

$$\mathbb{A}_{\infty,gel}(\underline{n}_{gel}^{(i)}) = [\mathbb{I} + \mathbb{P}_{gel}(\underline{n}_{gel}^{(i)}) : (\mathbb{C}_{gel}^{hom} - \mathbb{C}_{foam}^{hom})]^{-1} \quad (7.76)$$

$$\mathbb{A}_{\infty,cpor} = \mathbb{A}_{\infty,void} = (\mathbb{I} - \mathbb{S}_{cpor})^{-1}, \quad (7.77)$$

whereby we take advantage of the vanishing pore and void stiffness. Hill and Eshelby tensors can be found in the Appendix D, and transformation rule (7.58) – considering the angles ϑ^i and φ^i which describe the 15 orientation of $\underline{n}_{gel}^{(i)}$ – is again used to obtain the gel orientation-dependent tensor \mathbb{P}_{gel} . The sum in (7.76) and (7.77) can be rewritten as

$$\sum_{r=1}^{17} f_r^{foam} \mathbb{A}_{\infty,r} = \frac{1}{15} f_{gel}^{foam} \sum_{i=1}^{15} \mathbb{A}_{\infty,gel}(\underline{n}_{gel}^{(i)}) + (f_{cpor}^{foam} + f_{void}^{foam}) \mathbb{A}_{\infty,cpor} \quad (7.78)$$

The eigenstress influence tensors $\mathbb{Q}_{gel,gel}$, $\mathbb{Q}_{gel,cpor}$, $\mathbb{Q}_{cpor,gel}$, $\mathbb{Q}_{cpor,cpor}$, $\mathbb{Q}_{void,gel}$, and $\mathbb{Q}_{void,cpor}$, which occur in the phase strain expressions (7.27)-(7.28), follow for the polycrystalline nature of the RVE (the eigenstress of the infinite matrix in the matrix-inclusion problem is equal to

the homogenized eigenstress) as

$$\begin{aligned} \mathbb{Q}_{gel,gel}(\underline{n}_{gel}^{(i)}, \underline{n}_{gel}^{(j)}) &= \left[\delta_{ij} \mathbb{I} - \frac{1}{15} f_{gel}^{foam} \mathbb{A}_{gel}(\underline{n}_{gel}^{(i)}) \right] : \mathbb{A}_{\infty,gel}(\underline{n}_{gel}^{(i)}) : \mathbb{P}_{gel}(\underline{n}_{gel}^{(i)}) + \\ &\quad \left[\mathbb{A}_{gel}(\underline{n}_{gel}^{(i)}) : \sum_{r=1}^{17} f_r^{foam} \mathbb{A}_{\infty,r} : \mathbb{P}_r - \mathbb{A}_{\infty,gel}(\underline{n}_{gel}^{(i)}) : \mathbb{P}_{gel}(\underline{n}_{gel}^{(i)}) \right] \\ &\quad : \frac{1}{15} f_{gel}^{foam} \mathbb{A}_{gel}^T(\underline{n}_{gel}^{(j)}) \end{aligned} \quad (7.79)$$

$$\begin{aligned} \mathbb{Q}_{gel,cpor}(\underline{n}_{gel}^{(i)}) &= - \mathbb{A}_{gel}(\underline{n}_{gel}^{(i)}) : f_{cpor}^{foam} \mathbb{A}_{\infty,cpor} : \mathbb{P}_{cpor} + \\ &\quad \left[\mathbb{A}_{gel}(\underline{n}_{gel}^{(i)}) : \sum_{r=1}^{17} f_r^{foam} \mathbb{A}_{\infty,r} : \mathbb{P}_r - \mathbb{A}_{\infty,gel}(\underline{n}_{gel}^{(i)}) : \mathbb{P}_{gel}(\underline{n}_{gel}^{(i)}) \right] \\ &\quad : f_{cpor}^{foam} \mathbb{A}_{cpor}^T \end{aligned} \quad (7.80)$$

$$\begin{aligned} \mathbb{Q}_{cpor,gel}(\underline{n}_{gel}^{(i)}) &= - \mathbb{A}_{cpor} : \frac{1}{15} f_{gel}^{foam} \mathbb{A}_{\infty,gel}(\underline{n}_{gel}^{(i)}) : \mathbb{P}_{gel}(\underline{n}_{gel}^{(i)}) + \\ &\quad \left[\mathbb{A}_{cpor} : \sum_{r=1}^{17} f_r^{foam} \mathbb{A}_{\infty,r} : \mathbb{P}_r - \mathbb{A}_{\infty,cpor} : \mathbb{P}_{cpor} \right] : \frac{1}{15} f_{gel}^{foam} \mathbb{A}_{gel}^T(\underline{n}_{gel}^{(i)}) \end{aligned} \quad (7.81)$$

$$\begin{aligned} \mathbb{Q}_{cpor,cpor} &= \left[\mathbb{I} - f_{cpor}^{foam} \mathbb{A}_{cpor} \right] : \mathbb{A}_{\infty,cpor} : \mathbb{P}_{cpor} + \\ &\quad \left[\mathbb{A}_{cpor} : \sum_{r=1}^{17} f_r^{foam} \mathbb{A}_{\infty,r} : \mathbb{P}_r - \mathbb{A}_{\infty,cpor} : \mathbb{P}_{cpor} \right] : f_{cpor}^{foam} \mathbb{A}_{cpor}^T \end{aligned} \quad (7.82)$$

$$\begin{aligned} \mathbb{Q}_{void,gel}(\underline{n}_{gel}^{(i)}) &= - \mathbb{A}_{void} : \frac{1}{15} f_{gel}^{foam} \mathbb{A}_{\infty,gel}(\underline{n}_{gel}^{(i)}) : \mathbb{P}_{gel}(\underline{n}_{gel}^{(i)}) + \\ &\quad \left[\mathbb{A}_{void} : \sum_{r=1}^{17} f_r^{foam} \mathbb{A}_{\infty,r} : \mathbb{P}_r - \mathbb{A}_{\infty,void} : \mathbb{P}_{void} \right] : \frac{1}{15} f_{gel}^{foam} \mathbb{A}_{gel}^T(\underline{n}_{gel}^{(i)}) \end{aligned} \quad (7.83)$$

$$\begin{aligned} \mathbb{Q}_{void,cpor} &= - \mathbb{A}_{void} : f_{cpor}^{foam} \mathbb{A}_{\infty,cpor} : \mathbb{P}_{cpor} + \\ &\quad \left[\mathbb{A}_{void} : \sum_{r=1}^{17} f_r^{foam} \mathbb{A}_{\infty,r} : \mathbb{P}_r - \mathbb{A}_{\infty,void} : \mathbb{P}_{void} \right] : f_{cpor}^{foam} \mathbb{A}_{cpor}^T \end{aligned} \quad (7.84)$$

with the sum being equal to

$$\sum_{r=1}^{17} f_r^{foam} \mathbb{A}_{\infty,r} : \mathbb{P}_r = \frac{1}{15} f_{gel}^{foam} \sum_{i=1}^{15} \mathbb{A}_{\infty,gel}(\underline{n}_{gel}^{(i)}) : \mathbb{P}_{gel}(\underline{n}_{gel}^{(i)}) + \left(f_{cpor}^{foam} + f_{void}^{foam} \right) \mathbb{A}_{\infty,cpor} : \mathbb{P}_{cpor} \quad (7.85)$$

The homogenized (drained) stiffness \mathbb{C}_{foam}^{hom} follows from (7.22) in discretized form as

$$\mathbb{C}_{foam}^{hom} = \frac{1}{15} f_{gel}^{foam} \sum_{i=1}^{15} \mathbb{C}_{gel}^{hom} : \mathbb{A}_{gel}(\underline{n}_{gel}^{(i)}) . \quad (7.86)$$

The homogenized eigenstress of the C-S-H-foam related RVE, in turn, follows from (7.24) in discretized form as

$$\boldsymbol{\sigma}_{foam}^{hom,E} = \frac{1}{15} f_{gel}^{foam} \sum_{i=1}^{15} \mathbb{A}_{gel}(\underline{n}_{gel}^{(i)}) : \boldsymbol{\sigma}_{gel}^{hom,E}(\underline{n}_{gel}^{(i)}) - f_{cpor}^{foam} p_{cpor} \mathbf{1} : \mathbb{A}_{cpor}. \quad (7.87)$$

Within an RVE of cement paste, transversely isotropic CH crystals, oriented in 15 space directions (expressed in terms of orientation vector \underline{n}_{CH}), as well as spherical clinker grains are embedded within a C-S-H foam matrix. Phase strain expressions (7.18)-(7.20) involve strain concentration tensors and eigenstress influence tensor, given next. The phase strain concentration tensors read as

$$\mathbb{A}_{cem} = \mathbb{A}_{\infty,cem} : \left(\sum_{r=1}^{17} f_r^{cp} \mathbb{A}_{\infty,r} \right)^{-1} \quad (7.88)$$

$$\mathbb{A}_{CH,m} = \mathbb{A}_{\infty,CH,m} : \left(\sum_{r=1}^{17} f_r^{cp} \mathbb{A}_{\infty,r} \right)^{-1} \quad (7.89)$$

$$\mathbb{A}_{foam} = \mathbb{A}_{\infty,foam} : \left(\sum_{r=1}^{17} f_r^{cp} \mathbb{A}_{\infty,r} \right)^{-1}, \quad (7.90)$$

whereby the sum comprises 17 phases: CH phases oriented in 15 directions, clinker grains and the C-S-H foam matrix. Due to the matrix-inclusion-type RVE, the stiffness of the infinite matrix is chosen to be equal to the stiffness of the C-S-H foam (Mori-Tanaka scheme). This implies that $\mathbb{C}_{\infty} = \mathbb{C}_{foam}^{hom}$ and that Eshelby problem-related strain concentration tensors read as

$$\mathbb{A}_{\infty,cem} = \left[\mathbb{I} + \mathbb{P}_{cem} : \left(\mathbb{C}_{cem} - \mathbb{C}_{foam}^{hom} \right) \right]^{-1} \quad (7.91)$$

$$\mathbb{A}_{\infty,CH}(\underline{n}_{CH}^i) = \left[\mathbb{I} + \mathbb{P}_{CH}(\underline{n}_{CH}^i) : \left(\mathbb{C}_{CH,m} - \mathbb{C}_{foam}^{hom} \right) \right]^{-1} \quad (7.92)$$

$$\mathbb{A}_{\infty,foam} = \mathbb{I}. \quad (7.93)$$

Again, Hill tensors can be found in Appendix D. The sums in (7.88)-(7.90) can be rewritten as

$$\sum_{r=1}^{17} f_r^{cp} \mathbb{A}_{\infty,r} = f_{cem}^{cp} \mathbb{A}_{\infty,cem} + \frac{1}{15} f_{CH}^{cp} \sum_{i=1}^{15} \mathbb{A}_{\infty,CH}(\underline{n}_{CH}^i) + f_{foam}^{cp} \mathbb{A}_{foam} \quad (7.94)$$

The 17 eigenstress influence tensors $\mathbb{Q}_{cem,foam}$, $\mathbb{Q}_{CH,foam}$, $\mathbb{Q}_{foam,foam}$ follow from the general

eigenstrain influence tensor expressions presented in (Pichler and Hellmich, 2010) as

$$\begin{aligned} \mathbb{Q}_{cem,foam} = & -\mathbb{A}_{cem} : f_{foam}^{cp} \mathbb{A}_{\infty,foam} : \mathbb{P}_{foam} + \\ & \left[\mathbb{A}_{cem} : \sum_{r=1}^{17} f_r^{cp} \mathbb{A}_{\infty,r} : \mathbb{P}_r - \mathbb{A}_{\infty,cem} : \mathbb{P}_{cem} \right] : \\ & \left[\sum_{r=1}^{17} f_r^{cp} \left(\mathbb{C}_{cp}^{hom} - \mathbb{C}_r \right) : \mathbb{A}_{\infty,r} : \mathbb{P}_r \right]^{-1} : \\ & f_{foam}^{cp} \left[(\mathbb{I} - \mathbb{A}_{foam})^T + \left(\mathbb{C}_{cp}^{hom} - \mathbb{C}_{foam}^{hom} \right) : \mathbb{A}_{\infty,foam} : \mathbb{P}_{foam} \right] \end{aligned} \quad (7.95)$$

$$\begin{aligned} \mathbb{Q}_{CH,foam}(\underline{n}_{CH}^i) = & -\mathbb{A}_{CH}(\underline{n}_{CH}^i) : f_{foam}^{cp} \mathbb{A}_{\infty,foam} : \mathbb{P}_{foam} + \\ & \left[\mathbb{A}_{CH}(\underline{n}_{CH}^i) : \sum_{r=1}^{17} f_r^{cp} \mathbb{A}_{\infty,r} : \mathbb{P}_r - \mathbb{A}_{\infty,CH}(\underline{n}_{CH}^i) : \mathbb{P}_{CH}(\underline{n}_{CH}^i) \right] : \\ & \left[\sum_{r=1}^{17} f_r^{cp} \left(\mathbb{C}_{cp}^{hom} - \mathbb{C}_r \right) : \mathbb{A}_{\infty,r} : \mathbb{P}_r \right]^{-1} : \\ & f_{foam}^{cp} \left[(\mathbb{I} - \mathbb{A}_{foam})^T + \left(\mathbb{C}_{cp}^{hom} - \mathbb{C}_{foam}^{hom} \right) : \mathbb{A}_{\infty,foam} : \mathbb{P}_{foam} \right] \end{aligned} \quad (7.96)$$

$$\begin{aligned} \mathbb{Q}_{foam,foam} = & \left[\mathbb{I} - f_{foam}^{cp} \mathbb{A}_{foam} \right] : \mathbb{A}_{\infty,foam} : \mathbb{P}_{foam} + \\ & \left[\mathbb{A}_{foam} : \sum_{r=1}^{17} f_r^{cp} \mathbb{A}_{\infty,r} : \mathbb{P}_r - \mathbb{A}_{\infty,foam} : \mathbb{P}_{foam} \right] : \\ & \left[\sum_{r=1}^{17} f_r^{cp} \left(\mathbb{C}_{cp}^{hom} - \mathbb{C}_r \right) : \mathbb{A}_{\infty,r} : \mathbb{P}_r \right]^{-1} : \\ & f_{foam}^{cp} \left[(\mathbb{I} - \mathbb{A}_{foam})^T + \left(\mathbb{C}_{cp}^{hom} - \mathbb{C}_{foam}^{hom} \right) : \mathbb{A}_{\infty,foam} : \mathbb{P}_{foam} \right], \end{aligned} \quad (7.97)$$

with the sums reading as

$$\begin{aligned} \sum_{r=1}^{17} f_r \mathbb{A}_{\infty,r} : \mathbb{P}_r = & f_{cem}^{cp} \mathbb{A}_{\infty,cem} : \mathbb{P}_{cem} + \frac{1}{15} f_{CH}^{cp} \sum_{i=1}^{15} \mathbb{A}_{\infty,CH}(\underline{n}_{CH}^i) : \mathbb{P}_{CH}(\underline{n}_{CH}^i) \\ & + f_{foam}^{cp} \mathbb{A}_{\infty,foam} : \mathbb{P}_{foam} \end{aligned} \quad (7.98)$$

and

$$\begin{aligned} \sum_{r=1}^{17} f_r^{cp} \left(\mathbb{C}_{cp}^{hom} - \mathbb{C}_r \right) : \mathbb{A}_{\infty,r} : \mathbb{P}_r = & f_{cem}^{cp} \left(\mathbb{C}_{cp}^{hom} - \mathbb{C}_{cem} \right) : \mathbb{A}_{\infty,cem} : \mathbb{P}_{cem} \\ & + \frac{1}{15} f_{CH}^{cp} \sum_{i=1}^{15} \left(\mathbb{C}_{cp}^{hom} - \mathbb{C}_{CH}(\underline{n}_{CH}^i) \right) : \mathbb{A}_{\infty,CH}(\underline{n}_{CH}^i) : \mathbb{P}_{CH}(\underline{n}_{CH}^i) \\ & + f_{foam}^{cp} \left(\mathbb{C}_{cp}^{hom} - \mathbb{C}_{foam}^{hom} \right) : \mathbb{A}_{\infty,foam} : \mathbb{P}_{foam} \end{aligned} \quad (7.99)$$

The homogenized (drained) stiffness of cement paste is obtained by rewriting integral expression (7.15) for the 15 CH crystal orientation as

$$\mathbb{C}_{cp}^{hom} = f_{cem}^{cp} \mathbb{C}_{cem} : \mathbb{A}_{cem} + \frac{1}{15} f_{CH}^{cp} \sum_{i=1}^{15} \mathbb{C}_{CH}(\underline{n}_{CH}^i) : \mathbb{A}_{CH}(\underline{n}_{CH}^i) + f_{foam}^{cp} \mathbb{C}_{foam}^{hom} : \mathbb{A}_{foam}. \quad (7.100)$$

The homogenized eigenstress of the C-S-H-foam related RVE, in turn, is obtained from (7.17).

Next, the computational approach to obtain the undrained stiffness is discussed. Numerically, we consider 15 orientations of the C-S-H gel needles. Thus, we also deal with 15 particular gel pore pressures and additionally with the (orientation-independent) capillary pore pressure. First, we present, by analogy to (7.50), the relation between the porosity change in the 15 gel pore phases and in the capillary pore phase, respectively, as a function of all 16 pore pressures and as function of the macrostrain ϵ_{cp} . The procedure to obtain these expression is similar to the one given in Sec. 7.8. For the porosity change of the 15 gel pore phases, we arrive at

$$\Delta \phi_{gpor}^{cp}(\underline{n}_{gel}^{(i)}) = \mathbf{B}_{gpor}^{cp}(\underline{n}_{gel}^{(i)})^{cp} : \epsilon_{cp} + \sum_{j=1}^{15} \frac{p_{gpor}(\underline{n}_{gel}^{(j)})}{N_{gpor,gpor}^{cp}(\underline{n}_{gel}^{(i)}, \underline{n}_{gel}^{(j)})} + \frac{p_{cpor}}{N_{gpor,cpor}^{cp}}. \quad (7.101)$$

Therein, \mathbf{B}_{gpor}^{cp} denotes the cement paste-related Biot tensor for the gel pore phase in C-S-H gel RVE with orientation $(\underline{n}_{gel}^{(i)})$, and $N_{gpor,gpor}^{cp}$ as well as $N_{gpor,cpor}^{cp}$ denote the cement paste-related solid Biot moduli. They read as

$$\begin{aligned} \mathbf{B}_{gpor}^{cp}(\underline{n}_{gel}^{(i)}) &= \frac{1}{15} f_{foam}^{cp} f_{gel}^{foam} f_{gpor}^{gel} \mathbf{1} : \mathbb{A}_{gpor} : \mathbb{A}_{gel}(\underline{n}_{gel}^{(i)}) : \mathbb{A}_{foam} \\ \frac{1}{N_{gpor,gpor}^{cp}(\underline{n}_{gel}^{(i)}, \underline{n}_{gel}^{(j)})} &= \frac{1}{15} f_{foam}^{cp} f_{gel}^{foam} f_{gpor}^{gel} \mathbf{1} : \\ &\left[\frac{1}{15} f_{gel}^{foam} f_{gpor}^{gel} \mathbb{A}_{gpor} : \mathbb{A}_{gel}(\underline{n}_{gel}^{(i)}) : \mathbb{Q}_{foam,foam} : \mathbb{A}_{gel}(\underline{n}_{gel}^{(j)}) : \mathbf{1} : \mathbb{A}_{gpor} \right. \\ &\left. + f_{cpor}^{foam} \mathbb{A}_{gpor} : \mathbb{Q}_{gel,gel}(\underline{n}_{gel}^{(i)}, \underline{n}_{gel}^{(j)}) : \mathbf{1} : \mathbb{A}_{gpor} + \delta_{ij} \mathbb{Q}_{gpor,gpor} : \mathbf{1} \right] \\ \frac{1}{N_{gpor,cpor}^{cp}} &= \frac{1}{15} f_{foam}^{cp} f_{gel}^{foam} f_{gpor}^{gel} \mathbf{1} : \mathbb{A}_{gpor} : \\ &\left[f_{cpor}^{foam} \mathbb{A}_{gel}(\underline{n}_{gel}^{(i)}) : \mathbb{Q}_{foam,foam} : \mathbf{1} : \mathbb{A}_{cpor} + \mathbb{Q}_{gel,cpor}(\underline{n}_{gel}^{(i)}) : \mathbf{1} \right] \end{aligned} \quad (7.102)$$

whereby $N_{gpor,cpor}^{cp}$ is gel-orientation independent of which we can assure ourselves by evaluating (7.104) for all 15 gel orientations $i = 1, 2, \dots, 15$. By analogy to the gel porosity changes (7.101), we find the capillary porosity changes in discretized form of (7.53) as

$$\Delta \phi_{cpor}^{cp} = \mathbf{B}_{cpor}^{cp} : \epsilon_{cp} + \sum_{i=1}^{15} \frac{p_{gpor}(\underline{n}_{gel}^{(i)})}{N_{cpor,gpor}^{cp}} + \frac{p_{cpor}}{N_{cpor,cpor}^{cp}}. \quad (7.105)$$

Therein, \mathbf{B}_{cpor}^{cp} denotes the cement paste-related Biot tensor for the capillary pore phase, and $N_{cpor,gel}^{cp}$ as well as $N_{cpor,cpor}^{cp}$ denote the cement paste-related solid Biot moduli, and they

respectively read as

$$\mathbf{B}_{cpor}^{cp} = f_{foam}^{cp} f_{cpor}^{foam} \mathbf{1} : \mathbb{A}_{cpor} : \mathbb{A}_{foam} \quad (7.106)$$

$$\begin{aligned} \frac{1}{N_{cpor,gpor}^{cp}} &= f_{foam}^{cp} f_{cpor}^{foam} \mathbf{1} : \left(f_{gpor}^{gel} \mathbb{Q}_{cpor,gel}(\underline{n}_{gel}^{(i)}) : \mathbf{1} : \mathbb{A}_{gpor} \right. \\ &\quad \left. + \frac{1}{15} f_{gel}^{foam} f_{gpor}^{gel} \mathbb{A}_{cpor} : \mathbb{Q}_{foam,foam} : \mathbb{A}_{gel}(\underline{n}_{gel}^{(i)}) : \mathbf{1} : \mathbb{A}_{gpor} \right) \end{aligned} \quad (7.107)$$

$$\frac{1}{N_{cpor,cpor}^{cp}} = f_{foam}^{cp} f_{cpor}^{foam} \mathbf{1} : \left(\mathbb{Q}_{cpor,cpor} : \mathbf{1} + f_{cpor}^{foam} \mathbb{A}_{cpor} : \mathbb{Q}_{foam,foam} : \mathbf{1} : \mathbb{A}_{cpor} \right) . \quad (7.108)$$

Notably, $N_{i,j} = N_{j,i}$ for energetic reasons (Dormieux et al., 2006) and therefore whereby $N_{cpor,gpor}^{cp}$ is also gel-orientation independent.

Next, we calculate the 16 pore pressures as function of the macroscopic stresses, i.e. we try to find the gel orientation dependent tensors \mathbf{L}_{gpor} and the tensor \mathbf{L}_{cpor} , respectively, introduced in (7.44). Therefore, we compare gel porosity change relations (7.101) with the corresponding relations stemming from the gel water compressibility (7.42), and we compare capillary porosity change relation (7.105) with the corresponding relations stemming from the capillary water compressibility (7.43), allowing us to obtain a system of 16 equations for the 16 unknown pore pressures which can be given in matrix form, by analogy to the approach presented in (Hellmich et al., 2009), as

$$\mathcal{M} \times \begin{pmatrix} p_{gpor}(\underline{n}_{gel}^{(1)}) \\ p_{gpor}(\underline{n}_{gel}^{(2)}) \\ \vdots \\ p_{gpor}(\underline{n}_{gel}^{(15)}) \\ p_{cpor} \end{pmatrix} = \begin{pmatrix} -M_{gpor}^{cp} \mathbf{B}_{gpor}^{cp}(\underline{n}_{gel}^{(1)}) \\ -M_{gpor}^{cp} \mathbf{B}_{gpor}^{cp}(\underline{n}_{gel}^{(2)}) \\ \vdots \\ -M_{gpor}^{cp} \mathbf{B}_{gpor}^{cp}(\underline{n}_{gel}^{(15)}) \\ -M_{cpor}^{cp} \mathbf{B}_{cpor}^{cp} \end{pmatrix} : \boldsymbol{\varepsilon}_{cp} \quad (7.109)$$

with \mathcal{M} standing for the matrix

$$\mathcal{M} = \begin{pmatrix} 1 & \frac{M_{gpor}^{cp}}{N_{gpor,gpor}^{cp}(\underline{n}_{gel}^{(1)}, \underline{n}_{gel}^{(2)})} & \cdots & \frac{M_{gpor}^{cp}}{N_{gpor,gpor}^{cp}(\underline{n}_{gel}^{(1)}, \underline{n}_{gel}^{(15)})} & \frac{M_{gpor}^{cp}}{N_{gpor,cpor}^{cp}} \\ \frac{M_{gpor}^{cp}}{N_{gpor,gpor}^{cp}(\underline{n}_{gel}^{(2)}, \underline{n}_{gel}^{(1)})} & 1 & \cdots & \frac{M_{gpor}^{cp}}{N_{gpor,gpor}^{cp}(\underline{n}_{gel}^{(2)}, \underline{n}_{gel}^{(15)})} & \frac{M_{gpor}^{cp}}{N_{gpor,cpor}^{cp}} \\ \vdots & & \ddots & & \vdots \\ \frac{M_{gpor}^{cp}}{N_{gpor,gpor}^{cp}(\underline{n}_{gel}^{(15)}, \underline{n}_{gel}^{(1)})} & \frac{M_{gpor}^{cp}}{N_{gpor,gpor}^{cp}(\underline{n}_{gel}^{(15)}, \underline{n}_{gel}^{(2)})} & \cdots & 1 & \frac{M_{gpor}^{cp}}{N_{gpor,cpor}^{cp}} \\ \frac{M_{cpor}^{cp}}{N_{cpor,gpor}^{cp}} & \frac{M_{cpor}^{cp}}{N_{cpor,gpor}^{cp}} & \cdots & \frac{M_{cpor}^{cp}}{N_{cpor,gpor}^{cp}} & 1 \end{pmatrix} \quad (7.110)$$

and with modulus-type quantities M_{gpor}^{cp} and M_{cpor}^{cp} reading as

$$\frac{1}{M_{gpor}^{cp}} = \frac{1}{15} \frac{f_{gpor}^{gel}}{k_{H_2O}} + \frac{1}{N_{gpor,gpor}^{cp}(\underline{n}_{gel}^{(i)}, \underline{n}_{gel}^{(i)})} , \quad (7.111)$$

$$\frac{1}{M_{cpor}^{cp}} = \frac{f_{cpor}^{foam}}{k_{H_2O}} + \frac{1}{N_{cpor,cpor}^{cp}} . \quad (7.112)$$

Notably, the influence of the gel pore pressure on the porosity change of the very same gel pore is gel orientation-independent, hence, also M_{gpor}^{cp} is orientation-independent. Eq. (7.109)

represents a linear inhomogeneous system of equation which solution finally gives access to the 16 pore pressures as a function of the macrostrains ε_{cp} , i.e. it provides access to the sought tensors \mathbf{L}_{gpor}^{cp} and \mathbf{L}_{cpor}^{cp} as

$$\begin{pmatrix} \mathbf{L}_{gpor}^{cp}(\underline{n}_{gel}^{(1)}) \\ \mathbf{L}_{gpor}^{cp}(\underline{n}_{gel}^{(2)}) \\ \vdots \\ \mathbf{L}_{gpor}^{cp}(\underline{n}_{gel}^{(15)}) \\ \mathbf{L}_{cpor}^{cp} \end{pmatrix} = \mathcal{M}^{-1} \times \begin{pmatrix} -M_{gpor}^{cp} \mathbf{B}_{gpor}^{cp}(\underline{n}_{gel}^{(1)}) \\ -M_{gpor}^{cp} \mathbf{B}_{gpor}^{cp}(\underline{n}_{gel}^{(2)}) \\ \vdots \\ -M_{gpor}^{cp} \mathbf{B}_{gpor}^{cp}(\underline{n}_{gel}^{(15)}) \\ -M_{cpor}^{cp} \mathbf{B}_{cpor}^{cp} \end{pmatrix} \quad (7.113)$$

We are left with presenting the discretized counterpart to the expression of the undrained cement paste stiffness (7.57), which simply reads as

$$\mathbb{C}_{cp,ud}^{hom} = \mathbb{C}_{cp}^{hom} - \sum_{i=1}^{15} \mathbf{B}_{gpor}^{cp}(\underline{n}_{gel}^{(i)}) \otimes \mathbf{L}_{gpor}^{cp}(\underline{n}_{gel}^{(i)}) - \mathbf{B}_{cpor}^{cp} \otimes \mathbf{L}_{cpor}^{cp} \quad (7.114)$$

Appendix D: Accounting for phase shapes: Eshelby and Hill tensors

In order to complete the analytical derivations presented in Sec. 7.6-7.8 and Appendix C, we need analytical access to Hill Tensors for oblate spheroids (as this shape is assumed to represent the solid C-S-H crystals), for cylindrical inclusions (needle-shaped gel elements), for flat oblates (disc-shaped CH crystals), and for spherical inclusions (pores, cement clinker). We deal with a spheroidal inclusion with semi axis $a_\vartheta = a_\varphi, a_r$ with respect to the local base frame $\underline{e}_\vartheta, \underline{e}_\varphi, \underline{e}_r$, whereby \underline{e}_r is the axis of rotational symmetry and semi axis a_ϑ aligns with the base vector \underline{e}_ϑ (and similarly a_φ with \underline{e}_φ and a_r with \underline{e}_r), see Fig. 7.11. This inclusion is embedded within an infinite matrix exhibiting isotropic stiffness tensor \mathbb{C}_∞ with Poisson's ratio ν_∞ . Then the Hill tensor \mathbb{P} of the spheroid can be obtained from the Eshelby Tensor \mathbb{S} as

$$\mathbb{P} = \mathbb{S} : \mathbb{C}_\infty^{-1}, \quad (7.115)$$

whereby \mathbb{S} is a function of the inclusion's aspect ratio $X = a_r/a_\vartheta$ and of the stiffness of the infinite matrix (Eshelby, 1957). Notably, \mathbb{S} exhibit minor symmetries, i.e. $S_{ijkl} = S_{jikl} = S_{ijlk}$. Next, the components of \mathbb{S} , S_{ijkl} are given with respect to the local base $\underline{e}_\vartheta, \underline{e}_\varphi, \underline{e}_r$. We start with the general spheroidal inclusion and specify for the limit case of a penny-shaped disc, and for the other limit case of a cylinder. Thereafter, spherical inclusions are discussed. Conclusively, the construction of the Hill Tensors for the particular material phases is described.

The components of the Eshelby tensor for a spheroidal inclusion \mathbb{S}^{ell} read as

$$\begin{aligned}
 S_{\vartheta\vartheta\vartheta\vartheta}^{ell} &= S_{\varphi\varphi\varphi\varphi}^{ell} = \frac{3}{8(1-\nu_\infty)} \frac{X^2}{X^2-1} + \frac{1}{4(1-\nu_\infty)} \left(1 - 2\nu_\infty - \frac{9}{4(X^2-1)} \right) g; \\
 S_{rrrr}^{ell} &= \frac{1}{2(1-\nu_\infty)} \left[1 - 2\nu_\infty + \frac{3X^2-1}{X^2-1} - \left(1 - 2\nu_\infty + \frac{3X^2}{X^2-1} \right) g \right]; \\
 S_{\vartheta\vartheta\varphi\varphi}^{ell} &= S_{\varphi\varphi\vartheta\vartheta}^{ell} = \frac{1}{4(1-\nu_\infty)} \left\{ \frac{X^2}{2(X^2-1)} - \left[1 - 2\nu_\infty + \frac{3}{4(X^2-1)} \right] g \right\}; \\
 S_{\vartheta\vartheta rr}^{ell} &= S_{\varphi\varphi rr}^{ell} = -\frac{1}{2(1-\nu_\infty)} \frac{X^2}{X^2-1} + \frac{1}{4(1-\nu_\infty)} \left[\frac{3X^2}{X^2-1} - (1 - 2\nu_\infty) \right] g; \\
 S_{rr\vartheta\vartheta}^{ell} &= S_{rr\varphi\varphi}^{ell} = \frac{1}{2(1-\nu_\infty)} \left(-1 + 2\nu_\infty + \frac{1}{1-X^2} \right) + \frac{1}{4(1-\nu_\infty)} \left[2(1 - 2\nu_\infty) - \frac{3}{1-X^2} \right] g; \\
 S_{\vartheta\varphi\varphi\varphi}^{ell} &= \frac{1}{8(1-\nu_\infty)} \frac{X^2}{X^2-1} + \frac{1}{4(1-\nu_\infty)} \left[1 - 2\nu_\infty - \frac{3}{4(X^2-1)} \right] g; \\
 S_{\varphi r\varphi r}^{ell} &= S_{\vartheta r\vartheta r}^{ell} = \frac{1}{4(1-\nu_\infty)} \left(1 - 2\nu_\infty - \frac{X^2+1}{X^2-1} \right) - \frac{1}{8(1-\nu_\infty)} \left[1 - 2\nu_\infty - \frac{3(X^2+1)}{X^2-1} \right] g;
 \end{aligned} \tag{7.116}$$

with

$$g = \begin{cases} \frac{X}{(1-X^2)^{3/2}} \left[\arccos X - X(1-X^2)^{1/2} \right] & \forall X = \frac{a_r}{a_\vartheta} < 1 \\ \frac{X}{(X^2-1)^{3/2}} \left[X(X^2-1)^{1/2} - \operatorname{arccosh} X \right] & \forall X = \frac{a_r}{a_\vartheta} > 1. \end{cases} \tag{7.117}$$

As for the limit case of flat prolate spheroids ($X \rightarrow 0$), denoted as discs, we obtain the nonzero components of the Eshelby tensor as

$$\begin{aligned}
 S_{rrrr}^{disc} &= 1 \\
 S_{rr\vartheta\vartheta}^{disc} &= S_{rr\varphi\varphi}^{disc} = \frac{\nu_\infty}{1-\nu_\infty} \\
 S_{\varphi r\varphi r}^{disc} &= S_{1rr1}^{disc} = \frac{1}{2}.
 \end{aligned} \tag{7.118}$$

and for the case of a cylindrical inclusion ($X \rightarrow \infty$), nonzero components read as

$$\begin{aligned}
 S_{\vartheta\vartheta\vartheta\vartheta}^{cyl} &= S_{\varphi\varphi\varphi\varphi}^{cyl} = \frac{5-4\nu_\infty}{8(1-\nu_\infty)} \\
 S_{\vartheta\vartheta\varphi\varphi}^{cyl} &= S_{\varphi\varphi\vartheta\vartheta}^{cyl} = \frac{-1+4\nu_\infty}{8(1-\nu_\infty)} \\
 S_{\varphi r\varphi r}^{cyl} &= S_{\vartheta r\vartheta r}^{cyl} = \frac{1}{4} \\
 S_{\vartheta\varphi\varphi\varphi}^{cyl} &= \frac{3-4\nu_\infty}{8(1-\nu_\infty)}
 \end{aligned} \tag{7.119}$$

The fourth-order Eshelby tensor of a spherical inclusion $a_\vartheta = a_\varphi = a_r$, \mathbb{S}^{sph} , is given for example

in (Zaoui, 2002) and can be written as

$$S_{ijkl}^{sph} = \frac{5\nu_\infty - 1}{15(1 - \nu_\infty)} \delta_{ij} \delta_{kl} + \frac{4 - 5\nu_\infty}{15(1 - \nu_\infty)} (\delta_{ik} \delta_{jl} + \delta_{il} \delta_{jk}) \quad (7.120)$$

Finally, we discuss the construction of the Hill tensors for spheroidal and spherical elements used for cement paste homogenization based on the formulas (7.115)-(7.120). The Hill tensor for the solid C-S-H elements, $\mathbb{P}_{sCSH}(\underline{n}_{sCSH}^{(i)}, X_{sCSH})$, appearing in (7.65) and (7.70), is obtained after construction of the Eshelby tensor from its components given in (7.116) considering $\nu_\infty = \nu_{gel}^{hom}$ and tensor multiplication according to (7.115) considering $\mathbb{C}_\infty = \mathbb{C}_{gel}^{hom}$. Note that this tensor refers to a \underline{e}_3 -aligned spheroid. In order to obtain other orientations in terms of angles φ^i, ϑ^i transformation rule (7.58) has to be used. The Eshelby tensor of the spherical gel pores \mathbb{S}_{gpor} appearing in (7.66) is obtained from (7.120) considering $\nu_\infty = \nu_{gel}^{hom}$, and the corresponding Hill tensor, \mathbb{P}_{gpor} , follows from (7.115) with $\mathbb{C}_\infty = \mathbb{C}_{gel}^{hom}$. Hill tensor for voids and capillary pores at the C-S-H foam scale, appearing in (7.77) and (7.80)-(7.85) read as $\mathbb{P}_{cpor} = \mathbb{P}_{void} = \mathbb{S}_{cpor} : \mathbb{C}_{por}^{-1}$, whereby the Eshelby tensor of the spherical phases is given in (7.120) considering $\nu_\infty = \nu_{foam}^{hom}$. Hill tensors for \underline{e}_3 -aligned cylindrical gel elements, \mathbb{P}_{gel} , appearing in (7.76) and (7.79)-(7.85) are obtained from components (7.119) and (7.115) while considering $\nu_\infty = \nu_{foam}^{hom}$ and $\mathbb{C}_\infty = \mathbb{C}_{foam}^{hom}$. At the cement paste scale, we obtain the Hill tensor for spherical cement clinker grains, \mathbb{P}_{cem} appearing in (7.91), (7.95), and (7.98)-(7.99), from (7.120) considering $\nu_\infty = \nu_{foam}^{hom}$ and insertion into (7.115) considering $\mathbb{C}_\infty = \mathbb{C}_{foam}^{hom}$. $\mathbb{P}_{CH}(\underline{n}_{CH}^i)$, i.e. the Hill tensor for disc-like CH-elements appearing in (7.92), (7.96), and (7.98)-(7.99), follow from the Eshelby tensor components of disc-shaped inclusions, see (7.118) with $\nu_\infty = \nu_{foam}^{hom}$, and from (7.115) considering $\mathbb{C}_\infty = \mathbb{C}_{foam}^{hom}$. In the expression for the eigenstress influence tensors (7.95)-(7.99), also a Hill tensor for the C-S-H foam matrix occurs. Being a matrix phase, the shape for the foam is irrelevant and \mathbb{P}_{foam} can be obtained from e.g. a spherical representation (7.120) and (7.115), considering $\nu_\infty = \nu_{foam}^{hom}$ and $\mathbb{C}_\infty = \mathbb{C}_{foam}^{hom}$.

Appendix E: Notation

$\mathbf{1}$	second-order identity tensor
$(.)^T$	transpose of quantity $(.)$
$(.)^{-1}$	inverse of quantity $(.)$
\cdot	inner product
$:$	second-order tensor contraction
\otimes	dyadic product
\times	multiplication
\mathbb{A}	strain concentration tensor
\mathbb{A}_j	strain concentration tensor of phase j , whereby $j \in \{cem, CH, cpor, foam, gel, gpor, sCSH, void\}$
$\mathbb{A}_{\infty,j}$	Eshelby problem-related strain concentration tensor of phase j , whereby $j \in \{cem, CH, cpor, foam, gel, gpor, sCSH, void\}$
\mathbf{B}_j^{cp}	cement paste-related Biot tensor for the pore phase j with $j \in \{cpor, gpor\}$
$a_\vartheta, a_\varphi, a_r$	dimensions of the spheroidal phases in $\underline{e}_\vartheta, \underline{e}_\varphi, \underline{e}_r$ -directions
\mathbb{C}	elastic stiffness tensor
\mathbb{C}_∞	elastic stiffness tensor infinite matrix in Eshelby problem

\mathbb{C}_j	elastic stiffness tensor of phase j with $j \in \{cem, CH, sCSH\}$
\mathbb{C}_j^{hom}	homogenized elastic stiffness tensor for RVE j with $j \in \{cp, gel, foam\}$
$\mathbb{C}_{ud}^{hom,u}$	homogenized undrained elastic stiffness tensor for cement paste
$C-S-H$	calcium-silicate-hydrates
CH	portlandite (calcium hydroxide) crystals
cp	cement paste
$cpor$	capillary pores
d, d_2, d_3	characteristic sizes of the inclusions in an RVE
$\underline{e}_x, \underline{e}_y, \underline{e}_z$	unit base vectors of the global Cartesian base frame
$\underline{e}_\vartheta, \underline{e}_\varphi, \underline{e}_r$	unit base vectors of the local spherical base frame
E_{cp}^{hom}	homogenized Young's modulus for cement paste
f_j^{cp}	cement paste-related volume fraction of phase j with $j \in \{cem, CH, cpor, foam, gel, gpor, sCSH, void\}$
f_j^{foam}	C-S-H foam-related volume fraction of phase j with $j \in \{cpor, gel, void\}$
f_j^{gel}	C-S-H gel-related volume fraction of phase j with $j \in \{gpor, sCSH\}$
f_j^{sCSH}	solid C-S-H-related volume fraction of crystal family with aspect ratio $X_{sCSH}^{(j)}$, where $j = 1, 2, \dots, n_f$
$foam$	C-S-H foam
g	auxiliary variable
$gpor$	gel pores
gel	C-S-H gel
H_2O	water
\mathbb{I}	fourth-order identity tensor
$\mathbb{I}_{vol}, \mathbb{I}_{dev}$	volumetric and deviatoric parts of fourth-order identity tensor
k_j	bulk modulus of phase j with $j \in \{cp, H_2O\}$
\mathcal{L}	characteristic size of the structure containing an RVE
\mathbf{L}_j^{cp}	auxiliary, cement paste-related second-order tensor providing the link between cement paste strains and pore pressures in pore phase j with $j \in \{cpor, gpor\}$
ℓ, ℓ_2, ℓ_3	characteristic RVE sizes
M_j^{cp}	auxiliary, cement paste-related modulus-type scalar for pore phase j with $j \in \{cpor, gpor\}$
\mathcal{M}	auxiliary matrix
$N_{i,j}^{cp}$	cement paste-related solid Biot modulus relating pore pressures in phase j to pore volume changes in phase i , whereby $i, j \in \{cpor, gpor\}$
n_f	number of aspect ratio families of solid C-S-H crystals; herein $n_f = 20$
\underline{n}_j	orientation vector in line with the axis of rotational symmetry of the spheroidal element j with $j \in \{CH, gel, sCSH\}$
$\underline{n}_j^{(i)}$	orientation vector \underline{n}_j pointing in particular direction i whereby the direction i refers to a point located at the surface of a unit sphere regarding the numerical integration algorithm, herein $i = 1, 2, \dots, 15$
\mathbb{P}	Hill tensor
\mathbb{P}_j	Hill tensor for phase j with $j \in \{cem, CH, cpor, foam, gel, gpor, sCSH, void\}$
p_j	pore pressure in phase j with $j \in \{cpor, gpor\}$
p_{foam}	pressure exerted by the foam to the adjacent matter within the RVE of cement paste

Q	transformation matrix with elements Q_{ij} for transformation of the spherical $\underline{e}_\vartheta, \underline{e}_\varphi, \underline{e}_r$ -components of a second-order tensor to Cartesian $\underline{e}_x, \underline{e}_y, \underline{e}_z$ -components
\mathcal{Q}	transformation matrix for transformation of the spherical $\underline{e}_\vartheta, \underline{e}_\varphi, \underline{e}_r$ -components of a fourth-order tensor to Cartesian $\underline{e}_x, \underline{e}_y, \underline{e}_z$ -components
$Q_{i,j}$	eigenstress influence tensor quantifying the influence of eigenstresses in phase j on phase strains in phase i ; where $i \in \{cem, CH, cpor, foam, gel, gpor, sCSH, void\}$ and $j \in \{cpor, foam, gel, gpor\}$
T	auxiliary tensor with components T_{ijkl}
S_{ijkl}^r	Eshelby tensor components for inclusion r , whereby r refers the inclusion shape with $r \in \{cyl, disc, ell, sph\}$ standing for cylindrical, disc-like, ellipsoidal, or spherical shape
S	Eshelby tensor
S_j	Eshelby tensor for phase j with $j \in \{cpor, gpor\}$
$sCSH$	solid C-S-H
V_j	volume of phase j with $j \in \{cpor, gpor, sCSH\}$
w/c	initial water-to-cement mass ratio
X_{sCSH}	aspect ratio of solid C-S-H crystals
$X_{sCSH}^{(i)}$	aspect ratio X_{sCSH} for particular crystal family i , where $i = 1, 2, \dots, n_f$
X_{sCSH}^{max}	maximum aspect ratio X_{sCSH} at particular specific precipitation space γ
X	aspect ratio of ellipsoidal inclusion in Eshelby problem
\underline{x}	position vector
γ	specific precipitation space with $0 \leq \gamma \leq 1$
γ^*	a certain value of γ
$\gamma^{(i)}$	mean precipitation space γ in the current interval i with $i = 1, 2, \dots, n_f$
Δ	Auxiliary variable
Δ_{cpor}^{foam}	capillary pore volume change related to the C-S-H foam volume
Δ_{gpor}^{gel}	gel pore volume change related to the gel volume
Δ_j^{cp}	pore volume change of phase j related to the cement paste volume, with $j \in \{cpor, gpor\}$
$\Delta\gamma$	length of precipitation increment
$\Delta\gamma^{(i)}$	precipitation increment where solid C-S-H crystals exhibiting aspect $X_{sCSH}^{(i)}$ precipitate, with $i = 1, 2, \dots, n_f$
δ_{ij}	Kronecker delta
$\delta_{\underline{n}_{gel}, \underline{n}_{gel}^*}$	tensorial Kronecker delta
ε_j	strain tensor of phase j with $j \in \{cem, cp, CH, cpor, foam, gel, gpor, sCSH, void\}$
ϑ	zenith angle marking the orientation of hydrate needles
μ_{cem}	shear modulus of unhydrated cement clinker
μ_{cp}^{hom}	homogenized shear modulus of cement paste
ν_∞	Poisson's ratio of infinite matrix in Eshelby problem
ν_j^{hom}	homogenized Poisson's ratio for RVE j with $j \in \{cp, foam, gel\}$
ξ	hydration degree
ξ_{I-II}	hydration degree at the transition from hydration regime I to II
ξ_{II-III}	hydration degree at the transition from hydration regime II to III
ξ_{ult}	ultimate hydration degree, $\xi_{ult} \geq \xi$
ρ_j	mass density of phase j with $j \in \{gel, sCSH\}$

σ_j	stress tensor of phase j with $j \in \{cp, foam, gel\}$
σ^E	eigenstress
$\sigma_j^{hom,E}$	homogenized eigenstress for RVE j with $j \in \{cp, foam, gel\}$
φ	azimuth angle marking the orientation of hydrate needles
Ω_i	domain of phase j with $j \in \{cem, CH, cpor, foam, gel, gpor, sCSH, void\}$

Conclusions and outlook

8.1 Summary of the developed models

This thesis is built upon the philosophy that modeling physical phenomena of cementitious materials at the macroscopic scale requires to capture the underlying basic mechanisms at the microscale. Accordingly, a multiscale approach is used to get insight into macroscopic failure processes, creep processes, and the poroelastic behavior of cement pastes, mortars, and concretes. Careful representation of the materials' microstructures is a prerequisite for such an approach. In the framework of continuum micromechanics, the complex microstructure is resolved into material phases with distinct mechanical and morphological characteristics. In agreement with the principle of scale separation, four scales of observation are envisioned:

- At the centimeter-large scale of concrete or mortar, respectively, a matrix-inclusion composite is considered, consisting of spherical aggregates (sand or gravel), air voids, and a matrix of cement paste.
- At the scale of one millimeter, the microstructure of cement paste is again envisioned to be a matrix-inclusion morphology. Spherical clinker grains, potentially together with the plate-like portlandite hydrates, are considered to be embedded in a hydrate foam matrix.
- At the scale of one micron, the microstructure of hydrate foam is represented as a polycrystal, consisting of needle-shaped phases (particularly representing the C-S-H gel), potentially intermixed with spherical hydrates (such as sulfoaluminates), and intermixed with capillary porosity and shrinkage-induced voids.
- At the smallest scale of observation, the microstructure of C-S-H is considered to consist of five nanometer-thick solid C-S-H particles which are intermixed with the water-filled gel porosity to form another polycrystal.

The maturation during the hydration process is considered by evolving volumes of the material phases, on the one hand, and by solid C-S-H particle shapes which are a function of the material age at their precipitation, on the other hand. The elastic, viscoelastic, and strength properties of the phases, however, stay constant. Volume evolutions are either estimated based on the Powers model, if the micromechanical problem is restricted to the first three scales of observation. If the actual problem requires to start at the smallest observation scale, the evolution of the gel porosity has to be predicted reliably. Powers' model does not

qualify for that task since it assumes the gel pores to be maturity-independent. Recently published nuclear magnetic resonance relaxometry data, however, showed that the gel porosity decreases during the hydration process, implying a hydration-induced densification of C-S-H gel. Within this thesis, the measured data are cast into a mathematical model. Thereby, the progressively decreasing space available for new C-S-H to precipitate is considered to be the origin of the C-S-H densification. Powers model does only apply for bulk cement paste, i.e. it considers the paste to be a thermodynamically isolated domain. In mortars or concrete, however, water migration between aggregates and the cement paste matrix occurs and this influences the phase volume evolutions significantly. Therefore, the water flow from the aggregates to the cement paste is explicitly considered in this thesis, by developing yet another mathematical model, based on the idea that chemical shrinkage governs the suction of water residing in the aggregates' porosity to the hydrating cement paste matrix.

8.2 Research contribution and main findings

The presented microstructural modeling campaign contributes to the knowledge in cement and concrete science in three ways:

1. The models developed in this thesis can be evaluated in order to *predict* the evolution of mechanical behavior of cementitious materials. Thus, they might be able to replace costly and time-consuming experimental campaigns.
2. Mathematical modeling proves to be useful to identify the physical behavior at very small scales, where experimental insight is still limited.
3. Valuable insights into physical mechanisms and features at the nano- and microscale, which govern the macroscopic material behavior, are gained by the microstructural and micromechanical multiscale models developed herein.

Related main findings are summarized in the following.

In Chapter 3, the compressive strength evolution of ordinary Portland cement paste and mortar is predicted very reliably as a function of the material's composition (in terms of the water-to-cement mass ratio) and as a function of the material's maturity (in terms of the hydration degree). Macroscopic material failure is related to Mohr-Coulomb type material failure of hydrate needles, whereby the microscopic strength constants are taken from limit state analysis of nanoindentation tests. By considering stress peaks around stiff aggregates in mortar, the hydrates in the vicinity of the aggregate surfaces are shown to govern mortar failure. Unlike in Portland cement materials, the consideration of only one representative hydrate type in blended cement mixes does not allow for satisfactory model predictions. Instead, a more detailed representation based on several types of hydrates delivers model predicted strength values which are much closer to experimental results. Microfillers such as finely ground quartz and limestone act as strength-increasing reinforcements by filling the capillary porosity at the scale of the hydrates. Supplementary cementitious materials such as slag and fly ash, in turn, are found to increase the hydrates' cohesion once they start to react.

In Chapter 4, it is shown that the age- and composition-dependent creep behavior of cement paste subjected to compressive loads for some minutes up to 30 days can be traced back to an intrinsic (i.e. age- and composition-independent) viscous behavior of the hydrate needles. This result is obtained by downscaling the basic creep strains, as measured in a series of three-minute-long creep tests on cement pastes at early ages, to the hydrate level

and by upscaling the hydrate creep behavior for creep tests lasting for 30 days on 30-year-old cement paste specimen. Notably, in all the experiments, the microstructure of the material is nonaging. The macroscopically observed power-law creep function for time periods of minutes to weeks is reflected in the microscopic creep function which is of power-law-type as well.

Reliable creep upscaling from cement paste to mortar and concrete requires consideration of internal curing effects, i.e. of water migration processes from aggregates to the cement paste matrix, as it is shown in Chapter 5. By introducing two new material constants, namely the initial water uptake capacity of the aggregates and the void filling extent, mathematization of the aforementioned processes is achieved. This allows for very satisfactory predictions of mortar and concrete creep properties based on measured creep properties of cement paste.

By casting relaxometry data obtained from nuclear magnetic resonance (NMR) experiments into a mathematical framework, it was shown in Chapter 6 that the densification of the C-S-H gel is controlled by the available precipitation space. Moreover, the density is shown to be a universal function (i.e. it does not depend on the paste's water-to-cement mass ratio) of the specific precipitation space. This function is of highly nonlinear nature, but it can be traced back to two classes of C-S-H, a totally compact class and a linearly densifying class, respectively. Combining the density evolution with the traditional set of equations which cover the reaction of Portland cement paste, analytical expressions for the phase volume evolutions of clinker, portlandite, solid C-S-H, gel pores, capillary pores, and air voids are obtained. Hence, the obtained model provides a promising improvement of the widely used Powers hydration model.

As a very first application of the novel hydration model, the poroelastic properties of cement pastes are upscaled based on the stiffness of the solid C-S-H nanoparticles in Chapter 7. Taking the results from atomistic modeling for the stiffness of the solid C-S-H nanoparticles as an input into our micromechanics model, allows us to bridge the scales from the one of nanoscopic solid C-S-H all the way up to the macroscopic scale of cementitious materials. Using the eigenstress influence tensor concept to consider the pore pressures within gel and capillary pore spaces, the effect of entrapped water on macroscopic test results has been deciphered. While the homogenized elastic moduli in the case of drained and undrained pore spaces are very close to each other, the homogenized Poisson's ratio is found to be much larger in the undrained case, particularly so at early ages.

In summary, a significant knowledge gain has been achieved in all five key chapters of the thesis at hand. Micromechanics modeling turned out to be a very valuable tool for deciphering mechanisms happening at the microscale, catalyzed by the benefits that the quantification of these mechanisms by means of mathematical modeling provides.

8.3 Perspectives

Given the complexity of cementitious materials, there is still a lot of motivation for future research using microstructural modeling techniques. The very promising multiscale representation of hydrating cement paste incorporating the solid C-S-H nanoparticles and the gel porosity at the smallest scale of observation, as applied for the poroelasticity upscaling, qualifies to be used for strength and creep upscaling as well. This way, one can study the origin of the material failure at the nanoscale by identifying the macrostrength-governing nanoscopic failure mode potentially involving interface failure around the nanoparticles. Creep very likely originates from sliding processes along viscous interfaces within the nanoparticles. Successful casting this mechanism into a mathematical framework based on continuum micromechanics has been already achieved (Shahidi et al., 2014, 2015a,b). This provides the motivation to use

the concept as input for the creep behavior of the C-S-H nanoparticle in the framework of the multiscale material representation developed in this thesis and this way, to upscale the sliding processes occurring at the viscous nano-interfaces all the way up to the creep behavior of concrete.

Creep predictions obtained from our modeling approach follow a power-law creep function, as also found in short-term macroscopic creep tests. However, for loads applied for several months to several years, creep strains evolve logarithmically (Bažant et al., 2011). Deciphering the micromechanical reason for this change of the characteristic shape of the creep function provides also a lot of motivation for future research. Moreover, the modeling campaign was based on three-minute-long creep tests on one- to seven-day-old cement pastes, mortars, and concretes, i.e. the microstructure during the creep test virtually does not change. As for model validation, a 30-day-long creep test on 30-year-old cement paste was used. Again, the microstructure of cement paste remains virtually constant during the test period. If the characteristic time of the hydration-induced microstructure changes is not well separated from the creep period, however, one is faced with so-called aging creep. Extending the model to those situations might also be a next logical step in the future. In this context, the recently studied extension of the Eshelby problem for aging viscoelasticity (Lavergne et al., 2016) might be a very valuable theoretical basis.

As for the C-S-H densification model, future work might focus on the effect of different hydration temperatures. High temperatures during the hydration lead to a very coarse C-S-H gel, while low temperatures and the associated slow hydration reaction lead to very dense and homogeneous C-S-H gel. Incorporating the temperature effect into the densification model will significantly broaden the range of applicability.

The long overdue awareness of the climate-damaging effects of cement production has led to efforts to reduce the cement content in concretes in the recent years. The availability of different cement replacement materials provides scientific challenges, in particular for modeling campaigns. A first step to handle blended cement pastes and mortars within a multiscale micromechanical modeling framework has been made in this thesis. Several other steps might follow and might eventually lead to designing eco-concretes which do not suffer from the major disadvantage, the low early-age strength. In the same spirit, instead of natural virgin aggregates, crushed concrete from construction and demolition waste can be reused for the production of a more environmentally friendly eco-concrete. In order to use this recycled concrete for structural applications, one has to understand its perspectives and limitations, in particular from a micromechanical viewpoint. For instance, the recycled aggregates exhibit a large water absorption, and this significantly reduces the water available for the hydration process and might significantly affect the early-age cracking behavior of concrete.

Bibliography

- Abate, J. and Valkó, P. (2004). Multi-precision Laplace transform inversion. *International Journal for Numerical Methods in Engineering*, 60(5):979–993.
- Acker, P. (2001). Micromechanical analysis of creep and shrinkage mechanisms. In Ulm, F.-J., Bažant, Z., and Wittmann, F., editors, *Creep, shrinkage and durability mechanics of concrete and other quasi-brittle materials*, 6th International Conference CONCREEP@MIT, pages 15–26, Amsterdam. Elsevier.
- Acker, P. and Ulm, F.-J. (2001). Creep and shrinkage of concrete: physical origins and practical measurements. *Nuclear Engineering and Design*, 203(2):143–158.
- Ahrens, T. J., editor (1995). *Mineral Physics & Crystallography: A Handbook of Physical Constants*. American Geophysical Union.
- Allen, A., Thomas, J., and Jennings, H. (2007). Composition and density of nanoscale calcium–silicate–hydrate in cement. *Nature Materials*, 6(4):311–316.
- American Concrete Institute (ACI) Committee 318 (2014). ACI 318-14: Building code requirements for structural concrete.
- Atrushi, D. (2003). *Tensile and compressive creep of early age concrete: testing and modelling*. PhD thesis, Norwegian Univ. of Science and Technology, Trondheim, Norway.
- Barthélémy, J.-F. and Dormieux, L. (2003). Détermination du critère de rupture macroscopique d’un milieu poreux par homogénéisation non linéaire [Determination of a macroscopic failure criterion for porous materials using nonlinear homogenization]. *Comptes Rendus Mécanique*, 331(4):271 – 276.
- Bary, B. (2011). Estimation of poromechanical and thermal conductivity properties of unsaturated isotropically microcracked cement pastes. *International Journal for Numerical and Analytical Methods in Geomechanics*, 35(14):1560–1586.
- Bass, J. (2013). *Elasticity of Minerals, Glasses, and Melts*. American Geophysical Union.
- Bauchy, M., Abdolhosseini Qomi, M., Bichara, C., Ulm, F.-J., and Pellenq, R. (2014). Nanoscale structure of cement: viewpoint of rigidity theory. *The Journal of Physical Chemistry C*, 118(23):12485–12493.
- Bažant, Z., Asghari, A., and Schmidt, J. (1976). Experimental study of creep of hardened Portland cement paste at variable water content. *Matériaux et Constructions*, 9(4):279 – 290.

- Bažant, Z., Hubler, M., and Yu, Q. (2011). Pervasiveness of excessive segmental bridge deflections: Wake-up call for creep. *ACI Structural Journal*, 108(6):766–774.
- Bažant, Z. and L'Hermite, R. (1988). *Mathematical modeling of creep and shrinkage of concrete*. Wiley, Chichester, UK.
- Bažant, Z. and Prasannan, S. (1989a). Solidification theory for concrete creep. I: Formulation. *Journal of Engineering Mechanics (ASCE) (ASCE)*, 115(8):1691–1703.
- Bažant, Z. and Prasannan, S. (1989b). Solidification theory for concrete creep. II: Verification and application. *Journal of Engineering Mechanics (ASCE) (ASCE)*, 115(8):1704–1725.
- Bažant, Z., Yu, Q., and Li, G. (2012). Excessive long-time deflections of prestressed box girders. I: Record-span bridge in Palau and other paradigms. *Journal of Structural Engineering*, 138(6):676 – 686.
- Baweja, S., G.J., D., and Z.P., B. (1998). Triaxial composite model for basic creep of concrete. *Journal of Engineering Mechanics (ASCE)*, 124(9):959 – 965.
- Bentz, D. (2000). CEMHYD3D: A three-dimensional cement hydration and microstructure development modelling package. Version 2.0. *National Institute of Standards and Technology Interagency Report*, 7232.
- Bentz, D., Lura, P., and Roberts, J. (2005). Mixture proportioning for internal curing. *Concrete International*, 27(2):35 – 40.
- Benveniste, Y. (1987). A new approach to the application of Mori-Tanaka's theory in composite materials. *Mechanics of Materials*, 6(2):147–157.
- Bernard, O., Ulm, F.-J., and Germaine, J. (2003a). Volume and deviator creep of calcium-leached cement-based materials. *Cement and Concrete Research*, 33(8):1127–1136.
- Bernard, O., Ulm, F.-J., and Lemarchand, E. (2003b). A multiscale micromechanics-hydration model for the early-age elastic properties of cement-based materials. *Cement and Concrete Research*, 33(9):1293–1309.
- Beurthey, S. and Zaoui, A. (2000). Structural morphology and relaxation spectra of viscoelastic heterogeneous materials. *European Journal of Mechanics-A/Solids*, 19(1):1–16.
- Bishnoi, S. and Scrivener, K. (2009). μic : A new platform for modelling the hydration of cements. *Cement and Concrete Research*, 39(4):266–274.
- Blezard, R. (1998). *Hydration, setting and hardening of Portland cement*, chapter 1, pages 1–24. Butterworth Heinemann, Oxford, UK.
- Bonavetti, V., Rahhal, V., and Irassar, E. (2001). Studies on the carboaluminate formation in limestone filler-blended cements. *Cement and Concrete Research*, 31(6):853–859.
- Boulay, C., Crespini, M., Delsaute, B., and Staquet, S. (2012). Monitoring of the creep and the relaxation behaviour of concrete since setting time, part 1: compression. In *Strategies for Sustainable Concrete Structures*, pages 1 – 10, France. International Conference on Numerical Modeling Strategies for Sustainable Concrete Structures (SSCS).

- Briffaut, M., Benboudjema, F., Torrenti, J.-M., and Nahas, G. (2012). Concrete early age basic creep: Experiments and test of rheological modelling approaches. *Construction and Building Materials*, 36:373 – 380.
- Brisard, S. and Levitz, P. (2013). Small-angle scattering of dense, polydisperse granular porous media: Computation free of size effects. *Physical Review E*, 87(1):013305.
- Bullard, J., Jennings, H., Livingston, R., Nonat, A., Scherer, G., Schweitzer, J., Scrivener, K., and Thomas, J. (2011). Mechanisms of cement hydration. *Cement and Concrete Research*, 41(12):1208–1223.
- Bye, G. (1999). *Portland Cement: Composition, Production and Properties*. Thomas Telford, London, UK.
- Carrier, B., Vandamme, M., Pellenq, R.-M., Bornert, M., Ferrage, E., Hubert, F., and Van Damme, H. (2016). Effect of water on elastic and creep properties of self-standing clay films. *Langmuir*, 35(5).
- Carvalho, M., Calil Júnior, C., Savastano Junior, H., Tubino, R., and Carvalho, M. (2008). Microstructure and mechanical properties of gypsum composites reinforced with recycled cellulose pulp. *Materials Research*, 11:391–397.
- Chatterji, S. and Jeffery, J. (1966). Three-dimensional arrangement of hydration products in set cement paste. *Nature*, 209:1233–1234.
- Chiang, W.-S., Fratini, E., Baglioni, P., Liu, D., and Chen, S.-H. (2012). Microstructure determination of calcium-silicate-hydrate globules by small-angle neutron scattering. *The Journal of Physical Chemistry C*, 116(8):5055–5061.
- Chindaprasirt, P., Jaturapitakkul, C., and Sinsiri, T. (2005). Effect of fly ash fineness on compressive strength and pore size of blended cement paste. *Cement and Concrete Composites*, 27(4):425–428.
- Chindaprasirt, P., Jaturapitakkul, C., and Sinsiri, T. (2007). Effect of fly ash fineness on microstructure of blended cement paste. *Construction and Building Materials*, 21(7):1534–1541.
- Constantinides, G. and Ulm, F.-J. (2004). The effect of two types of C-S-H on the elasticity of cement-based materials: Results from nanoindentation and micromechanical modeling. *Cement and Concrete Research*, 34(1):67–80.
- Constantinides, G. and Ulm, F.-J. (2007). The nanogranular nature of C-S-H. *Journal of the Mechanics and Physics of Solids*, 55(1):64–90.
- Constantinides, G., Ulm, F.-J., and Van Vliet, K. (2003). On the use of nanoindentation for cementitious materials. *Materials and Structures*, 36(3):191–196.
- Coulomb, C. (1776). Sur une application des règles de maximis & minimis à quelques problèmes de statique, relatifs à l’architecture [On the application of rules of maxima and minima in problems of statics, related to architecture]. *Mémoires de Mathématiques et de Physique, Académie Royale des Sciences, Paris*, pages 343–382. In French.
- Coussy, O. (2004). *Poromechanics*. John Wiley & Sons, Chichester, UK.

- Cowin, S. and Mehrabadi, M. (1992). The structure of the linear anisotropic elastic symmetries. *Journal of the Mechanics and Physics of Solids*, 40(7):1459–1471.
- Cusatis, G., Pelessone, D., and Mencarelli, A. (2011). Lattice discrete particle model (ldpm) for failure behavior of concrete. i: Theory. *Cement and Concrete Composites*, 33(9):881–890.
- Delsaute, B., Boulay, C., Granja, J., Carette, J., Azenha, M., Dumoulin, C., Karaikos, G., Deraemaeker, A., and Staquet, S. (2016). Testing concrete E-modulus at very early ages through several techniques: An inter-laboratory comparison. *Strain*, 52(2):91–109.
- Delsaute, B. and Staquet, S. (2014). Monitoring of the creep and the relaxation modelling of concrete under tension and compression. In *RILEM International Symposium on Concrete Modelling - CONMOD 2014*, pages 168 – 175, Paris, France. RILEM.
- Delsaute, B., Staquet, S., and Boulay, C. (2012). Monitoring of the creep and the relaxation behaviour of concrete since setting time, part 2: tension. In *Strategies for Sustainable Concrete Structures*, pages 1 – 11, France. International Conference on Numerical Modeling Strategies for Sustainable Concrete Structures (SSCS).
- Diamond, S. (2004). The microstructure of cement paste and concrete—a visual primer. *Cement and Concrete Composites*, 26(8):919–933.
- Diamond, S. and Bonen, D. (1993). Microstructure of hardened cement paste—A new interpretation. *Journal of the American Ceramic Society*, 76(12):2993–2999.
- Diamond, S. and Huang, J. (2001). The ITZ in concrete – a different view based on image analysis and SEM observations. *Cement and Concrete Composites*, 23(2):179–188.
- Dormieux, L., Kondo, D., and Ulm, F.-J. (2006). *Microporomechanics*. Wiley, Chichester, UK.
- Dormieux, L., Molinari, A., and Kondo, D. (2002). Micromechanical approach to the behavior of poroelastic materials. *Journal of the Mechanics and Physics of Solids*, 50(10):2203–2231.
- Drugan, W. and Willis, J. (1996). A micromechanics-based nonlocal constitutive equation and estimates of representative volume element size for elastic composites. *Journal of the Mechanics and Physics of Solids*, 44(4):497–524.
- Dvorak, G. and Benveniste, Y. (1992). On transformation field analysis of damage evolution in composite materials. *Proceedings of the Royal Society London, Ser. A*, 437(1900):291–310.
- Dym, C. (2004). *Principles of mathematical modeling*. Academic Press, Burlington, USA.
- Eshelby, J. (1957). The determination of the elastic field of an ellipsoidal inclusion, and related problems. *Proceedings of the Royal Society London, Series A*, 241(1226):376–396.
- European Committee for Standardization (2004). EN 1992 Eurocode 2 : Design of concrete structures.
- Feldman, R., Carette, G., and Malhotra, V. (1990). Studies on mechanics of development of physical and mechanical properties of high-volume fly ash-cement pastes. *Cement and Concrete Composites*, 12(4):245–251.

- Fritsch, A., Dormieux, L., and Hellmich, C. (2006). Porous polycrystals built up by uniformly and axisymmetrically oriented needles: homogenization of elastic properties. *Comptes Rendus Mécanique*, 334(3):151–157.
- Fritsch, A. and Hellmich, C. (2007). 'Universal' microstructural patterns in cortical and trabecular, extracellular and extravascular bone materials: Micromechanics-based prediction of anisotropic elasticity. *Journal of Theoretical Biology*, 244(4):597 – 620.
- Fritsch, A., Hellmich, C., and Dormieux, L. (2010). The role of disc-type crystal shape for micromechanical predictions of elasticity and strength of hydroxyapatite biomaterials. *Philosophical Transactions of the Royal Society of London A: Mathematical, Physical and Engineering Sciences*, 368(1917):1913–1935.
- Fritsch, A., Hellmich, C., and Young, P. (2013). Micromechanics-derived scaling relations for poroelasticity and strength of brittle porous polycrystals. *Journal of Applied Mechanics (ASME)*, 80(2):020905.
- Gao, T., Shen, L., Shen, M., Chen, F., and Liu, L. and Gao, L. (2015). Analysis on differences of carbon dioxide emission from cement production and their major determinants. *Journal of Cleaner Production*, 103:160–170.
- Garrault, S., Finot, E., Lesniewska, E., and Nonat, A. (2005). Study of CSH growth on C_3S surface during its early hydration. *Materials and Structures*, 38(4):435–442.
- Gaver, D. (1966). Observing stochastic processes, and approximate transform inversion. *Operations Research*, 14(3):444 – 459.
- Germain, P. (1973). The method of virtual power in continuum mechanics. Part 2: Microstructure. *SIAM Journal on Applied Mathematics*, 25(3):556–575.
- Ghabezloo, S. (2010). Association of macroscopic laboratory testing and micromechanics modelling for the evaluation of the poroelastic parameters of a hardened cement paste. *Cement and Concrete Research*, 40(8):1197 – 1210.
- Gurtin, M. and Sternberg, E. (1962). On the linear theory of viscoelasticity. *Archive for rational mechanics and analysis*, 11(1):291–356.
- Haecker, C., Garboczi, E., Bullard, J., Bohn, R., Sun, Z., Shah, S., and Voigt, T. (2005). Modeling the linear elastic properties of Portland cement paste. *Cement and Concrete Research*, 35(10):1948–1960.
- Halperin, W., Jehng, J.-Y., and Song, Y.-Q. (1994). Application of spin-spin relaxation to measurement of surface area and pore size distributions in a hydrating cement paste. *Magnetic Resonance Imaging*, 12(2):169–173.
- Hansen, T. (1986). Physical structure of hardened cement paste. A classical approach. *Materials and Structures*, 19(6):423–436.
- Hashin, Z. (1983). Analysis of composite materials – a survey. *Journal of Applied Mechanics (ASME)*, 50(3):481–505.
- Hashin, Z. and Shtrikman, S. (1962). A variational approach to the theory of the effective magnetic permeability of multiphase materials. *Journal of Applied Physics (ASME)*, 33(10):3125–3131.

- Hellmich, C., Barthélémy, J.-F., and Dormieux, L. (2004). Mineral–collagen interactions in elasticity of bone ultrastructure—a continuum micromechanics approach. *European Journal of Mechanics A/Solids*, 23(5):783–810.
- Hellmich, C., Celundova, D., and Ulm, F.-J. (2009). Multiporoelasticity of hierarchically structured materials: micromechanical foundations and application to bone. *Journal of Engineering Mechanics (ASCE)*, 135(5):382–394.
- Hellmich, C. and Ulm, F.-J. (2005). Drained and undrained poroelastic properties of healthy and pathological bone: A poro-micromechanical investigation. *Transport in Porous Media*, 58(3):243–268.
- Helmuth, R. and Turk, D. (1966). Elastic moduli of hardened cement paste and tricalcium silicate pastes: Effect of porosity. *Proceedings of a Symposium on the Structure of Portland Cement Paste and Concrete, Highway Research Board Special Report 90, National Academy of Engineering Washington, DC*, pages 135–144.
- Hentz, S., Daudeville, L., and Donzé, F. (2004). Identification and validation of a discrete element model for concrete. *Journal of Engineering Mechanics (ASCE)*, 130(6):709–719.
- Hershey, A. (1954). The elasticity of an isotropic aggregate of anisotropic cubic crystals. *Journal of Applied Mechanics-Transactions (ASME)*, 21(3):236–240.
- Hill, R. (1963). Elastic properties of reinforced solids: Some theoretical principles. *Journal of the Mechanics and Physics of Solids*, 11(5):357–372.
- Hill, R. (1965). A self-consistent mechanics of composite materials. *Journal of the Mechanics and Physics of Solids*, 13(4):213–222.
- Hlobil, M., Šmilauer, V., and Chanvillard, G. (2016). Micromechanical multiscale fracture model for compressive strength of blended cement pastes. *Cement and Concrete Research*, 83:188–202.
- Holuj, F., Drozdowski, M., and Czajkowski, M. (1985a). Brillouin spectrum of $\text{Ca}(\text{OH})_2$. *Solid State Communications*, 56(12):1019–1021.
- Holuj, F., Drozdowski, M., and Czajkowski, M. (1985b). Brillouin spectrum of $\text{Ca}(\text{OH})_2$. *Solid State Communications*, 56(12):1019–1021.
- Hsu, T., Slate, F., Sturman, G., and Winter, G. (1963). Microcracking of plain concrete and the shape of the stress-strain curve. *American Concrete Institute Journal Proceedings*, 60(2):209–224.
- Ioannidou, K., Krakowiak, K., Bauchy, M., Hoover, C., Masoero, E., Yip, S., Ulm, F.-J., Levitz, P., Pellenq, R.-M., and Del Gado, E. (2016). Mesoscale texture of cement hydrates. *Proceedings of the National Academy of Sciences*, 113(8):2029–2034.
- Irfan-ul Hassan, M., Königsberger, M., Reihnsner, R., Hellmich, C., and Pichler, B. (2016). How water-aggregate interactions affect concrete creep: a multiscale analysis. *submitted to the Journal of Nanomechanics and Micromechanics*.
- Irfan-ul Hassan, M., Königsberger, M., Reihnsner, R., Pichler, B., and Hellmich, C. (2014). How water-aggregate interactions affect concrete creep: a multiscale analysis. *submitted to the Journal of Nanomechanics and Micromechanics*.

- Irfan-ul-Hassan, M., Pichler, B., Reihnsner, R., and Hellmich, C. (2016). Elastic and creep properties of young cement paste, as determined from hourly repeated minute-long quasi-static tests. *Cement and Concrete Research*, 82:36–49.
- Japan Society of Civil Engineers (JSCE) (2010). Standard specifications for concrete structures.
- Jennings, H. (2000). A model for the microstructure of calcium silicate hydrate in cement paste. *Cement and Concrete Research*, 30(1):101–116.
- Jennings, H. (2008). Refinements to colloid model of CSH in cement: CM-II. *Cement and Concrete Research*, 38(3):275–289.
- Jennings, H., Dalglish, B., and Pratt, P. (1981). Morphological development of hydrating tricalcium silicate as examined by electron microscopy techniques. *Journal of the American Ceramic Society*, 64(10):567–572.
- Jennings, H. and Tennis, P. (1994). Model for the developing microstructure in Portland cement pastes. *Journal of the American Ceramic Society*, 77(12):3161–3172.
- Jensen, O. and Lura, P. (2006). Techniques and materials for internal water curing of concrete. *Materials and Structures*, 39(9):817 – 825.
- Juenger, M. and Jennings, H. (2001). The use of nitrogen adsorption to assess the microstructure of cement paste. *Cement and Concrete Research*, 31(6):883–892.
- Justs, J., Wyrzykowski, M., Bajare, D., and Lura, P. (2015). Internal curing by superabsorbent polymers in ultra-high performance concrete. *Cement and Concrete Research*, 76:82 – 90.
- Karte, P., Hlobil, M., Reihnsner, R., Dörner, W., Lahayne, O., Eberhardsteiner, J., and Pichler, B. (2015). Unloading-based stiffness characterisation of cement pastes during the second, third and fourth day after production. *Strain*, 51(2).
- Kjellsen, K., Detwiler, R., and Gjörv, O. (1991). Development of microstructures in plain cement pastes hydrated at different temperatures. *Cement and Concrete Research*, 21(1):179–189.
- Kjellsen, K. and Justnes, H. (2004). Revisiting the microstructure of hydrated tricalcium silicate—a comparison to portland cement. *Cement and Concrete Composites*, 26(8):947–956.
- Klee, H. (2009). *The cement sustainability initiative: recycling concrete*. Report of the World Business Council for Sustainable Development.
- Kohlhauser, C. and Hellmich, C. (2013). Ultrasonic contact pulse transmission for elastic wave velocity and stiffness determination: Influence of specimen geometry and porosity. *Engineering Structures*, 47:115–133.
- Königsberger, M., Hellmich, C., and Pichler, B. (2016a). Densification of C-S-H is mainly driven by available precipitation space, as quantified through an analytical cement hydration model based on NMR data. *Cement and Concrete Research*, 88:170–183.
- Königsberger, M., Pichler, B., and Hellmich, C. (2014a). Micromechanics of ITZ-aggregate interaction in concrete – Part I: stress concentration. *Journal of the American Ceramic Society*, 97(2):535–542.

- Königsberger, M., Pichler, B., and Hellmich, C. (2014b). Micromechanics of ITZ-aggregate interaction in concrete – Part II: strength upscaling. *Journal of the American Ceramic Society*, 97(2):543–551.
- Königsberger, M., Irfan-ul-Hassan, M., Pichler, B., and Hellmich, C. (2016b). Downscaling-based identification of non-aging power-law creep of cement hydrates. *Journal of Engineering Mechanics (ASCE)*. DOI: 10.1061/(ASCE)EM.1943-7889.0001169.
- Kosse, S. (2015). Festigkeit zementgebundener Materialien: numerische Simulation und experimentelle Durchführung einaxialer Druckversuche an Zementsteinen, Mörteln und Betonen; [Strength of cementitious materials: numerical simulation and experimental realization of uniaxial strength tests for cement pastes, mortars, and concretes]. Bachelors Thesis, TU Wien – Vienna University of Technology. In German.
- Kröner, E. (1958). Berechnung der elastischen Konstanten des Vielkristalls aus den Konstanten des Einheitskristalls [Computation of the elastic constants of a polycrystal based on the constants of the single crystal]. *Zeitschrift für Physik. A: Hadrons and Nuclei*, 151(4):504–518. In German.
- Lam, L., Wong, Y. L., and Poon, C. S. (2000). Degree of hydration and gel/space ratio of high-volume fly ash/cement systems. *Cement and Concrete Research*, 30(5):747–756.
- Laplanche, P. (2003). *Propriétés mécaniques de bétons durcissants: Analyse comparée des bétons classique et à très hautes performances [Mechanical properties of hardening concrete: A comparative analysis of ordinary and high performance concretes]*. PhD thesis, Ecole Nationale des Ponts et Chaussées, Paris.
- Lavergne, F., Sab, K., Sanahuja, J., Bornert, M., and Toulemonde, C. (2016). Homogenization schemes for aging linear viscoelastic matrix-inclusion composite materials with elongated inclusions. *International Journal of Solids and Structures*, 80:545–560.
- Laws, N. (1977). The determination of stress and strain concentrations at an ellipsoidal inclusion in an anisotropic material. *Journal of Elasticity*, 7(1):91–97.
- Laws, N. and McLaughlin, R. (1978). Self-consistent estimates for the viscoelastic creep compliances of composite materials. *Proceedings of the Royal Society of London A: Mathematical, Physical and Engineering Sciences*, 359(1697):251–273.
- Levin, V. (1967). Thermal expansion coefficient of heterogeneous materials. *Mekhanika Tverdogo Tela*, 2(1):83–94.
- Li, S. and Gao, X. (2013). *Handbook of Micromechanics and Nanomechanics*. Pan Stanford Publishing, Singapore.
- Lin, F. and Meyer, C. (2009). Hydration kinetics modeling of Portland cement considering the effects of curing temperature and applied pressure. *Cement and Concrete Research*, 39(4):255–265.
- Lothenbach, B., Scrivener, K., and Hooton, R. (2011). Supplementary cementitious materials. *Cement and Concrete Research*, 41(12):1244–1256.
- Lothenbach, B. and Winnefeld, F. (2006). Thermodynamic modelling of the hydration of Portland cement. *Cement and Concrete Research*, 36(2):209–226.

- Mang, H. and Hofstetter, G. (2000). *Festigkeitslehre [Strength of Materials]*. Springer-Verlag, Wien, New York. In German.
- Manzano, H., Masoero, E., Lopez-Arbeloa, I., and Jennings, H. (2013). Shear deformations in calcium silicate hydrates. *Soft Matter*, 9(30):7333–7341.
- Manzano, H., Moeini, S., Marinelli, F., Van Duin, A., Ulm, F.-J., and Pellenq, R.-M. (2012). Confined water dissociation in microporous defective silicates: Mechanism, dipole distribution, and impact on substrate properties. *Journal of the American Chemical Society*, 134(4):2208–2215.
- MATLAB (2013). *Version R2013(b) including MATLAB Optimization Toolbox Version 6.4*. The MathWorks Inc., Natick, Massachusetts.
- Meredith, P., Donald, A., and Luke, K. (1995). Pre-induction and induction hydration of tricalcium silicate: an environmental scanning electron microscopy study. *Journal of Materials Science*, 30(8):1921–1930.
- Meyer, W. (2012). *Concepts of Mathematical Modeling*. Dover Publications, New York, US.
- Mohr, O. (1900). Welche Umstände bedingen die Elastizitätsgrenze und den Bruch eines Materials [What reasons cause the elastic limit and the failure of a material]. *Zeitschrift des Vereins Deutscher Ingenieure*, 46(1524-1530):1572–1577. In German.
- Monteiro, P. J. and Chang, C. (1995). The elastic moduli of calcium hydroxide. *Cement and Concrete Research*, 25(8):1605–1609.
- Mori, T. and Tanaka, K. (1973). Average stress in matrix and average elastic energy of materials with misfitting inclusions. *Acta Metallurgica*, 21(5):571–574.
- Muller, A. (2014). *Characterization of porosity & CSH in cement pastes by ^1H NMR*. PhD thesis, École Polytechnique Fédérale de Lausanne.
- Muller, A., Scrivener, K., Gajewicz, A., and McDonald, P. (2012). Densification of C–S–H measured by ^1H NMR relaxometry. *The Journal of Physical Chemistry C*, 117(1):403–412.
- Muller, A., Scrivener, K., Gajewicz, A., and McDonald, P. (2013). Use of bench-top NMR to measure the density, composition and desorption isotherm of C–S–H in cement paste. *Microporous and Mesoporous Materials*, 178:99–103.
- Nachbaur, L., Nkinamubanzi, P.-C., Nonat, A., and Mutin, J.-C. (1998). Electrokinetic properties which control the coagulation of silicate cement suspensions during early age hydration. *Journal of Colloid and Interface Science*, 202(2):261–268.
- Neville, A. (1964). Creep of concrete as a function of its cement paste content. *Magazine of Concrete Research*, 16(46):21–30.
- Neville, A. (1995). *Properties of concrete*. Pitman Publishing, London, UK, third edition.
- Němeček, J., Šmilauer, V., and Kopecký, L. (2011). Nanoindentation characteristics of alkali-activated aluminosilicate materials. *Cement and Concrete Composites*, 33(2):163–170.
- Odler, I. (1998). *Hydration, setting and hardening of Portland cement*, chapter 6, pages 241–297. Butterworth Heinemann, Oxford, UK.

- Ollivier, J., Maso, J., and Bourdette, B. (1995). Interfacial transition zone in concrete. *Advanced Cement Based Materials*, 2(1):30–38.
- Pane, I. and Hansen, W. (2005). Investigation of blended cement hydration by isothermal calorimetry and thermal analysis. *Cement and Concrete Research*, 35(6):1155–1164.
- Pellenq, R.-M., Kushima, A., Shahsavari, R., Van Vliet, K., Buehler, M., Yip, S., and Ulm, F.-J. (2009). A realistic molecular model of cement hydrates. *Proceedings of the National Academy of Sciences*, 106(38):16102–16107.
- Pichler, B. and Hellmich, C. (2010). Estimation of influence tensors for eigenstressed multiphase elastic media with nonaligned inclusion phases of arbitrary ellipsoidal shape. *Journal of Engineering Mechanics (ASCE)*, 136(8):1043–1053.
- Pichler, B. and Hellmich, C. (2011). Upscaling quasi-brittle strength of cement paste and mortar: A multi-scale engineering mechanics model. *Cement and Concrete Research*, 41(5):467–476.
- Pichler, B., Hellmich, C., and Eberhardsteiner, J. (2009). Spherical and acicular representation of hydrates in a micromechanical model for cement paste: Prediction of early-age elasticity and strength. *Acta Mechanica*, 203(3-4):137–162.
- Pichler, B., Hellmich, C., Eberhardsteiner, J., Wasserbauer, J., Termkhajornkit, P., Barbarulo, R., and Chanvillard, G. (2013a). Effect of gel-space ratio and microstructure on strength of hydrating cementitious materials: An engineering micromechanics approach. *Cement and Concrete Research*, 45:55–68.
- Pichler, B., Hellmich, C., Eberhardsteiner, J., Wasserbauer, J., Termkhajornkit, P., Barbarulo, R., and Chanvillard, G. (2013b). The Counteracting Effects of Capillary Porosity and of Unhydrated Clinker Grains on the Macroscopic Strength of Hydrating Cement Paste—A Multiscale Model. In *Mechanics and Physics of Creep, Shrinkage, and Durability of Concrete: A Tribute to Zdeněk P. Bažant*, pages 40–47. ASCE.
- Pichler, B., Scheiner, S., and Hellmich, C. (2008). From micron-sized needle-shaped hydrates to meter-sized shotcrete tunnel shells: Micromechanical upscaling of stiffness and strength of hydrating shotcrete. *Acta Geotechnica*, 3(4):273–294.
- Popper, K. (1959). *The logic of scientific discovery*. Hutchinson & Co, London, UK.
- Powers, T. (1958). Structure and physical properties of hardened Portland cement paste. *Journal of the American Ceramic Society*, 41(1):1–6.
- Powers, T. and Brownyard, T. (1946–1947). Studies of the physical properties of hardened Portland cement paste. *American Concrete Institute Journal Proceedings*, 18(2–8):101–992.
- Pratt, P., Ghose, A., Skalny, J., and Hewlett, P. (1983). Electron microscope studies of portland cement microstructures during setting and hardening [and discussion]. *Philosophical Transactions of the Royal Society of London. Series A, Mathematical and Physical Sciences*, pages 93–103.
- Presser, V., Gerlach, K., Vohrer, A., Nickel, K. G., and Dreher, W. F. (2010). Determination of the elastic modulus of highly porous samples by nanoindentation: a case study on sea urchin spines. *Journal of Materials Science*, 45(9):2408–2418.

- Qomi, M., Bauchy, M., Ulm, F.-J., and Pellenq, R.-M. (2014). Anomalous composition-dependent dynamics of nanoconfined water in the interlayer of disordered calcium-silicates. *The Journal of chemical physics*, 140(5):054515.
- Read Jr, W. (1950). Stress analysis for compressible viscoelastic materials. *Journal of Applied Physics*, 21(7):671–674.
- Richardson, I. (1999). The nature of CSH in hardened cements. *Cement and Concrete Research*, 29(8):1131–1147.
- Richardson, I. (2000). The nature of the hydration products in hardened cement pastes. *Cement and Concrete Composites*, 22(2):97–113.
- Richardson, I. (2004). Tobermorite/jennite-and tobermorite/calcium hydroxide-based models for the structure of CSH: applicability to hardened pastes of tricalcium silicate, β -dicalcium silicate, portland cement, and blends of portland cement with blast-furnace slag, metakaolin, or silica fume. *Cement and Concrete Research*, 34(9):1733–1777.
- Richardson, I. and Groves, G. (1993). The incorporation of minor and trace elements into calcium silicate hydrate (CSH) gel in hardened cement pastes. *Cement and Concrete Research*, 23(1):131–138.
- Rossi, P., Godart, N., Robert, J., Gervais, J., and Bruhat, D. (1994). Investigation of the basic creep of concrete by acoustic emission. *Materials and Structures*, 27(113):510 – 514.
- Rossi, P., Tailhan, J.-L., Le Maou, F., Gaillet, L., and Martin, E. (2011). Basic creep behavior of concretes investigation of the physical mechanisms by using acoustic emission. *Cement and Concrete Research*, 42(1):61 – 73.
- Sadowski, P., Kowalczyk-Gajewska, K., and Stupkiewicz, S. (2015). Classical estimates of the effective thermoelastic properties of copper–graphene composites. *Composites Part B: Engineering*, 80:278–290.
- Salençon, J. (2001). *Handbook of continuum mechanics: general concepts, Thermoelasticity*. Springer Verlag, Berlin, Heidelberg, New York.
- Sanahuja, J. (2013a). Effective behaviour of ageing linear viscoelastic composites: Homogenization approach. *International Journal of Solids and Structures*, 50(19):2846 – 2856.
- Sanahuja, J. (2013b). Effective behaviour of ageing linear viscoelastic composites: Homogenization approach. *International Journal of Solids and Structures*, 50(19):2846–2856.
- Sanahuja, J. and Dormieux, L. (2010). Creep of a C-S-H gel: a micromechanical approach. *Anais da Academia Brasileira de Ciências*, 82(1):25–41.
- Sanahuja, J., Dormieux, L., and Chanvillard, G. (2007). Modelling elasticity of a hydrating cement paste. *Cement and Concrete Research*, 37(10):1427–1439.
- Sanahuja, J., Dormieux, L., Meille, S., Hellmich, C., and Fritsch, A. (2010). Micromechanical explanation of elasticity and strength of gypsum: from elongated anisotropic crystals to isotropic porous polycrystals. *Journal of Engineering Mechanics (ASCE)*, 136(2):239–253.
- Sarris, E. and Constantinides, G. (2013). Finite element modeling of nanoindentation on C–S–H: Effect of pile-up and contact friction. *Cement and Concrete Composites*, 36:78–84.

- Scheiner, S. (2009). *Computational Mechanics and Physics Contributions to Corrosion, Geotechnical, Concrete, and Biomedical Engineering: Development and Experimental Validation of Semi-analytical and Numerical Models*. PhD thesis, TU Wien - Vienna University of Technology.
- Scheiner, S. and Hellmich, C. (2009). Continuum microviscoelasticity model for aging basic creep of early-age concrete. *Journal of Engineering Mechanics (ASCE) (ASCE)*, 135(4):307–323.
- Schwarzl, F. and Struik, L. (1968). Analysis of relaxation measurements. *Advances in molecular relaxation processes*, 1(3):201–255.
- Scrivener, K. (2004). Backscattered electron imaging of cementitious microstructures: Understanding and quantification. *Cement and Concrete Composites*, 26(8):935–945.
- Scrivener, K., Crumbie, A., and Laugesen, P. (2004). The interfacial transition zone (ITZ) between cement paste and aggregate in concrete. *Interface Science*, 12(4):411–421.
- Scrivener, K. and Nonat, A. (2011). Hydration of cementitious materials, present and future. *Cement and Concrete Research*, 41(7):651–665.
- Sercombe, J., Hellmich, C., Ulm, F.-J., and Mang, H. (2000). Modeling of early-age creep of shotcrete. I: model and model parameters. *Journal of Engineering Mechanics (ASCE)*, 126(3):284–291.
- Shah, S. and Chandra, S. (1968). Critical stress, volume change, and microcracking of concrete. *American Concrete Institute Journal Proceedings*, 65(9):770–780.
- Shah, S. and Sankar, R. (1987). Internal cracking and strain softening response of concrete under uniaxial compression. *American Concrete Institute Materials Journal*, 84(3):200–212.
- Shah, S. and Winter, G. (1966). Inelastic behavior and fracture of concrete. *American Concrete Institute Journal Proceedings*, 63(9):925–930.
- Shahidi, M., Pichler, B., and Hellmich, C. (2014). Viscous interfaces as source for material creep: A continuum micromechanics approach. *European Journal of Mechanics-A/Solids*, 45:41–58.
- Shahidi, M., Pichler, B., and Hellmich, C. (2015a). Interfacial micromechanics assessment of classical rheological models. I: Single interface size and viscosity. *Journal of Engineering Mechanics (ASCE)*, 142(3):04015092.
- Shahidi, M., Pichler, B., and Hellmich, C. (2015b). Interfacial micromechanics assessment of classical rheological models. II: Multiple interface sizes and viscosities. *Journal of Engineering Mechanics (ASCE)*, 142(3):04015093.
- Shahidi, M., Pichler, B., Wendner, R., Scheiner, S., and Hellmich, C. (2015c). Interfacial micromechanics assessment of rheological chain models and their application to early-age creep of concrete. In *10th International Conference on Mechanics and Physics of Creep, Shrinkage, and Durability of Concrete and Concrete Structures (CONCREEP-10)*, pages 260–269.
- Sips, R. (1951). General theory of deformation of viscoelastic substances. *Journal of Polymer Science*, 7(2-3):191–205.

- Sorelli, L., Constantinides, G., Ulm, F.-J., and Toutlemonde, F. (2008). The nano-mechanical signature of ultra high performance concrete by statistical nanoindentation techniques. *Cement and Concrete Research*, 38(12):1447 – 1456.
- Speziale, S., Reichmann, H., Schilling, F., Wenk, H., and Monteiro, P. (2008). Determination of the elastic constants of portlandite by brillouin spectroscopy. *Cement and Concrete Research*, 38(10):1148 – 1153.
- Stefan, L., Benboudjema, F., Torrenti, J.-M., and Bissonnette, B. (2010). Prediction of elastic properties of cement pastes at early ages. *Computational Materials Science*, 47(3):775–784.
- Stroud, A. (1971). *Approximate calculation of multiple integrals*. Prentice-Hall, New Jersey, USA.
- Stutzman, P. (2001). Scanning electron microscopy in concrete petrography. *Material Science of Concrete Special Volume: Proceedings of the Workshop on the Role of Calcium Hydroxide in Concrete*, pages 59–72.
- Sun, Z., Garboczi, E., and Shah, S. (2007). Modeling the elastic properties of concrete composites: Experiment, differential effective medium theory, and numerical simulation. *Cement and Concrete Composites*, 29(1):22–38.
- Tamtsia, B. and Beaudoin, J. (2000). Basic creep of hardened cement paste: A re-examination of the role of water. *Cement and Concrete Research*, 30(9):1465–1475.
- Tamtsia, B., Beaudoin, J., and Marchand, J. (2004). The early age short-term creep of hardening cement paste: load-induced hydration effects. *Cement and Concrete Composites*, 26(5):481–489.
- Taplin, J. (1959). A method for following the hydration reaction in Portland cement paste. *Australian Journal of Applied Science*, 10(3):329–345.
- Taylor, H. F. W. (1997). *Cement chemistry*. Thomas Telford Publishing, London, UK, 2nd edition.
- Tennis, P. and Jennings, H. (2000). A model for two types of calcium silicate hydrate in the microstructure of portland cement pastes. *Cement and Concrete Research*, 30(6):855–863.
- Termkhajornkit, P. and Barbarulo, R. (2012). Modeling the coupled effects of temperature and fineness of Portland cement on the hydration kinetics in cement paste. *Cement and Concrete Research*, 42(3):526–538.
- Termkhajornkit, P., Vu, Q. H., Barbarulo, R., Daronnat, S., and Chanvillard, G. (2014). Dependence of compressive strength on phase assemblage in cement pastes: Beyond gel-space ratio — Experimental evidence and micromechanical modeling. *Cement and Concrete Research*, 56(0):1–11.
- Thomas, J., Biernacki, J., Bullard, J., Bishnoi, S., Dolado, J., Scherer, G., and Luttge, A. (2011). Modeling and simulation of cement hydration kinetics and microstructure development. *Cement and Concrete Research*, 41(12):1257–1278.
- Thomas, J. and Jennings, H. (2006). A colloidal interpretation of chemical aging of the C-S-H gel and its effects on the properties of cement paste. *Cement and Concrete Research*, 36(1):30–38.

- Torquato, S. (2013). *Random Heterogeneous Materials: Microstructure and Macroscopic Properties*, volume 16. Springer, New York.
- TU1404, C. A. (2016). Towards the next generation of standards for service life of cement-based materials and structures. <http://www.tu1404.eu>. Accessed: 2016-09-01.
- Ulm, F.-J. and Coussy, O. (1995). Modeling of thermochemomechanical couplings of concrete at early ages. *Journal of Engineering Mechanics (ASCE)*, 121(7):785–794.
- Ulm, F.-J. and Coussy, O. (1996). Strength growth as chemo-plastic hardening in early age concrete. *Journal of Engineering Mechanics (ASCE)*, 122(12):1123–1132.
- Ulm, F. J. and Constantinides, G. and Heukamp, F. H. (2004). Is concrete a poromechanics materials? – a multiscale investigation of poroelastic properties. *Materials and Structures*, 37(1):43 – 58.
- Valkó, P. and Abate, J. (2004). Comparison of sequence accelerators for the Gaver method of numerical Laplace transform inversion. *Computers & Mathematics with Applications*, 48(3):629–636.
- Valori, A., McDonald, P., and Scrivener, K. (2013). The morphology of C–S–H: Lessons from ^1H nuclear magnetic resonance relaxometry. *Cement and Concrete Research*, 49:65–81.
- Van Breugel, K. (1995a). Numerical simulation of hydration and microstructural development in hardening cement-based materials (I) theory. *Cement and Concrete Research*, 25(2):319–331.
- Van Breugel, K. (1995b). Numerical simulation of hydration and microstructural development in hardening cement-based materials: (II) applications. *Cement and Concrete Research*, 25(3):522–530.
- Vandamme, M. (2008). *The nanogranular origin of concrete creep: a nanoindentation investigation of microstructure and fundamental properties of calcium-silicate-hydrates*. PhD thesis, Massachusetts Institute of Technology.
- Vandamme, M., Bažant, Z., and Keten, S. (2015). Creep of lubricated layered nano-porous solids and application to cementitious materials. *Journal of Nanomechanics and Micromechanics*, 5(4):04015002.
- Vandamme, M. and Ulm, F.-J. (2009). Nanogranular origin of concrete creep. *Proceedings of the National Academy of Sciences of the United States of America*, 106(26):10552 – 10557.
- Vandamme, M. and Ulm, F.-J. (2013). Nanoindentation investigation of creep properties of calcium silicate hydrates. *Cement and Concrete Research*, 52:38–52.
- Velez, K., Maximilien, S., Damidot, D., Fantozzi, G., and Sorrentino, F. (2001). Determination by nanoindentation of elastic modulus and hardness of pure constituents of Portland cement clinker. *Cement and Concrete Research*, 31(4):555–561.
- Venkovic, N., Sorelli, L., Sudret, B., Yalamas, T., and Gagné, R. (2013). Uncertainty propagation of a multiscale poromechanics-hydration model for poroelastic properties of cement paste at early-age. *Probabilistic Engineering Mechanics*, 32:5–20.

- Vorel, J., Šmilauer, V., and Bittnar, Z. (2012). Multiscale simulations of concrete mechanical tests. *Journal of Computational and Applied Mathematics*, 236(18):4882–4892.
- Šmilauer, V., Hlaváček, P., Škvára, F., Šulc, R., Kopecký, L., and Němeček, J. (2011). Micromechanical multiscale model for alkali activation of fly ash and metakaolin. *Journal of Materials Science*, 46(20):6545–6555.
- Wang, Y., Ye, G., and van Breugel, K. (2013). Microstructure of cement paste blended with micronized sand (MS). In *Durability of Building Materials and Components*, pages 61–84. Springer.
- Wasserbauer, J. (2014). *Mechanical properties of microstructural components of inorganic material*. PhD thesis, Vysoké učení technické v Brně. Fakulta chemická, Brno, Czech Republic.
- Williamson, R. (1972). Solidification of portland cement. *Progress in Materials Science*, 15(3):189–286.
- Worrell, E., Price, L., Martin, N., Hendriks, C., and Meida, L. (2001). Carbon dioxide emissions from the global cement industry. *Annual Review of Energy and the Environment*, 26(1):303–329.
- Wray, P. and Scrivener, K. (2012). Straight talk with Karen Scrivener on cements, CO₂ and sustainable development. *American Ceramic Society Bulletin*, 91:47–50.
- Wriggers, P. and Moftah, S. (2006). Mesoscale models for concrete: Homogenisation and damage behaviour. *Finite Elements in Analysis and Design*, 42(7):623–636.
- Wyrzykowski, M. and Lura, P. (2013). Controlling the coefficient of thermal expansion of cementitious materials—a new application for superabsorbent polymers. *Cement and Concrete Composites*, 35(1):49–58.
- Wyrzykowski, M., Lura, P., Pesavento, F., and Gawin, D. (2011). Modeling of internal curing in maturing mortar. *Cement and Concrete Research*, 41(12):1349 – 1356.
- Ye, G., Liu, X., De Schutter, G., Poppe, A.-M., and Taerwe, L. (2007). Influence of limestone powder used as filler in scc on hydration and microstructure of cement pastes. *Cement and Concrete Composites*, 29(2):94–102.
- Ylmén, R., Jäglid, U., Steenari, B.-M., and Panas, I. (2009). Early hydration and setting of Portland cement monitored by IR, SEM and Vicat techniques. *Cement and Concrete Research*, 39(5):433–439.
- Zadeh, V. and Bobko, C. (2013). Nanoscale mechanical properties of concrete containing blast furnace slag and fly ash before and after thermal damage. *Cement and Concrete Composites*, 37:215–221.
- Zaoui, A. (2002). Continuum micromechanics: Survey. *Journal of Engineering Mechanics (ASCE) (ASCE)*, 128(8):808–816.
- Zhang, Q., Le Roy, R., Vandamme, M., and Zuber, B. (2014). Long-term creep properties of cementitious materials: Comparing microindentation testing with macroscopic uniaxial compressive testing. *Cement and Concrete Research*, 58:89–98.

- Zhutovsky, S. and Kovler, K. (2012). Effect of internal curing on durability-related properties of high performance concrete. *Cement and Concrete Research*, 42(1):20 – 26.
- Zimbelmann, R. (1985). A contribution to the problem of cement-aggregate bond. *Cement and Concrete Research*, 15(5):801–808.

Personal information

Curriculum Vitae

Personal Data

Name:	Markus Königsberger
Academic Degree:	Dipl.-Ing.
Date of Birth:	26th August 1987
Place of Birth:	St. Pölten, Austria
Nationality:	Austrian
Current address:	Guntherstraße 13/20, 1150 Wien, Austria

Education

11/2012 – 10/2015	Doctoral studies in Civil Engineering at Vienna University of Technology (TU-Wien), Vienna, Austria
02/2011 – 10/2012	Master's studies in Civil Engineering at TU-Wien
03/2008 – 01/2011	Bachelor's studies in Civil Engineering at TU-Wien
09/2002 – 06/2007	Technical High School for Civil Engineering, Krems/Donau, Austria

Work Experience

11/2012 – 10/2015	University Assistant, Institute for Mechanics of Materials and Structures, Vienna University of Technology
01/2011 – 05/2012	Construction Designer at “Petz Ziviltechniker”, Vienna, Austria, part-time work
01/2008 – 09/2010	Technical Drafter at “Harrer Ziviltechniker”, Krems/Donau, Austria, part-time work

Activities Abroad

04/2016	Research stay at ULB Brussels, Belgium
06/2016	Research stay at CVUT Prague, Czech Republic

Awards and Scholarships

2013	Honorary price – awarded to the 50 best master's students in Austria, granted by the Federal Ministry of Science, Research, and Economy
2012	Research Scholarship, granted for 5 months by the Institute for Mechanics of Materials and Structures, Vienna University of Technology
2008, 2009, 2010	Award for excellent performance as a student, granted by the Faculty of Civil Engineering, Vienna University of Technology

Scientific Dissemination

Publications

- M. Königsberger, B. Pichler, and C. Hellmich. Micromechanics of ITZ-aggregate interaction in concrete – Part I: stress concentration. *Journal of the American Ceramic Society*, 97(2): 535–542, 2014a.
- M. Königsberger, B. Pichler, and C. Hellmich. Micromechanics of ITZ-aggregate interaction in concrete – Part II: strength upscaling. *Journal of the American Ceramic Society*, 97(2): 543–551, 2014b.
- M. Königsberger, C. Hellmich, and B. Pichler. Densification of C-S-H is mainly driven by available precipitation space, as quantified through an analytical cement hydration model based on NMR data. *Cement and Concrete Research*, 88:170–183, 2016a.
- M. Königsberger, M. Irfan-ul-Hassan, B. Pichler, and C. Hellmich. Downscaling-based identification of non-aging power-law creep of cement hydrates. *Journal of Engineering Mechanics (ASCE)*, 2016b. DOI: 10.1061/(ASCE)EM.1943-7889.0001169.
- M. Irfan-ul Hassan, M. Königsberger, R. Reihnsner, C. Hellmich, and B. Pichler. How water-aggregate interactions affect concrete creep: a multiscale analysis. *submitted to the Journal of Nanomechanics and Micromechanics*, 2016.
- M. Hlobil, M. Königsberger, P. Termkhajornkit, R. Barbarulo, C. Hellmich, and B. Pichler. Hydration-driven evolution of compressive strength of OPC and blended cementitious materials: microstructural characterization, strength testing, and multiscale modeling. *planned to be submitted to the Cement and Concrete Research*, 2016.
- M. Königsberger, B. Pichler, and C. Hellmich. Molecular-to-continuum poroelasticity upscaling of hydrating cement pastes, considering progressive C-S-H gel densification. *planned to be submitted to Cement and Concrete Research*, 2016c.

Conference Papers

- M. Königsberger, B. Pichler, and C. Hellmich. How do porous interfacial transition zones (ITZ) trigger elastic limits of concrete?-micromechanics of ITZ failure and ITZ-aggregate separation. In C. Hellmich, B. Pichler, and D. Adam, editors, *Proceedings of the Fifth Biot Conference on Poromechanics (BIOT-5), Vienna, Austria*, pages 1847–1856. ASCE, 2013.
- M. Königsberger, B. Pichler, and C. Hellmich. ITZ-induced crack initiation in concrete: Micromechanics-based sensitivity analyses regarding concrete phase properties. In N. Bćanić, H. Mang, G. Meschke, and R. De Borst, editors, *Computational Modelling of Concrete Structures (EURO-C 2014), St. Anton, Austria*, pages 307–317. CRC Press, 2014a.
- M. Königsberger, B. Pichler, and C. Hellmich. Micromechanics multiscale approach for ITZ-induced crack initiation in concrete. In B. Topping and P. Iványi, editors, *Proceedings of the Twelfth International Conference on Computational Structures Technology (CST 2014), Naples, Italy*. Civil-Comp Press, 2014b. Paper 84, 19 pages.

- M. Königsberger, B. Pichler, and C Hellmich. Micromechanics of ITZ-aggregate interaction in concrete: Crack initiation. In K. Li, P. Yan, and R. Yang, editors, *Proceedings of the RILEM International Symposium on Concrete Modelling (CONMOD 2014)*, Beijing, China, pages 215–221. RILEM, 2014. ISBN 978-2-35158-140-7.
- M. Königsberger, B. Pichler, and Hellmich C. Micromechanics of hydrating cement pastes considering C-S-H gel densification. In C. Hellmich, B. Pichler, and J. Kolleger, editors, *Proceedings of the 10th International Conference on Mechanics and Physics of Creep, Shrinkage, and Durability of Concrete and Concrete Structures (CONCREEP 10)*, Vienna, Austria, pages 574–583. American Society of Civil Engineers (ASCE), 2016a.
- M. Königsberger, M. Irfan-ul Hassan, B. Pichler, and Hellmich C. Short-term creep of cement paste: Experiments and multiscale modeling. In O.M. Jensen, editor, *Materials, Systems and Structures in Civil Engineering, MSSCE 2016, Lyngby, Copenhagen, Denmark*. RILEM, 2016b. 9 pages.

Conference Presentations and Posters

- M. Königsberger, B. Pichler, and C. Hellmich. How do porous interfacial transition zones (ITZ) trigger elastic limits of concrete?-micromechanics of ITZ failure and ITZ-aggregate separation. Oral presentation at the “Fifth Biot Conference on Poromechanics (BIOT-5)”, Vienna, Austria, 2013.
- M. Königsberger, B. Pichler, and C. Hellmich. Micromechanics of ITZ-aggregate interaction in concrete: Stress concentration and strength upscaling, a. Oral presentation at the “19th Inter-Institute Seminar for Young Researchers”, Vienna, Austria, 2013.
- M. Königsberger, B. Pichler, and C Hellmich. ITZ-induced crack onset in concrete: A micromechanics approach, b. Oral presentation at the “XII. International Conference on Computational Plasticity (COMPLAS XII)”, Barcelona, Spain, 2013.
- M Königsberger, B Pichler, and C Hellmich. ITZ-induced crack initiation in concrete: Micromechanics-based sensitivity analyses regarding concrete phase properties, a. Oral presentation at the conference “Computational Modelling of Concrete Structures (EURO-C 2014)”, St. Anton, Austria, 2014.
- M. Königsberger, B. Pichler, and C. Hellmich. Micromechanics multiscale approach for ITZ-induced crack initiation in concrete, b. Oral presentation at the Twelfth International Conference on Computational Structures Technology (CST 2014), Naples, Italy, 2014.
- M. Königsberger, B. Pichler, and C. Hellmich. Micromechanics of ITZ-induced crack initiation in concrete, a. Oral presentation at the “14th European Mechanics of Materials Conference (EMMC14)”, Gothenburg, Sweden, 2014.
- M. Königsberger, B. Pichler, and Hellmich C. Micromechanics of hydrating cement pastes considering C-S-H gel densification, b. Oral presentation at the “10th International Conference on Mechanics and Physics of Creep, Shrinkage, and Durability of Concrete and Concrete Structures (CONCREEP 10)”, Vienna, Austria, 2015.
- M. Königsberger, B. Pichler, and C. Hellmich. Micromechanics of hydrating cement pastes considering c-s-h gel densification, c. Poster presentation at the “1st Vienna Young Scientists Symposium”, Vienna, Austria, 2015.

- M. Königsberger, B. Pichler, and C. Hellmich. Micromechanics of hydrating cement pastes considering progressive c-s-h gel densification, d. Oral presentation at the “3rd Polish Congress of Mechanics & 21st Computer Methods in Mechanics (PCM-CMM 2015)”, Gdansk, Poland, Vienna, Austria, 2015.
- M. Königsberger, B. Pichler, and C. Hellmich. Upscaling of creep of calcium-silicate-hydrates to creep of concrete by means of homogenization schemes, e. Oral presentation at the “12th World Congress on Computational Mechanics & 6th Asia-Pacific Congress on Computational Mechanics (WCCM XII & APCOM VII)”, Seoul, Korea, 2016.